Ollscoil na hÉireann, Corcaigh

National University of Ireland, Cork

Simplified Electric Vehicle Powertrain Modelling

Thesis presented by

Kevin Davis BE (Elec) MBA MSc

ORCID 0000-0002-2344-6350

for the degree of

Doctor of Philosophy

University College Cork

School of Engineering

Head of School: Dr. Jorge Oliveira

Supervisor: Dr. John G. Hayes

2020

Declaration

"This is to certify that the work I am submitting is my own and has not been submitted for another degree, either at University College Cork or elsewhere. All external references and sources are clearly acknowledged and identified within the contents. I have read and understood the regulations of University College Cork concerning plagiarism."

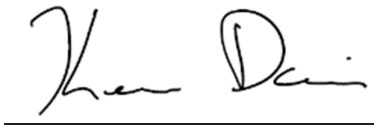

Abstract

Rapid development and adoption of electric vehicle technology has driven the requirement for simplified powertrain models. In this thesis, a simplified electric vehicle powertrain (SEVP) model, which calculates energy consumption for a battery electric vehicle (BEV) based on the minimum number of published vehicle parameters, is presented. The SEVP utilises published coast-down coefficients to model the tractive force and simplifies the traction motor model by using a surface-mounted permanent (SPM) motor. The SEVP is benchmarked for energy consumption estimation, with two industry-standard vehicle simulators, ADVISOR and FASTSim. The comparison is enabled by combining all three simulators in a single MATLAB model, which permits the interchange of the individual powertrain component models and establishes their impact on the cumulative energy consumption in a drive cycle. The three simulators are validated for ten BEVs using dynamometer test data from Argonne National Laboratory. Energy consumption estimation deficiencies of the SEVP are addressed by; (i) a simple cabin thermal load model, and (ii) including machine saturation and flux weakening in the SPM model.

For electrical circuit simulation, the ideal battery model of the SEVP was expanded to include a Lithium-ion (Li-ion) battery pack model and the SPM motor was replaced with a more complex internal permanent magnet (IPM) design. In the Li-ion model, the output voltage is a function of the depth of discharge and a simple ageing function is included to estimate battery capacity over the lifetime of the vehicle. A comparison of the choice of internal impedance network on the dynamic performance of the battery model is conducted. The IPM motor model parameters are derived based on finite element analysis (FEA) of five traction motor designs, rated from 50 kW to 165 kW. The FEA models are validated based on test data from Oakridge National Laboratory.

Finally, an energy management strategy (EMS) for a fuel cell electric vehicle (FCEV) is proposed. The EMS minimises the fuel consumption and the overall operating costs. Prerequisites for achievement of the minimum overall operating costs are minimising the battery and the fuel cell degradation.

List of Publications

Journal.

K. Davis and J. G. Hayes, "Fuel cell vehicle energy management strategy based on the cost of ownership," *IET Electrical Systems in Transportation*, vol. 9, no. 4, pp. 226-236, 12 2019, doi: 10.1049/iet-est.2019.0021.

Conferences.

J. G. Hayes and K. Davis, "Simplified electric vehicle powertrain model for range and energy consumption based on EPA coast-down parameters and test validation by Argonne National Lab data on the Nissan Leaf," 2014 IEEE Transportation Electrification Conf. and Expo (ITEC), Dearborn, MI, 2014, pp. 1-6, doi: 10.1109/ITEC.2014.6861831.

K. Davis and J. G. Hayes, "Analysis of electric vehicle powertrain simulators for fuel consumption calculations," 2016 Int. Conf. on Electrical Systems for Aircraft, Railway, Ship Propulsion and Road Vehicles & Int. Transportation Electrification Conf. (ESARS-ITEC), Toulouse, 2016, pp. 1-6, doi: 10.1109/ ESARS-ITEC.2016.7841414.

K. Davis and J. G. Hayes, "Energy management strategy development to minimize the operating costs for a fuel cell vehicle," 2017 IEEE Vehicle Power and Propulsion Conf. (VPPC), Belfort, 2017, pp. 1-6, doi: 10.1109/ VPPC.2017.8330990.

K. Davis and J. G. Hayes, " Comparison of lithium-ion battery pack models based on test data from Idaho and Argonne national laboratories," *2020 IEEE Energy Conversion Congress and Exposition (ECCE)*, Detroit, IL, pp. 5626-5632, 2020.

Acknowledgements

I would like to acknowledge the financial support from my employer, Munster Technological University (formerly known as Cork Institute of Technology) which allowed me to pursue this research. I am grateful to my supervisor, Dr. John G. Hayes, for his guidance throughout this study. I would like to express my gratitude towards other UCC staff in the electrical engineering department for their support and encouragement to complete this research.

It was my pleasure and privilege to work alongside a very special bunch of postgraduates during my time in UCC. They included me in all their social and sporting activities and their general comradery was truly uplifting. I have very happy memories of the time I spent in their company.

To my daughters Maria and Áine, thank you for all your support over the last seven years and hopefully, I will now have more time to support you going forward.

Last, and most importantly, I want to thank my wife, Sarah, for all your endless patience, motivation, and advice throughout the writing of this thesis. I am forever in your debt.

Table of Contents

Appendix A

Appendix B

Appendix C

Appendix D

List of Figures

List of Tables

1 INTRODUCTION

Reported range anxiety associated with the low energy capacity battery electric vehicles (BEVs) was the motivating driver for beginning this research in 2014. The first study aim was to develop a powertrain model that calculated energy consumption based on the minimum number of published vehicle parameters. A simplified electric vehicle powertrain (SEVP) model was developed. Dynamometer test data from Argonne National Laboratory (ANL) was used to validate the SEVP for ten vehicles based on cumulative BEV energy consumption over a defined route and on energy consumption for each 1 s test period. The SEVP model was then benchmarked against two widely used vehicle simulators, ADVISOR and FASTSim.

With the rapid development of an electrified transportation sector, the aims of the research expanded to develop the SEVP as a BEV electrical circuit powertrain simulator. This development involved more detailed electrical models for both the Lithium-ion battery packs and for the traction internal-permanent-magnet (IPM) motor.

In the heavy-duty transportation sector, fuel cells are being considered as the primary power source. An energy-management strategy (EMS) was developed for fuel cell electric vehicles (FCEV) as a research resource in this relatively new technology area.

This introductory chapter provides a background to the research topics underpinning this thesis. The chapter is organized as follows: Section 1.1 presents an overview of the rationale for this research; Section 1.2 outlines one overall thesis objective and three addition specific thesis objectives; Section 1.3 reviews the methods of calculating the power required at a vehicle's wheels to achieve a desired speed; Section 1.4 examines the power losses in the powertrain components from a vehicle's wheels to its battery; Section 1.5 provides an overview of the common test drive cycles that are used to determine energy consumption in vehicles; The structure of subsequent thesis chapters is presented in Section 1.6. Additional background material supporting this chapter is provided in Appendix A.

1.1 Overview

The internal-combustion engine (ICE) vehicle, fuelled by either petrol (gasoline) or diesel, has dominated the transportation sector for more than one hundred years. Within the light-duty (passenger) vehicle sector, ICE vehicles achieve driving ranges of 500 to 1000 km [1]. Their relatively low purchase costs and their long lifetimes have resulted in the widespread adoption of ICE technology to meet the light-duty transportation needs, in both developed and developing economies. Research into alternatively-fuelled vehicles was largely dormant until the oil crisis in the 1970s, which highlighted the ICE technology's over-reliance on a single energy source [2]. Initially, post-fuel crisis development of alternatively-fuelled vehicles focused largely on various types of gases that could be combusted using the existing ICE technology [3]. More importantly, the fuel crisis resulted in legalisation that set limits for permissible fuel consumption levels of these light-duty vehicles [4]. Contemporaneous attempts to develop battery-powered electric vehicles were restricted as the available low energy density lead-acid battery technology resulted in low driving ranges [5].

In the 1980's, batteries with higher energy densities, constructed with nickel metal-hydride (NiMH) and lithium-ion (Li-ion) were developed. As a further development, in 1997 Toyota launched a hybrid-electric vehicle (HEV) that used two energy sources, a petrol fuel tank and a NiMH battery [6]. ICE technology was still the primary power source for this vehicle, but fuel consumption could be reduced by operating the vehicle either solely or partially, on battery power during the low-efficiency operating regions of the ICE. ICE technology operates optimally under continuous high-speed operation, such as occurs during highway driving. Fuel consumption is relatively low in these conditions. But in urban environments, which are characterised by low average speed operation and by frequent braking and acceleration operations, ICE fuel consumption is high. In such conditions, HEV fuel consumption is lower as battery-only operation is possible. Fuel consumption is also reduced for higher performance outputs in HEVs as the battery output is combined with the ICE output, to avoid operating the ICE in high fuel consumption modes. Additional fuel consumption improvements are achieved by the HEV's capability to recover a portion of the kinetic energy lost during vehicle braking. Regenerative braking systems, applied to the driven wheels, allow recharging of the battery.

In addition to advances in battery technology, HEV designs benefited from improvements in semiconductor technology, such as the introduction of the insulated gate bipolar transistor (IGBT) in the 1980s that simplified the design requirements for inverters [7]. The introduction of high-strength permanent magnets enabled the development of improved motor designs with very high torque, low weight, reduced volume and high efficiency. These motor designs are particularly suitable for the high-power traction requirements of a light-duty vehicle [8].

The development of BEVs, in the 2000s, coincided with widely-reported environmental concerns about air-quality in large cities and rising global temperatures attributed to CO_2 emissions [9]. As transportation was responsible for at least 24% of all global emissions, an alternative to ICE technology was required [10]. Li-ion batteries had been widely used in portable equipment since the 1990s, and this mature battery technology was migrated into BEV designs. The BEV offered the possibility of zero tail-pipe emissions in urban environments and improving the local air quality. As the electricity required to recharge the batteries could be generated from multiple resources, including zero CO_2 emission resources, such as wind energy and solar photovoltaics, transportation would no longer be reliant on a single non-renewable energy resource. The power electronic circuit technology for HEV designs is very similar to that found in BEV designs, with modifications required for both the higher power ratings and higher energy capacities needed for full electric-only operation over long driving ranges.

The adoption of BEV technology has faced significant economic and technological barriers [11]. The principle economic barrier is associated with the high cost of modern battery packs that results in increased purchase price for a BEV compared to an equivalent ICE vehicle. This economic barrier is expected to reduce as battery production quantities increase, and with increasing BEV adoption, the improved economies of scale will further reduce the BEV purchase price. Increasing the operating costs of ICE technology by increasing the taxation applied to the CO_2 emissions from vehicles is another method of reducing the economic barriers. For example, congestion charges for ICE vehicles in cities result in overall lower lifecycle costs for BEVs compared to ICE vehicles [12]. A further economic barrier is associated with vehicle manufacturers change processes. Manufacturers who have optimised their manufacturing processes for ICE vehicles, appear reluctant to invest in new processes for BEV production until consumer demand increases [13].

The technology barriers are largely associated with two elements, the vehicle system design and charging infrastructure development. Although the individual BEV powertrain component technologies were mature in lower power applications with controlled ambient environments, technology challenges remain when these components are combined in a BEV that must operate at a high-power output in a very wide range of ambient environments. In addition, these vehicles require the design and implementation of a recharging infrastructure to replace the traditional petrol station. This infrastructure will be influenced by many factors, including population density, electrical network power ability and the driving range of typical BEVs [14]. As BEVs have a reduced driving range compared to typical ICE vehicles, the “range anxiety” felt by a BEV driver will depend on the charging infrastructure available.

Both of the technology challenges to the wider adoption of BEVs require simple accurate BEV simulators to estimate a vehicle’s energy consumption over any route and in any environmental condition.

1.2 Thesis Objectives

The BEV industry has developed at a rapid pace during the seven-year timeframe (2014-2020) of this thesis with global BEV sales of approximately 300,000 in 2014 rising to 1.2 million in 2019 [15]. The initial objective of the thesis was to develop models of the powertrain components to establish the driving range of a BEV and to combine these models in a vehicle simulator to overcome the "range anxiety" reported by BEV owners [14],[16]. The range is determined mainly by the available battery capacity and by the efficiency of the powertrain components from the battery to the wheels. In 2014, apart from the luxury models from Tesla that had capacities up to 60 kWh, a typical production volume BEV had a rated battery capacity that ranged from 16 kWh to 24 kWh. By 2019, a wide variety of BEVs with increased battery capacities up to 64 kWh were available, such as the Hyundai Kona and Chevy Bolt, which eliminated the "range anxiety" for most BEV owners and somewhat reduced the importance of the initial objective to establish an accurate driving range [17].

The rapid development and widespread adoption of BEVs has increased the necessity for educational resources to explain the operating technology of these vehicles. The thesis objectives evolved to meet these educational resource gaps by developing accessible equivalent-electrical-circuit (EEC) models for BEV powertrains. As both environmental and charging infrastructural studies require an integrated simplified BEV simulator, the models developed in this study are based on a minimum number of published parameters and target high accuracy while being computationally efficient. Annual reviews of the on-going research findings and the changing nature of the industry resulted in three specific objectives for this thesis.

The first objective is the validation of a Simplified Electric Vehicle Powertrain (SEVP) model, first proposed in 2011 and modified in 2014, using dynamometer test data from multiple BEVs [18],[19]. The initial work on this objective, including the structure of the SEVP model, is reported in Chapter 2. Then the SEVP model is benchmarked by comparing its predicted instantaneous and cumulative energy consumption over a route, with that from two widely used vehicle simulators, ADVISOR and FASTSim, in Chapter 3 [20],[21].

The second objective is to develop new powertrain-component EEC models for the two principle components, namely, the Li-ion battery pack and the interior-permanent-magnet (IPM) motor. As the production of BEVs rapidly expands, a clear

trend is observed, which sees the use of Li-ion batteries and of IPM motors in most of the new vehicles on the market. This development has occurred over a relatively short period of time, which results in many of the current vehicle simulators lacking accurate models for these components. The development of a Li-ion EEC model is addressed in Chapter 4 and the development of the IPM motor model is presented in Chapter 5.

The third objective addresses FCEVs that are regarded as a possible future technology to replace ICE technology in heavy-duty vehicles. These vehicles require the same BEV powertrain component models but further require additional component models associated with the fuel cell. Within the restricted development timeframe of this thesis, the third objective is to develop an energy-management strategy (EMS) for these vehicles that minimises both fuel consumption and component degradation. This EMS minimises the operational costs of these vehicles [22]. This objective is addressed in Chapter 6.

1.3 Vehicle Power Requirements

The power required from the energy source of a vehicle may be subdivided into two elements; the power to propel the vehicle on a road and the power losses in the powertrain components. The propelling or tractive effort power P_{te} is further subclassified into; road-load power, and acceleration power. The road-load power depends on the resistance of the tyres to the road surface, the aerodynamic drag resulting from the shape of the vehicle, and the required climbing power associated with inclines in the road. The road load at any instant is difficult to define absolutely due to a number of factors; (i) the variability of road surfaces that impacts the tyre contact resistances; (ii) the complex relationship between drag forces, instantaneous wind speeds and wind directions; (iii) the difficulties in determining the road incline angle.

The individual elements of the combined road load are defined, by convention, as having positive power values when the power flow direction is from the energy source to the tyres. The friction resistance of the tyres, also called the rolling resistance, and the aerodynamic drag will always result in positive power values. The climbing power has a positive value when the vehicle is travelling up an incline but will have a negative value when descending. Acceleration power is required when the vehicle is changing speed and has positive values when the vehicle's speed is increasing and negative values when the vehicle is decelerating. As these propelling powers are a function of vehicle speed v, they may be individually characterised by their force requirements and the combined force requirement is defined as the tractive force F_{te} requirement of the vehicle. The relationship between the tractive effort power P_{te} and the tractive force F_{te} is given by

$$P_{te} = F_{te} v \tag{1.1}$$

1.3.1 Tractive Force

Two alternative methods may be used to calculate the tractive force F_{te}. The most commonly applied calculation method is based on standard kinematic equations that sum the vehicle road-load forces with the required acceleration force. The

vehicle's resistive forces include the rolling resistance force F_R, the aerodynamic drag force F_D, and the road grade or climbing force F_c. The acceleration forces include the vehicle's linear acceleration force F_a, and the rotational acceleration force F_{inert} which is required by the wheels, motor, gearbox and powertrain shafts. The parameters to specify the tractive force comprise the vehicle mass M in kg, the acceleration due to gravity g in m/s^2, the tyre rolling resistance coefficient C_{rr}, the road inclination angle θ_r in degrees, the air density ρ in kg/m^3, the drag coefficient C_d , the frontal area A_f in m^2, the speed v in m/s, headwind speed v_{air} in m/s, the vehicle's linear acceleration a in m/s^2, the combined inertia of all the rotating components referenced to the drive axle J_{axle} in kg m^2, the angular acceleration of the drive axle α_{axle} in radians/s^2, and the radius of the vehicle's wheels r_{wh} in m. The tractive force at the point of contact between the tyre and the road surface is then expressed as

$$F_{te} = F_R + F_D + F_c + F_a + F_{inert} \tag{1.2}$$

where

$$F_R = MgC_{rr} \tag{1.3}$$

$$F_D = 0.5C_dA_f(v + v_{air})^2 \tag{1.4}$$

$$F_c = Mg\,sin\,\theta_r \tag{1.5}$$

$$F_a = Ma \tag{1.6}$$

and

$$F_{inert} = J_{axle}\left(\frac{\alpha_{axle}}{r_{wh}}\right) \tag{1.7}$$

These tractive forces are illustrated in Figure 1-1.

Many of these parameters must be approximated as they vary with ambient temperatures and with environmental conditions. Air density ρ is generally assumed to be 1.225 kg/m^3, the international standard atmosphere value at sea level, and the gravitational acceleration g is taken as 9.81 m/s^2. As the inertial force F_{inert} is difficult

to assess, it is frequently combined with the linear acceleration force F_a and estimated by increasing the vehicle mass in (1.6) by a factor of 1.03 to 1.05 [23].

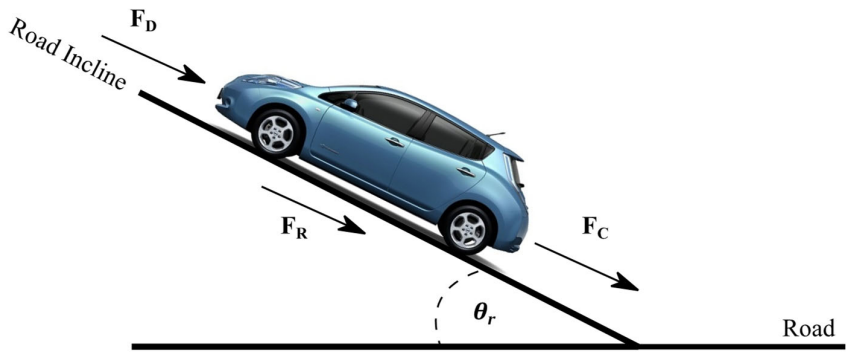

Figure 1-1. Tractive force components

The value of the coefficient of rolling resistance C_{rr} varies with tyre temperature, tyre pressure, tyre materials, vehicle speed, vehicle weight and road surface [24], [25]. The variation in the C_{rr} value is approximated using empirical equations. Examples of C_{rr} equations from [24] that relate C_{rr} to vehicle speed v and to tyre pressure include

$$C_{rr} = 0.01\left(1 + \frac{v}{44.704}\right) \tag{1.8}$$

and

$$C_{rr} = C_0 + 3.24C_{spd}\left(\frac{v}{44.704}\right)^{2.5} \tag{1.9}$$

The coefficients C_0 and C_{spd} are determined based on tyre pressures, with values of 0.0085 and 0.0035, respectively, for a typical EV tyre pressure of 248 kPa (36 psi). Over a speed range of 0 to 130 km/h (v =36.111 m/s), these equations will result in C_{rr} value ranges of 0.01 to 0.018 based on (1.8) and 0.0085 to 0.015 based on (1.9). Recent models of BEVs, fitted with low rolling resistance tyres to improve fuel consumption, have significantly lower C_{rr} values in the range of 0.0055 to 0.0084 [26].

Measurement of the frontal area A_f of a vehicle is difficult due to the irregular shape of most vehicles. Vehicle manufacturers tend not to publish the value of this area. A projection of the vehicle on a wall is one method used to approximate this

parameter. Frequently in the literature, a correction factor of between 0.8 to 0.9 is applied to the product of the vehicle's published width and height to estimate a value for this frontal area [21],[27].

As one objective of this study is the development of a vehicle simulator based on published vehicle parameters, an alternative F_{te} calculation method is required, based on the Society of Automotive Engineers (SAE) coast-down technique. This test eliminates the need to approximate a C_{rr}value and a A_f value. It replaces the F_R and F_D in (1.2) with a vehicle road-load force F_v calculated with the coast-down coefficients derived from the test [28]. The F_v is derived in a test where a vehicle is accelerated to a high speed (range 80-113 km/h) on a dry, straight, level road and is then allowed to coastdown while in neutral. The regenerative braking systems are obviously disabled when testing BEVs and HEVs. The coast-down technique can be performed in a laboratory with the driven wheels of the vehicle attached to a roller, whose rotation force is controlled by a dynamometer. The vehicle's speed during coastdown is measured at defined intervals and regression techniques are used to determine second-order polynomial coefficients A_{cd}, B_{cd}, and C_{cd} for the coast-down force. A single coast-down test cannot be used to establish these coefficients and the published coefficient values represent repeated road test measurements until a statistically significant result is achieved [29]. The resultant tractive force equation is

$$F_{te} = F_v + F_c + F_a + F_{inert} \tag{1.10}$$

where

$$F_v = A_{cd} + B_{cd}v + C_{cd}v^2 \tag{1.11}$$

The coefficients A_{cd} and C_{cd} correlate to the forces F_R and F_D respectively. The calculation of the tractive effort in the SEVP simulator is simplified using the coast-down coefficients A_{cd}, B_{cd}, and C_{cd} as these coefficients are published both by the Environmental Protection Agency (EPA) in the USA, based on road tests, and by the Argonne National Laboratory (ANL), based on dynamometer tests [30],[31]. The coast-down coefficient values also incorporate an error associated with the regression method, ambient test conditions, tyre temperatures and road surface during the tests.

1.3.1.1 Comparison of Tractive Force Calculation Methods

In this thesis, a total of ten BEVs were studied, namely a 2012 and a 2013 version of the Nissan Leaf, a 2013 Ford Focus EV, a 2015 Kia Soul, a 2015 Chevrolet Spark, a 2015 BMW i3, a 2012 Mitsubishi MiEV, a 2014 Smart Fortwo EV, a 2015 Volkswagen eGolf and a 2015 Mercedes B-class EV. The minimum, maximum and average tractive force parameter values for F_{te} calculation are summarised in Table 1-1. In this table, the frontal area values were calculated based on the published vehicle's width and height, multiplied by a profile factor of 0.8.

Table 1-1. Range of tractive effort parameter values for the ten BEVs in this study.

Parameter		Units	Min. (vehicle)	Max. (vehicle)	Average Value
Vehicle Mass	M	kg	1050 (MiEV)	1790 (Focus)	1485
Frontal Area	A_f	m^2	1.924 (Smart)	2.305 (Soul)	2.15
Drag Coefficient	C_d		0.28 (Leaf)	0.35 (Soul)	0.31

When an estimated value of 0.008 for the rolling road resistance coefficient C_{rr} was selected, a comparison of the F_R and F_D forces in the Kia Soul, over the vehicle's full speed range of 0 to 130 km/h is shown, in terms of the force in Figure 1-2(a) and in terms of power in Figure 1-2(b). This comparison illustrates that F_R is the dominant force at urban environments speeds of 0 to 50 km/h, whereas F_D is dominant in highway environments speeds of 80 to 120 km/h.

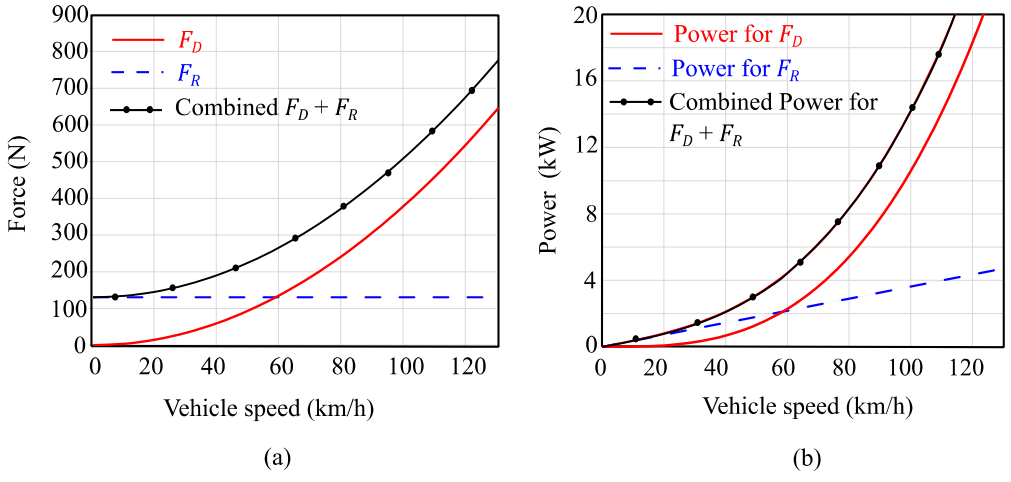

Figure 1-2. Comparison of impact of rolling resistance and aerodynamic drag with vehicle speed (a) force comparison (b) power requirement comparison.

The combined power required to overcome F_R and F_D is compared to the power required for climbing an incline in the road in Figure 1-3(a), and to the power required for vehicle acceleration in Figure 1-3(b). This analysis shows that the tractive effort calculation is more sensitive to small changes in either the road incline or the vehicle acceleration than to changes in the previously mentioned vehicle parameters of C_{rr} and A_f. In Figure 1-3(a), the climbing power component is shown for a 2.6% road grade that equates to a $sin(1.5^o)$ incline and for a 10.5% grade that is equivalent to a 6^o incline. Even at a low grade of 2.6%, the climbing power exceeds the combined F_R and F_D forces at all vehicle speeds above 90 km/h.

In Figure 1-3(b), the accelerating power is presented for two conditions, namely a relatively slow acceleration of 0.55 m/s^2 and a higher acceleration of 0.83 m/s^2. These acceleration power requirements are significantly higher than the combined rolling resistance and aerodynamic drag powers at all vehicle speeds.

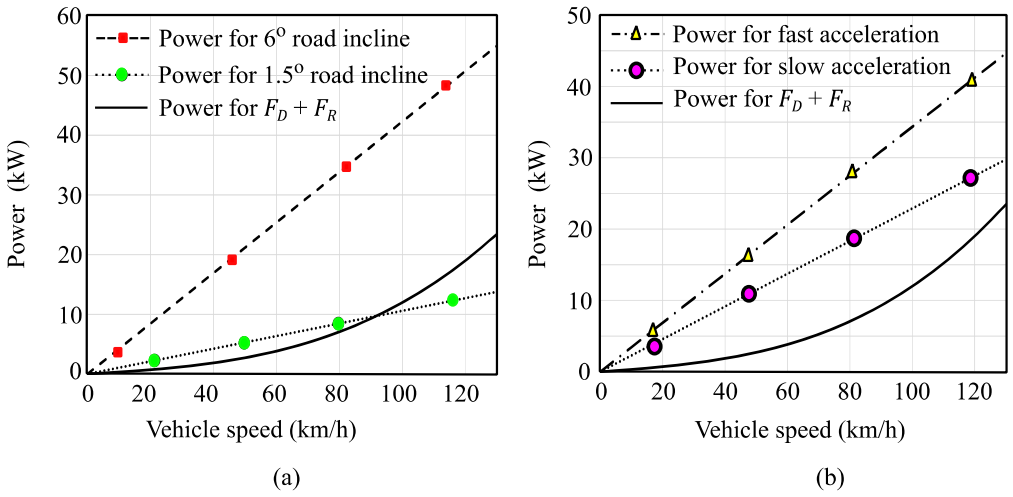

Figure 1-3. Comparison of climbing power and acceleration power with combined F_R and F_D powers (a) climbing power comparison (b) acceleration power comparison.

The high-power flow required for vehicle acceleration necessitates an accurate estimation of the vehicle's acceleration for vehicle simulators and this is examined further in Chapter 2. The power values presented in Figure 1-2 represent the power needed at the vehicle's wheels. However, over a route where an acceleration event is followed by a similar deceleration event, the net power requirement from the battery is considerably reduced, as energy is recovered using the regenerative braking converter in the powertrain. This net power requirement is dependent on the proportion

of the braking achieved with the regenerative braking circuit Reg_{ach}, as opposed to friction braking, and the bidirectional power flow losses in the powertrain components.

A comparison of the tractive effort for a 2013 version of the Nissan Leaf, calculated with standard equations and using coast-down test coefficients, is shown in terms of force in Figure 1-4(a) and in terms of power in Figure 1-4(b). These equations are calculated using the *ABC*'s published by the EPA and the *ABC*'s generated by ANL. There is a good correlation between both calculation methods for urban speed ranges (up to 60 km/h) but above this 60 km/h speed, the EPA published coast-down coefficients result in higher tractive effort values. The ANL dynamometer test coast-down coefficients provide a better correlation to the standard equation's tractive effort calculations over the full speed range of the vehicle. This higher tractive effort trend at higher speeds with the EPA coast-down coefficients was also observed in the other BEVs studied.

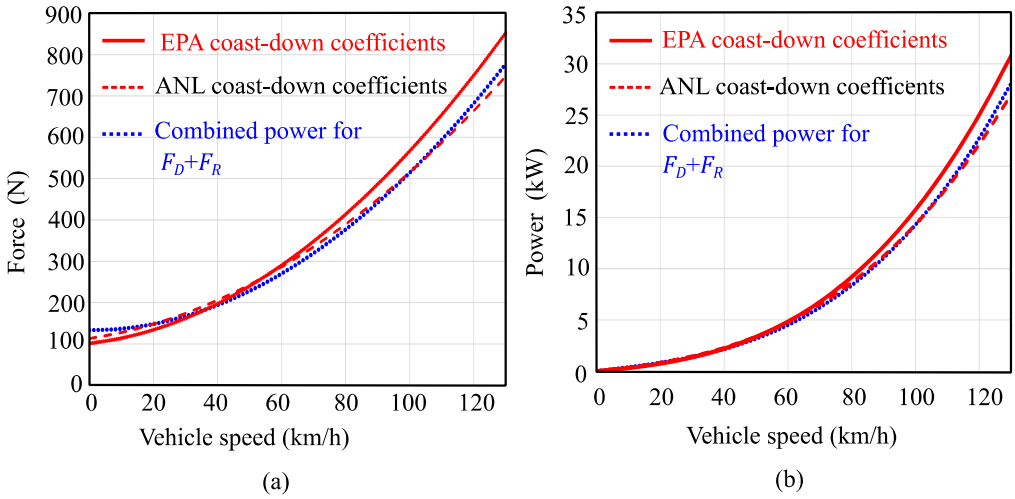

Figure 1-4. Comparison of tractive effort calculated with standard equations and with coast-down coefficients (a) force comparison (b) power comparison.

1.4 Powertrain Modelling

The total power required from the energy sources on a vehicle is the combined tractive effort power and the power losses in the powertrain components. The number of components between the energy sources and the road depends on architecture of the powertrain. The structure of a typical BEV powertrain is illustrated in Figure 1-5. The development of EEC models for these components is a key objective of this thesis. Although the BEV architecture includes an onboard charger, this charger is not usually modelled in vehicle simulators. For lifetime cost studies or for well-to-wheel environmental studies, the efficiency of the on-board charger is required, and ANL measured this efficiency as 85% in the 2012 Nissan Leaf [32].

The components comprising the powertrain of a BEV are defined with Figure 1-5. The powertrain includes all the major components from the Li-ion battery pack to the point where the tyres contact the road. This includes a component model shown as auxiliary loads P_{aux} in Figure 1-5. The auxiliary loads include the low-power accessory loads P_{acc} associated with vehicle lights, computer control systems, etc., and the high-power heating, ventilation and air-conditioning (HVAC) loads. The power associated with these HVAC loads P_{HVAC} and the impact on the range of a BEV is examined in Section 1.4.6 and in Chapter 2.

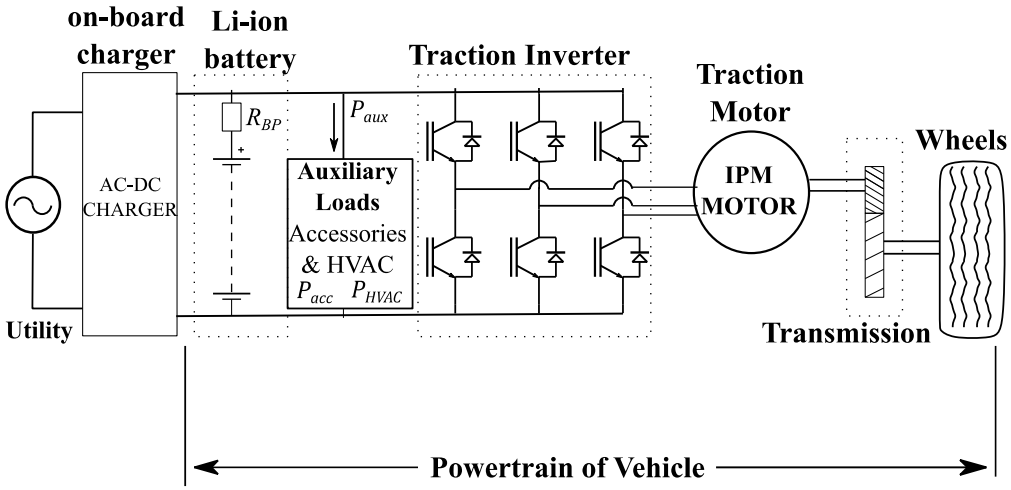

Figure 1-5. BEV powertrain definition for this study.

This powertrain architecture translates into a power flow block diagram as shown in Figure 1-6. The power flow is bidirectional and is defined as positive power from the battery to the wheels in motoring mode and negative power from the wheels to the battery in regenerative braking mode.

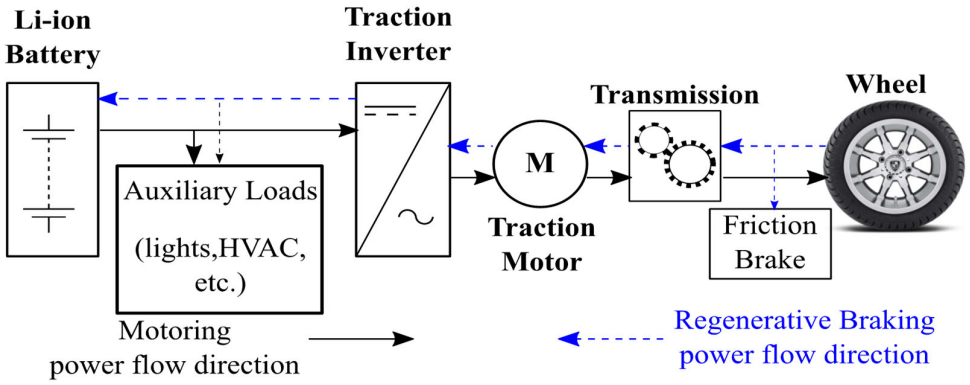

Figure 1-6. BEV bidirectional power flow in the powertrain.

The power flow diagram for a typical FCEV powertrain is shown in Figure 1-7. In FCEV powertrains, two or more power sources provide the tractive effort required during motoring mode operation. FCEV powertrain modelling requires an energy management strategy that assigns the power output from each of the sources to optimise the vehicle's performance. Power flow during braking mode is restricted to the power sources that are capable of being recharged, namely batteries and supercapacitors.

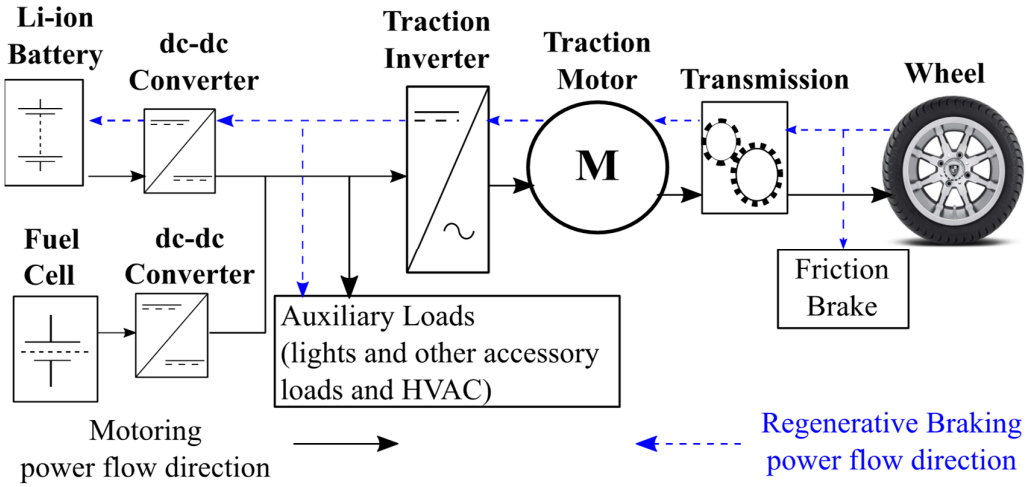

Figure 1-7. Bidirectional battery-only power flow in a FCEV powertrain.

The options for powertrain modelling include: (i) developing an individual power loss component for each powertrain component; (ii) combining two or more components into a single power loss model; (iii) a simple fixed percentage power loss model for the complete powertrain. For all three options, a component may have two separate power loss models to reflect the direction of power flow in the powertrain. The SEVP simulator was developed, in line with option (i), with individual powertrain component models and the power loss calculations are the same in both power flow directions. Further details of the initial SEVP powertrain component models are provided in Chapter 2.

1.4.1 Wheel Model

The power loss in a wheel results from the friction of the wheel's bearing and from wheel slip between the tyre and the road surface [20]. Wheel slip results in a requirement for additional motor torque to achieve the desired vehicle speed. The wheels of the vehicle represent a large rotating mass and require power from the energy source as the vehicle accelerates to overcome wheel inertia. Inertial power is required to accelerate all four wheels, but inertial energy can only be recovered from the driven wheels during regenerative braking. The power loss in the wheel model is calculated in both power flow directions. If the bearing friction and slip power losses are negligible, then only the wheel inertial power loss must be modelled. In this study, only the ADVISOR simulator has a wheel model and impacts of removing this model are examined in Chapter 3 when three simulators are compared.

1.4.2 Braking Model

A braking model is only applied in the regenerative braking power flow direction and it determines the power split between friction braking and regenerative braking. Friction braking increases the energy consumption in a BEV as a portion of the kinetic energy is dissipated as heat. The power-split fraction Reg_{ach} between friction and regenerative braking depends on the braking algorithm developed by the vehicle manufacturer. In vehicle simulators, such as FASTSim, the power split is based on the vehicle's speed [21]. At speeds above 15 km/h, 80% of the braking is regenerative and this percentage decreases to just 20% at a speed of 8 km/h. Alternative regenerative

braking models are found in the literature [33],[34],[35]. Optimum vehicle energy efficiency is achieved when 100% regenerative braking is available at all vehicle speeds. This optimum operating mode would also remove the requirement for a braking model in the powertrain. The BEV test data from ANL is examined in Chapter 2 to determine the percentage of braking energy recovered by the battery of the ten vehicles over a range of vehicle speeds. A more detailed examination of the regenerative braking in three of the BEVs shows that a speed dependent power-split braking strategy does not correlate well with the test data. Instead a power split based on the deceleration rate is proposed for these three vehicles.

1.4.3 Transmission Model

In a conventional ICE powertrain, the transmission model includes the power losses of the torque coupler between the engine and the gearbox; the discrete power losses of the multiple gear ratios; and the power losses of the drive shaft and differential gearing on the axis of the driven wheels. This complex interaction of ICE transmission components results in high power losses and a low transmission model efficiency η_{gear} of between 80% to 90% [24]. However, as the torque-speed profile of the BEV electric traction motor closely matches the required torque-speed profile at the wheels, there is no need for a torque-coupler component and only a simplified gearbox is required with a single gear ratio. This reduces the transmission power losses to between 3% to 5% of the transmitted power. The BEV transmission can be assumed to have a fixed percentage loss model in both power flow directions [36]. This is the default transmission model for BEVs in the FASTSim simulator and it is also implemented in the SEVP simulator. The older ADVISOR simulator only contains transmission models suitable for ICE vehicles.

1.4.4 Traction Motor Model

The traction motor model is critical in accurate estimation of the powertrain losses of a BEV. A motor efficiency map for the Leaf BEV is provided in Figure 1-8 and this shows an IPM motor power efficiency η_{mot} as high as 97% and as low as 70%, depending on the motor's torque-speed operating point [37]. The sources of motor losses are briefly reviewed and then the alternative motor models are presented.

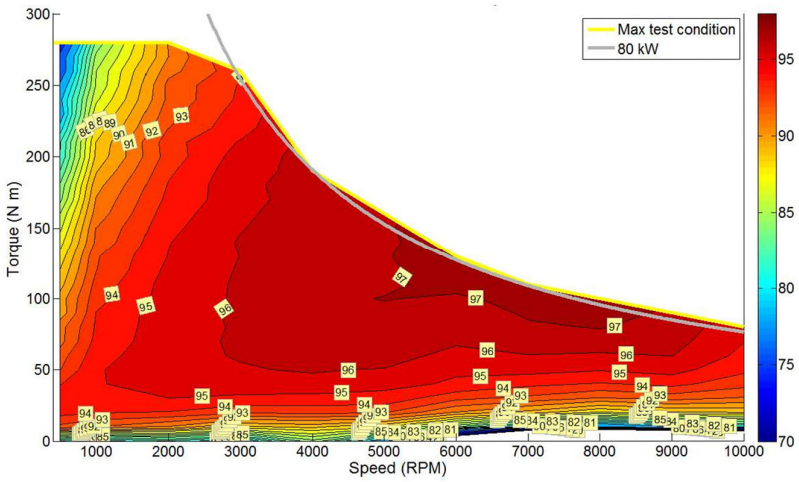

Figure 1-8. 2012 Leaf motor efficiency map [37].

Typically, either induction motors or high-efficiency internal permanent-magnet (IPM) motors are chosen for BEVs [38]. Except for the Mercedes Benz B-class that utilises induction motor technology from Tesla, all of the vehicles studied in this research utilised IPM motors. This research only focused on permanent-magnet (PM) motor models.

1.4.4.1 Sources of Losses in Motors

Power losses in electric motors are split between (i) magnetic circuit induced losses in the steel of the stator and rotor (known as core loss) and (ii) resistive losses in the windings (known as winding loss). Additional motor losses include windage, friction and magnet losses. These additional losses are usually insignificant compared to the winding and core losses. As the friction and windage losses are motor speed dependent, they can be combined with the core losses.

A motor power loss model is required to estimate the input phase currents from the inverter. However, these phase currents are dependent on the operating mode of the motor. At low speeds, the current in the stator depends on the torque output requirement and maximum torque is limited by the available current from the inverter. The motor is assumed to operate with a maximum-torque-per-ampere (MTPA) strategy at lower speeds. As shown in Chapter 5, there is a non-linear relationship between phase current and torque output due to magnetic saturation in IPM motors.

Rated motor power $P_{r(rated)}$ is achieved at the rated or base motor speed $\omega_{r(rated)}$. The available torque at rated speed is equivalent to the maximum torque and is referred to as the rated torque $T_{r(rated)}$. As the motor speed increases to a rated speed value, the back-emf of the motor increases until the back-emf voltage value becomes the limiting operational factor due to low dc voltage at the input of the inverter. Higher speed operation is only possible if the back-emf voltage is reduced, typically achieved by applying a phase current that flux weakens the PM magnetic field of the motor. This operational strategy is called maximum-torque-per-voltage (MTPV). In MTPV mode, the input phase current is dependent on both the torque output and flux-weakening requirements. Both MTPA and MTPV operation of IPM motors are discussed further in Chapter 5.

Core losses are dependent both on the motor's current (torque) and on its speed. Benchmark testing of IPM motors, over the full torque and speed ranges, produces motor efficiency maps [37],[39],[40],[41]. However, accurate determination of the core loss elements of these efficiency maps requires detailed knowledge of the magnetic circuit design of the motor. Even when these details are available, parasitic effects from harmonics in the input phase currents can result in higher than expected core losses than those calculated from standard magnetic loss equations, such as the Steinmetz equation. A typical empirical approach to estimating core loss in a motor is to lump these losses together with the friction and windage losses. These combined speed-related losses are viewed as a no-load torque T_{nl}.

1.4.4.2 Options for Motor Modelling

Three options for motor modelling in vehicle simulators are: (i) analytical equations based on the power loss factors discussed in Section 1.4.4.1; (ii) efficiency maps constructed from test measurements on the motors; and (iii) power loss estimation based on typical power loss characterisation curves for electric motors.

The analytical equations approach relies on published motor specifications such as rated power, rated torque and maximum speed. The torque-speed operating point of the motor is estimated based on the wheel torque and the required vehicle speed. Knowledge of the gearbox ratio is required to convert these parameters to traction motor shaft torques and shaft speeds. Estimation of the internal parameters of the motor such as winding resistance and torque constant are required, and these

parameters are estimated based on published vehicle specifications. This motor modelling option (i) is implemented in the SEVP simulator and the design procedure is described in Chapter 2. An improved motor model specifically for IPM motors is presented in Chapter 5.

The complex procedure and the technical expertise needed to estimate the individual loss sources in motors means that many vehicle simulators adopt the alternative option (ii) efficiency maps approach. The test data is converted to look-up-tables (LUTs) to represent the motor power loss model in the powertrain. This modelling option is adopted in the ADVISOR simulator. However, application of this option for BEV modelling is very limited due to the lack of published test data on the motors.

The FASTSim simulator implements option (iii), a power loss motor model based on a characteristic efficiency curve. The efficiency curve is derived from a set of efficiency values for normalised output powers and customised using the published rated output power for a specified motor.

A comparison of all three simulators in Chapter 3 shows the impact of these motor modelling options on the accuracy of a simulator. The largest differences in power loss estimation between these models are seen when simulating the BEVs in low-speed, low-power urban driving environments.

1.4.5 Traction Inverter Model

The three-phase inverter of a BEV is typically constructed of six switching devices, as illustrated in Figure 1-9. Each device consists of a switching transistor (typically an IGBT in BEV inverters) and a parallel diode. The on-state (conduction) losses and the switching losses must be calculated for each device. For high current inverters, it is common to use multiple paralleled IGBT-diode modules for each device in the inverter. Once the input phase currents, phase voltages and power factors of the IPM motor model have been established, it is then possible to estimate the losses in the inverter based on these parameters. The accurate calculation of these losses requires detailed inverter device information and system operating information, which is not published by vehicle manufacturers. For example, the switching losses are dependent on both the switching frequency f_{sw} and the pulse-width-modulation scheme used for driving the IGBT devices.

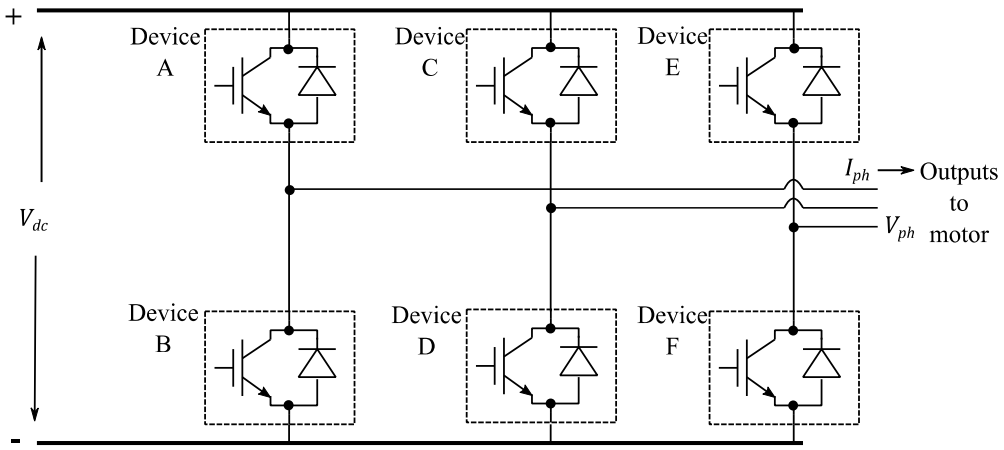

Figure 1-9. Typical inverter for IPM motor drive.

A frequently used inverter loss model, provided by Semikron [42], establishes the loss in each device. This model assumes sinusoidal pulse-width-modulation (SPWM) of the inverter devices, which produce sinusoidal output voltages at the motor. The losses are based on several component factors as listed in Table 1-2. The electrical system parameters include; the motor power factor $cos\,\phi$, the amplitude of the output phase current $\hat{I}_{ph}$, the amplitude of the output phase voltage $\hat{V}_{ph}$, the dc voltage at the input to the inverter V_{dc}, and the modulation index m, which is defined as

$$m = \frac{\hat{V}_{ph}}{\left(\frac{V_{dc}}{2}\right)} \tag{1.12}$$

The on-state conduction losses in the IGBT $P_{IGBT(cond)}$ are estimated by

$$P_{IGBT(cond)} = \left(\frac{1}{2\pi} + \frac{m\,cos\,\phi}{8}\right) V_{CE0}\hat{I}_{ph} + \left(\frac{1}{8} + \frac{m\,cos\,\phi}{3\pi}\right) r_{CE}\hat{I}_{ph}^2 \tag{1.13}$$

and the on-state conduction losses in its associated parallel diode $P_{D(cond)}$ are determined by

$$P_{D(cond)} = \left(\frac{1}{2\pi} - \frac{m\,cos\,\phi}{8}\right) V_{F0}\hat{I}_{ph} + \left(\frac{1}{8} - \frac{m\,cos\,\phi}{3\pi}\right) r_{F}\hat{I}_{ph}^2 \tag{1.14}$$

The corresponding switching losses in the IGBT $P_{IGBT(sw)}$ are estimated using

$$P_{IGBT(sw)} = f_{sw}E_{on+off}\frac{\sqrt{2}}{\pi}\frac{I_{ph}}{I_{ref}}\left(\frac{V_{dc}}{V_{ref}}\right)^{K_{v\_IGBT}}\left[1 + TC_{Esw}\left(T_j - T_{ref}\right)\right] \quad (1.15)$$

and switching losses in the diode $P_{D(sw)}$ are calculated as

$$P_{D(sw)} = f_{sw}E_{rr}\frac{\sqrt{2}}{\pi}\left(\frac{I_{ph}}{I_{ref}}\right)^{K_i}\left(\frac{V_{dc}}{V_{ref}}\right)^{K_{v\_diode}\left[1+TC_{Err}\left(T_j - T_{ref}\right)\right]} \quad (1.16)$$

Table 1-2 Inverter model component parameters.

V_{CE0}	Threshold on-state voltage for IGBT	
r_{CE}	Bulk on-state resistance for IGBT	
V_{F0}	Threshold on-state voltage for diode	
r_F	Bulk on-state resistance for diode	
E_{on+off}	Combined turn-on and turn-off energies of the IGBT	
E_{rr}	Turn-off energy of the diode	
TC_{Esw}	IGBT switching-loss temperature coefficient,	~ 0.003 (1/°C)
TC_{Err}	Diode switching-loss temperature coefficient,	~ 0.006 (1/°C)
K_{v_IGBT}	Voltage dependency exponent for IGBT,	~1.3…1.4
K_i	Current dependency exponent for diode,	~0.6
K_{v_diode}	Voltage dependency exponent for diode,	~0.6

The subscript ref indicates a test reference component parameter such as the current I_{ref}, voltage V_{ref} or junction temperature T_{ref}, and these component parameters are used by the IGBT manufacturer in device characterisation testing. Typically, V_{ref} may be only 50% of the components' rated voltage, while I_{ref} is usually the components' rated current. These parameters are adjusted to simulate the actual operating conditions of the BEV, such as the rms output current I_{ph} and the actual component junction temperature T_j.

In [26], a similar inverter model is presented. The IGBT on-state conduction loss is written as

$$P_{IGBT(cond)} = V_{CE0}I_{IGBT\_ave} + r_{CE}I^2_{IGBT\_rms} \quad (1.17)$$

where I_{IGBT_ave} is the average IGBT current and I_{IGBT_rms} is the rms IGBT current. The on-state conduction loss in its parallel diode $P_{D(cond)}$ is presented as

$$P_{D(cond)} = V_{F0} I_{D\_ave} + r_F I_{D\_rms}^2 \tag{1.18}$$

where I_{D_ave} is the average diode current and I_{D_rms} is the rms diode current. These the average currents in the IGBT and diode over the cycle are stated as

$$I_{IGBT\_ave} = I_{ph}\left(\frac{1}{\sqrt{2}\pi} + \frac{V_{ph}}{2V_{dc}} cos\,\phi\right) \tag{1.19}$$

$$I_{D\_ave} = I_{ph}\left(\frac{1}{\sqrt{2}\pi} - \frac{V_{ph}}{2V_{dc}} cos\,\phi\right) \tag{1.20}$$

and the equivalent rms currents over the cycle are provided by

$$I_{IGBT\_rms} = I_{ph}\sqrt{\frac{1}{4} + \frac{4\sqrt{2}V_{ph}}{3\pi V_{dc}} cos\phi} \tag{1.21}$$

$$I_{D\_rms} = I_{ph}\sqrt{\frac{1}{4} - \frac{4\sqrt{2}V_{ph}}{3\pi V_{dc}} cos\phi} \tag{1.22}$$

The corresponding switching losses in the IGBT $P_{IGBT(sw)}$ are estimated using

$$P_{IGBT(sw)} = \frac{f_{sw}}{2}\left(E_{on} + E_{off}\right)\frac{V_{dc}}{V_{ref}} \tag{1.23}$$

and the switching losses in the diode $P_{D(sw)}$ are estimated using

$$P_{D(sw)} = \frac{f_{sw}}{2}\left(E_{rr}\right)\frac{V_{dc}}{V_{ref}} \tag{1.24}$$

The high number of parameters required for these inverter models represents a significant challenge during model development. The Leaf BEV inverter efficiency map based on measured traction inverter efficiencies is presented in Figure 1-10. This map shows efficiencies as high as 99% for the typical highway driving conditions of high-speed/low-torque and efficiencies of less than 90% for the typical low-speed

urban-driving conditions. Such high efficiencies partially explain why the inverter model is combined with the motor model in simulators such as ADVISOR and FASTSim. The efficiency map contours also suggest that an alternative simpler inverter modelling approach is possible.

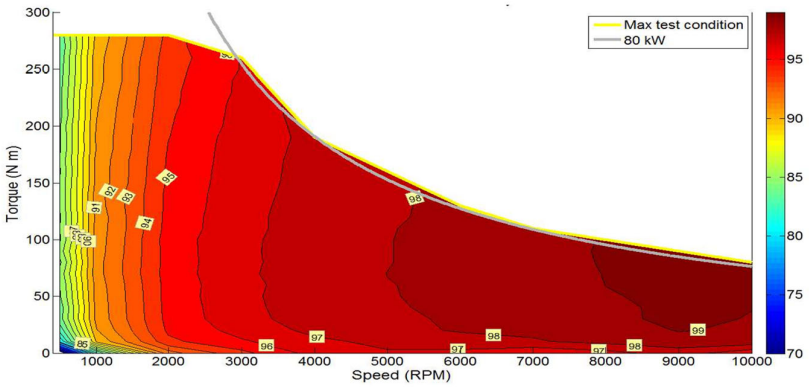

Figure 1-10. 2012 Leaf inverter efficiency map [37].

1.4.5.1 Alternative Inverter Model

In the SEVP, a simplified approach to inverter modelling is taken. The three-phase dc-ac traction inverter is modelled with an estimated efficiency at the rated condition $\eta_{inv(rated)}$ of 98 %. The inverter power loss at this rated condition $P_{inv(rated\_loss)}$ is determined by

$$P_{inv(rated\_loss)} = \frac{P_{inv(rated)}\left(1 - \eta_{inv(rated)}\right)}{\eta_{inv(rated)}} \tag{1.25}$$

The source of the inverter losses is assumed to be dominated by conduction losses, which are dependent on the amplitude of the output phase current. The phase current amplitude in the traction motor is assumed to be proportional to the rotor torque T_r . This simplified inverter model determines inverter power loss $P_{inv(loss)}$ at any torque output as

$$P_{inv(loss)} = P_{inv(rated\_loss)} \left(\frac{T_r}{T_{r(rated)}} \right) \quad (1.26)$$

A further advantage of the SEVP approach is that the inverter loss calculation is not dependent on the accuracy of the motor model to determine the output phases currents and voltages required for all motoring operating points.

1.4.6 Auxiliary Load Model

Auxiliary loads are defined in this thesis as any vehicle function that is not directly contributing to the tractive effort. These include the low-power accessory loads associated with the use of fans, lights, and pumps, and high-power loads associated the heating, ventilation and cooling (HVAC) of the passenger cabin and the battery. The impact on these loads is considerably different in BEV and ICE vehicles.

In ICE vehicles, the low-power accessory loads are represented as a small additional mechanical load on the drive shaft output and the cabin heating load requirement can be partially met from the high heat losses of the low efficiency engine. When driving in cold climate conditions, the recovery of waste heat from the engine minimises the impact of the HVAC load on the range of the vehicle.

In BEV designs, these auxiliary loads are provided by the dc-dc converter at the battery output and are not included in the coast-down test coefficients. Quantifying the power requirements for the HVAC loads is difficult due to their load dependence on external ambient temperature conditions. However, high-power HVAC requirements significantly increase the energy consumption from the battery and reduce the available range for these vehicles. There is a lack of literature available on the modelling of HVAC loads in BEVs. The limited studies found, tend to provide simplified equations that relate the additional fixed auxiliary power to the external ambient temperature or to include an additional energy consumption per km based on the external temperature [43],[44],[45]. Such simplified load model equations do not correlate well with the ANL test data [31].

An exploratory study into HVAC modelling is presented in Chapter 2. This introductory study clearly shows the requirement for a transient thermal model of the vehicle's cabin for a BEV simulation in extreme ambient temperature environments. Such development work is not within the scope of this thesis. As an alternative, an

average HVAC-power-to-external-temperature relationship model is developed to improve the accuracy of the SEVP simulator in environments that require HVAC operation.

Simple auxiliary load models found in existing vehicle simulators represent these auxiliary loads as fixed power loads, rated between 100 W to 700 W. The ANL test data shows that these low levels of auxiliary power represent vehicle operation when there is no requirement for HVAC power.

1.4.7 Battery Model

Several approaches are available for the modelling of batteries including mathematical, electrochemical and equivalent-electrical-circuit (EEC) models [46],[47],[48]. The EEC model is the preferred approach to battery modelling in vehicle simulators. A simple EEC battery model is represented as an ideal power source in series with a low value battery pack series resistor R_{BP}, with typical R_{BP} values of 100 mΩ to 200 mΩ. A complex battery model considers the open-circuit voltage's (OCV) dependence on the state of charge (SOC) of the battery and uses internal RC networks to model the dynamic voltage changes during high charge/ discharge current operation. The steady-state electrical performance of the complex battery model is determined by establishing an OCV to SOC relationship. The dynamic electrical performance of the complex model is determined by the choice of the internal impedance circuit. The power losses in the battery are determined by the ohmic losses in both the simple and complex battery models.

The difficulty in providing an accurate battery model is that most of the battery's parameters change with SOC, temperature, and operating mode (charge or discharge) and the parameters also change as the battery ages. The rate of battery ageing varies depending on the driving style and on several other factors, such as the ambient temperatures when the vehicle is not operating. In addition, there is considerable variation in the battery manufacturing processes and in the proprietary chemical compositions of batteries from different manufacturers, all of which adds to the complexity in predicting battery performance. While some vehicle simulators utilize complex battery models, most do not incorporate the impact of ageing on the battery and are based on test data from a single battery manufacturer. This issue is examined in Chapter 4.

The ADVISOR simulator provides a range of battery modelling options, where the user can select between simple resistor or Thevenin circuit internal impedances. The open-circuit voltage to capacity function is based on a simple LUT that defines this function at three ambient temperature of 0°C, 20°C and 40°C. The internal series resistance is also based on a LUT that specifies the SOC-dependent resistance value at the same three temperatures. The majority of the ADVISOR battery models are based on the testing of lead-acid batteries. There is only one Li-ion cell model available with a temperature dependent capacity of between 5.94 Ah to 7.41 Ah.

FASTSim simulator only considers the power flow into and out of the battery model. The FASTSim battery model contains a simple round-trip efficiency of 95.1% to estimate energy losses during charging and discharging.

The SEVP simulator evaluates the battery losses using a simple series-resistance battery model. The battery voltage is assumed to be constant during the short test period and the battery current is determined from this battery voltage. An improved battery model for the SEVP simulator is developed in Chapter 4 that models the battery voltage as a function of remaining battery capacity.

1.4.8 FCEV Energy Management Strategy

While a BEV has a single energy source to provide all of the power requirements of the vehicle, a FCEV has two, or more, energy sources and requires an energy management strategy (EMS) to determine which energy source can best provide the vehicle's power requirement. A typical EMS is not a physical powertrain component but is a software algorithm that sets the operating power level of each energy source according to the multiple constraints associated with that source. The EMS is optimised to achieve an overall vehicle objective. For instance, the objective of minimising the hydrogen fuel consumption of the vehicle may be achieved by operating on the battery whenever this source has adequate energy to meet the tractive requirements.

Implementing an EMS is more difficult than the previously described component models because the EMS is a control module rather than an efficiency model. Efficiency models are defined by a low number of fixed input and output parameters, whereas the inputs required for an EMS model are highly dependent on the control algorithm. If the source code for the vehicle simulator is open source, then it is possible

to integrate a custom EMS model into the overall powertrain model. This requires a complete understanding of the execution flow of the simulation code. Some vehicle simulators reduce the intellectual effort involved by providing a simple, rule-based EMS where the operating values of the rules are adjusted by the user. For instance, the vehicle simulator FASTSim has an EMS based on user-specified battery SOC levels. Battery power for the traction drive is permitted only when the battery SOC is above a minimum level and below a maximum SOC level. In this EMS, battery operation is constrained by the maximum power ratings for charge and discharge of the battery [21].

An EMS to optimise the operating costs of an FCEV was developed as part of this research. In addition to the direct hydrogen fuel cost, the EMS considers the degradation of the fuel cell and the battery as operating costs. The EMS uses these three factors as constraints and seeks to optimise the power split between power sources while satisfying the tractive power requirement of the test vehicle. The slow power response rate of the fuel cell in the test vehicle adds an additional constraint in this EMS. The EMS is modified to match the faster power response seen in ANL testing of the Toyota Mirai [49]. Further details of EMS implementations are presented in Chapter 6.

1.5 Drive Cycles

The fuel consumption of an ICE-powered vehicle is determined by measuring the flow rate from the fuel tank as the vehicle follows a speed profile. Standard test vehicle speed profiles, known as drive cycles, are designed to mimic the speed conditions in different road environments, such as urban or city driving, rural road driving, and extra-urban or highway driving. The cumulative fuel consumption during the drive cycle divided by the distance completed, is converted to provide a vehicle's fuel consumption in litres per 100 km. The related CO_2 emissions per km from this fuel consumption is calculated by the combustion equation where the mass ratio of fuel to CO_2 emissions given by

$$\mathrm{C}_x\mathrm{H}_y + \left(x + \frac{y}{4}\right)\mathrm{O}_2 = x\mathrm{CO}_2 + \left(\frac{y}{2}\right)\mathrm{H}_2\mathrm{O} \tag{1.27}$$

where $\mathrm{C}_x\mathrm{H}_y$ term is the fuel input, the $\left(x + \frac{y}{4}\right)\mathrm{O}_2$ term is the oxygen required for combustion, the $x\mathrm{CO}_2$ term represents the emissions and $\mathrm{H}_2\mathrm{O}$ is the water vapour from the combustion process. From (1.27), the emissions associated with petrol (C_8H_{18}, density 0.72-0.775 kg/L) is lower than those from diesel ($C_{12}H_{23}$, density 0.82-0.845 kg/L) but the higher energy density of diesel, 9.8-10.1 kWh/L compared to petrol's 8.0-9.0 kWh/L, means a lower fuel consumption for a given distance travelled, hence a diesel ICE has lower CO_2 emissions per km [27].

For a BEV, there is no direct fossil fuel consumption and hence no related tailpipe CO_2 emissions. There is a requirement to measure the cumulative energy consumption from the battery over a given driving cycle to estimate the driving range of the vehicle from a new, fully-charged battery. Vehicle energy consumption certification in the United States is based on two distinct drive cycles, namely, the Urban Dynamometer Drive Schedule (UDDS), shown in Figure 1-11(a) and the Highway Fuel Economy Test (HWFET), shown in Figure 1-11(b). The UDDS and HWFET energy consumption results are multiplied by 0.55 and 0.45 respectively, to get a combined energy consumption [1]. These tests are conducted either on a flat road, under no wind conditions, or more commonly, in a laboratory using dynamometers. As energy consumption in real-life driving conditions tends to be higher than under these test conditions, the EPA reflect this testing discrepancy by dividing the combined

laboratory test results by 0.7, which they then publish as the certified energy consumption of the vehicle.

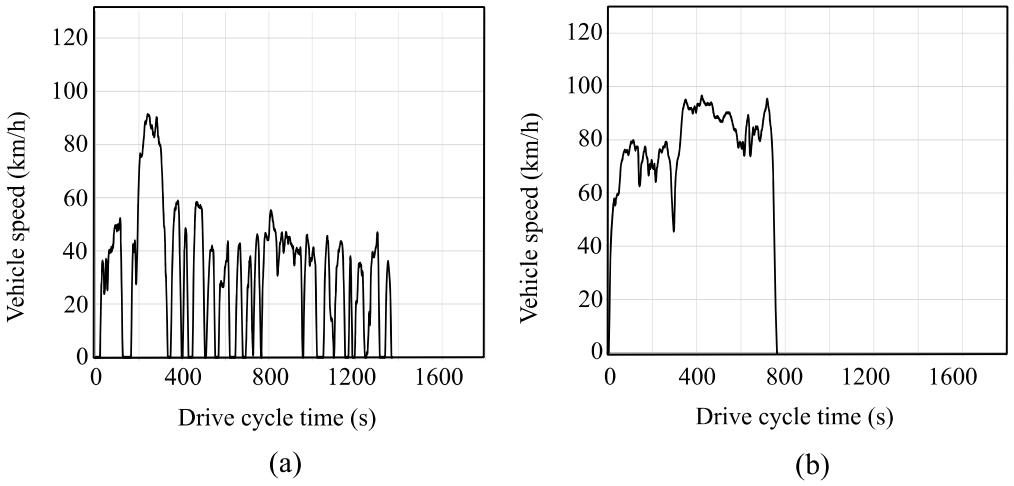

Figure 1-11. USA legislative drive cycles (a) UDDS (b) HWFET.

This multiplier is not applied if the vehicle is tested over three additional tests, including a high-speed, aggressive driving, US06 test, shown in Figure 1-12 (a). These additional tests reflect higher energy consumption conditions and when combined with the UDDS and HWFET results, the energy consumption then closely matches real-life test data.

Until 2017, certification of a vehicle's energy consumption in Europe involved a single combined drive cycle known as the New European Drive Cycle (NEDC), which is shown in Figure 1-12(b). This drive cycle consisted of an Urban drive cycle (average speed 18.35 km/h, maximum speed 50 km/h) that repeats four consecutive times (total distance 3976 m in 780 s), followed by an Extra-Urban driving cycle (average speed 62.6 km/h, maximum speed 120 km/h, total distance 6956 m in 400 s). Research studies, such as the ARTEMIS project, identified that the NEDC did not reflect typical driving profiles, particularly in terms of the acceleration rates [50]. The slow acceleration rates of the NEDC underestimated the energy consumption in real driving conditions and this resulted in optimistic driving ranges for these vehicles.

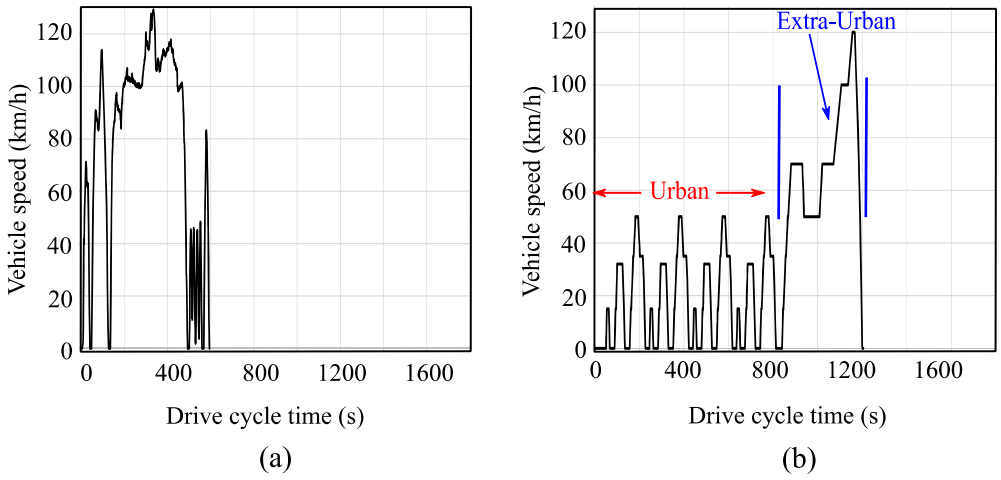

Figure 1-12. (a) US06 drive cycle (b) NEDC combined drive cycle.

Drive cycles with higher acceleration rates are shown in Figure 1-13. The ARTEMIS research project proposed several alternative drive cycles, such as their urban cycle as shown in Figure 1-13(a) [50]. In addition, a Worldwide Harmonized Light Vehicles Test Procedure (WLTP), as shown in Figure 1-13(b), was developed to standardise emissions testing in a wide range of countries [51]. Since 2017, energy consumption of passenger vehicles in Europe is measured using this new WLTP standard. The WLTP is a combined drive cycle, split into Low, Medium, High and Very-High driving conditions. As it is intended as a worldwide test standard, the speed profile specifications in terms of maximum speeds and acceleration rates, has to match the performance abilities of all possible test vehicles. This results in three different WLTP drive cycles (Class 1, Class 2 and Class 3) and the appropriate WLTP is selected based on the test vehicle's rated Power-to-Weight ratio (PWr). All the BEVs studied in this thesis have a PWr >34, which means that their energy consumption is measured with the WLTP Class 3 drive cycle.

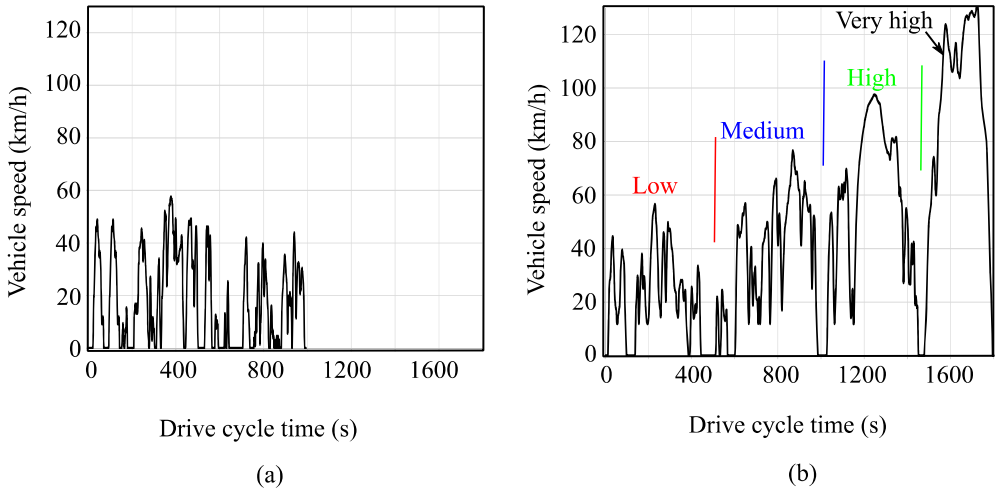

Figure 1-13. (a) ARTEMIS urban drive cycle and (b) WLTP.

Figure 1-14 shows the torque and speed operating points for the traction motor of a 2013 Leaf BEV in six drive cycles. As shown by this figure, the choice of test drive cycle can limit the validation of the traction motor model to specific regions of the torque-speed operations map. Most of the legislative drive cycles (vehicle energy or emission certification drive cycles) are dominated by vehicle operation at low levels of torque output from the traction motor. These operating points help to identify the regions in the torque-speed efficiency map for the traction inverter model and motor model that require high accuracy in a vehicle simulator. Apart from the US06 drive cycle, high accuracy in the high-torque, low speed region is not required based on the legislative drive cycle operating point shown in Figure 1-14.

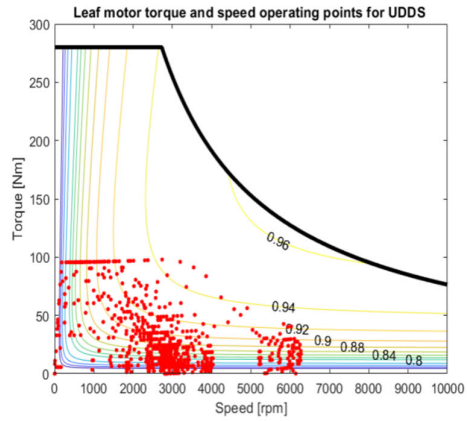

(a) UDDS drive cycle

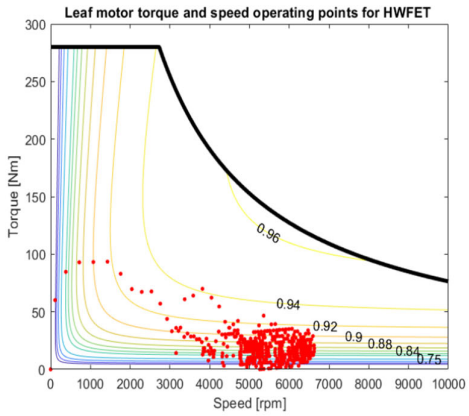

(b) HWFET drive cycle

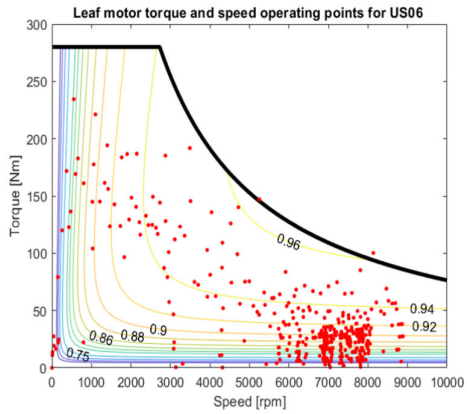

(c) US06 drive cycle

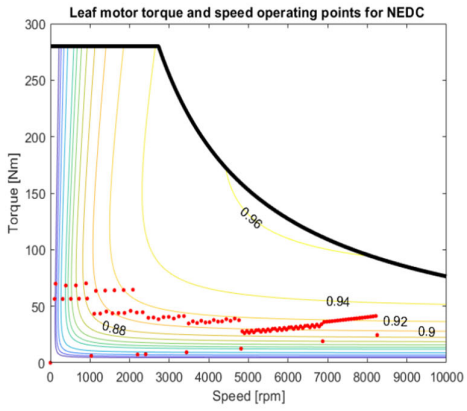

(d) NEDC drive cycle

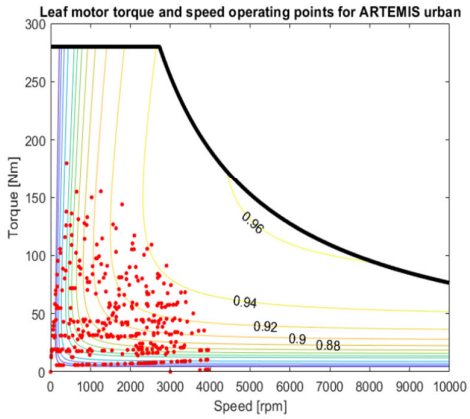

(e) ARTEMIS Urban drive cycle

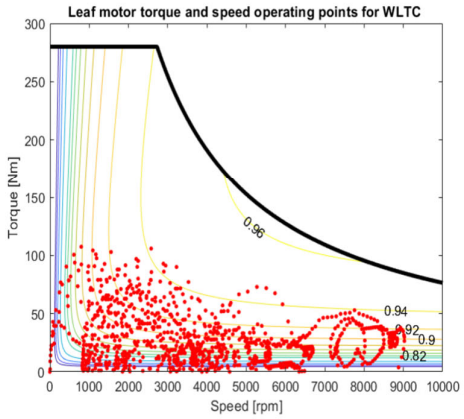

(f) WLTC drive cycle

Figure 1-14. 2012 Leaf motor torque and speed operating points when tested in various drive cycles.

1.6 Thesis Structure and Contributions

This section provides a simple overview of the thesis structure and describes the contributions to knowledge from my research studies.

1.6.1 Thesis Structure

The structure of the thesis is based on six chapters. This chapter has presented a basic introduction and an overview of the research topics of interest and is followed by five chapters, each written in a self-contained journal-paper style. There may be a small amount of intentional repetition of materials from one chapter to the next, as this structure eliminates the need for the reader to jump between chapters to find the relevant sections.

Chapter 2 describes the structure of the SEVP simulator and the improvements made to an earlier 2011 version of this simulator including: (i) modifying the vehicle model to use EPA coastdown coefficients to replace drag and rolling resistance; (ii) using a surface-mounted permanent-magnet (SPM) AC machine to replace the dc machine and (iii) validating the new model using experimental dynamometer test data, published in 2012 by ANL. This chapter further addresses some of the deficiencies of the SEVP by; (i) creating a simple HVAC model and (ii) including machine saturation and flux-weakening in the SPM traction motor model. This chapter expands the research presented at a 2014 conference [19].

Chapter 3 compares three vehicle simulators for BEV energy consumption applications. Two widely used simulators, ADVISOR and FASTSim, are compared with the proposed SEVP simulator. The three simulators are validated using ANL test data for ten vehicles. The comparison is enabled by combining all three simulators into a single Matlab model. This single model permits the interchange of the individual powertrain component models between the simulators to establish the impact of each component model on the cumulative energy consumption over a drive cycle. This chapter extends the research presented at a 2016 conference [52].

Chapter 4 presents empirical versions of Lithium-ion (Li-ion) battery models for the simulation of a BEV. This work expands the ideal battery model used in the SEVP simulator to include: (i) the available output voltage at the battery terminal as a function of the depth of discharge of the battery; (ii) the impact of the internal

impedance network on the dynamic performance of the battery model; and (iii) an ageing model to estimate the battery capacity fade over the lifetime of the vehicle. The empirical models are based on constant discharge battery test data from Idaho National Laboratories (INL) for eight BEVs and the vehicle dynamometer test data from ANL for the same eight BEVs. For concept vehicle designs, where battery test data is not yet available, a simplified Li-ion battery model is proposed based on the common characteristics observed in the INL test data. This chapter develops on the research presented at a 2020 conference [53].

Chapter 5 reviews the motor model in the SEVP simulator. Benchmarking reports from Oak Ridge National Laboratory (ORNL) are used to establish the construction of the internal permanent magnet (IPM) motors designs found in both BEV and HEV vehicles. Finite element analysis software, FEMM, is then used to analyse the torque-current relationships, the core losses and the parameter variation associated with magnetic saturation in these motors. This leads to a new IPM motor model for BEVs. This recent work has not yet been submitted for publication.

Chapter 6 proposes an energy management strategy (EMS) for a fuel cell electric vehicle (FCEV). In common with other EMS models for HEVs, the proposed EMS minimises the fuel consumption but improves on other EMS models by minimising the total cost of vehicle ownership. This is accomplished by including the degradation of the battery and fuel cell as operating costs in the EMS. The initial design structure of the EMS was presented at a conference in 2017 [54] and the final EMS was published in a peer-reviewed journal in 2019 [55].

Finally, in Chapter 7, a summary of the key results and possible future research work is presented.

1.6.2 Contributions

This thesis describes the development and validation of a computationally lightweight “backwards-facing” electric vehicle simulation tool. This energy consumption tool was validated with ten mid-sized BEVs and is shown to be sufficiently accurate for driving ranges prediction in different drive cycles.

This research further addresses the need for electrical models of BEV powertrain components with the development of equivalent electrical circuit models for both a Li-ion battery pack and an IPM traction motor.

Two options for the development of a battery model are presented, based on whether battery test data is available or not. Additionally, a capacity ageing model is developed that models the new Li-ion battery over the lifetime of the vehicle.

The developed IPM motor model allows the estimation of input phase currents and voltages based on the output torque and speed required from the motor. The model also displays the changing ratio between permanent-magnet torque and synchronous-reluctance torque over the full speed range of the motor. This model provides a seamless transition from maximum torque per amp to maximum torque per volt operation based on the motors' torque, speed, and the available battery voltage.

Finally, an energy management strategy that considers the degradation of both the fuel cell and the battery, is proposed for a fuel cell electric vehicle. The cost of ownership of a test vehicle is minimised over a journey, when operating the fuel cell close to its optimum power level and when restricting on-off operation of the fuel cell. For short journeys, the advantages of a plug-in version of a fuel cell electric vehicle, is presented in this research.

1.7 References

[1] US Department of Energy, *Fuel economy data*, [Online]. Available: www.fueleconomy.gov/feg/download.shtml. [Accessed: 10-Jul-2020].

[2] W. D. Nordhaus, "The energy crisis and macroeconomic policy," *Energy J.*, vol. 1, no. 1, pp. 11–19, 1980. doi: 10.5547/ISSN0195-6574-EJ-Vol1-No1-2

[3] F. Mustovic, *Autogas Propulsion Systems for Motor Vehicles*, 1st ed. Sarajevo, Bosnia and Herzegovina: IBC Engineering and Publishing, 2011.

[4] F. An, R. Earley, and L. Green-Weiskel, "Global overview on fuel efficiency and motor vehicle emission standards: Policy options and perspectives for international cooperation", UN Dept. of Econ. and Soc. affairs, CSD19/2011/ BP3, May 2011.

[5] G. l. Hunt, "The great battery search [electric vehicles]," *IEEE Spectrum*, vol. 35, no. 11, pp. 21-28, Nov. 1998, doi: 10.1109/6.730516.

[6] F. A. Wyczalek, "Market mature 1998 hybrid electric vehicles," *IEEE Aerospace and Electronic Systems Magazine*, vol. 14, no. 3, pp. 41-44, March 1999, doi: 10.1109/62.750428.

[7] H. R. Chang, B. J. Baliga, J. W. Kretchmer and P. A. Piacente, "Insulated gate bipolar transistor (IGBT) with a trench gate structure ", *1987 International Electron Devices Meeting*, Washington, DC, USA, 1987, pp. 674-677, doi: 10.1109/IEDM.1987.191518.

[8] H. Weh, H. Mosebach and H. May, "Design concepts and force generation in inverter-fed synchronous machines with permanent magnet excitation," *IEEE Transactions on Magnetics*, vol. 20, no. 5, pp. 1756-1761, September 1984, doi: 10.1109/TMAG.1984.1063488.

[9] M. P. Walsh, "Assessing transportation-related air pollution in major cities," *J. Urban Technology*, vol. 6, no. 1, pp. 1–24, 1999, doi: 10.1080/ 10630739983713

[10] Internation Energy Agency (IEA), "Fuel consumption of cars and vans." [Online]. Available: https://www.iea.org/reports/fuel-consumption-of-cars-and-vans [Accessed: 10-Jul-2020].

[11] S. Steinhilber, P. Wells, and S. Thankappan, "Socio-technical inertia: Understanding the barriers to electric vehicles," *Energy Policy*, vol. 60, pp. 531–539, September 2013, doi: 10.1016/j.enpol.2013.04.076.

[12] K. Davis, P. Rowley and S. Carroll, "Assessing the viability of electric vehicle technologies for UK fleet operators," *2013 48th Int. Universities' Power Eng. Conf. (UPEC)*, Dublin, 2013, pp. 1-6, doi: 10.1109/ UPEC.2013.6714947.

[13] K. Gyimesi and R. Viswanathan, "The shift to electric vehicles: putting consumers in the driver's seat," IBM Global Business Services, Exec. Rep. GBE03454-USEN-01, 2011.

[14] T. Franke, I. Neumann, F. Bühler, P. Cocron, and J. F. Krems, "Experiencing range in an electric vehicle: Understanding psychological barriers," *Appl. Psychology.*, vol. 61, no. 3, pp. 368–391, July 2012. doi: 10.1111/j.1464-0597.2011.00474.x

[15] Internation Energy Agency (IEA), "Global EV Outlook 2019." [Online]. Available: www.iea.org/reports/global-ev-outlook-2019. [Accessed: 10-Jul-2020].

[16] J. Neubauer and E. Wood, "The impact of range anxiety and home, workplace, and public charging infrastructure on simulated battery electric vehicle lifetime utility," *J. Power Sources*, vol. 257, pp. 12–20, 1 July 2014, doi: 10.1016/ j.jpowsour.2014.01.075.

[17] EVSpecifications, "EVSpecifications, News and Comparisons." [Online]. Available: www.evspecifications.com. [Accessed: 10-Jul-2020].

[18] J.G. Hayes, R.P.R. de Oliveira, S. Vaughan and M.G. Egan, "Simplified electric vehicle power train models and range estimation," *2011 IEEE Vehicle Power and Propulsion Conf.(VPPC)*, Chicago, IL, 2011, pp. 1-5, doi: 10.1109/ VPPC.2011.6043163.

[19] J. G. Hayes and K. Davis, "Simplified electric vehicle powertrain model for range and energy consumption based on EPA coast-down parameters and test validation by Argonne National Lab data on the Nissan Leaf," *2014 IEEE Transportation Electrification Conf. and Expo (ITEC)*, Dearborn, MI, 2014, pp. 1-6, doi: 10.1109/ITEC.2014.6861831.

[20] T. Markel, A Brooker, T. Hendricks, V. Johnson, K. Kelly, B. Kramer, M.O'Keefe, S. Sprik, and K.Wipke, "ADVISOR : a systems analysis tool for advanced vehicle modeling," *J. Power Sources,* vol. 110, no. 2, pp. 255–266, 22 August 2002, doi: 10.1016/S0378-7753(02)00189-1.

[21] A. Brooker, J. Gonder, L. Wang, E. Wood, S. Lopp, and L. Ramroth, "FASTSim : A model to estimate vehicle efficiency , cost and performance," *SAE World Congress and Exhibition*, Detroit, MI., USA, 2015, pp.1-12, doi:10.4271/2015-01-0973.

[22] C. Dépature, S. Jemeï, L. Boulon, A. Bouscayrol, N. Marx, and S. Morando, "IEEE VTS Motor Vehicles Challenge 2017 - energy management of a fuel cell/battery vehicle," *2016 IEEE Vehicle Power and Propulsion Conf. (VPPC)*, Hangzhou, 2016, pp. 1-6, doi: 10.1109/VPPC.2016.7791701.

[23] J. Larminie and J. Lowry, *Electric Vehicle Technology Explained*, 2nd ed. Chichester, West Sussex, UK: Wiley, 2012.

[24] T. D. Gillespie, *Fundamentals of Vehicle Dynamics*, 1st ed., Warrendale, PA, USA: Society of Automotive Engineers, 1992.

[25] M. Ehsani, Y. Gao, A. Emadi, *Modern Electric, Hybrid Electric and Fuel Cell Vehicles: Fundamentals, Theory, and Design*, 2nd ed., Boca Raton, FL. USA CRC Press, 2009.

[26] J. G. Hayes and G. A. Goodarzi, *Electric Powertrain:Energy Systems, Power Electronics and Drives for Hybrid, Electric and Fuel Cell Vehicles, 1*st ed., Chichester, West Sussex, UK: Wiley, 2018.

[27] R. Bosch GmbH, *Bosch Automotive Handbook*, 10th ed., Chichester, West Sussex, UK: Wiley, 2018.

[28] *Road Load Measurement and Dynamometer Simulation using Coastdown Techniques*, J1263, SAE International, 2010.

[29] P. Norrby, "Prediction of coast-down test results," M.S. thesis, Dept. of Prod. Dev., Chalmers University of Technology, Gothenburg, Sweden, 2012.

[30] United States Environmental Protection Agency, *Annual certification data for Vehicles, Engines and Equipment*, [Online]. Available: https://www.epa.gov/compliance-and-fuel-economy-data [Accessed: 10-Jul-2020].

[31] Argonne National Laboratory, Energy Systems Division, "Downloadable Dynamometer Database." [Online]. Available: https://www.anl.gov/es/downloadable-dynamometer-database. [Accessed: 10-Jul-2020].

[32] H. Lohse-Busch, M. Duoba, E. Rask and M. Meyer, "Advanced Powertrain Research Facility AVTA Nissan Leaf Testing and Analysis," Argonne National Laboratory (ANL), October 2012.

[33] X. Huang and J. Wang, "Nonlinear model predictive control for improving energy recovery for electric vehicles during regenerative braking," *2011 50th IEEE Conf. on Decision and Control and European Control Conf.*, Orlando, FL, 2011, pp. 7458-7463, doi: 10.1109/CDC.2011.6160619.

[34] A. Caratti, G. Catacchio, C. Gambino and N. C. Kar, "Development of a predictive model for regenerative braking system," *2013 IEEE Transp. Electrific. Conf. and Expo (ITEC)*, Detroit, MI, 2013, pp. 1-6, doi: 10.1109/ ITEC.2013.6573497.

[35] C. Fiori, K. Ahn, and H. A. Rakha, "Power-based electric vehicle energy consumption model: Model development and validation," *Appl. Energy*, vol. 168, pp. 257–268, 15 April 2016. doi: 10.1016/j.apenergy.2016.01.097.

[36] E. A. Grunditz and T. Thiringer, "Characterizing BEV powertrain energy consumption, efficiency, and range during official and drive cycles from Gothenburg, Sweden," *IEEE Transactions on Vehicular Technology*, vol. 65, no. 6, pp. 3964-3980, June 2016, doi: 10.1109/TVT.2015.2492239.

[37] T.A. Burress, "Benchmarking of competitive technologies, 2012 Nissan LEAF," Oak Ridge National Laboratory (ORNL), Presentation at US DOE Hydrogen and Fuel Cell Peer Evaluation Meeting, May 2012.

[38] J. De Santiago, H. Bernhoff, B. Ekergård, S. Eriksson, S. Ferhatovic, R. Waters and M. Leijon, "Electrical motor drivelines in commercial all-electric vehicles: A Review," *IEEE Transactions on Vehicular Technology*, vol. 61, no. 2, pp. 475-484, Feb. 2012, doi: 10.1109/TVT.2011.2177873.

[39] T.A. Burress, C.L. Coomer, S.L. Campbell, L.E. Seiber, L.D. Marlino, R.H. Staunton, J.P. Cunningham, "Evaluation of the 2007 Toyota Camry hybrid synergy drive system," Oak Ridge National Laboratory (ORNL), ORNL/TM-2007/190, April 2008.

[40] T.A. Burress C.L. Coomer, S.L. Campbell, A.A. Wereszczak, J.P. Cunningham, L.D. Marlino, L.E. Seiber, H.T. Lin, "Evaluation of the 2008 Lexus LS 600H hybrid synergy drive system," Oak Ridge National Laboratory (ORNL), ORNL/TM-2008/185, January 2009.

[41] T. A. Burress, S. L. Campbell, C. L. Coomer, C. W. Ayers, A. A. Wereszczak, J. P. Cunningham, L. D. Marlino, L. E. Seiber, H. T. Lin, "Evaluation of the 2010 Toyota Prius hybrid synergy drive system," Oak Ridge National Laboratory (ORNL), ORNL/TM-2010/253, March 2011.

[42] A. Wintrich, U. Nicolai, W. Tursky, and T. Reimann, *Application Manual Power Semiconductors*, 2nd ed., Nuremburg, Germany: Semikron International GmbH, 2015.

[43] J.R.M. Delos Reyes, R.V. Parsons and R. Hoemsen, "Winter happens: The effect of ambient temperature on the travel range of electric vehicles," *IEEE Transactions on Vehicular Technology*, vol. 65, no. 6, pp. 4016-4022, June 2016, doi: 10.1109/TVT.2016.2544178.

[44] K. Liu, J. Wang, T. Yamamoto, and T. Morikawa, "Exploring the interactive effects of ambient temperature and vehicle auxiliary loads on electric vehicle energy consumption," *Appl. Energy*, vol. 227, pp. 324–331, 1 October 2018, doi: 10.1016/j.apenergy.2017.08.074.

[45] L. P. Rodgers, "Electric vehicle design , racing and distance to empty algorithms," Ph.D. dissertation, Dept. Mech. Eng., MIT, Boston, MA. USA, 2013.

[46] A. Nedungadi, M. Pozolo and M. Mimnagh, "A general purpose vehicle powertrain modeling and simulation software - VPSET," *2008 World Automation Congress*, Hawaii, HI, 2008, pp. 1-6.

[47] A. Fotouhi, D. J. Auger, K. Propp, S. Longo, and M. Wild, "A review on electric vehicle battery modelling : From Lithium-ion toward Lithium – Sulphur," *Renew. Sustain. Energy Rev.*, vol. 56, pp. 1008–1021, April 2016, doi: 10.1016/j.rser.2015.12.009.

[48] M. Einhorn, F. V. Conte, C. Kral and J. Fleig, "Comparison, selection, and parameterization of electrical battery models for automotive applications," *IEEE Transactions on Power Electronics*, vol. 28, no. 3, pp. 1429-1437, March 2013, doi: 10.1109/TPEL.2012.2210564.

[49] H. Lohse-Busch, M. Duoba, K. Stutenberg and S. lliev, "Technology assessment of a fuel cell vehicle : 2017 Toyota Mirai," Argonne National Laboratory (ANL), ANL/ESD-18/12, January 2018.

[50] M. André, "The ARTEMIS European driving cycles for measuring car pollutant emissions.," *Sci. Total Environ.*, vol. 334–335, pp. 73–84, 1 December. 2004, doi: 10.1016/j.scitotenv.2004.04.070.

[51] M. Tutuianu, A. Marotta, H. Steven, E. Ericsson, T. Haniu, N. Ichikawa and H. Ishii, "Development of a worldwide harmonized light duty driving test cycle," *UN-ECE Technical Report*, GRPE-68-03, 2014.

[52] K. Davis and J. G. Hayes, "Analysis of electric vehicle powertrain simulators for fuel consumption calculations," *2016 Int. Conf. on Electrical Systems for Aircraft, Railway, Ship Propulsion and Road Vehicles & Int. Transportation Electrification Conf. (ESARS-ITEC)*, Toulouse, 2016, pp. 1-6, doi: 10.1109/ESARS-ITEC.2016.7841414.

[53] K. Davis and J. G. Hayes, " Comparison of lithium-ion battery pack models based on test data from Idaho and Argonne national laboratories," *2020 IEEE Energy Conversion Congress and Exposition (ECCE)*, Detroit, IL, 2020.

[54] K. Davis and J. G. Hayes, "Energy management strategy development to minimize the operating costs for a fuel cell vehicle," *2017 IEEE Vehicle Power and Propulsion Conf. (VPPC)*, Belfort, 2017, pp. 1-6, doi: 10.1109/VPPC.2017.8330990.

[55] K. Davis and J. G. Hayes, "Fuel cell vehicle energy management strategy based on the cost of ownership," *IET Electrical Systems in Transportation*, vol. 9, no. 4, pp. 226-236, 12 2019, doi: 10.1049/iet-est.2019.0021.

2 SIMPLIFIED ELECTRIC VEHICLE POWERTRAIN MODEL

The focus of this chapter is an extended version of a widely-cited 2014 conference paper on a simplified electric vehicle powertrain (SEVP) model for energy consumption estimation and for electrical circuit simulation in battery electric vehicles (BEVs) is [1]. The purpose of the 2014 paper was to improve on an earlier 2011 paper [2] by (i) modifying the vehicle model to use United States Environment Protection Agency (EPA) coast-down coefficients to replace the external load forces of drag and rolling resistance; (ii) using a surface-mounted permanent magnet (SPM) AC machine model to replace the dc machine and (iii) validating the new model using experimental dynamometer test data, published in 2012, by Argonne National Laboratory (ANL). The SEVP model was applied to the data of the 2012 Nissan Leaf BEV. Excellent correlation is demonstrated between the SEVP model predictions and the experimental data values for estimation of vehicle performance, such as energy consumption and range.

This chapter extends further to address some of the deficiencies of the 2014 version of the SEVP by (i) creating a simple HVAC model and (ii) including magnetic saturation and flux-weakening in the SPM traction motor model. Further improvements will include:(i) a more comprehensive validation of the SEVP, based on ten vehicles, in Chapter 3; (ii) improvements to the SEVP battery model in Chapter 4; and (iii) an alternative interior-permanent-magnet (IPM) traction motor model for the SEVP in Chapter 5.

2.1 Introduction

In recent years, societal interest in the development, production and sale of battery electric vehicles (BEVs) has increased significantly. Concerns regarding global warming due to CO_2 emissions and poor air quality in cities are the principle drivers for this interest in BEVs [3]. Announcements occur regularly on proposed new BEV product introductions into the automotive marketplace [4],[5],[6]. Key factors in customer acceptance of such new technologies will be the performance, cost and range of the battery electric vehicles. During this 2014 research study, most of the new BEVs had rated battery capabilities of 16 kWh to 24 kWh, apart from the luxury models from Tesla that had capacities of greater than 60 kWh. Battery capacity limited their published drive ranges in Europe to between 134 km and 175 km. The official driving range for all new vehicles was based on the New European Drive Cycle (NEDC), which when compared to real-world driving conditions, was known to lead to optimistic fuel consumption and low emissions in internal-combustion engine (ICE) vehicles [7],[8]. The unrealistic low dynamic performance requirements for a vehicle during a NEDC test also impacted BEV users, who reported feeling anxiety (range anxiety) about their ability to complete their journeys. This anxiety was based on their inability to estimate the achievable range as their typical energy consumption in real-world conditions exceeded the NEDC published values [9].

Given the inherent range limitations of BEVs and the associated driver range anxiety, a vehicle model to estimate vehicle energy consumption for varied sets of battery, road and driving conditions was required. However, range and energy consumption cannot be fully defined or predicted due to the stochastic aspects of completing a journey in a vehicle. In addition, environmental factors such as wind speed and ambient temperatures impact on the battery load of a BEV [10],[11]. The goals of this study were to develop a simplified structure of the BEV powertrain loss mechanisms and to combine this structure with a minimum parameter tractive effort model, resulting in an energy consumption model with low computational requirements in vehicle simulators.

Since 2014, interest in vehicle simulation models has broadened to include vehicle models for sustainable environment simulators. These simulators are involved in the diverse range of topics in mobility studies. Mobility study objectives can include optimising the route selection to minimise energy consumption (eco-routing),

providing the driver with the necessary indicators to maximise range (eco-coaching), establishing energy consumption with real-world driving conditions, or optimising charging infrastructure locations [12],[13],[14].

The choice of vehicle model depends on the accuracy required, the availability of detailed vehicle parameters, and the computational load of running the model. Typically, vehicle performance simulation requires component models in the form of look-up tables (LUT), and energy consumption is based on loss efficiency maps indexed by the vehicle's torque and speed over a drive cycle [15],[16],[17],[18]. These LUT models give rise to high computational loads, and are generally unsuited to mobility simulators where the vehicle model is only one component within a large logistics model. In mobility studies, the preferred vehicle model implements a simplified powertrain loss that is modelled as either a constant efficiency or as a piecewise function of power loss [19],[20],[21].

A compromise approach to vehicle modelling that fits between the LUT powertrain model and the constant efficiency models, is a simplified equation-based powertrain loss model, as previously described in [2]. In this model, the vehicle loads were calculated based on the published vehicle drag coefficient and using other experience-based assumptions on vehicle loads. This model has been widely applied or referenced across a diverse number of applications, from range prediction to economic dispatch to system or component performance [22],[23],[24],[25]. A deficiency of [2] is the lack of model validation. The SEVP model, outlined in this chapter, provides an improved version of the model presented in [2] and incorporates published EPA coast-down test parameters to calculate the vehicle road load [26]. Since its publication in 2014 [1], this improved model has been widely referenced, particularly in mobility studies [12],[13],[14],[19],[27].

The four objectives of this chapter are: (i) to present the structure of this improved vehicle model (SEVP model); (ii) to validate the SEVP model against the 2012 test data published by ANL; (iii) to outline the deficiencies of the model attributed to its simplified structure, and (iv) to address these identified deficiencies with potential solutions in the form of a slightly more complex powertrain power loss model.

With validation a key requirement, the Nissan Leaf is the specific vehicle of interest in this study and an image of this vehicle is presented in Figure 2-1. Argonne National Laboratory (ANL) has published detailed system and component test data

based on a 2012 model of the Nissan Leaf [28]. The ANL testing was conducted for a variety of drive cycles and temperature conditions, providing a very useful research tool. The ANL test data provides verifiable measured data that is difficult to obtain otherwise. Generally, such detailed information is not provided for the many BEVs coming on the market. This lack of published information resulted in using engineering experience to assume values for certain vehicle parameters in order to develop the SEVP model. These limitations are further discussed later in the chapter in Section 2.4.

Figure 2-1. 2012 version of the Nissan Leaf BEV [29].

The chapter is organised as follows: Section 2.2 summarises the procedures adopted to develop powertrain component models for the SEVP; Section 2.3 presents the validation results; Section 2.4 outlines the deficiencies of the SEVP model and of the validation method used in 2014. The conclusions are presented in Section 2.5.

2.2 Powertrain Model Development

A significant body of literature and a wide variety of software tools are available for vehicle modeling [30],[31],[32],[33]. In this chapter, engineering assumptions are applied to various powertrain components that enable calculation of the efficiency and other relevant parameters under a variety of driving conditions. This section provides an overview of the powertrain structure, the model parameters used for the 2012 Nissan Leaf and the model equations used to calculate the power at the input and output of each drivetrain component from the wheels to the battery terminals.

For this study, the powertrain models were implemented using Excel, but they may easily be implemented using other mathematical software such as MATLAB\Simulink. An overview of the SEVP model and some of its associated parameters is presented in Figure 2-2. The SEVP model estimates the energy consumption at the battery pack terminals at 1 second intervals as a vehicle completes a drive cycle. This calculation procedure is described in Section 2.2.6. A separate offline calculation is required to calculate the AC energy consumption from the utility.

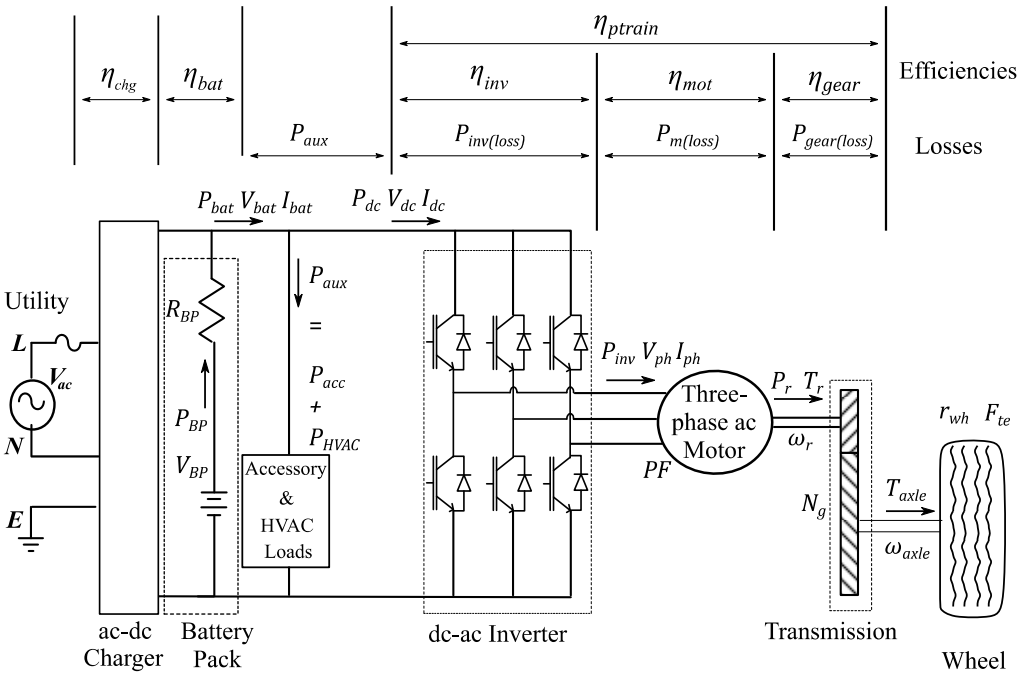

Figure 2-2. Electric vehicle system diagram to define powertrain parameter locations.

The SEVP electric vehicle parameters for the 2012 Nissan Leaf are presented in Tables 2-1 and 2-2. Table 2-1 outlines the published vehicle parameters from the manufacturer and those vehicle parameters as determined by ANL testing in [28]. The two most notable of these test parameters are the usable battery storage, and the battery pack's internal resistance R_{BP}. The usable battery energy of approximately 18 kWh was determined experimentally by stopping the dynamometer test when the vehicle was no longer capable of meeting a prescribed drive cycle speed [34]. This usable capacity is significantly lower than the nominal 24 kWh storage rating in the vehicle's specification. The table also includes the three coast-down test coefficients published by the EPA for the 2012 Leaf.

For PM traction motors such as that used in the Leaf, maximum torque output is available up to the base or rated speed of the motor. As maximum power output is also achieved at this rated motor speed, the maximum torque output is the rated torque output. Throughout this thesis, the maximum power and torque outputs of the motor are described as the rated power $P_{r(rated)}$ and rated torques $T_{r(rated)}$.

Table 2-1. Published 2012 Leaf parameters from Nissan, ANL and EPA [26],[28],[35].

Published Parameters		Symbol	Value	ANL Test Parameters		Symbol	Value
Rated battery storage	(kWh)		24	Usable battery storage	(kWh)		18
Curb weight	(kg)	M	1521	Test weight	(kg)	M	1701
Gear ratio	(-)	N_g	7.9377	Battery pack resistance	(mΩ)	R_{BP}	110
Rated output torque	(Nm)	$T_{r(rated)}$	280	Charging efficiency	(%)	η_{chg}	85
Rated output power	(kW)	$P_{r(rated)}$	80	Battery pack ave. voltage	(V)	V_{BP}	345
Coast-down A	(N)	A_{cd}	150	Auxiliary load power	(W)	P_{aux}	165
Coast-down B	(N/ms^{-1})	B_{cd}	0.61	Maximum HVAC	(W)	P_{HVAC}	6000
Coast-down C	(N/ m^{2}s^{-2})	C_{cd}	0.51	0 – 60 mph (0 - 96.5 kmph)	(s)		9.9
Wheel radius	(m)	r_{wh}	0.315				

Table 2-2 outlines all assumptions and several estimated parameters used to generate the SEVP models in the 2012 Leaf. Note that all efficiency assumptions are for the rated condition of 280 Nm/80 kW at the shaft of the traction motor. For simplicity, it was assumed in the 2014 study that a value of 85% provided a reasonable estimation of the efficiency of the grid-interface power-factor-corrected battery

charger plus the battery management system (BMS), including charging and cell equalization. This estimated value correlates well with the test data published in [28].

Table 2-2. Assumed and estimated 2012 Leaf parameters for powertrain component models.

Assumed Parameters	Symbol	Value	Estimated Parameters	Symbol	Value
Motor efficiency	η_{mot}	96%	Rated base speed (kmph)		40.8
Inverter efficiency	η_{inv}	98%	Machine constant (Nm/A)	k	0.327
Gear efficiency	η_{gear}	97%	Phase resistance (mΩ)	R_S	10.2
Battery efficiency	η_{bat}	97%	Phase inductance (μH)	L_S	444
Poles	p	8	No-load torque (Nm)	T_{nl}	2.9
Power factor of motor	$cos\varphi$	0.9	Maximum regen (kW)		20
Moment of inertia (kg m^2)	J_{axle}	2			

2.2.1 Vehicle Road Load

The vehicle road-load force, F_v, is determined from a 120 km/h coast-down test. The force equation coefficients A_{cd}, B_{cd}, and C_{cd} are provided in [26],[36] for many vehicles, including several BEVs. The force is evaluated from

$$F_v = A_{cd} + B_{cd}v + C_{cd}v^2 \tag{2.1}$$

where v is the vehicle speed in m/s. The plot of vehicle load force versus speed is provided in Figure 2-3. Alternatively, such a curve can easily be generated using data for the vehicle's drag and rolling resistance coefficients. However, the coast-down data curve is particularly useful as it contains additional speed-related losses within the vehicle powertrain, in addition to the external load forces such as drag and rolling resistance.

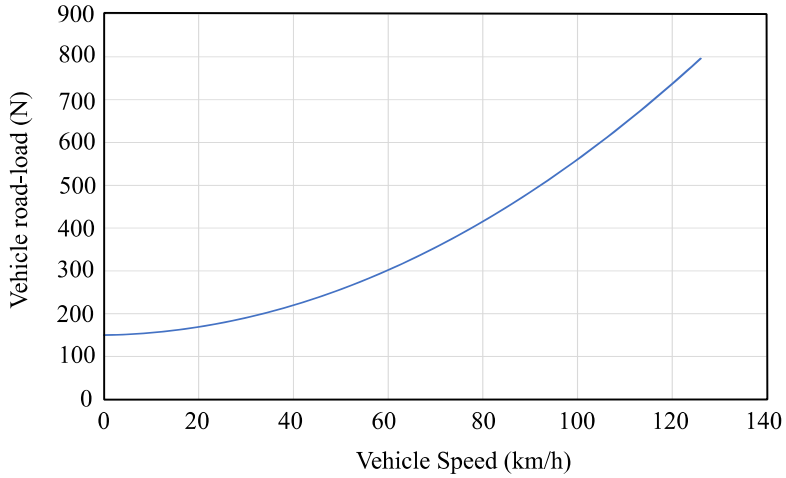

Figure 2-3. Vehicle road-load force for 2012 Nissan Leaf using coast-down coefficients.

The total motive or tractive force F_{te} is the combination of the road-load force F_v, climbing force F_c, acceleration force F_a and an drive-axle referenced inertial force F_{inert} for the rotating force required for the wheels and the powertrain components.

$$F_{te} = F_v + F_c + F_a + F_{inert} \tag{2.2}$$

The acceleration force is

$$F_a = Ma \tag{2.3}$$

where M is the vehicle test mass in kg and a is the linear acceleration of the vehicle in m/s^2. The climbing force is

$$F_c = Mgsin\theta_r \tag{2.4}$$

where g is the acceleration due to gravity in m/s^2 and θ_r is the road inclination angle in degrees. The inertia force is

$$F_{inert} = J_{axle}\frac{dv}{dt} = J_{axle}\frac{\alpha_{axle}}{r_{wh}} \tag{2.5}$$

where J_{axle} is an estimated axle-referenced moment of inertia in kg m^2, α_{axle} is the axle angular acceleration in radians/s^2 and r_{wh} is the tyre radius in m.

In this study, the vehicle models are validated against dynamometer data and the climbing force element of the motive force is equated to zero. The drive axis torque is

$$T_{axle} = \frac{F_{te}}{r_{wh}} \tag{2.6}$$

The traction motor torque output T_r is calculated as

$$T_r = \frac{T_{axle}}{(N_g \eta_{gear})} \tag{2.7}$$

where N_g is the transmission gear ratio and η_{gear} is the transmission gear efficiency. The transmission efficiency η_{gear} in (2.7) is an assumed value for the load friction losses within the gearing [37] and does not consider the spin or windage losses. This assumes that the traction drivetrain gearing is engaged during the coast-down test and that the test captures the no-load friction and windage losses of the gearing, and of the other drivetrain components.

2.2.2 Traction Motor Model

The Leaf battery is interfaced to a high-efficiency IPM ac traction machine by a three-phase dc-ac inverter outputting variable ac voltage, current and frequency as previously shown in Figure 2-2 [38]. Torque output from an IPM machine results from a combination of electromagnetic torque and reluctance torque. As explained in Chapter 5, maintaining a constant torque output from an IPM motor over a wide speed range requires detailed knowledge of the internal magnetic parameters of these motors.

In this 2014 version of the SEVP, the IPM motor is replaced by a less complicated SPM motor. This replacement is justified as the SPM motor has very similar power loss characteristics to the IPM motor. The advantage of an SPM model is that fewer machine parameters are required, and these parameters can be estimated by assuming a nominal efficiency η_{mot} and power factor $cos\varphi$ at the rated power condition.

As illustrated in Figure 2-4, the SPM motor is modelled as a simple equivalent electrical circuit (EEC). The EEC is a series circuit comprising of a per-phase stator series resistance $R_{S,}$ a per-phase synchronous inductance L_S and the motor's per-phase

back-emf E_{ph}. Under operating conditions of rated motor power output $P_{r(rated)}$ and minimum battery voltage $V_{bat(min)}$, the input phase voltage V_{ph} is calculated as $V_{ph(rated-min)}$ and the input phase current I_{ph} is calculated as $I_{ph(max)}$. Then the three required motor parameters, R_S , L_S and machine constant k, are derived using these phase voltages and phase currents at the rated speed $\omega_{r(rated)}$. The voltage drop across the synchronous reactance V_{Ls} can also be calculated as $\omega_e L_S$.

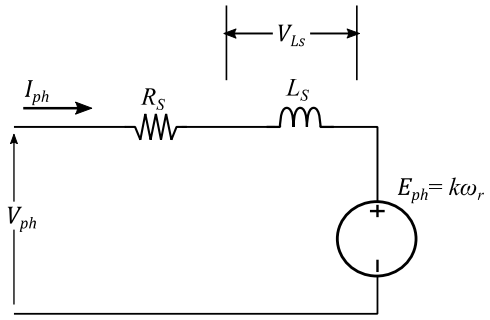

Figure 2-4. SPM traction motor model in the SEVP shown as a per-phase equivalent circuit.

2.2.2.1 Motor Electrical Inputs

The calculation of machine parameters k, R_S and L_S all depend on an estimation of the maximum input phase current $I_{ph(max)}$ to the motor. This current is defined as occurring when the motor is operating at its rated output power $P_{r(rated)}$ and the battery is operating at its minimum open-circuit voltage $V_{BP(min)}$. The electrical parameters for the motor model are calculated based on a procedure that is summarised in block diagram form in Figure 2-5.

The procedure for the calculation of $I_{ph(max)}$ relies on the assumed SEVP powertrain component efficiencies at the rated power condition. These include the rated motor efficiency η_{mot} of 96%, rated inverter efficiency η_{inv} of 98%, and the rated battery efficiency η_{bat} of 97%.

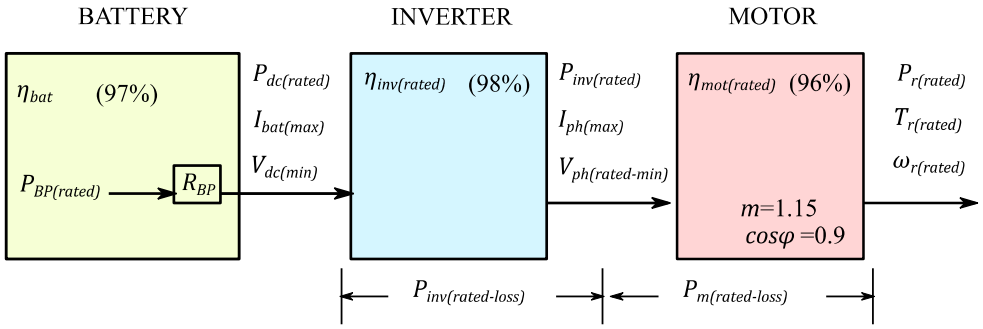

Figure 2-5. Block diagram to define powertrain parameters used in SEVP development.

The calculation procedure converts the rated motor output power $P_{r(rated)}$ to a rated inverter output power $P_{inv(rated)}$ using the assumed rated motor efficiency $\eta_{mot(rated)}$ as given by

$$P_{inv(rated)} = \frac{P_{r(rated)}}{\eta_{mot(rated)}} \tag{2.8}$$

The rated input power to the inverter $P_{dc(rated)}$ is then determined based on the rated inverter efficiency $\eta_{inv(rated)}$ by

$$P_{dc(rated)} = \frac{P_{inv(rated)}}{\eta_{inv(rated)}} \tag{2.9}$$

The rated battery pack power $P_{BP(rated)}$ is then determined based on the rated battery efficiency η_{bat} by

$$P_{BP(rated)} = \frac{P_{dc(rated)}}{\eta_{bat}} \tag{2.10}$$

This $P_{BP(rated)}$ is converted to a maximum battery current $I_{bat(max)}$ at minimum battery pack voltage $V_{BP(min)}$ using

$$I_{bat(max)} = \frac{P_{BP(rated)}}{V_{BP(min)}} \tag{2.11}$$

Assuming low-power requirements for auxiliary loads, the maximum input dc current to the inverter $I_{dc(max)}$ is approximately the same as $I_{bat(max)}$. This input

inverter current is converted to an equivalent output inverter current $I_{ph(max)}$ by first establishing the voltage conversion across the inverter.

At the $I_{bat(max)}$ input condition, the inverter is operating at its minimum input voltage $V_{dc(min)}$ as determined by

$$V_{dc(min)} = \frac{P_{dc(rated)}}{I_{bat(max)}} \tag{2.12}$$

The inverter's input to output voltage relationship is described using a modulation index m, which is defined as

$$m = \frac{\hat{V}_{ph}}{\left(\frac{V_{dc}}{2}\right)} \tag{2.13}$$

where $\hat{V}_{ph}$ is the amplitude of the output phase voltage and V_{dc} is the dc input voltage of the inverter. In the 2012 Leaf BEV and in several other BEVs, the battery output is directly connected to the dc input of the inverter. This equates to V_{bat} equal to V_{dc}.

Sinusoidal pulse-width modulation (SPWM) of the inverter devices produce sinusoidal output voltages with a maximum m value of 1. SPWM results in relatively low phase voltages that impact the achievable speed range of the motor. A commonly used alternative to SPWM is space-vector modulation (SVM) [39], [40]. The non-sinusoidal outputs of SVM result in a higher phase voltage and may have an m value up to 1.15 (over-modulation).

When the inverter is operating at rated power and at a minimum input voltage condition $V_{dc(min)}$, the SEVP assumes SVM inverter operation at an m of 1.15. Under these conditions the inverter rms output phase voltage $V_{ph(rated-min)}$ is determined by

$$V_{ph(rated-min)} = 1.15\left(\frac{V_{dc(min)}}{2\sqrt{2}}\right) \tag{2.14}$$

The maximum rms phase current from the inverter $I_{ph(max)}$ is then calculated using the previously estimated rated inverter output power in (2.8), an assumed rated condition power factor $cos\varphi$ and the inverter output voltage (2.14). This $I_{ph(max)}$ current is determined as

$$I_{ph(max)} = \frac{P_{inv(rated)}}{3V_{ph(rated-min)} \times cos\varphi} \tag{2.15}$$

Based on the estimation of $V_{ph(rated-min)}$ from (2.14) and of $I_{ph(max)}$ from (2.15), the components in the equivalent circuit of the traction motor model of Figure 2-4 are determined in the following subsections.

2.2.2.2 Motor Constant *k*

For optimum torque generation in the SPM motor, the phase current I_{ph} is vector-controlled to be in phase with the back-emf E_{ph}. The per-phase current and electromagnetic torque T_r are related by the machine constant, k. The basic SEVP energy consumption model neither factors in flux-weakening above the rated speed, nor magnetic saturation in the motor at high phase currents. Incorporation of these features is discussed in Section 2.4.

The machine constant k for this non-saturated SPM motor is calculated based on the published rated torque $T_{r(rated)}$ using

$$k = \frac{T_{r(rated)}}{3I_{ph(max)}} \tag{2.16}$$

2.2.2.3 Stator Winding Resistance *Rs*

The calculation of R_S also requires $I_{ph(max)}$. The SEVP model assumes a traction motor rated power efficiency $\eta_{mot(rated)}$ of 96%. The motor losses at the published rated motor power output are determined by

$$P_{m(rated-loss)} = \frac{P_{r(rated)}\left(1 - \eta_{mot(rated)}\right)}{\eta_{mot(rated)}} \tag{2.17}$$

These losses are assumed to be nominally distributed in the ratio of 75 % and 25 % between the stator copper loss P_{RS} and the lumped core and load-related friction losses P_{cfw}, respectively. The ohmic power losses in the stator winding resistance R_S, at this rated power and $V_{BP(min)}$ conditions, are given by

$$P_{m(rated-loss)} \times 75\% = 3\left(I_{ph(max)}\right)^2 R_S \tag{2.18}$$

This equation can be rearranged to estimate the value of R_S as

$$R_S = \left(\frac{P_{m(rated-loss)}}{3\left(I_{ph(max)}\right)^2}\right) \times 75\% \tag{2.19}$$

2.2.2.4 Synchronous Inductance L_S

The synchronous inductance L_S is calculated using the previously estimated values of k, R_S, $I_{ph(max)}$ and $V_{ph(rated-min)}$. The value of L_S is determined based on the voltage drops across the equivalent-circuit components, shown in Figure 2-4. At this rated condition, the rotor speed ω_r is equal to $\omega_{r(rated)}$. This rated speed of the motor is determined by

$$\omega_{r(rated)} = \frac{P_{r(rated)}}{T_{r(rated)}} \tag{2.20}$$

The motor's rms back-emf phase voltage $E_{ph(rated)}$ is then written as

$$E_{ph(rated)} = k\omega_{r(rated)} \tag{2.21}$$

The quadrature voltage-drop across L_S is determined by

$$V_{Ls} = \omega_e L_S I_{ph(max)} \tag{2.22}$$

where the electrical angular frequency ω_e, which in a motor with p poles and operating at the rated speed, is expressed as

$$\omega_{e(rated)} = \left(\frac{p}{2}\right)\omega_{r(rated)} \tag{2.23}$$

Thus, the voltage equation for the equivalent motor circuit becomes

$$\left(V_{ph(rated-min)}\right)^2 = \left(R_S I_{ph(max)} + E_{ph(rated)}\right)^2 + \left(\left(\frac{p}{2}\right)\omega_{r(rated)} L_S I_{ph(max)}\right)^2 \tag{2.24}$$

When (2.24) is rearranged, the synchronous inductance at this rated condition and at the minimum battery voltage, is calculated as

$$L_S = \left[\frac{\sqrt{V_{ph(rated-min)}^2 - \left(R_S I_{ph(max)} + k\omega_{r(rated)}\right)^2}}{\left(\frac{p}{2}\right)\omega_{r(rated)} I_{ph(max)}} \right] \tag{2.25}$$

2.2.2.5 Core Friction Windage Losses

The lumped core, friction and windage losses of the motor are modelled as a constant no-load torque loss T_{nl}. As previously stated, 25 % of the motor losses at the rated condition are assumed to result from the lumped core and load-related friction losses $P_{cfw(rated)}$. This loss is estimated using the previously estimated motor power loss at the rated condition in (2.17) to give

$$P_{cfw(rated)} = \left[P_{m(rated-loss)}\right] \times 25\% \tag{2.26}$$

The value of T_{nl} at the rated condition is then estimated as

$$T_{nl} = \frac{P_{cfw(rated)}}{\omega_{r(rated)}} \tag{2.27}$$

When the SEVP is used as an energy consumption model in a vehicle simulator, the combined motor losses at any torque-speed operating point can be estimated using

$$P_{m(loss)} = T_{nl}\omega_r + 3\left(\frac{T_r}{3k}\right)^2 R_S \tag{2.28}$$

2.2.3 Traction Inverter Model

The three-phase inverter of a BEV is constructed with six switching devices. Each device is composed of several switching components connected in a parallel configuration. Each component is normally an insulated gate bipolar transistor (IGBT) and its associated free-wheeling-diode (FWD) although silicon carbide mosfets are used on vehicles such as the Tesla Model 3. The inverter losses are composed of

conduction losses and switching losses in both the IGBT and FWD. The inverter loss model, described in Chapter 1, requires detailed component information and system operating information, which is not published by vehicle manufacturers.

In the SEVP, a simplified approach to inverter modelling is taken. The three-phase dc-ac traction inverter is modelled with an estimated rated condition efficiency $\eta_{inv(rated)}$ of 98 %. The inverter output power at this condition $P_{inv(rated)}$ is calculated in (2.8). At this rated condition, the inverter losses are estimated as

$$P_{inv(rated-loss)} = \frac{P_{inv(rated)}\left(1 - \eta_{inv(rated)}\right)}{\eta_{inv(rated)}} \tag{2.29}$$

The source of the inverter losses is assumed to be dominated by conduction losses that are dependent on the amplitude of the output phase current I_{ph}. As given by (2.16), the rms phase current in a SPM motor is proportional to the rotor torque T_r and the constant of proportionality is given by the machine constant k (no saturation assumed). The ratio of the inverter loss at any operating torque T_r to the inverter loss at the rated torque $T_{r(rated)}$ is given as

$$\frac{P_{inv(loss)}}{P_{inv(rated-loss)}} = \frac{T_r}{T_{r(rated)}} \tag{2.30}$$

This equation can be rearranged to estimate an inverter loss model at any torque output of

$$P_{inv(loss)} = P_{inv(rated-loss)}\left(\frac{T_r}{T_{r(rated)}}\right) \tag{2.31}$$

In addition to calculating the inverter losses without detailed component specification, a further advantage of this inverter modelling approach is that the losses are not dependent on the estimated phase currents and voltages from the motor model. A comparison of this inverter model to the inverter models described in Chapter 1 is presented in Section 2.3.2.1.

2.2.4 Auxiliary Load Model

Auxiliary loads are defined in this thesis as any vehicle function that is not directly contributing to the tractive effort. These include low-power accessory loads associated with the use of fans, lights, pumps, and high-power loads associated with the heating, ventilation and air conditioning (HVAC) of the passenger cabin. As this 2014 version of the SEVP did not include a thermal load model for the passenger cabin, the simulator is only suitable for ambient test conditions where the HVAC load is turned off. The low-power accessory load is modelled as a fixed load of 165 W for the 2012 Leaf.

The impact of ambient temperature on BEV energy consumption is presented in Section 2.4.2. A simplified average power HVAC model is proposed to partially address this deficiency of the 2014 version of the SEVP. Analysis of new ANL test data is presented in Section 2.4.3 and this analysis identified the requirement for a high-power transient HVAC load model to accurately model the total auxiliary load in a BEV.

2.2.5 Battery Model

The SEVP battery pack model is based on a simple series circuit, consisting of a voltage source and a series resistance as shown in Figure 2-5, where V_{BP} is the open-circuit voltage. Positive values of output battery power P_{bat} and output battery current I_{bat} represent a battery discharging. The battery efficiency η_{bat} is the round-trip efficiency associated with losses in the internal battery pack series resistance R_{BP} during charging and discharging of the battery. This battery efficiency is not included in the calculation of energy consumption during vehicle operation as validation of the SEVP model is based on test data measured at the battery terminals by ANL. The battery efficiency is only included in the calculation of recharging energy from the utility.

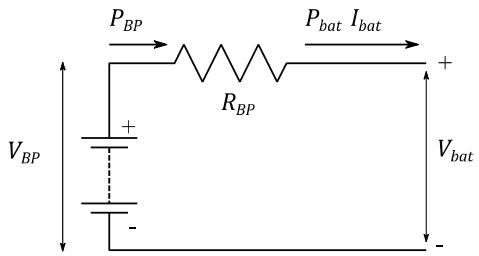

Figure 2-6. Battery model in the 2014 version of the SEVP simulator.

2.2.6 Calculation Sequence in Simulations

The SEVP is a backward-facing simulator model and therefore the calculation sequence starts by determining the vehicle speed in each 1 second time period in the test drive cycle as illustrated in Figure 2-7. Parameter $v_{(n)}$ represents the speed required in the n^{th} time period and $v_{(n-1)}$ represents the speed in the previous time period.

The acceleration of the vehicle is calculated based in the change in speed required between two 1 second periods. For each time period n, the vehicle's speed and acceleration are converted to an axle torque $T_{axle(n)}$ using equations (2.1) to (2.6). The axle angular speed $w_{axle(n)}$ in this period is then given by

$$\omega_{axle(n)} = \left(\frac{v_{(n)}}{r_{wh}}\right) \tag{2.32}$$

Then the $T_{axle(n)}$ is converted to the equivalent traction motor torque output $T_{r(n)}$ using (2.7). The $\omega_{axle(n)}$ is changed to a traction motor shaft speed $\omega_{r(n)}$ using

$$\omega_{r(n)} = \omega_{axle(n)} N_g \tag{2.33}$$

The output rotor power in this time period is then determined by

$$P_{r(n)} = T_{r(n)} \omega_{r(n)} \tag{2.34}$$

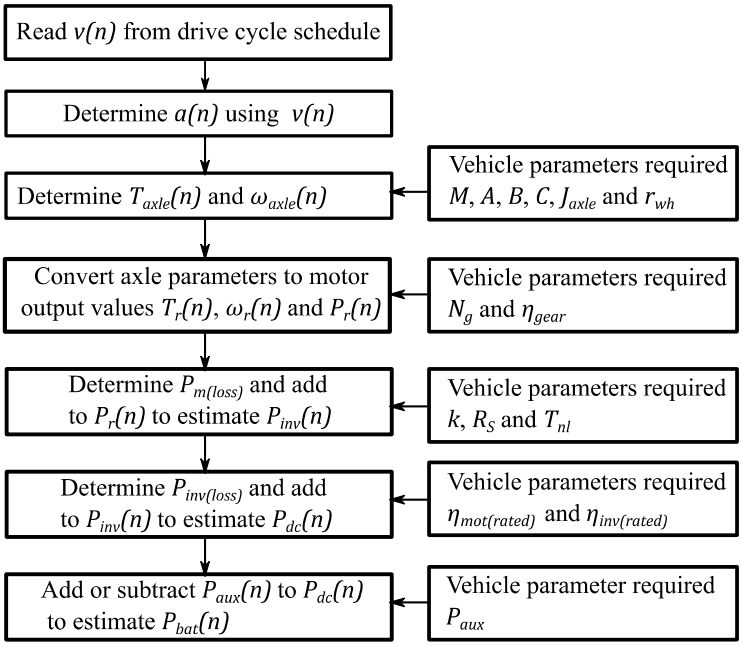

Figure 2-7. Flowchart of backward energy consumption simulation sequence in SEVP.

All of these calculations are required for both energy consumption simulation and for electrical circuit simulation. At this point the calculation sequence branches depending on the type of simulation required, energy consumption or powertrain electrical circuit.

2.2.6.1 Energy Consumption Calculation Sequence

Energy consumption simulation is based on a positive value of P_r, arising when the power flow direction is from the battery to the wheels. A negative P_r value occurs during high regenerative braking conditions, when the power flow direction is from the wheels to the battery. In both situations, the motor power loss (2.28) and inverter power loss (2.31) are determined by the instantaneous values of $T_{r(n)}$ and $\omega_{r(n)}$. The the powertrain losses are added to the $P_{r(n)}$ value to estimate the battery output power. The total battery output power P_{bat} must also include the power required for auxiliary load P_{aux} and the battery power discharged or recharged in each period is calculated as

$$P_{bat} = P_{aux} + P_{inv(loss)} + P_{m(loss)} + P_r \tag{2.35}$$

2.2.6.2 Electrical Circuit Calculation Sequence

The electrical circuit simulation calculation sequence is very similar to the energy consumption calculation sequence except that the emphasis is on determining the electrical parameters at the output of the inverter and battery in the powertrain. This sequence begins by converting $T_{r(n)}$ to the motor's input phase current $I_{ph(n)}$ using

$$I_{ph(n)} = \frac{T_{r(n)}}{3k} \tag{2.36}$$

During high regenerative braking events, the phase current will have a negative value due to the negative rotor torques at the output of the motor.

With an assumed fixed battery pack output voltage V_{bat} equal to the inverter input voltage V_{dc} and an assumed modulation index of m =1.15, the input phase voltage V_{ph} is determined using

$$V_{ph(n)} = 1.15\left(\frac{V_{dc}}{2\sqrt{2}}\right) \tag{2.37}$$

The input apparent power to the motor S_{mot} is then calculated using

$$S_{mot} = 3I_{ph}V_{ph} \tag{2.38}$$

The inverter output power is the real power input to the motor $P_{inv(n)}$ and is the sum of the motor losses (2.28) and the rotor output power $P_{r(n)}$. The input power factor of the motor $cos\varphi$ is the ratio of $P_{inv(n)}$ to $S_{mot(n)}$. The real input power to the inverter $P_{dc(n)}$ is the sum of the motor input power $P_{inv(n)}$ and the inverter power loss $P_{inv(loss)}$ calculated using (2.31). The total battery output power $P_{bat(n)}$ is estimated by adding the auxiliary loads (including any HVAC load) to the $P_{dc(n)}$ value. With an assumed fixed battery pack voltage V_{BP}, this $P_{bat(n)}$ value is converted to an equivalent battery output current $I_{bat(n)}$ using

$$I_{bat(n)} = \frac{\left(V_{BP} - \sqrt{V_{BP}^2 - 4R_{BP}P_{bat(n)}}\right)}{2R_{BP}} \tag{2.39}$$

There are several simplifications applied in the SEVP model that impact the accuracy of the model for electrical circuit simulation of a BEV powertrain. The input phase currents are underestimated by the lack of consideration of flux weakening during high-speed operation and by not including magnetic saturation when operating with high-torque outputs. The value of the input power factor is also a function of the flux-weakening operating mode. The actual voltage of a battery pack is dependent on the state of charge (SOC) of the battery, so that the accuracy of the battery current as calculated by (2.39) with an assumed fixed battery voltage, will depend on the battery SOC at any period in the drive cycle. Some of these electrical circuit simulation deficiencies are addressed in Section 2.4 and the remainder are addressed in Chapter 4 with an improved battery model, and in Chapter 5 with a new IPM motor model.

2.3 Simulation Results

An initial test on the SEVP model, the acceleration curve with rotor output torque, provided results as shown in Figure 2-8. The 0-60 mph (0-96 kmph) time of 9.8 s is an excellent correlation to the published time of 9.9 s. This plot has been generated using the procedure outline on page 57 of [33].

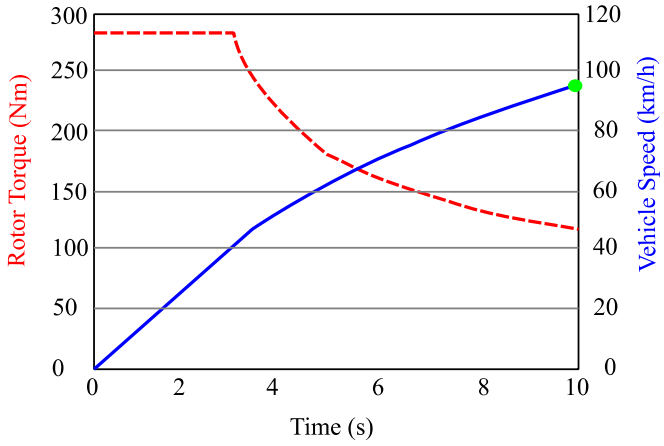

Figure 2-8. 2012 Nissan Leaf model 0-60 mph (0-96 kmph) acceleration and torque.

The validation of the component models in the SEVP model is based on a comparison of their individual component efficiency maps with the measured efficiencies of these components in the 2012 Leaf.

2.3.1 Motor Model Efficiency

The SEVP motor model efficiency map can be compared to benchmark testing carried out on the 2012 Leaf motor by Oakridge National Laboratory (ORNL) [41]. A map of efficiency versus motor torque and speed is shown in Figure 2-9. ORNL measured the motor's efficiency as greater than 90% for most of the operating range of the Leaf motor. At the rated condition of 80 kW and 280 Nm, the measured efficiency is approximately 93%.

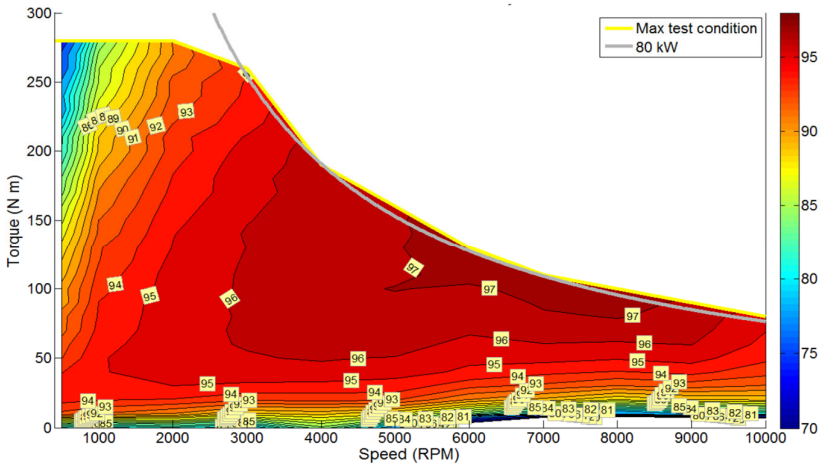

Figure 2-9. LEAF motor efficiency map as measured by ORNL [41].

The efficiency map of the SEVP model is shown in Figure 2-10. The efficiency contours show good agreement to the ORNL test data. The model estimates slightly higher losses when the torque is less than 25 Nm and does not capture the reduced efficiency seen in the ORNL for two specific regions; (i) below base speed with high-torque conditions and (ii) at high speeds. The reasons for these model digressions will be discussed in Section 2.4.

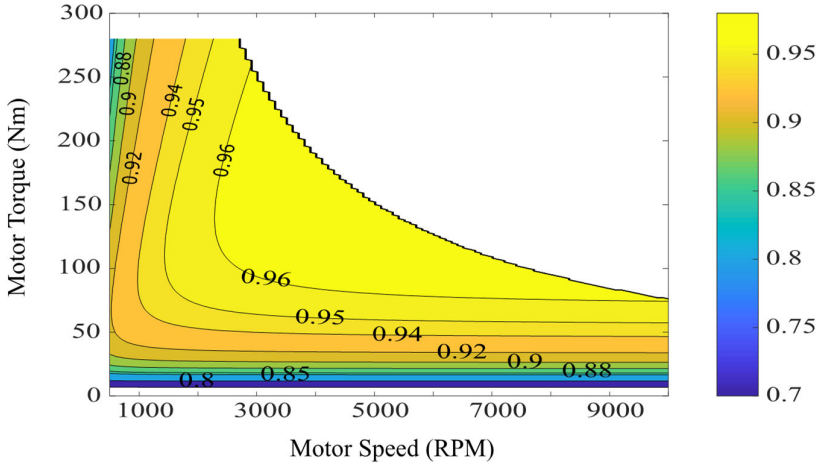

Figure 2-10. SEVP motor model efficiency map for 2012 Leaf.

2.3.2 Inverter Model Efficiency

An efficiency map of the 2012 Nissan Leaf inverter published by ORNL is shown in Figure 2-11. In the ORNL 2012 Leaf tests, the inverter's efficiency is approximately 96% at the rated condition and increases to 99%. Below 1000 rpm the measured inverter efficiency is between 85% and 91%.

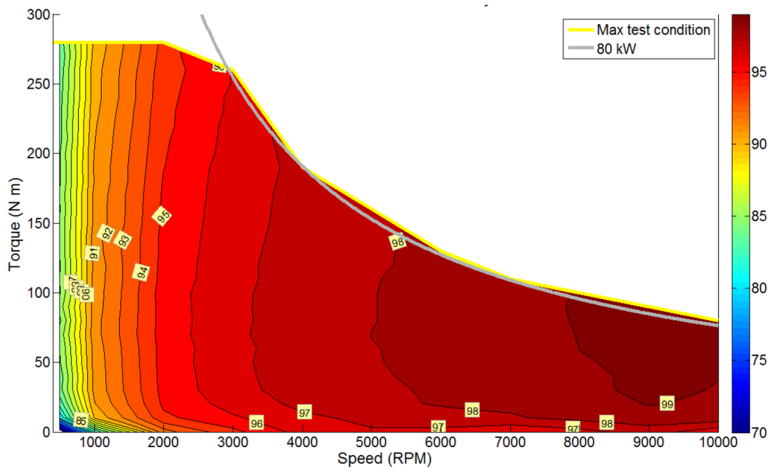

Figure 2-11. LEAF inverter efficiency map as measured by ORNL [41].

Two efficiency maps for the 2014 SEVP inverter model are shown in Figure 2-12. The efficiency map for the original 2014 SEVP inverter model is shown in Figure 2-12(a) and a modified model that includes a fixed housekeeping supply is shown in Figure 2-12 (b). Both versions of the inverter model report slightly higher efficiency than the ORNL test values at the rated condition (98%) and at speeds below 1000 rpm (91% to 95%). The unmodified 2014 inverter models' efficiency contours show poor agreement to the ORNL test data at very low torque outputs. In this version of the model, as shown in Figure 2-12(a), inverter efficiency approaches 98% irrespective of power output.

In a practical inverter, a low level of power is required by the control and by the gate drive circuitry. This is known as a housekeeping supply and the power level required is relatively independent of the inverter output power. When a constant housekeeping load of 75 W is applied to the inverter model, as shown in Figure 2-12(b), the model efficiency map contours more closely matches the efficiency contours of the ORNL test data.

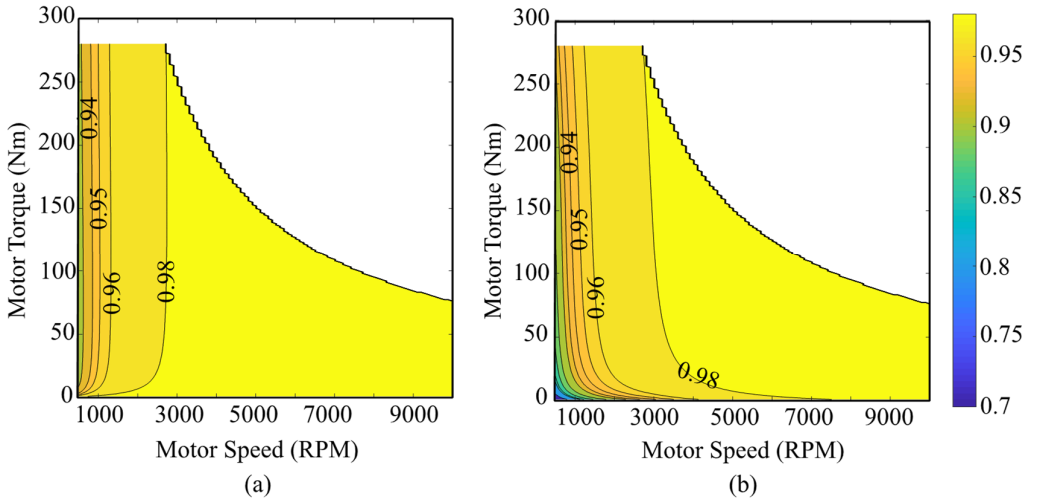

Figure 2-12. SEVP inverter model efficiency map for 2012 Nissan Leaf (a) without and (b) with a constant housekeeping load.

A comparison of the SEVP inverter with alternative inverter models as introduced in Chapter 1, is presented in Section 2.4.5. The impact of the simplifications to the SEVP inverter model are reviewed in this section also.

2.3.3 Combined Motor and Inverter Model Efficiency

The ORNL efficiency map for the combined motor and inverter efficiencies is presented in Figure 2-13. The equivalent SEVP combined efficiency map for these components is shown in Figure 2-14. Both maps show peak efficiencies of 96%. At the rated condition, ORNL measured an efficiency of approximately 89% while the SEVP shows a higher combined motor and inverter efficiency of approximately 93%. The SEVP model efficiencies below 1000 rpm are also higher than those measured by ORNL.

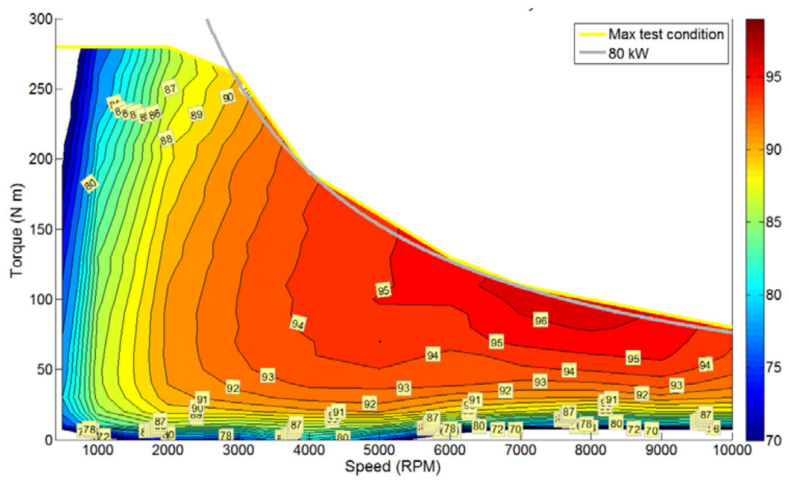

Figure 2-13. 2012 Leaf combined motor and inverter efficiency map measured at ORNL [41].

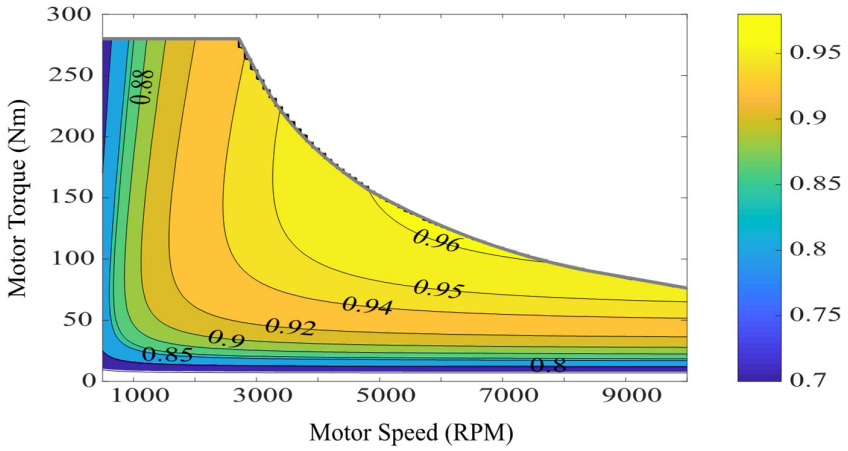

Figure 2-14. SEVP model combined motor and inverter efficiency map for 2012 Leaf.

Component validation of the SEVP traction effort model and the transmission model was not possible, as no test measurements are available for these components. Instead the validation of the complete SEVP vehicle model is based on the energy consumption over one complete test drive cycle. As noted in Chapter 1, the choice of test drive cycle for the validation process influences which region is being tested of the torque-speed map of the motor and inverter. Full validation of a powertrain model

requires consideration of several different drive cycles to ensure that a wide range of regions in the efficiency maps are sampled in the validation process.

2.3.4 Validation of Vehicle Model

Many types of standardized drive cycles are used around the world. In Europe the NEDC was the legislative test drive cycle until 2017 when it was replaced with the Worldwide Harmonized Light Vehicles Test Procedure (WLTP) drive cycle. Both the NEDC and WLTP drive cycles have two or more distinct phases that simulate driving conditions in several specific driving environments, such as city streets, rural roads or highways. The approach followed by the EPA in the USA is to test the vehicle over two or more different drive cycles where each drive cycle tests the vehicle in a specific driving environment. The four basic EPA drives cycles are: the Urban dynamometer Drive Schedule (UDDS) that simulates low speed, start and stop driving conditions found in city driving conditions; the Highway Fuel Economy Test (HWFET) that simulates the constant high-speed driving conditions of highways and motorways; a high-speed drive cycle with aggressive braking and acceleration events that is known as the US06 test; the SC03 is an urban drive cycle and is the only drive cycle where HVAC power is required in the test. The validation of the SEVP for the 2012 Leaf is based on three of the EPA cycles, UDDS, HWFET, and US06, as the dynamometer testing carried out by ANL was also based on these cycles.

The SEVP model calculates the energy required for motoring and for regenerating. The SEVP model results are then compared to the experimental data published by ANL in [28]. This 2014 version of the SEVP model assumes that the available regenerative energy is returned to the battery provided the regenerative power level is 20 kW or less.

The UDDS drive cycle has the longest test duration of the three test cycles. The range of vehicle speeds for the UDDS is presented in Figure 2-15(a), while the battery power from the model is presented in Figure 2-15(b). The high frequency of regenerative braking events in the UDDS provides test data for the validation of the powertrain component models during power flow from the wheel to the battery.

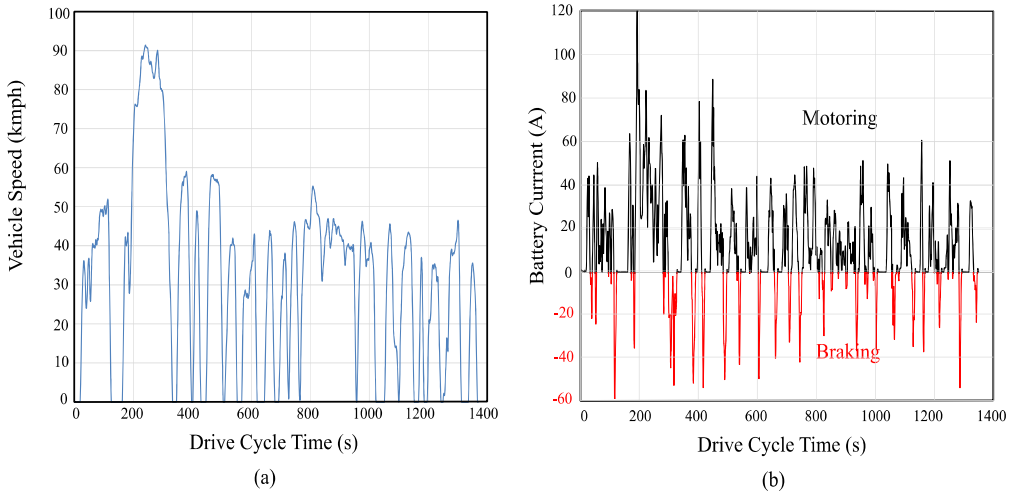

Figure 2-15. UDDS drive cycle: (a) speed profile and (b) battery currents for 2012 Leaf.

In addition, ANL gathered a significant amount of data for the 2012 Leaf, tested on the UDDS, which was published in [28]. A summary of the ANL measured energy flows over the complete cycle is presented in Figure 2-16. The auxiliary load in the ANL tests is limited to low-power accessory loads only as HVAC was turned off in this test. The motor losses, shown in Figure 2-16, represent the combined motor and inverter losses. The significantly high level of energy recovered with regenerative braking is a characteristic of the UDDS drive cycle and is not replicated in the other two types of test cycles.

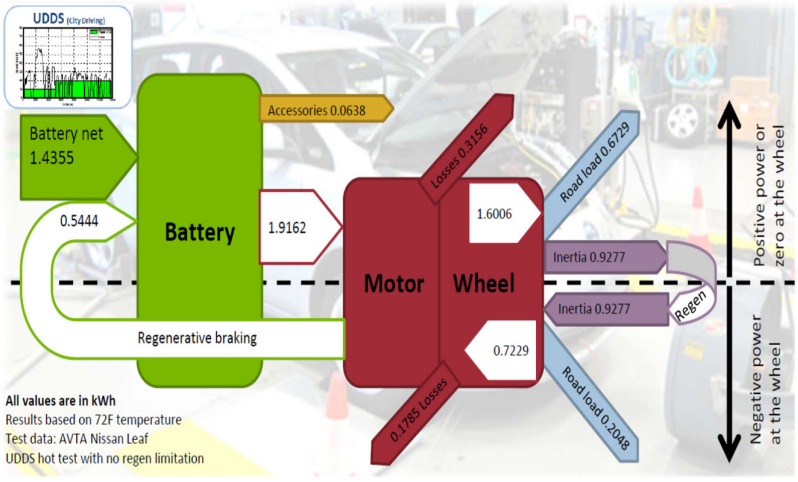

Figure 2-16. Distribution of energy over UDDS drive cycle for 2012 Leaf [28].

Table 2-3 provides a detailed comparison between the SEVP model and the test results presented by ANL. In general, there is an excellent correlation between the model results and the measurement data with a 4.5 % error in the net battery energy over the complete cycle. The error band derives from the engineering assumptions on the electromechanical powertrain. The high underestimation (-14%) in the powertrain losses occurs mainly during braking (negative power at the wheel). As presented in Figure 2-16, the powertrain losses in the ANL tests, with positive power and with negative power at the wheels, are 0.3156 kWh and 0.1785 kWh, respectively. The corresponding values in the SEVP simulator are 0.295 kWh and 0.129 kWh. This is equivalent to an accuracy of 94% for positive power loss estimation and to a significantly lower accuracy of 72% in the negative power loss estimation. A full explanation of this modelling issue with regenerative braking in the 2012 Leaf is presented in Chapter 3.

Table 2-3. Comparison of SEVP model predictions and ANL measurements in UDDS test.

UDDS Drive Cycle Results	**Model (kWh)**	**ANL (kWh)**	**Error (%)**
Battery Out (Traction & Accessory)	2.046	1.980	3.3
Battery In (Regen)	0.538	0.5444	-1.2
Battery Net	1.508	1.436	5.0
Inertia (average)	0.915	0.9277	-1.4
Dc kWh/mile	0.202	0.194	4.1
Road Load & Vehicle Spin loss	0.900	0.8777	2.5
Powertrain losses	0.424	0.4941	-14
(Inverter Loss)	0.084		
(Motor Copper & Core Loss)	0.268		
Gearing Loss (w\o spin)	0.072		

Table 2-4 contains a summary of the net energy consumption comparison test results for the 2012 Leaf in all three drive cycles. The net energy consumption is the energy discharged from the battery during motoring minus the energy recovered to the battery during regenerative braking. The SEVP model predictions and the ANL experimental tests for the UDDS, HWFET and US06 drive cycles, show a good correlation for this net energy consumption. The maximum error of 4.5% occurs in the

UDDS cycle due to the previously mentioned modelling issue with regenerative braking.

Table 2-4. 2012 Leaf net energy consumption per drive cycle at battery output.

Test	Model (kWh/cycle)	ANL (kWh/cycle)	Error (%)	Model (kWh/mile)	ANL (kWh/mile)	Error (%)
UDDS	1.508	1.440	4.5	0.202	0.193	4.5
HWFET	2.37	2.36	0.4	0.231	0.230	0.4
US06	2.62	2.68	-2.4	0.327	0.335	-2.4

Table 2-5 shows the predicted range for the 2012 range based on the SEVP model and on the measured ANL energy consumption per mile. The calculation of this range is based on the ANL useful battery storage value of 18 kWh rather than its rated capacity value of 24 kWh. This comparison again shows a good correlation with a maximum error of 4.5% occurring in the UDDS cycle.

Table 2-5. Estimated range of 2012 Leaf in a given drive cycle type.

Test	Model miles (km)	ANL miles (km)	Error (%)
UDDS	89 (143)	93 (150)	-4.5
HWFET	78 (125)	78 (125)	0.4
US06	55 (88)	54 (87)	+2.4

Tables 2-3, 2-4 and 2-5 show clearly that the SEVP model achieves its objective of accurately estimating the energy consumption for this vehicle, and for a given usable battery capacity, it predicts the range of the vehicle with a maximum error of 4.5%. The shortcomings of the presented SEVP model and the limitations of the current validation process are examined in Section 2.4.

2.3.4.1 Vehicle Utility Energy Consumption

When the SEVP model is required to determine the economic feasibility of a BEV, the energy consumption must be estimated at the wall socket rather than using the battery output dc energy consumption as provided in Table 2-4. The utility or ac energy consumption is the dc energy consumption in Table 2-4 divided by the recharging system efficiency. The recharging system efficiency is the product of the on-board charger efficiency and the battery efficiency. The recharging system

efficiency is presented in Figure 2-17 as the ratio of the "Point E" energy divided by the "Point A" energy. This is different to the on-board charger efficiency, which is defined as the ratio of the "Point C" energy divided by the "Point A" energy.

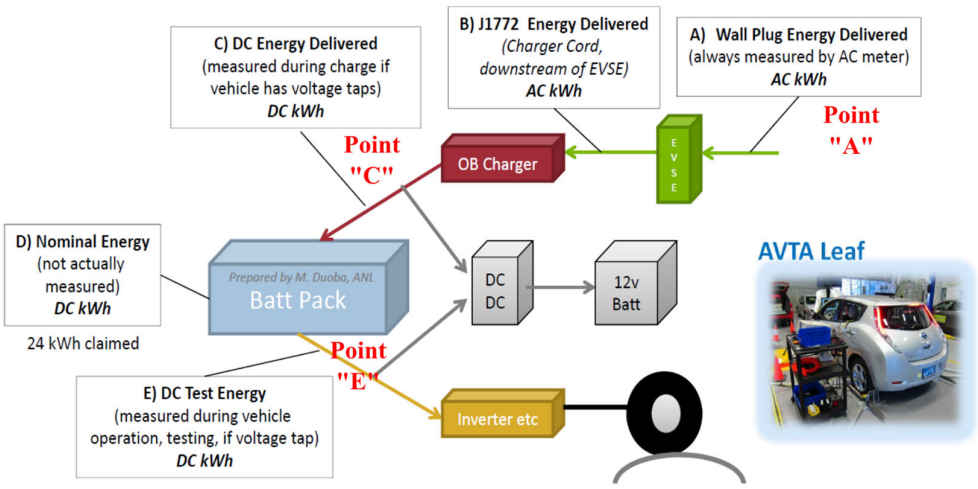

Figure 2-17. Classification method for charging efficiencies [28].

The ac energy consumption in the SEVP model was evaluated based on the 2012 Leaf recharge system efficiency that ANL established as an on-board charger efficiency of 85% and a battery efficiency of 97%. The resultant recharging system efficiency for ac energy consumption is 82.5%. Subsequent ANL test data on other BEVs is presented in Table 2-6 and published in [36]. As illustrated in Figure 2-18, this data shows that the higher on-board charger efficiencies in the five tested BEVs are in the region of 88% to 91.5%. Insufficient charging data in the ANL published files for the 2012 Leaf meant that this vehicle could not be included in Figure 2-18.

The recharging system efficiency in these vehicles ranges from 85.6% to 88.2%. These are significantly higher efficiencies than the 82.5% efficiency in the 2012 Leaf and lead to additional modelling errors for ac energy consumption estimation in the SEVP. Based on this analysis, the charger efficiency value in the 2014 version of the SEVP model needs to be increased from 85% to 90% to reflect the observed average charger efficiencies in the BEVs tested at ANL in 2015.

Table 2-6 Charger efficiency, battery efficiency and recharge efficiency.

Vehicle	Point A	Point C	Point E	Charger efficiency	Battery efficiency	Recharge efficiency	Additional model error for ac consumption
		(kWh)		(%)	(%)	(%)	(%)
Leaf (2013)	22039	19682	19100	89.3	97.0	86.7	4.2
eGolf	21816	19957	19239	91.5	96.4	88.2	5.7
BMW i3	21537	19487	18834	90.5	96.6	87.4	4.9
Soul	27364	24161	23405	88.3	96.9	85.6	3.1
B-class	34021	31059	29285	91.4	94.3	86.2	3.7

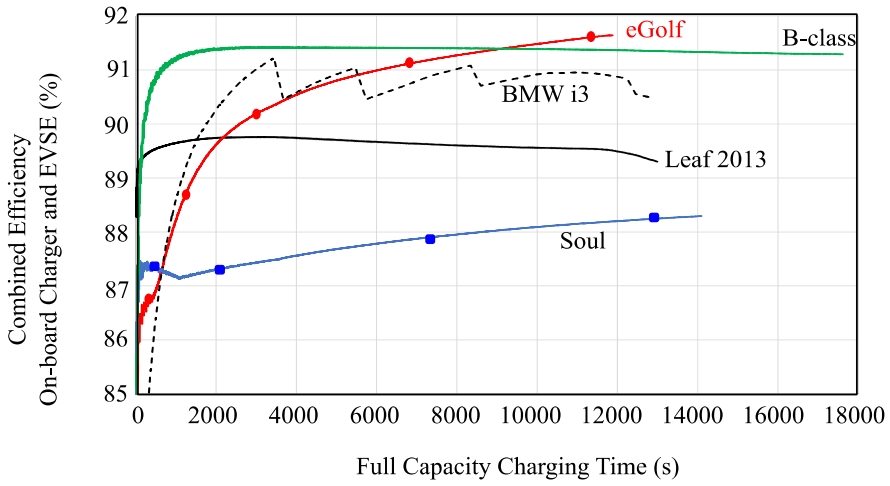

Figure 2-18. On-board charger efficiencies based on 2015 ANL test data.

2.4 Deficiencies of the SEVP Model

The SEVP model is based on deriving the electrical parameters for an SPM motor. These parameters allow the SEVP model to be used either as an energy consumption model or as an electrical circuit model for a BEV powertrain. Up to this point in the thesis, only a limited validation of the model based on a single vehicle has been presented and this validation is limited to energy consumption applications. Validation of the model as an electrical circuit model was not prioritised in the early stages of this research as addressing range anxiety was then the clear focus of the study. However, electrical circuit simulation also requires an improved battery model and the development of such a battery model is described in Chapter 4.

The SEVP model deliberately applied simplified powertrain component models to minimise the computational load of the simulator and to reduce the required vehicle parameters for specification of the vehicle model. These simplifications impact the model accuracy, both as an energy consumption model and as an electrical circuit model. These deficiencies in the 2014 version of the SEVP model include: (i) a limited vehicle validation process, (ii) the lack of a thermal model for the passenger cabin to determine HVAC power, (iii) the lack of field weakening and magnetic saturation in the SPM motor model and (iv) a comparison of its inverter model to standard inverter models. Each of these deficiencies is reviewed in this section.

2.4.1 Limitations of the 2014 Validation Process

The 2014 version of the SEVP was validated against the published energy consumption data from ANL. This data was limited to a single model of BEV. The data was extracted from a summary data table of the dynamometer testing and from a technology benchmarking powerpoint presentation on the general findings of the vehicle tests [28]. As range anxiety was a major barrier to the adoption of these vehicles, the published ANL data was mostly based on averaged energy consumption per mile. Later, ANL published more detailed test measurements for each 0.1 s test period of the drive cycles and tested nine further models of BEVs at their test facilities. This detailed test data allowed a more comprehensive validation of the SEVP model and these extensive validation results are presented in Chapter 3.

2.4.2 Impact of Outside Ambient Temperature

In ICE vehicles, the impact of HVAC loads is a well-researched topic, where it can significantly impact emissions [42]. HVAC load is also referenced in the literature on BEVs where it can restrict the electric driving range significantly [43],[44]. The maximum HVAC load P_{HVAC} is 6 kW for the 2012 Nissan Leaf. Driving in extreme temperature conditions can result in significant range reduction, as HVAC is required for the passenger cabin and for the batteries. ANL tested the 2012 Leaf in all drive cycles at three ambient temperatures, specifically at -6°C (20°F), 23°C (72°F) and 35°C (95°F). The climate control HVAC system for the passenger cabin of the vehicle was turned off in the 23°C tests. It was turned on and set at a control temperature of approximately 22.5°C in the other two ambient test conditions.

As shown in Figure 2-19, ANL identifies the potentially high impact of the power required for cabin climate control on the energy consumption per mile for this vehicle. The ANL low ambient temperature results show the impact of P_{HVAC} as a 92% increase in energy consumption per mile in the UDDS cycle, with lower increases of 42% and 25% in HWFET and US06 cycles. These summary results provide a distorted view of HVAC load impacts as they are highly influenced by the average traction power and the duration of each cycle.

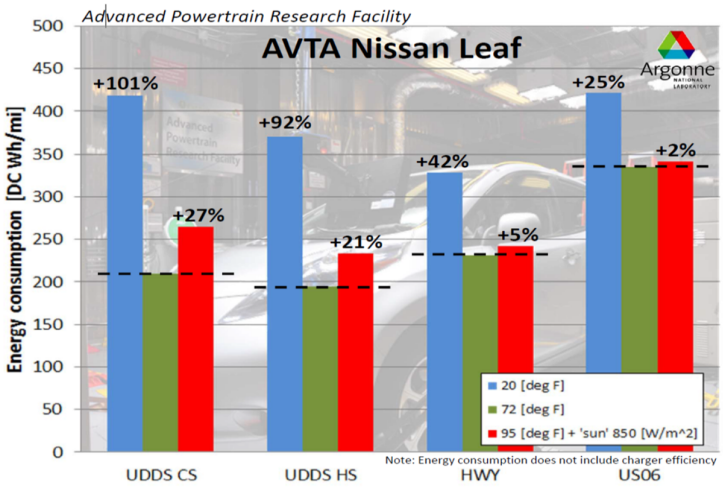

Figure 2-19. Impact of outside ambient temperature on energy consumption [28].

The low average traction power requirement of the UDDS cycle results in higher HVAC power impacts while the high average traction power requirements in

the US06 cycle, results in lower HVAC power impacts on overall energy consumption per mile calculations.

In addition, HVAC power is dependent on the temperature difference between the actual passenger cabin temperature and the temperature control setpoint. The highest HVAC power is required when this temperature difference is high, which is typically the case at the start of a journey. As the journey progresses, the temperature difference reduces and so does the average P_{HVAC} value. The three test drive cycles have durations of 1370 s for UDDS, 765 s for HWFET and 600 s for the US06. The HVAC power impacts are higher in the shorter test cycles than would be the case if all the test cycles had the same duration.

As the ANL test data did not include P_{HVAC} values or passenger cabin temperatures, the 2014 version of the SEVP model was designed without a thermal model for the cabin. This restricted the validation of the SEVP model to the ANL testing at 23°C, as the climate control system was turned off in these tests. This deficiency is partially addressed in the following sections.

2.4.2.1 Analysis of ANL HVAC Data

Approximately three years post publication of the 2014 SEVP model validation, ANL provided the author with a more comprehensive data set for two BEVs, namely the Kia Soul and the BMW i3. This more recent data included cabin temperature measurements during the various dynamometer tests. A preliminary investigation into the transient response of the cabin thermal system power requirements was then conducted as part of this research.

Results confirmed that the rated 6 kW of the HVAC system is only required for the initial heating of the cabin, as illustrated in Figure 2-20(a). The initial cooling of the cabin in high ambient temperatures is presented in Figure 2-20(b). The results from the long duration UDDS cycle are presented as they show a considerably lower steady-state HVAC power is required to maintain the cabin at the required temperature as the journey continues.

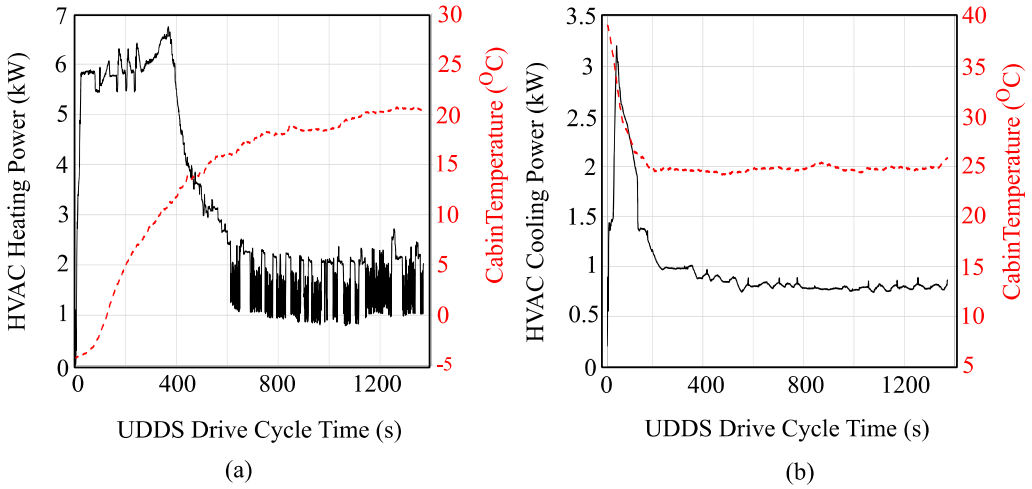

Figure 2-20. Estimate of average HVAC power in UDDS drive cycle [based on ANL test data].

The development of a complex transient thermal model of the cabin and the HVAC system that accurately estimates the additional battery energy required on a journey was considered to be outside the scope of this research study. Instead a simplified average HVAC power model is proposed where the P_{HVAC} value is dependent only on the external ambient temperature value T_{amb}.

2.4.2.2 Proposed Simplified HVAC Model

In environments that require cabin climate control, the deficiency of the 2014 version of the SEVP as an energy consumption vehicle simulator, is partially addressed by the incorporation of a simplified averaging thermal model. This averaging thermal power model was constructed by comparing the ANL measured energy consumption for a given drive cycle at the three tested ambient temperatures. The UDDS drive cycle was selected for this comparison due to its long 1370 s duration. Using the summary test datasheets for six vehicles from ANL, the additional average power required during the minus 6°C and 35°C tests was determined.

The accuracy of this average power method is impacted by the BEV testing procedure at ANL. Each BEV was tested by combining several drive cycles tests into a single testing session and ANL published the test data for these combined test sessions. In testing, the vehicle is placed in the test chamber prior to the start of the test session and remains there for a period sufficient to allow each vehicle component

to reach thermal equilibrium with the air in the test chamber. Hence, the cabin air temperature matched the test chamber air temperature for the first test.

This leads to either very high cooling or heating loads in the first test. For subsequent tests, the ambient air in the test chamber is maintained at the required level and the thermal load in the cabin is lower as the cabin environment has been pre-heated or pre-cooled by the prior test. The cabin temperatures during a sequence of four low ambient temperature tests on the Kia Soul is shown in Figure 2-21 (a) and for a sequence of four high ambient tests in Figure 2-21(b). The measured HVAC power for these tests is presented in Figure 2-21(c) and Figure 2-21(d) respectively. The ambient temperatures outside the vehicle remained constant at -6°C for the heating tests and at 35°C for the cooling tests.

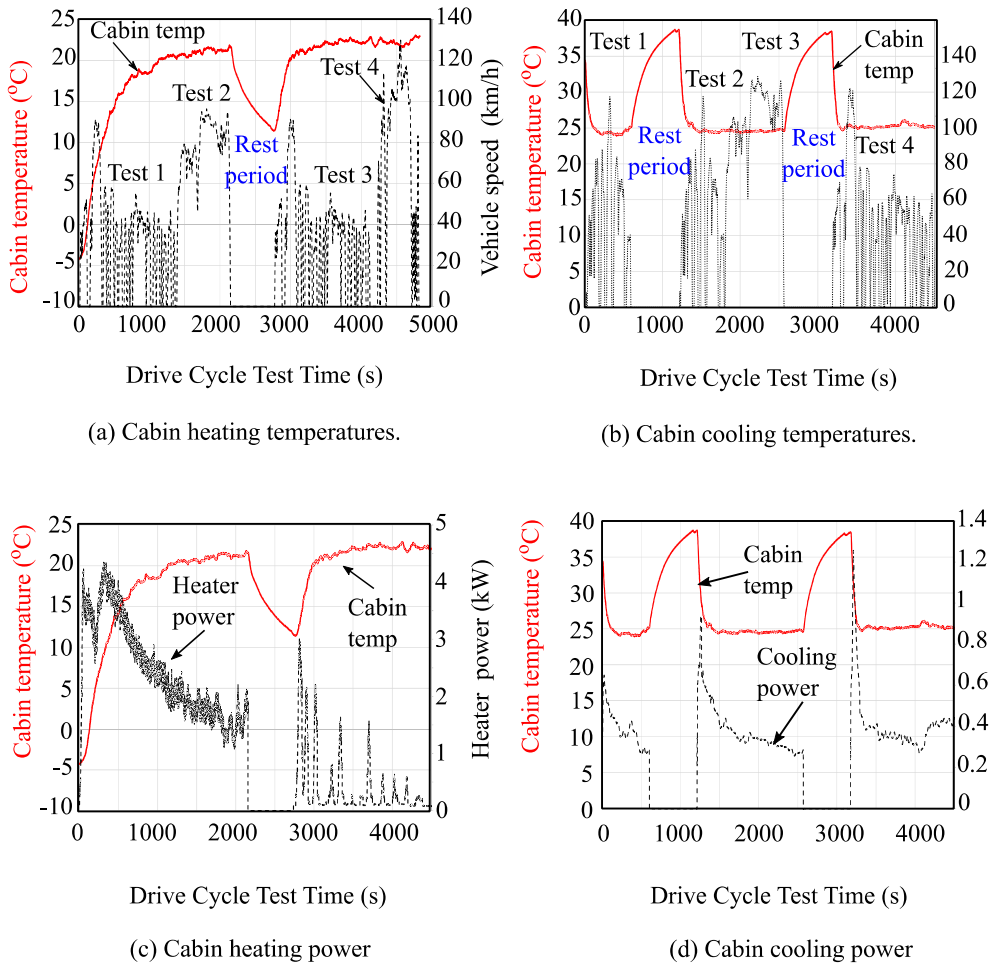

Figure 2-21. Cabin heating and cooling system analysis [based on ANL test data].

Vehicles with larger capacity batteries had more than one UDDS test at each temperature and the HVAC impact depended on where in the testing sequence each UDDS occurred. For the proposed simplified HVAC model, an average HVAC power impact at each ambient temperature was determined for the UDDS tests.

A third-order polynomial was loosely fitted to these HVAC power values as shown in Figure 2-22. The ANL data included some vehicles that were tested at up to five ambient temperatures and these additional tests were included to improve the curve-fit of the polynomial. The average HVAC power required at any ambient temperature T_{amb} (°C) is evaluated from

$$P_{HVAC} = -0.027T_{amb}^3 + 5T_{amb}^2 - 162T_{amb} + 1560 \quad (2.40)$$

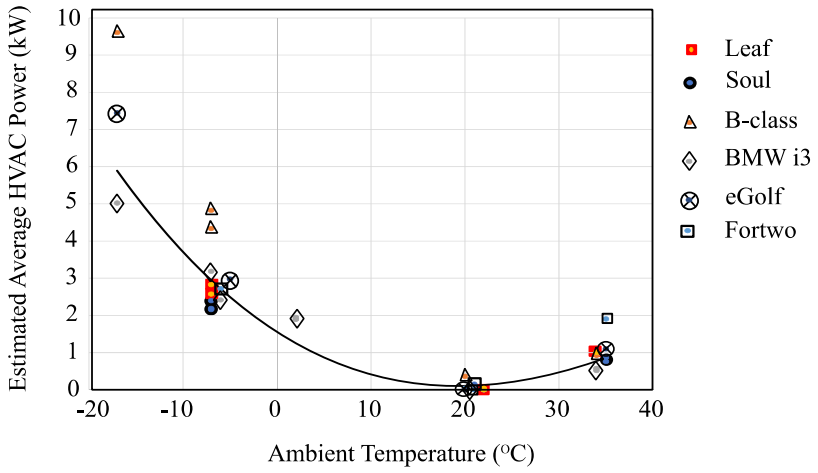

Figure 2-22. Polynomial for average HVAC power to ambient temperature.

The validation of the SEVP model at three ambient temperatures with and without the average power thermal model is shown in Table 2-7. In the absence of the HVAC thermal model, the energy consumption in the UDDS drive cycle is underestimated by 82.7% at an ambient temperature of minus 6°C.

The lower underestimation of 15.4% seen at an external ambient temperature of 35°C, is partially explained by the lower temperature differential between the temperatures inside and outside the cabin. Inclusion of the HVAC average power model improves these underestimates to 8.4% and 5.1%, respectively.

Table 2-7. SEVP model of 2012 Leaf with, and without, average thermal model.

Test	Temperature	ANL	Model without P_{HVAC}	Model with P_{HVAC}	Error without P_{HVAC}	Error with P_{HVAC}
	(°C)	(kWh/cycle)			(%)	(%)
UDDS	-6	2.756	1.508	2.543	-82.7	-8.4
	23	1.436		1.508	4.8	4.8
	35	1.741		1.834	-15.4	5.1
HWFET	-6	3.368	2.372	3.023	-42	-11.4
	23	2.358		2.372	0.6	0.6
	35	2.477		2.628	-4.4	5.7
US06	-6	3.355	2.622	3.073	-28	-9.2
	23	2.68		2.622	-2.2	-2.2
	35	2.736		2.762	-4.35	0.95

2.4.3 Upgrades to the SPM Motor Model in the SEVP

In terms of electrical circuit simulation, the choice of a simplified SPM motor model, to represent the typical IPM traction motors of BEVs leads to errors in parameter estimation. This deficiency is addressed in Chapter 5, where an alternative complex IPM motor model is proposed. Within this chapter, the accuracy of the SPM motor model is improved, for both energy consumption and electrical circuit simulation, by incorporating flux-weakening operation and magnetic saturation into the SPM model.

2.4.3.1 Flux Weakening

The maximum no-load speed of an electric motor is determined by the back-emf of the motor. At this speed, the amplitude of the back-emf is approximately equal to the input voltage supply. This back-emf is directly related to the angular speed of the motor by the machine constant k. In metric units, the back-emf to speed machine constant is the same as the torque constant k. The amplitude of k is proportional to the flux linkage of the magnetic field. Operation at speeds higher than the maximum no-load speeds are possible by reducing the value of the flux linkage, which effectively reduces the value of k for the back-emf but not for the torque. This process is known as flux weakening.

In a simple dc motor design with a shunt field winding, flux weakening is achieved by reducing the magnetic field excitation current. In permanent magnet (PM) motors designs, such as the SPM, the magnetic field strength of the PM can only be weakened by applying an opposing magnetic field to the PM field.

In a BEV, the SPM or IPM traction motor is an ac synchronous motor supplied by three phase currents from an inverter drive, which in turn is fed from a dc supply. Using the phase current, the opposing magnetic field required for flux weakening is generated by setting the electric angle between the magnetic field and phase current magnetic axis beyond the optimum 90° for maximum-torque-per-ampere (MTPA) operation. This procedure is known as phase or current advance. Phase advance is usually analysed in the *dq* reference frame, where the impacts of a phase current are determined by separating the phase current vector into two orthogonal axis vectors, *d* and *q*. A negative *d*-axis current flux weakens the PM field for higher speed operation in the SPM and a positive *q*-axis current produces electromagnetic torque. A brief introduction to the *dq* reference frame is provided in Appendix A.

2.4.3.1.1 Flux Weakening in SPM Motors

While it is common to describe currents and voltages in the *dq* reference frame in terms of their peak values such as i_d, i_q, v_d, and v_q, the convention adopted in this thesis is to present these parameters as their equivalent rms quantities I_d, I_q, V_d and V_q. This convention was used in [33] and provides intuitive relationships between these *dq* parameters and the input rms phase voltages and currents.

In the *dq* reference frame, the EEC of the SPM motor is split into two equivalent circuits based on the orthogonal axis currents. These two circuits, as shown in Figure 2-23, include the dynamic voltage drops and can be represented as axis-aligned voltage drops as shown in Figure 2-24. The flux-weakening process in the *dq* reference frame assumes a constant k value and involves adjusting the ratio of I_d to I_q to constraint the overall circuit voltage drop to a maximum available V_{ph} value.

The magnetic circuit of the motor in each axis is represented by its equivalent inductances L_d and L_q. In an SPM motor, both axis inductances are identical as the magnetic path reluctance is dominated by the combination of the airgap permeability and the low permeability of the magnets on the surface of the rotor. As such, each axis inductance can be represented by a synchronous reactance L_S value. In contrast, the

axis inductances in IPM motors have significantly different values and must be viewed as two separate components. Further analysis of the *dq* model for IPM motors is provided in Chapter 5.

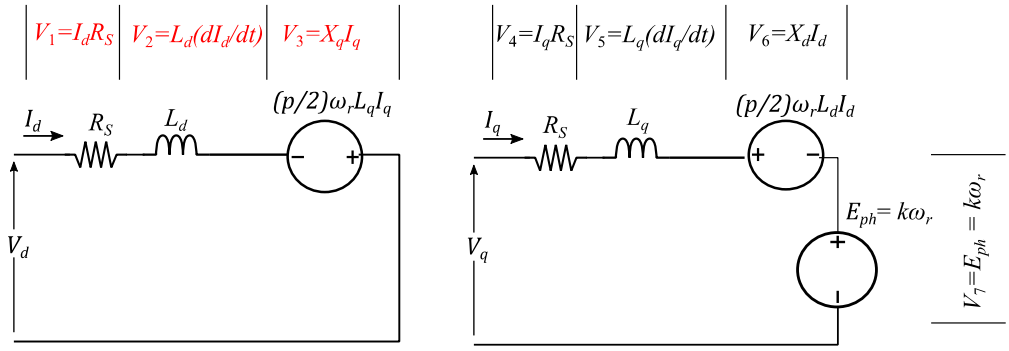

(a) *d*-axis equivalent electrical circuit (b) *q*-axis equivalent electrical circuit

Figure 2-23. Equivalent electrical circuits of an SPM motor in the *dq* reference frame.

The quantity of flux weakening or negative I_d required, for a given motor speed, is determined by the input phase voltage V_{ph}. As previously mentioned, the phase voltage amplitude is limited by the available voltage on the dc link. The value of V_{ph} is related to the combined *d*-axis aligned voltage drops V_d and the combined *q*-axis aligned voltage drops V_q. This voltage relationship is given as

$$V_{ph}^2 = V_d^2 + V_q^2 \tag{2.41}$$

Each of the individual voltage drops across the components of the EEC in Figure 2-23 are mapped in the *dq* reference plane in Figure 2-24(a). For steady-state current analysis, the dynamic voltage drops (V_2 and V_5) are neglected, and the remaining component voltage drops are illustrated in Figure 2-24(b). As shown in Figure 2-24(b), the combined *d*-axis aligned voltage drops are determined by

$$V_d = R_S I_d - \left(\frac{p}{2}\right)\omega_r L_q I_q \tag{2.42}$$

and the combined *q*-axis aligned voltage drops are determined by

$$V_q = R_S I_q + k\omega_r + \left(\frac{p}{2}\right)\omega_r L_d I_d \tag{2.43}$$

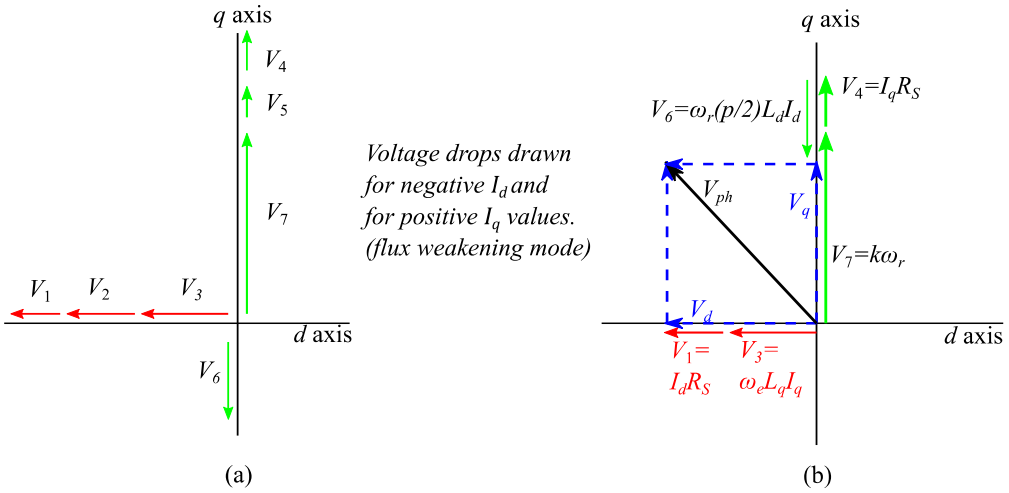

Figure 2-24. (a) Dynamic and static voltage drops, (b) Axis aligned steady-state voltage drops.

Complex control strategies for flux weakening in IPM motors, with boundary constraints based on the maximum allowable phase current and phase voltage, are examined in Chapter 5. The impact of flux weakening on the SPM motor of the SEVP simulator is explored in this chapter, based on a simple strategy that derived the required negative value of I_d based on the maximum value of $V_{ph(max)}$.

In the simplified flux-weakening strategy, the small voltage drops across the stator resistance are neglected in both the d-axis and q-axis equivalent circuits and the axis inductances L_d and L_q are both assumed to be constant and equal to a synchronous inductance value L_S. Torque generation in an SPM motor is dependent only on the q-axis current I_q. For the required value of T_r, the value of I_q is determined in (2.36) based on the machine constant k.

This results in a d-axis aligned voltage V_d that is dependent only on the torque producing current I_q and the shaft speed ω_r. For high-speed operation the V_d amplitude can only be controlled by limiting I_q, which in effect limits the torque output.

However, the q-axis aligned voltage V_q is dependent on the value of I_d and the shaft speed ω_r. For high-speed operation the V_q amplitude can be controlled by balancing any increase in the back-emf term $k\omega_r$ with increased negative amplitudes of I_d in the $\left(\frac{p}{2}\right)\omega_r L_d I_d$ term of (2.43). The resultant v_q value can be represented as

$$V_q = k\omega_r + \left(\frac{p}{2}\right)\omega_r L_S I_d = \sqrt{V_{ph(max)}^2 - V_d^2} \tag{2.44}$$

or

$$k\omega_r + \left(\frac{p}{2}\right)\omega_r L_S I_d = \sqrt{V_{ph(max)}^2 - \left[-\left(\frac{p}{2}\right)\omega_r L_S I_q\right]^2} \tag{2.45}$$

In a BEV simulator, the output motor torque T_r and shaft speed ω_r are determined from the traction effort calculations and the drive cycle specified speed. The required I_q is based on the estimated machine constant k and T_r to give

$$k\omega_r + \left(\frac{p}{2}\right)\omega_r L_S I_d = \sqrt{V_{ph(max)}^2 - \left[-\left(\frac{p}{2}\right)\omega_r L_S \left(\frac{T_r}{3k}\right)\right]^2} \tag{2.46}$$

For a specified $V_{ph(max)}$, T_r, ω_r operating point, the required value of I_d is found by re-arranging the terms in (2.46) to give

$$I_d = \frac{\sqrt{V_{ph(max)}^2 - \left[-\left(\frac{p}{2}\right)\omega_r L_S \left(\frac{T_r}{3k}\right)\right]^2} - k\omega_r}{\left(\frac{p}{2}\right)\omega_r L_S} \tag{2.47}$$

In the SPM motor this I_d current is only required above rated speed when the maximum phase voltage is reached. Under low torque outputs requirements, this voltage limit occurs at a significantly higher speed than the rated speed. In the IPM motor, as modelled in Chapter 5, this current is required to achieve MTPA operation and maximum torque output at all speeds, above, and below, the rated speed.

2.4.3.1.2 Impact of flux weakening on the combined efficiency map

The flux-weakening strategy in 2.4.3.1.1 increases the required phase currents for a specified torque output at all motor speeds above the rated speed. This results in increased ohmic losses in the motor. As illustrated in Figure 2-25, the impact of flux weakening on the combined motor and inverter efficiency map is slightly lower efficiencies, as the motor approaches its maximum speed value of 10000 rpm.

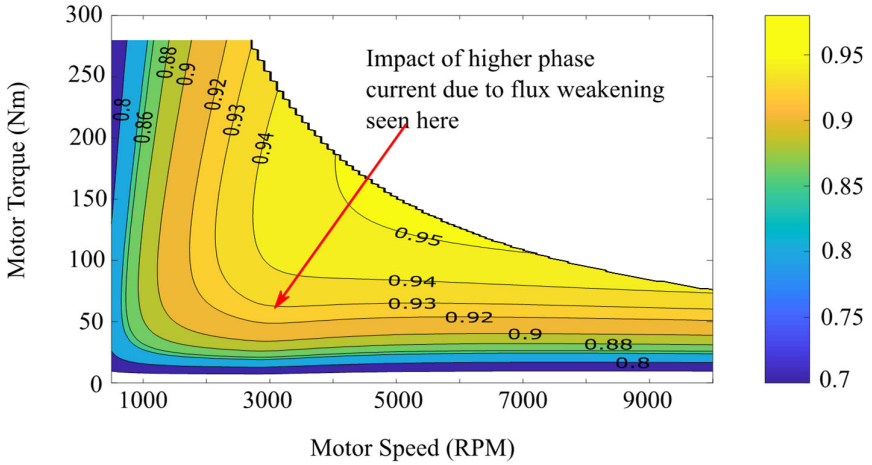

Figure 2-25. 2012 Leaf combined motor and inverter efficiency with flux weakening included.

2.4.3.2 Magnetic Saturation

High-torque outputs require high phase currents and the resultant high magnetic flux causes magnetic saturation in the stator laminations. This magnetic saturation reduces the flux linkage ψ_f and a corresponding reduction in k is observed. Any reduction in k results in increased I_q currents, with corresponding increases in winding losses and lower motor efficiencies. This magnetic saturation is typically observed at high-torque output below the rated speed, where I_q is equal to I_{ph}.

As noted previously in Figure 2.10, in the SEVP motor model without magnetic saturation, at below the rated speed the efficiency contours show almost constant efficiency at a specified speed, even under high-torque conditions. When this motor model is modified to include magnetic saturation at torques greater than 150 Nm, as shown in Figure 2-26, the efficiency reduces as the torque approaches its maximum value. The efficiency contours of an SPM motor model with magnetic saturation provide an improved correlation to the ANL measured contours for an IPM motor as shown in Figure 2-9.

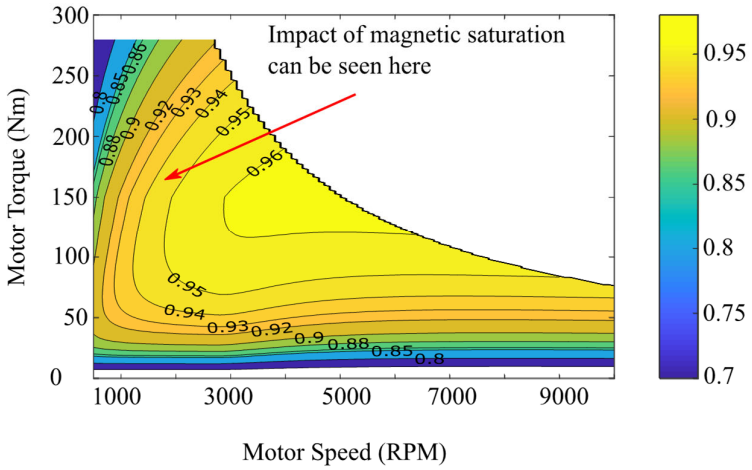

Figure 2-26. Efficiency map of an SPM motor model with magnetic saturation included.

The magnetic saturation shown in Figure 2-26 was implemented by assuming the same $tanh$ relationship between saturation and the value of k as that implied in [33]. This model assumes a maximum reduction in k of 25%. The onset of saturation is assumed to occur at a torque value T_{sat}. For any torque T_r above T_{sat}, the saturation impacted machine constant k_{sat} is determined using

$$k_{sat} = k\left(1 - tanh\left[\frac{T_r - T_{sat}}{(T_{r(rated)} - T_{sat})/atanh(dk)}\right]\right) \tag{2.48}$$

where k is the non-saturated machine constant and dk is the assumed maximum reduction of k.

2.4.4 Alternative Power-Based Model of the SEVP

Estimating the machine parameters using equations (2.8) to (2.31) is a pre-requisite, if the SEVP model is to simulate the electrical performance of the powertrain in a BEV. If, however, only the energy consumption in the motor and in the inverter is required for a vehicle simulation, then it is possible to reconfigure these equations to predict the combined power loss of the motor and inverter.

Starting with the motor loss in (2.28), when the T_{nl} is substituted using (2.27), the result is

$$P_{m(loss)} = \left(\frac{P_{cfw(rated)}}{\omega_{r(rated)}}\right)\omega_r + 3\left(\frac{T_r}{3k}\right)^2 R_S \tag{2.49}$$

Substituting for $P_{cfw(rated)}$, using (2.26), yields

$$P_{m(loss)} = \left(P_{m(rated-loss)} \times 25\%\right)\left(\frac{\omega_r}{\omega_{r(rated)}}\right) + 3\left(\frac{T_r}{3k}\right)^2 R_S \tag{2.50}$$

Then substituting R_S, using (2.19), results in

$$P_{m(loss)} = 25\%\left[\left(P_{m(rated-loss)}\right)\left(\frac{\omega_r}{\omega_{r(rated)}}\right)\right] + 75\%\left[3\left(\frac{T_r}{3k}\right)^2\left(\frac{P_{m(rated-loss)}}{3\left(I_{ph(max)}\right)^2}\right)\right]$$

(2.51)

Substituting for $I_{ph(max)}$, using (2.16), and re-arranging the terms in (2.51) gives

$$P_{m(loss)} = P_{m(rated-loss)}\left[25\%\left(\frac{\omega_r}{\omega_{r(rated)}}\right) + 75\%\left(\frac{T_r}{T_{r(rated)}}\right)^2\right] \tag{2.52}$$

As shown in (2.17), $P_{m(rated-loss)}$ is related to the published rated motor power $P_{r(rated)}$, which means that the motor loss in (2.52) can easily be determined at any motor operating ω_r and T_r, without the need to determine any of the motor EEC parameters using

$$P_{m(loss)} = P_{r(rated)}\frac{\left(1-\eta_{mot(rated)}\right)}{\eta_{mot(rated)}}\left[25\%\left(\frac{\omega_r}{\omega_{r(rated)}}\right) + 75\%\left(\frac{T_r}{T_{r(rated)}}\right)^2\right]$$

(2.53)

When a similar parameter substitution procedure is applied to the inverter loss equations, it is possible to define the inverter loss $P_{inv(loss)}$ in terms of the motor output torque T_r. Substituting the $P_{inv(rated-loss)}$ in (2.31) with the parameters in (2.29) gives

$$P_{inv(loss)} = \frac{P_{inv(rated)}\left(1-\eta_{inv(rated)}\right)}{\eta_{inv(rated)}}\left(\frac{T_r}{T_{r(rated)}}\right) \tag{2.54}$$

and substituting $P_{inv(rated)}$ in (2.54) with the parameters in (2.8) results in

$$P_{inv(loss)} = \frac{P_{r(rated)}\left(1-\eta_{inv(rated)}\right)}{\eta_{mot(rated)}\eta_{inv(rated)}}\left(\frac{T_r}{T_{r(rated)}}\right) \tag{2.55}$$

Therefore, the losses $P_{m(loss)}$, $P_{inv(loss)}$, at any operating point, can be calculated based only on the rated power and rated torque of the motor and the assumed motor and inverter efficiencies at the rated condition, provided estimates of the torque T_r and speed ω_r outputs of the traction motor can be made.

2.4.5 Comparison of Inverter Models.

As ANL did not publish inverter output voltage and current test data, it was not possible to independently compare the SEVP inverter model with the standard inverter models presented in Chapter 1. This deficiency is partially addressed by comparing the inverter models using ORNL test data for a 2004 Toyota Prius inverter [45].

The ORNL inverter test results are based on a motor power rating of $P_{r(rated)}$ = 40 kW and a motor torque rating of $T_{r(rated)}$ = 330 Nm. The inverter is tested at a dc input voltage of approximately 500 V and at 5 kHz switching frequency. The efficiency map for the 2004 Prius is presented in Figure 2-27. It shows similar high inverter efficiencies of 98% to 99% for most of the torque-speed operating range, as was also seen in the 2012 Leaf. The maximum input current from the dc supply was 124.5 A. The SEVP inverter model assumes an efficiency of 98% at rated conditions and the inverter loss at all other operating points is proportional to the motor torque outputs as determined by (2.55).

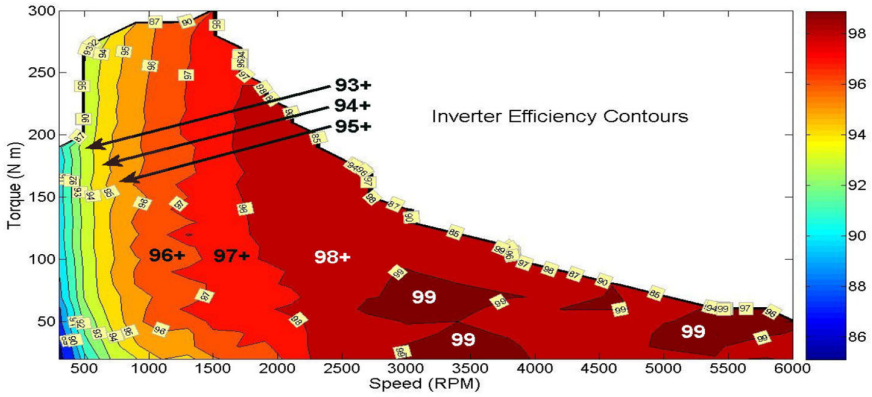

Figure 2-27. Efficiency map for 2004 Toyota Prius inverter [45]

A preliminary comparison of the Semikron inverter loss model [46], with the alternative loss model presented in [33], shows that both models produce the same on-state losses but the Semikron model predicts slightly lower switching losses. Given this result, only the Semikron model was compared to the SEVP inverter model. This model requires switch device specifications that were not published by ORNL. Based on the ORNL test voltages and current, a 1200 V Semikron IGBT was chosen as a possible switching device. The specifications for this IGBT are presented in Table 2-8.

Table 2-8. IGBT specification applied to Semikron inverter model for comparison.

Device	**(SEMiX151GAR12E4s)**				
Voltage rating V_{CES}	1200 V	Current rating I_{Cnom}	150 A		
V_{ref}	600 V	I_{ref}	150 A		
E_{on}	16 mJ	E_{off}	18.4 mJ	E_{rr}	8.9 mJ
V_{CE0}	0.75 V	V_{F0}	1.1V		
r_{CE}	8 mΩ	r_F	6.5 mΩ		

The SEVP inverter model assumes the power losses are dependent only on torque output. The Semikron inverter model bases the power losses on inverter output voltages and currents. The limited ORNL test data provides inverter output voltages and currents, at set torque outputs, over a range of motor speeds.

2.4.5.1 Comparison Results

The ORNL inverter power loss test data for approximate torque outputs of 30 Nm, 50 Nm, 149 Nm and 250 Nm are compared in Figure 2-28 to the estimated power losses of both inverter models. Both the SEVP and Semikron inverter model results are provided with an additional constant 75 W housekeeping load.

As shown in Figure 2-28(a), at a low torque output of 30 Nm, the SEVP inverter model, which assumed constant power loss with torque, agrees with the Semikron model up to rotor speeds of 3000 rpm. At higher speeds, the ORNL test data shows inverter output current increasing and these increased currents are reflected as increased inverter losses in the Semikron model. The impact of not increasing the SEVP inverter losses at higher speeds, is low as these losses represent less than 10% of the combined motor and inverter losses at higher speeds. The inverter losses at a torque output of 50 Nm are shown in Figure 2-28(b). These results reflect the results observed at the 30 Nm output level.

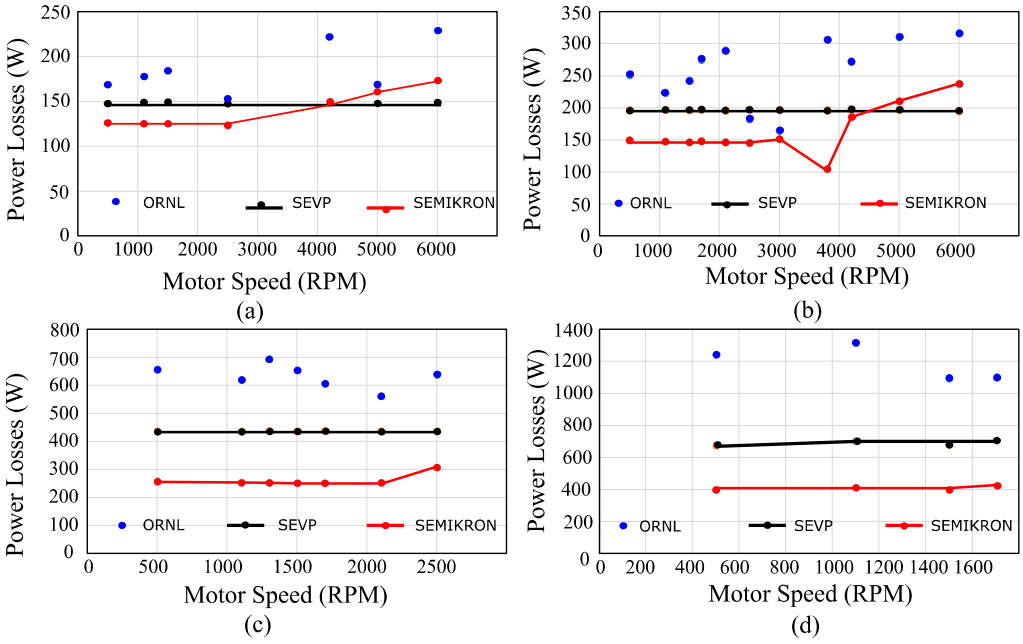

Figure 2-28. Comparison results (a) at 30 Nm, (b) at 50 Nm, (c) at 150 Nm and (d) at 250 Nm.

The comparison at a higher torque of approximately 150 Nm is presented in Figure 2-28(c). Both inverter models underestimate the losses at this torque level. The

Semikron inverter, which is based on sinusoidal modulation, estimates less than 50% of the measured inverter losses. The ORNL measurements indicate that the inverter losses actually represent between 15% to 30% of the combined motor and inverter losses in this speed range. The highest percentage is seen at the lower operating speeds.

The comparison results at a torque output of 250 Nm are illustrated in Figure 2-28(d). Similar to the 150 Nm results, both inverter models significantly underestimate the inverter losses. The ORNL measurements indicate that the inverter losses represent between 15% to 25% of the combined motor and inverter losses in this speed range.

The overall conclusion from this comparison is that the simplified inverter model of the SEVP represents a good first approximation of the inverter losses and increasing the complexity of the model to reflect the Semikron approach would not improve the loss approximation. Further study is required to identify the sources of the losses of the inverter at higher torque output and higher operating speeds.

.

2.5 Conclusions

In this chapter, a detailed description of the procedure used in 2014 to develop a simplified electric vehicle powertrain model is presented. The objective of the model was to accurately predict the driving range of a BEV using a minimum set of vehicle parameters. The vehicle parameters required were minimized by using the coast-down coefficients, published by the EPA, to determine the vehicle road-load and spin losses in the powertrain. This model, applied to the 2012 Nissan Leaf, was validated as an energy consumption model against the experimental test data published by the ANL. Excellent correlation is demonstrated between the model predictions and the experimental data for range estimation and energy consumption projections. The estimated powertrain losses during regenerative braking were significantly less than the experimental measurements and an improved model should address this error. The limitation that this 2014 research study only validated the powertrain model based on test data for one vehicle were noted and addressed with an expanded validation of the SEVP model presented in Chapter 3.

A deficiency in the model, in terms of energy consumption prediction for conditions that require HVAC power to control the passenger cabin temperature, was partly addressed, in this chapter, by incorporating a simple third-order polynomial to relate average HVAC power to outside ambient temperatures. The HVAC load was incorporated into the existing SEVP model as an increased auxiliary power load at the output of the battery. Validation of the powertrain model with a HVAC load, showed improved general correlation to the Argonne energy consumption measurements taken at three specific ambient temperatures.

The SEVP model was designed as a simple energy consumption model for range estimation. It has been shown to function alternatively as an electrical circuit powertrain model, subject to a few acknowledged limitations. Deficiencies, such as incorporation of flux weakening at high motor speeds and magnetic saturation at high motor torques, were addressed with relatively simple changes to the traction motor model. These changes were shown to slightly improve matching of the model's efficiency map to the measured efficiency map. Further improvements for electrical circuit modelling will require a new improved battery model. Consideration of a new battery model is presented in Chapter 4 and a new IPM traction motor model, to replace the SPM model, is presented in Chapter 5.

As an educational resource, the SEVP model has a wide variety of uses. For environmental studies, it provides a low computational load vehicle model, where the vehicle road load is determined by the coast-down test coefficients and the powertrain losses are mostly determined by two minimum parameter equations, as presented in Section 2.2.3. Incorporating the average HVAC load model improves the range estimation accuracy of the SEVP model to real-world conditions. For electrical and transportation engineering studies, parameter estimations of the traction motor and of its simplified electrical model provide a first approximation of the values of voltages and currents in a BEV powertrain for a wider variety of driving conditions. Additional models to address flux weakening and magnetic saturation extended the basic 2014 version of the SEVP model. The SEVP model, as presented in this chapter, is suitable for introductory studies into electric vehicle operation and the noted limitation that this model was validated against a single vehicle is addressed in Chapter 3.

In advanced educational engineering studies, a deeper understanding of powertrain performance limitations is required. Further improvements in the SEVP model to meet the needs of more advanced studies require comprehensive models for the battery and the traction IPM motor. These are considered in Chapters 4 and 5.

2.6 References

[1] J. G. Hayes and K. Davis, "Simplified electric vehicle powertrain model for range and energy consumption based on EPA coast-down parameters and test validation by Argonne National Lab data on the Nissan Leaf," *2014 IEEE Transportation Electrification Conf. and Expo (ITEC)*, Dearborn, MI, 2014, pp. 1-6, doi: 10.1109/ITEC.2014.6861831.

[2] J. G. Hayes, R. P. R. de Oliveira, S. Vaughan and M. G. Egan, "Simplified electric vehicle power train models and range estimation," *2011 IEEE Vehicle Power and Propulsion Conf. (VPPC)*, Chicago, IL, 2011, pp. 1-5, doi: 10.1109/ VPPC.2011.6043163.

[3] M. E. Biresselioglu, M. Demirbag Kaplan, and B. K. Yilmaz, “Electric mobility in Europe: A comprehensive review of motivators and barriers in decision making processes,” *Transp. Res. Part A Policy Pract.*, vol. 109, pp. 1–13, March 2018, doi.org/10.1016/j.tra.2018.01.017.

[4] Electrek, “5 things Tesla is bringing to market in 2020.” [Online]. Available: https://electrek.co/2019/12/28/5-things-tesla-bring-market-2020/. [Accessed: 01-Jul-2020].

[5] Volkwagen, “Volkswagen significantly raises electric car production forecast for 2025.” [Online]. Available: https://www.volkswagen-newsroom.com/en/ press-releases/volkswagen-significantly-raises-electric-car-production-forecast-for-2025-5696. [Accessed: 01-Jul-2020].

[6] “Ford and General Motors’ electric vehicle plans.” [Online]. Available: https://www.reuters.com/article/us-autos-emissions-suvs-lineup-factbox/ factbox-ford-and-general-motors-electric-vehicle-plans-idUSKBN21D1LT. [Accessed: 01-Jul-2020].

[7] P. Mock, J. German, A. Bandivadekar, and I. Riemersma, “Discrepancies between type- approval and real-world fuel-consumption and CO2 values Assessment for 2001-2011 European passenger cars,” The Int. Council on Clean Transportation, Working Paper 2012-02, 2012.

[8] S. Tsiakmakis, G. Fontaras, C. Cubito, J. Pavlovic, K. Anagnostopoulos, and B. Ciuffo, “From NEDC to WLTP: effect on the type-approval CO2 emissions of light-duty vehicles,” EUR 28724 EN, Publications Office of the European Union, JRC107662, Luxembourg, 2017, doi:10.2760/93419

[9] J. Neubauer and E. Wood, “The impact of range anxiety and home, workplace, and public charging infrastructure on simulated battery electric vehicle lifetime utility,” *J. Power Sources*, vol. 257, pp. 12–20, 1 July 2014, doi.org/10.1016/j.jpowsour.2014.01.075.

[10] M. Smuts, B. Scholtz and J. Wesson, "A critical review of factors influencing the remaining driving range of electric vehicles," *2017 1st Int. Conf. on Next Generation Computing Applications (NextComp)*, Mauritius, 2017, pp. 196-201, doi: 10.1109/NEXTCOMP.2017.8016198.

[11] Z. Yi and P. H. Bauer, "Sensitivity Analysis of Environmental Factors for Electric Vehicles Energy Consumption," *2015 IEEE Vehicle Power and Propulsion Conf. (VPPC)*, Montreal, QC, 2015, pp. 1-6, doi: 10.1109/VPPC.2015.7353012.

[12] L. Thibault, G. De Nunzio and A. Sciarretta, "A unified approach for electric vehicles range maximization via eco-routing, eco-driving, and energy consumption prediction," in *IEEE Transactions on Intelligent Vehicles*, vol. 3, no. 4, pp. 463-475, Dec. 2018, doi: 10.1109/TIV.2018.2873922.

[13] A. Le Rhun, F. Bonnans, G. De Nunzio, T. Leroy and P. Martinon, "A stochastic data-based traffic model applied to vehicles energy consumption estimation," in *IEEE Transactions on Intelligent Transportation Systems*, vol. 21, no. 7, pp. 3025-3034, July 2020, doi: 10.1109/TITS.2019.2923292.

[14] A. Shirmohammadli and D. Vallée, “Developing a location model for fast charging infrastructure in urban areas,” *Int. J. Transp. Dev. Integr.*, vol. 1, no. 2, pp. 159–170, 2017, doi: 10.2495/TDI-V1-N2-159-170.

[15] E. A. Grunditz and T. Thiringer, "Characterizing BEV powertrain energy consumption, efficiency, and range during official and drive cycles from Gothenburg, Sweden," in *IEEE Transactions on Vehicular Technology*, vol. 65, no. 6, pp. 3964-3980, June 2016, doi: 10.1109/TVT.2015.2492239.

[16] A. Damiano, C. Musio and I. Marongiu, "Experimental validation of a dynamic energy model of a battery electric vehicle," *2015 Int. Conf. on Renewable Energy Research and Applications (ICRERA)*, Palermo, 2015, pp. 803-808, doi: 10.1109/ICRERA.2015.7418523.

[17] Argonne National Laboratory , “Autonomie”, [Online]. Available: https://www.autonomie.net/. [Accessed: 10-Jul-2020].

[18] AVL List GmbH, “AVL Cruise ” [Online]. Available: https:// www.avl.com/ cruise. [Accessed: 10-Jul-2020].

[19] M. Faria, G. Duarte, and P. Baptista, “Assessing electric mobility feasibility based on naturalistic driving data,” *J. Clean. Prod.*, vol. 206, pp. 646–660, 1 January 2019. doi.org/10.1016/j.jclepro.2018.09.217

[20] C. Fiori, K. Ahn, and H. A. Rakha, “Power-based electric vehicle energy consumption model: Model development and validation,” *Appl. Energy*, vol. 168, pp. 257–268, 15 April 2016. doi.org/10.1016/j.apenergy.2016.01.097

[21] K. N. Genikomsakis and G. Mitrentsis, “A computationally efficient simulation model for estimating energy consumption of electric vehicles in the context of route planning applications,” *Transp. Res. Part D Transp. Environ.*, vol. 50, pp. 98–118, January 2017, doi.org/10.1016/j.trd.2016.10.014

[22] Gilsu Choi and T. M. Jahns, "Design of electric machines for electric vehicles based on driving schedules," *2013 Int. Electric Machines & Drives Conf.*, Chicago, IL, 2013, pp. 54-61, doi: 10.1109/IEMDC.2013.6556192.

[23] H. J. Yu, W. Gu, N. Zhang and D. Q. Lin, "Economic dispatch considering integration of wind power generation and mixed-mode electric vehicles," *2012 IEEE Power and Energy Society General Meeting*, San Diego, CA, 2012, pp. 1-7, doi: 10.1109/PESGM.2012.6344900.

[24] M. Andrews, M.K. Dogru, J.D. Hobby, Y. Jin, G.H. Tucci, “Modeling and optimization for electric vehicle charging infrastructure” In *IEEE innovative smart grid technologies conference*., Washington, D.C., 2013, pp.1-7.

[25] L. Rodgers. “Improving electric vehicle range predictions,” PhD proposal, MIT, 2012.

[26] United States Environmental Protection Agency, *Annual certification data for Vehicles, Engines and Equipment*, [Online]. Available: https://www.epa.gov/ compliance-and-fuel-economy-data [Accessed: 10-Jul-2020].

[27] Z. Yi and P. H. Bauer, "Optimal Speed Profiles for Sustainable Driving of Electric Vehicles," *2015 IEEE Vehicle Power and Propulsion Conf. (VPPC)*, Montreal, QC, 2015, pp. 1-6, doi: 10.1109/VPPC.2015.7352989.

[28] H. Lohse-Busch, M. Duoba, E. Rask and M. Meyer, “Advanced Powertrain Research Facility AVTA Nissan Leaf Testing and Analysis,” Argonne National Laboratory (ANL), October 2012.

[29] The Car Connection, “Image of 2012 Nissan Leaf.” [Online]. Available: https://www.thecarconnection.com/overview/nissan_leaf_2012. [Accessed: 01-Jul-2020].

[30] M. Ehsani, Y. Gao, A. Emadi, *Modern Electric, Hybrid Electric and Fuel Cell Vehicles: Fundamentals, Theory, and Design*, 2nd ed., Boca Raton, FL. USA CRC Press, 2009.

[31] M. Zhang, "HEV powertrain fundamentals," *2011 IEEE Vehicle Power and Propulsion Conf. (VPPC)*, Chicago, IL, 2011, pp. 1-144, doi: 10.1109/ VPPC.2011.6042976.

[32] J. Larminie and J. Lowry, *Electric Vehicle Technology Explained*, *1*st ed. Chichester, West Sussex, UK: Wiley, 2003, pp. 183-188

[33] J. G. Hayes and G. A. Goodarzi, *Electric Powertrain:Energy Systems, Power Electronics and Drives for Hybrid, Electric and Fuel Cell Vehicles, 1*st ed., Chichester, West Sussex, UK: Wiley, 2018

[34] Battery Electric Vehicle energy consumption and range test procedure, J1634, SAE International, 2012

[35] Nissan Motor Corporation website, [Online] Available: www.nissanusa.com . [Accessed: 10-Jul-2020].

[36] Argonne National Laboratory, Energy Systems Division, “Downloadable Dynamometer Database.” [Online]. Available: https://www.anl.gov/es/ downloadable-dynamometer-database. [Accessed: 10-Jul-2020].

[37] A. Grunwald, B. James, “System approach to consider efficiency, NVH, and durability in the optimization of an electric all-wheel drive gearbox,” *Vehicle Concept Modelling in Automotive Sector,* Brussels, 2011.

[38] Y. Sato, S. Ishikawa, T. Okubo, M. Abe, K. Tamai, “Development of high response motor and inverter system for the Nissan Leaf electric vehicle,” *SAE Technical Paper*, no. 2011-01-0350, 2011, doi: 10.4271/2011-01-0350.

[39] D. O. Neacsu, “SPACE VECTOR MODULATION – An Introduction : Tutorial at IECON2001.,” in *The 27th Annual Conference of the IEEE Industrial Electronics Society*, 2001, vol. 00, no. 2, pp. 1583–1592.

[40] J. P. John, S. S. Kumar and B. Jaya, "Space Vector Modulation based field oriented control scheme for brushless DC motors," *2011 Int. Conf. on Emerging Trends in Electrical and Computer Technology*, Nagercoil, 2011, pp. 346-351, doi: 10.1109/ICETECT.2011.5760141.

[41] T. A. Burress, "Benchmarking of Competitive Technologies 2012 Nissan LEAF," Oak Ridge National Laboratory (ORNL), Presentation at US DOE Hydrogen and Fuel Cell Peer Evaluation Meeting, May 2012.

[42] R. Farrington and J. Rugh, "Impact of Vehicle Air-Conditioning on Fuel Economy, Tailpipe Emissions, and Electric Vehicle Range," National Renewable Energy Laboratory, NREL/CP-540-28960, September 2000.

[43] K. R. Kambly and T. H. Bradley, "Estimating the HVAC energy consumption of plug-in electric vehicles," *J. Power Sources*, vol. 259, pp. 117–124, 1 August 2014, doi.org/10.1016/j.jpowsour.2014.02.033.

[44] N. Meyer, I. Whittal, M. Christenson, and A. Loiselle-Lapointe, "The Impact of Driving Cycle and Climate on Electrical Consumption & Range of Fully Electric Passenger," *EVS26 International Battery, Hybrid and Fuel Cell Electric Vehicle Symposium*, Los Angeles, California, 2012, pp. 1–11.

[45] R. H. Staunton, C.W. Ayers, L. D. Marlino, J. N. Chiasson and T. A. Burress, "Evaluation of 2004 Toyota Prius hybrid electric drive system interim report", Oak Ridge National Lab. (ORNL), ORNL/TM-2006/423, May 2006.

[46] A. Wintrich, U. Nicolai, W. Tursky, and T. Reimann, *Application Manual Power Semiconductors*, 2nd ed., Nuremburg, Germany: Semikron International GmbH, 2015.

3 SIMULATOR COMPARISON

This chapter establishes the precision of a simplified electric vehicle powertrain (SEVP) simulator by comparing its energy consumption results for battery electric vehicles (BEVs) with two widely used vehicle simulators. The SEVP powertrain model is based on mathematical component models that determine second-by-second energy consumption for a BEV. ADvanced VehIcle SimulatOR (ADVISOR), and Future Automotive Systems Technology Simulator (FASTSim) are two widely used simulators that provided similar second-by-second energy consumption.

As the software environments of the three simulators are different, the comparison required replicating all three simulators in a single MATLAB script, which in this study is termed a Multi-Simulator (M-Sim). This comparison method offers plug-and-play functionality where the individual powertrain component models and their impact on overall energy consumption of the vehicle can be examined. The precision of each simulator was then determined by comparing the M-Sim energy consumptions to dynamometer test data from Argonne National Laboratory (ANL), a research facility in the USA [1]. This work represents an extended version of a conference paper, presented at the 2016 IEEE ESAR-ITEC conference, in Toulouse, France [2]. In this chapter, the comparison of the three simulators is expanded from the two BEVs in the 2016 study, to a total of ten BEVs.

The chapter is organized as follows: Section 3.1 provides a brief literature review of vehicle simulators; Section 3.2 compares the individual powertrain component models for the three selected simulators; Section 3.3 explains the development and replicated-software validation of a combined simulator; Section 3.4 outlines the comparison results and identifies some of the error sources in each simulator; The conclusions are presented in Section 3.5. M-Sim Matlab script, an example of a vehicle input data file, some model calculation procedures, and additional test results are provided in Appendix B.

3.1 Introduction

In an attempt to reduce CO_2 emissions and improve air quality in urban areas, the transportation sector is transitioning from fossil fuels to electrified powertrains in the form of hybrid (HEV), plug-in hybrid (PHEV), fuel cell (FCEV) and battery (BEV) electric vehicles. This transition process has driven the requirement for energy consumption vehicle models to assess the environmental benefits and the impacts on the electrical networks. In BEVs, the energy source limitations, in terms of limited driving range and required charging infrastructure, necessitate high accuracy in vehicle energy consumption models. Applications for BEV simulators include mobility studies to establish eco-routing of traffic flow based on minimising a vehicle's energy consumption to complete a trip. Mobility studies can also provide details of the availability of the vehicle to support the electricity network using vehicle-to-grid (V2G) interfaces [3],[4]. A balance is needed between the precision required for good range estimation, and the low computational load to allow the vehicle models to be embedded into logistics applications.

3.1.1 Specific Energy Consumption Models

Many studies have used a simple steady-state vehicle model where the specific energy consumption, usually in terms of Wh/km, is based on an averaged vehicle speed in a transport environment (city driving, rural roads or highways) . In recent published literature, the specific energy consumption is often determined by a data analysis modelling approach based on multi-variate linear regression models of real-world driving data [5],[6]. Many of these models are validated based on their ability to predict average energy consumption over a given trip or route, but the averaging of the energy data can mask the inaccuracies of the model in different driving environments [7].

3.1.2 Dynamic Vehicle Simulators

Energy consumption estimation is not the primary focus of dynamic vehicle simulators. Instead, they focus on gaining an understanding of the short-term transient response of each component in the powertrain, required to determine the overall performance of the vehicle. The principle applicational area for these simulators is in the design of new or concept vehicles. Dynamic simulators are widely used for FCEV, HEV and PHEV designs where it is important to develop energy management strategies

for the two power sources in these vehicles [8],[9],[10],[11]. The capture of a component's dynamic response requires short simulation time-steps, thereby increasing the computing time and the computational load in these simulators. The accuracy depends on the ability of the vehicle model developer to obtain extensive parametric information on all the components in the powertrain.

3.1.3 Quasi-static Mathematical Models

Simple static mathematical vehicle models estimate energy consumption as a function of vehicle speed. They achieve a low computational load by assuming powertrain losses based on either (i) constant efficiencies for each powertrain component, or (ii) total-powertrain losses often calculated as a third-order polynomial function of speed [12],[13].

Improved accuracy in the determination of energy consumption requires quasi-static vehicle models. These incorporate a simple dynamic element, such as acceleration or deceleration, and can provide instantaneous second-by-second energy consumption [14]. The magnitude of the computational load is largely determined by the choice of method employed for the calculation of the power losses in the powertrain components. These quasi-static models often require a high number of vehicle parameters and, with limited published data from manufacturers, it is difficult to develop a quasi-static model for a vehicle.

3.1.3.1 ADVISOR

ADVISOR, developed by the National Renewable Energy Laboratory (NREL) in the period 1994 to 2002, is a good example of a quasi-static simulator [15]. ADVISOR is written in the MATLAB environment and is supplied with a graphical user interface (GUI). This free-to-download vehicle simulator software provides a limited range of components suitable for HEVs and BEVs. It has not been supported by NREL since 2002. The powertrain components are modelled with efficiency maps. In the software, the efficiency maps are implemented as look-up tables (LUTs) indexed by the required torque and speed of the vehicle in any one second period. The efficiency maps are developed by testing each component over the full torque-speed operating range. Development of new vehicle models in ADVISOR is problematic due to the lack of published data needed for the efficiency maps of powertrain components.

3.1.3.2 FASTSim

Recently NREL developed another quasi-static simulator called FASTSim [16]. The modelling approach is very similar to the earlier MATLAB based ADVISOR model but FASTSim is released as a macro-enabled Excel file. Powertrain losses are determined based on the magnitude of the power flow in the components rather than the torque or speed requirements. The LUTs of ADVISOR have been replaced by a fourth-order polynomial power loss model. This powertrain loss model is configurable based on the rated power for a new vehicle. This simulator includes four default BEV models based on the 2012 Nissan Leaf, 2009 Tesla Roadster, 2011 SMART Fortwo Electric and 2009 MINI E.

3.1.3.3 SEVP

The SEVP simulator is a quasi-static model, first proposed in 2011 to estimate the range of BEVs [17]. In common with ADVISOR and FASTSim, the traction effort required by the vehicle was calculated based on vehicle parameters such as the kerb weight, frontal area, estimated rolling resistance of the tyres and published aerodynamic drag coefficients. The losses in the powertrain components were simple mathematical models, based on the required torque and speed of the vehicle. Limited validation of the first version of the SEVP was carried out. This involved a driving range comparison between the SEVP and the manufacturer's published driving range for two vehicles, a Nissan Leaf and a Tesla Roadster.

This research study began in 2014 to improve the SEVP simulator. An improved version calculated the traction effort using coast-down coefficients, published by the environmental protection agency (EPA) in the USA [18]. In addition, the efficiency calculations in the powertrain components were adjusted and the regenerative power was limited to a maximum power level of 20 kW [19]. Improved validation involved using ANL dynamometer test data for a 2012 model of the Leaf over three legislative drive cycles. The maximum error recorded was a 4.5% overestimation of the consumed battery energy in the UDDS drive cycle. The improved accuracy of the SEVP simulator was attributed to the use of the EPA coast-down coefficients. The educational benefits of this simulator were also highlighted in a further publication [20].

3.1.4 Calculation Direction in Simulators

The simulation direction, or calculation direction, of the powertrain losses impacts the design and complexity of a vehicle model. A forward-facing model is defined when the powertrain losses or responses are calculated from the power source, the battery for a BEV, to the wheels. This calculation approach is typically employed in dynamic simulators. Forward-facing models are found in sophisticated commercial vehicle simulators, for instance, Cruise and Autonomie [21],[22]. A torque or speed command is applied to a driver model, which mimics the driving style or driver's response and converts the input command to a battery power output level. The transient responses of all the powertrain components are determined and ultimately produce a vehicle performance response, based on the changing traction power available at the wheels. Component performance limits are easily identified in concept vehicle designs with this type of simulator. The time interval, or time-steps, for simulation loop calculations can be as low as 50 μs for high accuracy in determining a dynamic response but at the expense of a high computational overhead.

The alternative method of simulation is a backwards-facing model, where the traction power at the wheels is determined first and used as an input command to ultimately determine the power output from the vehicle's battery, after the losses in each powertrain component have been estimated. Such an approach is typically used in modelling for mobility studies but only provides steady-state or quasi-static responses. A typical interval for simulation calculations is 1s time steps, ignoring powertrain component response times and parameter limits, such as maximum torque in the motor. The resulting fast computational time and reduced model complexity allows the overall vehicle model to be incorporated into other applications, such as traffic flow simulators. This is the calculation procedure as applied in the SEVP model.

If inclusion of the powertrain component operating limits is required in vehicle simulation, a forward-facing calculation path needs to be placed in parallel with a backward-facing calculation path, in order to adjust the traction effort input to match the component limits of the powertrain. This bidirectional calculation procedure is utilised in both the ADVISOR and FASTSim simulators. The resultant computational load is higher than that for a unidirectional backward-facing procedure.

3.2 Simulator Powertrain Models

The backward-facing simulation structure of the three simulator powertrain models is illustrated in Figure 3-1. The forward-facing paths implemented in ADVISOR and FASTSim for component limits are not shown, for clarity purposes. The ADVISOR simulator includes the most powertrain component models, while SEVP has the simplest powertrain structure. The same design of transmission and auxiliary load models is applied in all three simulators. There are considerable differences in the design approaches taken to model the other components and these differences are detailed in the following subsections.

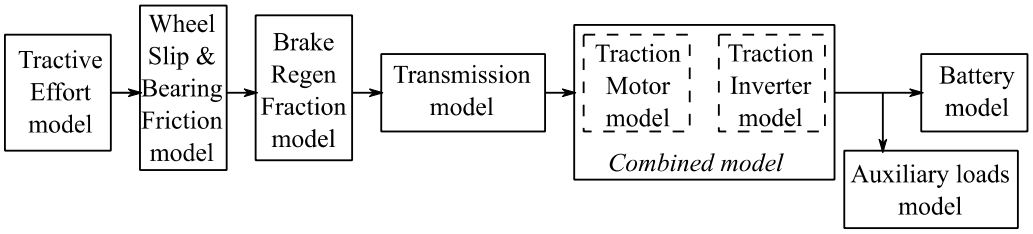

(a) ADVISOR

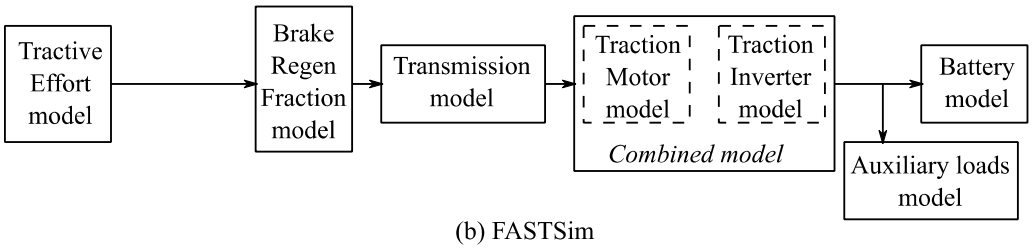

(b) FASTSim

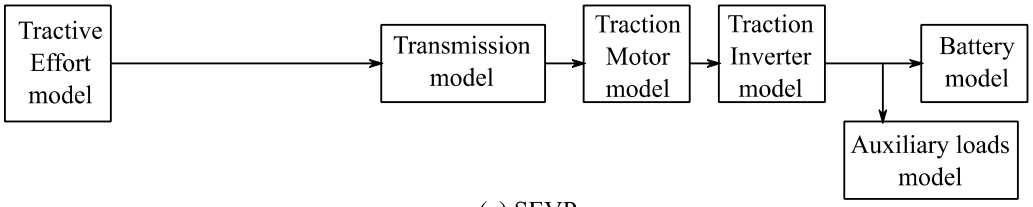

(c) SEVP

Figure 3-1. Powertrain component models for the three simulators in this comparison.

3.2.1 Tractive Effort Models

All three simulators start the energy consumption calculations by determining the power or force required at the vehicle's wheels, i.e. the tractive effort required. In ADVISOR and FASTSim, the tractive effort is calculated based on standard kinematic equations. These equations sum the vehicle resistance forces, including the rolling resistance force F_R; the aerodynamic drag force F_D; the road grade force F_c; the required linear acceleration force F_a; and the rotational acceleration force F_{inert}. This results in a tractive force F_{te} determined as

$$F_{te} = F_R + F_D + F_c + F_a + F_{inert} \tag{3.1}$$

The vehicle parameters required to calculate these individual forces are given by

$$F_{te} = MgC_{rr} + 0.5\rho C_d A_f (v + v_{air})^2 + Mg\ sin\,\theta_r + Ma + J_{axle}\left(\frac{\alpha_{axle}}{r_{wh}}\right) \tag{3.2}$$

with parameters: M the vehicle mass in kg, g the acceleration due to gravity in m/s^2, C_{rr} tyre rolling resistance coefficient, θ_r road inclination angle in degrees, ρ air density in kg/m^3, C_d drag coefficient , A_f frontal area in m^2, v vehicle speed in m/s, v_{air} headwind speed in m/s, a the vehicle's linear acceleration in m/s^2, J_{axle} the combined inertia of all the rotating components referenced to the drive axle in kg m^2, α_{axle} the angular acceleration of the drive axle in radians/s^2, and r_{wh} the radius of the vehicle's wheels in m.

In SEVP, an alternative F_{te} calculation method is used, based on the Society of Automotive Engineers (SAE) coast-down technique [23]. The vehicle road-load force F_v is derived from the test, where the vehicle is accelerated up to a high speed in the range of 80 to113 km/h on a dry, straight, level road and is then allowed to coast-down while in neutral gear. For this test, the regenerative braking must be disabled. The vehicle speed during coastdown is measured at defined intervals and regression techniques are used to determine second-order polynomial coefficients A_{cd}, B_{cd}, and C_{cd} that can replace the F_R and F_D components in (3.1). The resultant simplified tractive force equation is provided as

$$F_{te} = (A_{cd} + B_{cd}v + C_{cd}v^2) + Mg\,sin\,\theta_r + Ma + J_{axle}\left(\frac{\alpha_{axle}}{r_{wh}}\right) \quad (3.3)$$

An advantage of this method is that the coefficients A_{cd}, B_{cd}, and C_{cd} are published, both by the EPA and by the ANL, for the vehicles tested in this study [18],[24]. Use of the coast-down parameters circumvents the requirement for the difficult-to-estimate vehicle parameters C_{rr}, A_f and C_d in the vehicle model.

As the simulators are validated using dynamometer test data, the road inclination angle θ_r is zero and the headwind speed v_{air} is taken as zero in the simulator comparison. FASTSim converts the tractive force F_{te} to a tractive power P_{te} value by multiplying the force with the vehicle's speed v . This force-to-power conversion impacts the design of some of the other FASTSim powertrain components, such as the traction inverter and motor models.

Both the ADVISOR and SEVP simulators, multiply the tractive force by the wheel radius r_{wh} to calculate a wheel torque. Wheel torque T_{axle} and wheel rotational speed ω_{axle}, rather than tractive effort power, are used to determine the power losses in these simulators' traction inverter and traction motor models.

3.2.2 Wheel Model

ADVISOR is the only simulator that includes a wheel model in its powertrain. This model estimates wheel slip on a given surface, power loss due to bearing friction losses and non-applied brake friction losses in the wheel. Wheel slip results in the wheel's tangential velocity being slightly higher than the requested vehicle road speed specified by the drive cycle. The wheel slip model can be implemented for both the front and rear tyres by specifying a wheel slip coefficient s_f, which is determined as

$$s_f = \frac{F_{te} f_{axle\_f}}{Mg f_{axle\_mg}} \quad (3.4)$$

where f_{axle_f} is the fraction of the tractive force applied to a given axle and f_{axle_mg} is the fraction of the vehicle's mass on this same axle. This slip coefficient is only calculated for the axle(s) of the driven wheels. For all of the two-wheel-drive

vehicles in this study, f_{axle_f} is 1 and a default ADVISOR value of 0.59 is used for f_{axle_mg}.

As shown in Figure 3-2, the slip-coefficient s_f is related to the wheel slip s. The s_f determined by (3.4) is converted to a wheel slip s using a one-dimensional interpolation.

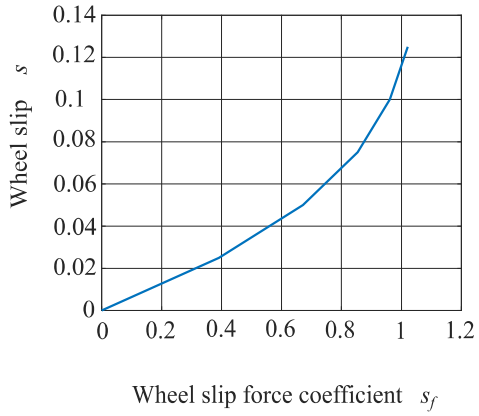

Figure 3-2. ADVISOR wheel model slip coefficient s_f to slip s relationship [25].

Then the required angular speed of the wheel ω_{axle} to achieve a linear vehicle speed v, with a wheel slip factor s, is calculated using

$$\omega_{axle} = (s+1)\frac{v}{r_{wh}} \tag{3.5}$$

Figure 3-3 shows the relationship between wheel torque losses and the mass of the vehicle. The torque losses are associated with the friction in the wheel bearings and the brake friction when the brakes are not applied. These losses in ADVISOR are estimated using a fixed empirical relationship (0.004 Nm/kg +1.5 Nm).

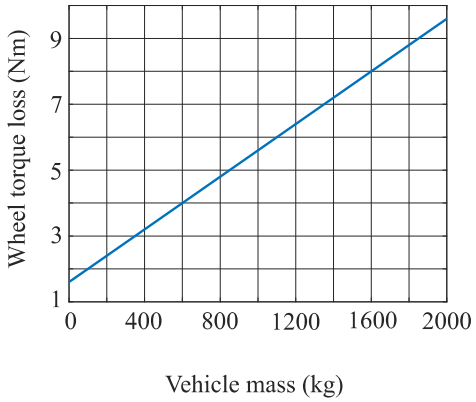

Figure 3-3. ADVISOR wheel model bearing friction torque loss functions [25].

The impact of this wheel model on the energy consumption of a BEV is analysed in the M-Sim comparison tests and presented in Section 3.4.6.4.

3.2.3 Brake Models

Brake models are only active when the power flow direction is from the wheels to the battery, such as when the vehicle is braking, decelerating or going downhill. Brake models are power-control models that determine the torque-split or power-split fraction between friction braking and regenerative braking. Both ADVISOR and FASTSim simulators incorporate brake models while SEVP assumes 100% regenerative braking $Reg_{ach} = 1$, effectively eliminating the requirement for a brake model. The ADVISOR and FASTSim brake models are relatively simple braking split strategies, as they are based only on one control input, vehicle speed v. The ADVISOR and FASTSim braking model relationships are shown in Figure 3-4.

The ADVISOR brake model uses the vehicle's speed and a piecewise-linear relationship to specify the percentage of braking energy that can be recovered with regenerative braking Reg_{ach}. The maximum regenerative braking fraction Reg_{max} and the speed values where the profile changes, are both user-configurable in ADVISOR. The default model values were used to generate two of the waveforms in Figure 3-4, and show that the maximum regenerative braking fraction is 0.8 for all vehicle speeds higher than 96 km/h or 60 mph. Preliminary testing of the simulator showed that the default ADVISOR brake model values did not reflect actual recovered braking energy at vehicle speeds above 80 km/h. For this simulator comparison, the

braking profile was modified to allow for 100% regenerative braking for all speeds over 25 kmph and these modified profiles are also illustrated in Figure 3-4.

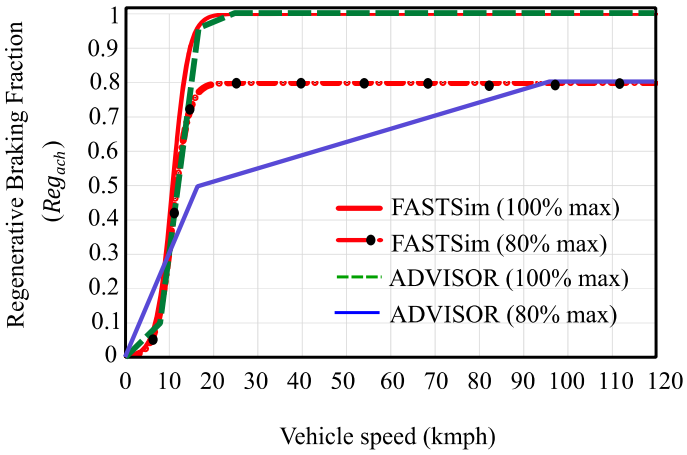

Figure 3-4. Regenerative braking fraction models in ADVISOR and FASTSim simulators.

In FASTSim, the regenerative braking fraction Reg_{ach} is determined by

$$Reg_{ach} = \frac{Reg_{max}}{1 + A_{brk} exp\left(-B_{brk}\left[v_{mph} + 1\right]\right)} \tag{3.6}$$

where A_{brk} and B_{brk} are two profile shape coefficients and v_{mph} is the linear speed of the vehicle specified in miles per hour (mph). Similar to the ADVISOR simulator, the maximum regenerative braking fraction Reg_{max} is user configurable. The FASTSim braking fraction profiles shown in Figure 3-4 are the default 0.8 maximum regenerative fraction profile and a modified profile for simulator comparison testing where the maximum regenerative braking fraction is changed to 1. The default values of the profile shape coefficients A_{brk} and B_{brk} are used in both FASTSim profiles shown in Figure 3-4. Results of the impact of this component model on a vehicle's energy consumption are presented in Section 3.4.3.2.

3.2.4 Transmission Model

The transmission is the system of components that connect the ICE or electric motor shaft to the wheels. Transmission models can include losses in the clutches,

multi-gear ratio gearbox, prop shaft and the differential to equalise the torque on the driven wheels. The efficiency of each component is typically represented as a torque loss or power loss [26]. These non-linear losses are dependent on oil lubrication properties, speed and torque load, making them very complex to model in vehicle simulators [27]. Fortunately, a simpler transmission system design is required for a BEV as the torque-speed characteristics of the electric motor closely match the load requirements at the wheels. Tests on transmissions for BEVs record efficiencies in the range of 93% to 97% [28] and a simple BEV transmission model can be represented as a fixed efficiency model [29].

3.2.4.1 ADVISOR Transmission Model

ADVISOR does not adopt a fixed efficiency transmission model. Instead it includes a final drive model and a single-speed gearbox model. The final drive model with a gear ratio of 1, is modelled as having zero torque loss. The gearbox model, with a default gear ratio calculated based on a requirement to reach 144.8 km/h (90 mph) at the maximum motor speed, assumes a wheel slip of 10% at this vehicle speed. The gearbox losses are calculated using an efficiency look-up-table (LUT), which is indexed by the required wheel torque and speed and is based on a research study of automatic gearbox efficiencies [30]. Over a vehicle speed range of 10 kmph to 100 kmph and the full torque range of a typical BEV motor, the ADVISOR efficiency map ranges from efficiency values of 70% at maximum speed and minimum torque condition, to 99% at minimum speed and maximum torque condition. These values are based on testing completed more than 20 years ago and do not reflect current transmission efficiency studies. In this comparative study, a new ADVISOR transmission model was constructed with a simple fixed efficiency model of 97% for the BEV tests.

3.2.4.2 FASTSim and SEVP Transmission Models

As FASTSim uses power rather than torque and speed, the gear ratio is not required in this simulator. A constant efficiency transmission model is used with default values of 85% for ICE vehicles, 95% for HEVs and 97% for a BEV powertrain. The SEVP simulator was designed specifically for BEVs and also employs a constant efficiency transmission model of 97%.

3.2.5 Traction Motor and Inverter Models

Three different modelling approaches are seen in the three simulators for the electric motor and the power electronics inverter in the BEV powertrain. Figure 3-5 illustrates these modelling approaches. The motor and inverter are modelled as a combined component in both the ADVISOR and FASTSim simulators and are modelled as two separate component models in the SEVP simulator.

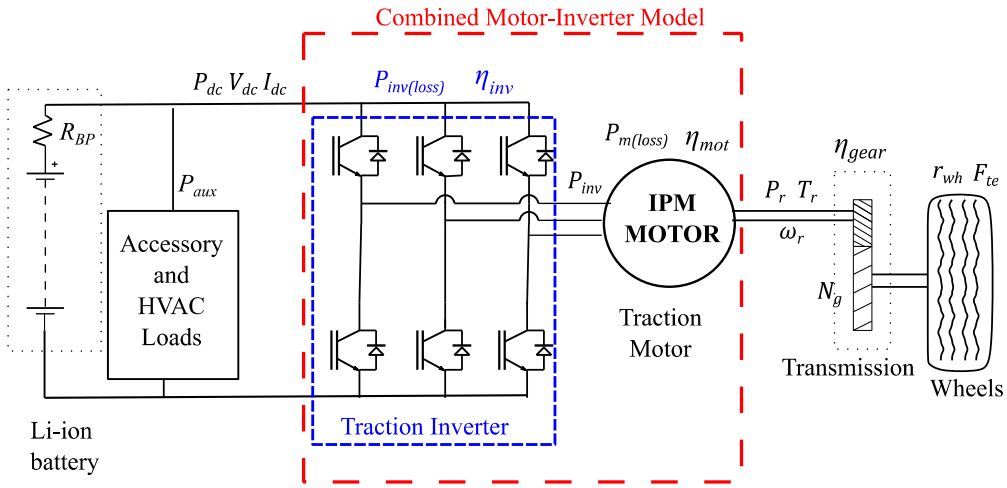

Figure 3-5. Combined motor-inverter model approach used in ADVISOR and FASTSim

3.2.5.1 ADVISOR Motor-Inverter Model

In ADVISOR, the motor and inverter are modelled as a combined component using efficiency maps. These efficiency maps are derived from efficiency testing of the combined motor-inverter system at defined torque and speed outputs. Figure 3-6 illustrates two examples of combined traction motor and inverter efficiency maps. In Figure 3-6(a) the combined motor and inverter efficiency map for a 2012 model Leaf is reproduced based on benchmark testing measurements carried out by Oakridge National Laboratory (ORNL) [31]. In Figure 3-6(b), a scaled version of an ADVISOR Honda HEV efficiency map is presented. The scaling was carried out to allow a comparison between the lower power (49 kW) Honda motor with the higher power (80 kW) Leaf motor. The efficiency at all other torque-speed operating points is derived using linear interpolation of the efficiency map. While the Leaf efficiency map only

includes efficiencies for propulsion i.e. positive torque output motoring operation, the typical vehicle simulator efficiency map also includes negative torque output braking operation.

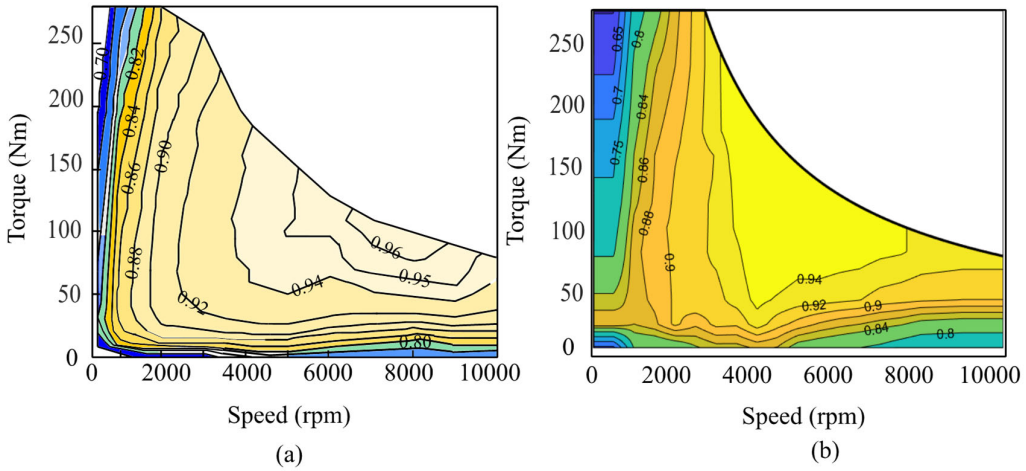

Figure 3-6. Combined motor and inverter efficiency maps for (a) 2012 Leaf based on ORNL data [31] and (b) ADVISOR Honda HEV efficiency map modified to match power output of Leaf.

Published BEV data does not generally include an efficiency map for the motor-inverter, making it difficult to model a BEV in ADVISOR. The default BEV motor-inverter efficiency map has efficiencies varying from 78% to 92%, and this model resulted in excessive powertrain losses. The closest match in ADVISOR to the ORNL efficiency map for the 2012 Leaf was a 49 kW Honda HEV motor-inverter efficiency map with a peak efficiency of 94%. This Honda map was scaled to match the power and speed of the Leaf. As demonstrated by Figure 3-6(b), the resultant modified efficiency map provides a much-improved approximation to the ORNL measurements.

3.2.5.2 FASTSim Motor-Inverter Model

The FASTSim combined motor-inverter model is based on two fourth-order polynomials that define the input to output power relationships; one for motoring operation with power flow from P_{dc} to P_r in Figure 3-5 and one for regenerative braking operation when power flows from P_r to P_{dc}. Sample model polynomials as well as a shape profile are shown in Figure 3-7.

Both polynomials require the user to specify the maximum motor power output $P_{r(rated)}$ when motoring and to specify the peak efficiency η_{peak} of the combined

motor-inverter model. The default values of peak motor-inverter efficiency in FASTSim are given as 89% for the 2012 Leaf and 93% for the other BEVs in the simulator. The polynomial profile shape is based on four discrete operating points. These shape profile points are defined as 0%, 9%, 65% and 100% of the user specified $P_{r(rated)}$ value.

FASTSim assumes a minimum efficiency of 30% when P_r is close to 0% of the $P_{r(rated)}$ and a peak efficiency η_{peak} when P_r is 65% of $P_{r(rated)}$. The efficiency values at P_r = 9% and 100% of $P_{r(rated)}$ are both determined as (η_{peak} -1%) * 0.98. Using these four defined efficiency-power operating points, it is possible to apply linear regression and curve-fitting techniques to create the two required polynomials.

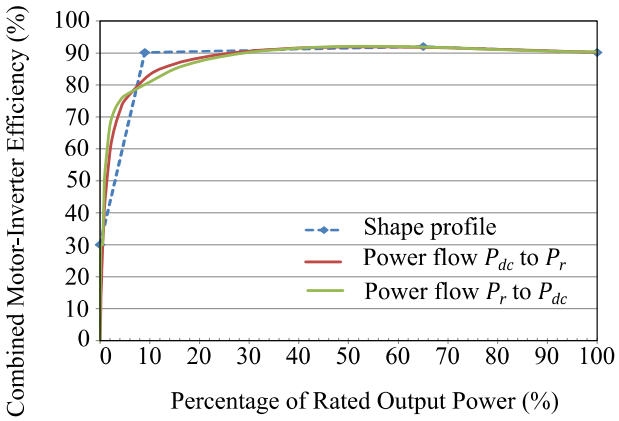

Figure 3-7. Motor-Inverter efficiency polynomials in FASTSim simulator.

The resultant FASTSim efficiency map for the motor-inverter model is shown in Figure 3-8. This map was generated with a user specified peak efficiency of 89%, as this was the default efficiency value for this vehicle in FASTSim. The FASTSim model predicts significantly higher losses than those measured by ORNL for this vehicle. The reduction in efficiency in the low torque, low speed driving conditions found in urban environments is more than 10% in the FASTSim model. The impact of this FASTSim modelling approach is discussed further in Section 3.4.5.

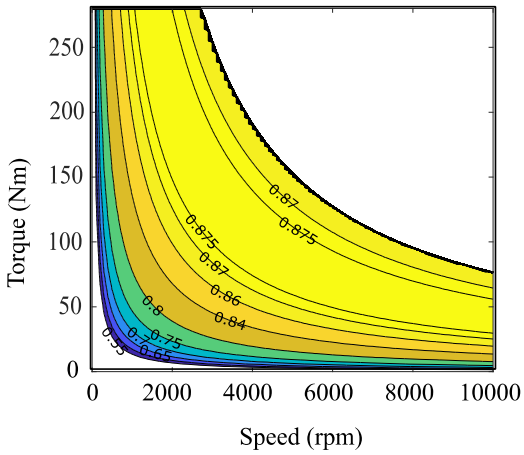

Figure 3-8. Combined motor-inverter efficiency in FASTSim for 2012 Leaf with peak efficiency specified as 89%.

3.2.5.3 SEVP Motor Model and Inverter Model

The motor and the inverter are modelled as separate components in the SEVP simulator. As explained in Chapter 2, both of these component models are based on the published values for maximum motor output power $P_{r(rated)}$, maximum motor torque output $T_{r(\text{rated})}$, as well as three operating assumptions when the motor output is at both the rated speed ω_{rated} and rated power $P_{r(\text{rated})}$condition: (i) the peak motor efficiency $\eta_{mot(rated)}$ is 96%; (ii) the peak inverter efficiency $\eta_{inv(rated)}$ is 98%; (iii) the motor winding losses are 75% of the total motor power losses $P_{m(rated-loss)}$ and the combined core, friction, windage power loss P_{cfw} comprises the remaining 25% power loss.

The resultant motor power loss equation for any motor output torque (T_r) and speed (ω_r), is evaluated as

$$P_{m(loss)} = P_{r(rated)} \frac{\left(1-\eta_{mot(rated)}\right)}{\eta_{mot(rated)}} \left[25\% \left(\frac{\omega_r}{\omega_{r(rated)}}\right) + 75\% \left(\frac{T_r}{T_{r(rated)}}\right)^2\right] \tag{3.7}$$

The corresponding inverter power loss equation for any motor output torque (T_r) is provided by

$$P_{inv(loss)} = \frac{P_{r(rated)}\left(1-\eta_{inv(rated)}\right)}{\eta_{mot(rated)}\eta_{inv(rated)}}\left(\frac{T_r}{T_{r(rated)}}\right) \tag{3.8}$$

The derivation of equations (3.7), (3.8) is available in Chapter 2. The combined efficiency map, for the SEVP motor and inverter models, is shown in Figure 3-9. The SEVP simulator efficiency map shows a reasonable approximation to the ORNL measurements. The differences in the map are most pronounced in the high-torque/low-speed region, associated with vehicle acceleration, and in the low-torque/high-speed region, associated with very high-speed highway driving. These efficiency differences were shown in Chapter 2 to result from the exclusion of magnetic saturation in the motor model under high-torque conditions and the exclusion of flux weakening in the motor model under high-speed conditions.

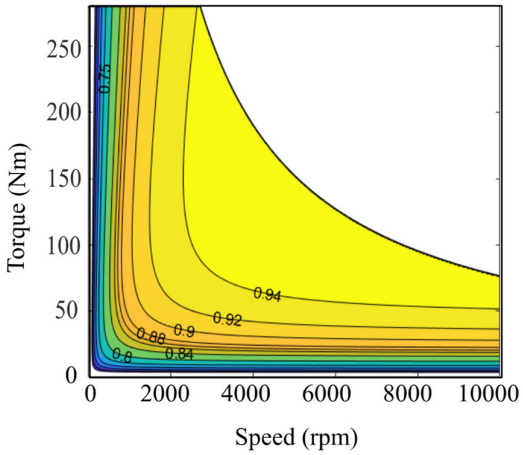

Figure 3-9. Combined efficiency map for 2012 Leaf's motor-inverter in SEVP simulator.

3.2.6 Auxiliary Load Models

Auxiliary loads comprise both the low-power accessory loads associated with fans, lights, pumps and the high-power loads associated with the heating, ventilation and air-conditioning (HVAC) loads necessary to regulate the temperature in the passenger cabin of the vehicle. In BEV designs, these loads are provided by a dc-dc converter at the battery output and are not included in the coast-down test coefficients.

The validation of the three simulators is based on data measured in dynamometer tests where the HVAC system was turned off. Therefore, only the low-power accessory loads are included in the model for the comparison of the three simulators.

These accessory loads are typically modelled as a constant power load P_{aux} on the battery. In the literature, a wide range of auxiliary power values are used for model validation with values from 100 W to 700 W [2],[3],[14],[19],[32]. Results, showing the high impacts of the magnitude selected for the auxiliary power model on each vehicle's energy consumption, are presented in Section 3.4.6.1. An improved validation result for a vehicle model in a given drive cycle test is achieved by optimising the selected constant power value of P_{aux}.

The default P_{aux} value in ADVISOR is 700 W for all light-duty vehicles. In FASTSim, the default P_{aux} value depends on the vehicle type, with a P_{aux} of 700 W used for ICE vehicles and HEVs, and a P_{aux} of 300 W is used for BEVs. The default P_{aux} is 165 W in SEVP and it models BEVs only.

In this comparison, the ANL test data for all ten vehicles was analysed to determine an average P_{aux} value for all three simulators. ANL did not measure the auxiliary power in their tests. Therefore, ANL measurements of battery output power, when the test vehicle was stationary were used to derive the P_{aux} value for each vehicle. As shown in Table 3-1, the average battery output values when the vehicle was stationary ranged from 85 W for the MiEV to 435 W for the Spark. Based on this analysis, a constant P_{aux} load of 200 W was applied to the three simulators.

Table 3-1. Battery output power values when the vehicles were stationary during ANL testing.

Vehicle	**Battery Output Power (W)**		
	Min.	**Max.**	**Ave.**
Leaf 2012	217	237	224
Leaf 2013	380	420	400
MiEV	78	90	85
Focus	365	390	380
BMW i3	170	240	190
Smart	225	248	238
Soul	147	173	155
Spark	427	447	435
eGolf	170	178	175
B-class	250	330	280

3.2.7 Battery Models

All the BEVs in this study utilise Lithium-ion (Li-ion) battery packs. The Li-ion batteries in the three simulators are modelled as power loss components either by using the fixed battery round-trip efficiency value of 95.1% in FASTSim, or as in ADVISOR and SEVP, by specifying a value of internal battery serial resistance R_{INT} or R_{BP}. In this thesis R_{INT} refers to the resistance of a single cell and R_{BP} refers to the total resistance of the battery pack.

The power loss in the battery model is not included in the comparison of the three simulators provided in this chapter. This exclusion of a battery model occurs due to the method used to validate the accuracy of the simulators. ANL test data only included measurements made at the battery terminals, so the component power losses can only be validated up to this point in the powertrain. In Chapter 4, a detailed analysis of battery models for vehicle simulators is presented. Equivalent-electrical-circuit battery models are developed for the vehicle model. These battery models provide: (i) battery output voltages based on state of charge for applications, such as V2G simulators; and (ii) a simple ageing model for the battery that enables lifetime studies on the changes in range estimation of the vehicle.

3.3 Combined Simulator (M-Sim) Development

Until recently, validation of energy consumption results from BEV simulators was hampered as the published data was limited to concept electric vehicles only. The simulators included a small number of default-BEV models and limited powertrain component models that were suitable to create additional BEV models. As legislative limits of permitted vehicle carbon dioxide (CO_2) emissions decrease, an increased number of vehicle manufacturers now sell BEVs as part of their product range.

ANL have tested and published detailed measurement data based on its testing of ten models of production volume BEVs. The test data is sampled at a frequency of 10 Hz (0.1 s) for a variety of drive cycles and temperature conditions. Measurements of voltage and current at the high-voltage battery output terminals, allow the calculation of the energy consumed; positive values of battery currents indicate a battery discharge, referred to as motoring (propulsion) energy consumption, where the power flow is from the battery to the wheels; negative values of battery currents represent battery charge, referred to as regenerative energy, where the power flow is from the wheels to the battery. The net energy consumed per drive cycle is the motoring energy minus the regenerative energy. For validation of the simulators, both the motoring and regenerative energy results are used. This allows for separate validation of the powertrain component models based on a given power flow direction.

The simulator validations are based on vehicles tested over three legislative drive cycles used in the USA; the Urban Dynamometer Drive Schedule (UDDS), the HighWay Federal Economy Test (HWFET) and the aggressive high-speed drive cycle, known as the US06 test cycle. In this study, as previously mentioned, only data from ANL tests, where the vehicle's air-conditioning system and heating systems are turned off, are used for the simulator validation.

The three simulators produce an overall drive cycle net energy consumption result. In-depth understanding of the impacts of an individual powertrain component model on this overall result can be evaluated by providing component model plug-and-play functionality to the simulators' powertrain structures. As each simulator has a different software environment, it was proposed to provide this functionality by first replicating each simulator in a common software language.

The most complex simulator, ADVISOR, was written in a MATLAB environment. This software was selected as the common language and the other two

Excel based simulators were replicated in the MATLAB environment. The GUI of ADVISOR was removed and the structure of the code was simplified to simulate only BEV powertrain designs. This replicated-ADVISOR simulator offered improved plug-and-play functionality in the choice of powertrain component models.

Each replicated simulator was first validated using the results from the original simulator software as explained in Section 3.3.2. The three validated script files were then combined to create a single multi-simulator (M-Sim) model file. This file was used to compare the accuracy of each simulator in determining the motoring, regenerative and net energy consumption, over the three drive cycles for the ten BEVs. Using a single vehicle data source file in the form of an Excel spreadsheet, the M-Sim imports this data in MATLAB and concurrently calculates the power flows in the three simulators.

3.3.1 M-Sim Modifications

During the M-Sim development, two design issues became apparent: (i) there were two possible definitions of regenerative energy, and (ii) the requirement for component power limits in each simulator.

The first design issue came about as the SEVP simulator defined regenerative energy as a time step when the wheel torque T_{axle} was negative while the other two simulators defined regenerative energy as negative power at the battery terminals. The solution to this issue simply involved changing the SEVP regenerative energy definition to make it compatible with the other two simulators.

The second design issue came about as both the ADVISOR and FASTSim simulators have a forward-facing calculation path that allows for the calculation of achieved speed when a powertrain component limit is reached. In the SEVP simulator, the specified drive cycle speed is assumed to be achieved in all drive cycle time steps. A requirement for a forward-facing path increases the complexity of replicating the simulators and reduces the possibility of introducing the desired plug-and-play functionality in the M-Sim. Given that the comparison of the three simulators is restricted to testing over low-to-moderate speed legislative drive cycles, where powertrain component limits are not be expected to be reached, the three M-Sim simulators were designed with a backward-facing calculation path only. This design decision was made after models for the ten test vehicles were constructed in the

original simulator software environments and the models were simulated over the three specified drive cycles.

3.3.1.1 Power Limit in MiEV for US06 Test

The ANL test data was also analysed to identify any timesteps where the vehicle specified speed was not achieved due to component power limits. The ANL test data revealed that for nine of the ten vehicles tested, powertrain components were operating within their power limits over all three drive cycles. The one exception is presented in Figure 3-10 and was found in the test data of the MiEV when operating in the US06 drive cycle. As seen in Figure 3-10 (a), the 49 kW MiEV motor could not achieve the high-acceleration power requirements of this drive cycle. Battery power is displayed in Figure3-10 (a) as the ANL data did not contain motor output power measurements. The three simulators were tested to check if the detected test-measurement component power limit was also observed in the MiEV model for the US06 drive cycle.

When the MiEV vehicle is simulated, the component power limits of the original ADVISOR and FASTSim simulators capture this performance limitation. As noted in Figure 3-10 (b), the SEVP simulator does not capture this power limit. As the M-Sim does not contain component limits, it also does not limit the high-acceleration power in the MiEV in this drive cycle. The net result was a 1.4% overestimation of the MiEVs' US06 net energy consumption in the M-Sim replicated FASTSim simulator, compared to the original FASTSim software. The resulting difference between the net energy in M-Sim and ADVISOR was an overestimation of only 0.2%. These results suggested that the forward-facing path in the M-Sim file could be removed, provided that the error associated with power-limited vehicles, such as the MiEV operating in the US06, are clearly stated in the comparison study.

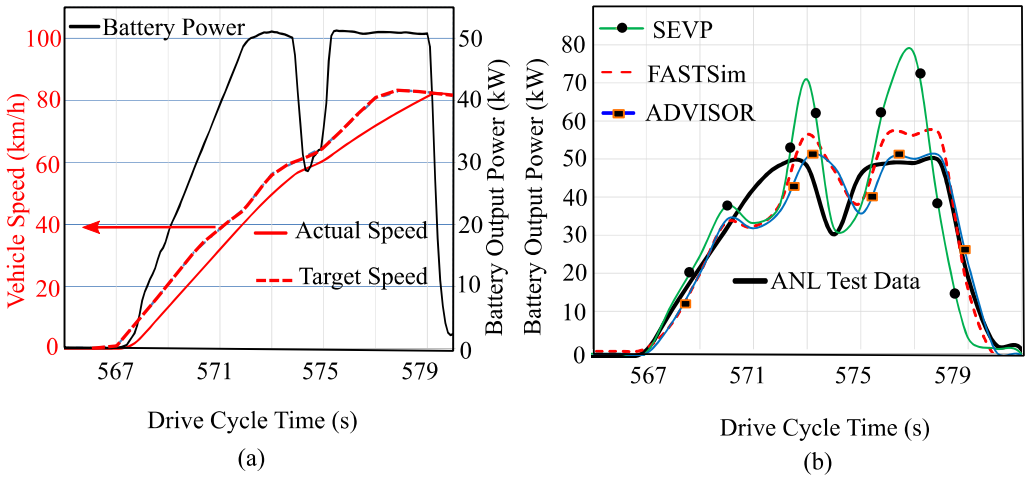

Figure 3-10. MiEV Powertrain limits in (a) ANL testing, (b) Simulator testing.

3.3.1.2 FASTSim Power Limits

In the original software for the FASTSim simulator, component limits were observed in a number of other vehicles during simulation in the US06 drive cycle. However, these component limits were not supported by the ANL test results. For instance, the default FASTSim model for a 2012 Leaf BEV, displayed powertrain component limits in a total of 51 s out of the 600 s time period of the US06 drive cycle. The power limits resulted in the drive cycle speed not being achieved in some drive cycle time steps.

Two design specifications of the FASTSim vehicle model were identified as the sources of the component power limit errors. The majority of the missed cycle speeds, 49 s out of 51 s, were due to the use of an electric motor ramp parameter called “motor time to full power output”. This imposed a 5 s ramp rate for the electric motor to go from zero to full power output. The ramp rate observed in the ANL test data was less than 2 s to full power output. When this higher ANL ramp rate was used, the simulator periods where the FASTSim component power limits were activated reduced from a total of 51 s to only 2 s.

The second component power limit source was the combination of a FASTSim imposed 90 kW battery output limit with the low FASTSim motor-inverter model efficiency during high-torque, low-speed driving conditions. These powertrain model specifications restrict the motor output power to 77.5 kW, which is below the

manufacturer's specification of 80 kW. When this limit was modified to allow the rated 80 kW output, the powertrain is no longer limited in the FASTSim simulator. Based on these results, the M-Sim implements a simple backward-facing only approach without component power limits. This design choice allows the simulator to be validated with the ANL test data, with the noted exception of very low-power rated vehicles in the US06 drive cycle.

3.3.2 M-Sim Software Authentication

Each of the three simulators replicated in MATLAB was individually compared to that simulator in its original software environment to authenticate the powertrain model replication process. Three vehicle models, based on the 2012 Leaf, 2013 Leaf and the Focus EV, were developed in the original software of each simulator. For this software authentication process, the vehicle models used some of the same powertrain component values as the four default FASTSim BEV models namely, a C_{rr} of 0.008, a wheel inertia of 0.815 kg m^2 per wheel that is equivalent to a J_{axle} value of 3.26 kg m^2, a transmission efficiency of 97%, and an auxiliary load of 300W. An additional inertia for the electric motor estimated as 0.0507 kg m^2 was required in the ADVISOR simulator. The ANL measured test weights for each vehicle were used and the SEVP simulator used the coast-down test coefficients from the ANL published data. The purpose of this authentication testing was to prove that the M-Sim results accurately reflected the original simulator results. The process did not involve validating the simulator results to the ANL test data measurements. A separate simulator energy consumption validation process for each vehicle is presented in Section 3.4.

3.3.2.1 Replication issues for ADVISOR and FASTSim

Developing the combined motor-inverter models for ADVISOR and FASTSim was challenging. The ADVISOR motor-inverter power loss model is based on an efficiency map LUT indexed by motor output torque T_r and shaft speed ω_r values. As these efficiency maps were not provided for the three test vehicles, a 49 kW HONDA motor-inverter model in ADVISOR was scaled to meet the maximum torque and maximum speed of the three higher-power rated vehicles, namely the two 80 kW Leaf motors and the 106.6 kW Focus motor.

The motor-inverter power loss polynomials used in FASTSim were generated using curve-fitting techniques in Excel. When these techniques were replicated in MATLAB, a small difference in polynomial coefficients was observed. Compatibility with the original FASTSim software was achieved by using the Excel derived coefficient values in the MATLAB version of this simulator.

3.3.2.2 Authentication Results

The three vehicle models were simulated in both the original software and the replicated M-Sim model in MATLAB over three drive cycles. The software authentication results are summarised in Table 3-2. Results given in Wh values in Appendix B.2. The maximum observed error in the motoring energy power flow direction is 0.1%. This represents an overestimation of motoring energy in the M-Sim results compared to the original simulator. The corresponding maximum error observed for regenerative energy power flow direction is 0.6%. The maximum net-energy error is -0.3%, which represents an M-Sim underestimate of 0.3%. This comparison was conducted with the initial battery SOC set to 80% to avoid over-charging limits during regenerative braking events. The source of these small errors could not be identified. The level of error was sufficiently low to state that the M-Sim models are an accurate replication of the original simulator software models.

Table 3-2. Software authentication results between original simulators and M-Sim versions.

	2012 Leaf								
	UDDS			**HWY**			**US06**		
	Regen	*Motor*	Net	*Regen*	*Motor*	Net	*Regen*	*Motor*	Net
M-Sim SEVP	0.2%	0.0%	-0.1%	0.0%	0.0%	0.0%	0.2%	0.0%	0.0%
M-Sim FASTSim	0.0%	0.0%	0.0%	0.6%	0.0%	0.0%	0.6%	-0.1%	-0.3%
M-Sim ADVISOR	0.0%	0.0%	0.0%	0.0%	0.0%	0.0%	0.2%	0.1%	0.1%
	2013 Leaf								
M-Sim SEVP	0.4%	0.0%	-0.1%	0.0%	0.0%	0.0%	0.2%	0.0%	0.0%
M-Sim FASTSim	0.0%	0.0%	0.0%	0.0%	0.0%	0.0%	0.2%	0.0%	0.0%
M-Sim ADVISOR	-0.2%	0.0%	0.1%	0.0%	0.0%	0.1%	0.0%	0.0%	0.0%
	Focus EV								
M-Sim SEVP	0.3%	0.0%	-0.1%	0.5%	0.0%	0.0%	0.2%	0.0%	0.0%
M-Sim FASTSim	0.0%	0.0%	0.1%	0.0%	0.0%	0.0%	0.0%	0.0%	0.0%
M-Sim ADVISOR	0.3%	0.2%	0.1%	0.5%	0.0%	0.0%	-0.3%	-0.1%	0.0%

3.4 Simulator Validation based on ANL Data

Based on the software authentication of the three simulators in a single MATLAB script (M-Sim), the M-Sim was applied to other vehicles. Ten BEV models were simulated over the UDDS, HWFET and US06 drive cycles with M-Sim and each simulation result was compared to appropriate ANL test measurements.

3.4.1 Configuring ANL Measurements

The ANL prescribed test schedule for each vehicle is given as a UDDS test, followed by a HWFET test, then another UDDS and two US06 tests. If enough battery capacity is available, testing continues with another UDDS test, followed by a HWFET and another UDDS test. The BEVs are fully charged at the start of the test schedule and the first UDDS test in the test schedule is labelled a "cold start" (CdSt) test, signifying a test that starts with a maximum battery SOC and with all cooling fluids in the vehicle at ambient temperature. All other tests in the schedule are in effect "hot start" tests as the battery SOC is less than 100% and the cooling fluids are at a working temperature from previous tests in the schedule.

The cold-start tests displayed higher levels of energy consumption than the equivalent hot start tests. Analysis of the ANL test data identified two possible reasons for the increased consumption. First, the UDDS has a high braking event 115 s after the start of the cycle. In these cold-start tests, the battery SOC is still close to 100% and the battery does not have the capacity to absorb the regenerative energy from this braking event. Second, the power levels in the dc/dc converter, which charges the low voltage (12 V) electrical system from the high voltage battery, are very high during the initial stage of the cold-start UDDS test. The likely load for this power is the requirement to recharge the 12 V battery after the 12 hours inactive period needed to ensure the ambient temperatures in the vehicle have reached the ambient levels required in each test. As these two unique operating conditions do not reflect standard operating conditions for a BEV, the cold-start test results were excluded from the M-Sim validation. In addition to cold-start tests, all tests carried out at ambient temperatures of -7°C (20°F) and 35°C (95°F) were excluded as the component models for the vehicle HVAC are not included in the simulators reviewed in this chapter.

The 0.1s ANL test measurements are averaged to 1 s test measurements for the M-Sim energy consumption validation. For each test, the 1 s averaged test measurements were sorted and summed in motoring energy and regenerative energy. The net energy consumption in each drive cycle was then determined from the difference between the summed motoring and regenerative energies. As each vehicle was tested more than once in a specific drive cycle, an examination of the reliability of a given ANL energy consumption result was possible. Table 3-3 presents the ANL testing measurements for two test vehicles and the reliability analysis on this data carried out in this study. The average test energy consumption does not include the CdSt test results. The full results of this reliability analysis for all ten vehicles are presented in Table 3-4.

The results indicate tolerance bands associated with the three repeated UDDS tests, two HWFET tests and two US06 tests for each vehicle. Given that these tests required a driver to follow rapidly changing speed profiles, a tolerance band of less than +/-1% in 23 out of the 30 net energy consumption results is reasonable.

Table 3-3. Sample of ANL test results and repeatability analysis for two vehicles (Units Wh).

ANL Tests	**2015 Soul**				**2015 B-class**		
UDDS	**Regen**	**Motoring**	**Net**	**UDDS**	**Regen**	**Motoring**	**Net**
61506042CdSt	551	2006	1455	61512013CdSt	634	2474	1840
61506042	571	1908	1337	61512013	**658**	2430	1772
61506044	**566**	**1890**	1324	61512015	664	2313	1649
61506044	570	1897	**1327**	61512015	661	**2295**	**1634**
ave.	**569**	**1898**	**1329**	*ave*	**661**	**2346**	**1685**
"-tol"	-0.5%	-0.4%	-0.4%	*"-tol"*	-0.5%	-2.2%	-3.0%
"+tol"	0.4%	0.5%	0.6%	*"+tol"*	0.5%	3.6%	5.2%
HWY	**Regen**	**Motoring**	**Net**	**HWY**	**Regen**	**Motoring**	**Net**
61506042	174	2447	2273	61512013	**219**	2823	2604
61506044	182	2373	2191	61512015	240	**2434**	2194
ave	**178**	**2410**	**2232**	*ave*	**230**	**2629**	**2399**
"-tol"	-2.2%	-1.5%	-1.8%	*"-tol"*	-4.6%	-7.4%	-8.5%
"+tol"	2.2%	1.5%	1.8%	*"+tol"*	4.6%	7.4%	8.5%
US06	**Regen**	**Motoring**	**Net**	**US06**	**Regen**	**Motoring**	**Net**
61506042	630	2950	2320	61512013	**715**	3272	2557
61506043	653	2912	2259	61512014	719	**3161**	2442
ave	**642**	**2931**	**2290**	*ave*	**717**	**3217**	**2500**
"-tol"	-1.8%	-0.6%	-1.3%	*"-tol"*	-0.3%	-1.7%	-2.3%
"+tol"	1.8%	0.6%	1.3%	*"+tol"*	0.3%	1.7%	2.3%

The high variation in the B-class test results was investigated with the available data and an analysis of the test speed profiles eliminated the driver's performance as the source of the variations recorded. More extensive powertrain measurements would be required to identify where the increased energy losses occurred in the first version of each test. The wide tolerance band in the B-class will have to be included in any simulator validation with this vehicle.

Table 3-4. Reliability results for the ANL test data.

Vehicle	Drive Cycle	Initial M-Sim Models (All results in +/- % unless otherwise specified)		
		Regen Energy	Motoring Energy	Net Energy
Leaf (2012 model)	UDDS	+1.1, -1.2	+0.3, -0.2	+0.2, -0.3
	HWFET	2.5	0.3	0.5
	US06	1.9	0.7	1.0
Leaf (2013 model)	UDDS	+0.2, -0.4	+0.4, -0.3	0.5
	HWFET	0.6	0.1	0.1
	US06	0.4	0.1	0.0
MiEV (2012 model)	UDDS	+0.7, -0.3	+0.1, -0.2	+0.5, -0.1
	HWFET	0.9	0.5	0.5
	US06	0.0	0.2	0.3
Focus EV (2013 model)	UDDS	+1.1, -1.2	+0.8, -1.1	1.1
	HWFET	1.2	0.7	0.9
	US06	0.1	0.6	0.8
BMW i3 (2014 model)	UDDS	+0.7, -0.8	+0.4, -0.5	+0.5, -0.3
	HWFET	0.0	0.5	0.6
	US06	2.9	0.4	0.3
Smart EV (2014 model)	UDDS	+2.0, -1.2	+1.0, -0.8	+0.7, -0.8
	HWFET	2.3	0.5	0.3
	US06	1.1	0.4	0.3
Soul EV (2015 model)	UDDS	+0.4, -0.5	+0.5, -0.4	+0.6, -0.4
	HWFET	2.2	1.5	1.8
	US06	1.8	0.6	1.3
Spark (2015 model)	UDDS	+0.8, -1.6	0.4	+0.2, -0.3
	HWFET	0.7	0.1	0.2
	US06	1.5	0.6	0.3
eGOLF (2015 model)	UDDS	+3.8, -3.4	+1.5, -1.8	+3.8, -0.6
	HWFET	5.1	0.8	0.5
	US06	0.5	0.3	0.6
B-class (2015 model)	UDDS	0.5	+3.6, -2.2	+5.2, -3.0
	HWFET	4.6	7.4	8.5
	US06	0.3	1.7	2.3

For the simulator validation, an averaged ANL test value over the multiple drive cycle tests is determined for each vehicle's motoring energy consumption and regenerative energy recovered in a specific drive cycle type.

3.4.2 Initial Simulator Validation Results

The initial M-Sim test results, based on power flow direction, are compared to the averaged ANL test values in Table 3-5. The results for the overall net energy consumption for each drive cycle are then summarised in Table 3-6. A summary showing which simulator provided net energy consumption values closest to the average ANL values in all 30 tests (10 vehicles and 3 drive cycles per vehicle) is presented in Table 3-7. The summary results in Table 3-7 indicate that the SEVP simulator is comparable to the two widely used vehicle simulators, both of which had significantly more complex powertrain structures.

When the simulators are compared in terms of accuracy in estimating the regenerative energy, the motoring energy consumption and the net energy consumption, four trends can be observed. First, as seen in Table 3-5, in the US06 tests for three vehicles (2012 Leaf, MiEV, and Smart EV), the regenerative energy is significantly overestimated by up to 65.6% in all three simulators. The analysis and proposed solution for this issue is presented in Section 3.4.3. Second, as noted in Table 3-5, the SEVP simulator significantly over-estimates the motoring energy consumption and underestimates the regenerative energy in all drive cycles of two vehicles, namely the BMW i3 and eGOLF. The combined impact of these errors is shown in Table 3-6 as a significant overestimation of the net energy consumption in these two vehicles. The analysis of this SEVP issue is presented in Section 3.4.4. Third, as shown in both Tables 3-5 and 3-6, the FASTSim simulator results show a drive-cycle dependency energy consumption pattern. For instance, if FASTSim over-estimates the motoring energy consumption in all three cycles, the highest over-estimation always occurs in the UDDS cycle and if FASTSim under-estimates in all three cycles, the lowest under-estimation occurs in the UDDS cycle. This FASTSim issue is investigated in Section 3.4.5. Fourth, validation of a vehicle model, based solely on net energy consumption in a drive cycle, can disguise significant modelling errors. This is shown in Table 3-6 for the 2012 Leaf, which has a relatively low net energy consumption error of -5.0% for the US06 drive cycle but the regenerative energy estimate for this vehicle in Table 3-5, shows a significant overestimation of 53.7%.

Table 3-5. Initial comparison of three simulations given in Wh and percentage compatibility to test data (underestimates given as negative % values).

	UDDS		HWFET		US06	
	Regen	**Motor**	**Regen**	**Motor**	**Regen**	**Motor**
	2012 Leaf					
M-Sim (SEVP)	539 (3.3)	2033 (2.8)	169 (5.0)	2523 (0.1)	621 (**53.7**)	3149 (2.7)
M-Sim (FASTSim)	526 (0.8)	1981 (0.2)	180 (11.8)	2257 (-10.4)	669 (**65.6**)	2854 (-6.9)
M-Sim (ADVISOR)	553 (5.9)	1897 (-4.1)	182 (13.0)	2273 (-9.8)	656 (**62.4**)	2888 (-5.8)
ANL Test Data	**522**	**1978**	**161**	**2520**	**404**	**3066**
	2013 Leaf					
M-Sim (SEVP)	464 (-8.1)	1859 (4.1)	143 (-7.7)	2341 (3.8)	539 (1.7)	2830 (3.8)
M-Sim (FASTSim)	452 (-10.5)	1803 (1.0)	152 (-1.9)	2101 (-6.8)	575 (8.5)	2626 (-3.7)
M-Sim (ADVISOR)	480 (-5.0)	1718 (-3.8)	153 (-1.3)	2139 (-5.1)	565 (6.6)	2673 (-1.9)
ANL Test Data	**505**	**1786**	**155**	**2255**	**530**	**2726**
	2012 MiEV					
M-Sim (SEVP)	406 (5.7)	1665 (2.5)	119 (2.6)	2204 (3.4)	457 (**27.3**)	2621 (1.7)
M-Sim (FASTSim)	408 (6.3)	1568 (-3.4)	132 (13.8)	1909 (-10.4)	497 (**38.4**)	2378 (-7.7)
M-Sim (ADVISOR)	411 (7.0)	1562 (-3.8)	128 (10.3)	2002 (-6.1)	479 (**33.4**)	2472 (-4.0)
ANL Test Data	**384**	**1624**	**116**	**2131**	**359**	**2576**
	2013 Focus EV					
M-Sim (SEVP)	539 (-11.6)	2207 (5.3)	170 (-17.1)	2726 (10.1)	637 (-5.3)	3300 (7.4)
M-Sim (FASTSim)	536 (-12.1)	2134 (1.8)	184 (-10.2)	2406 (-2.8)	695 (3.3)	3013 (-2.0)
M-Sim (ADVISOR)	583 (-4.4)	1978 (-5.6)	195 (-4.9)	2319 (-6.3)	695 (3.3)	2978 (-3.1)
ANL Test Data	**610**	**2096**	**205**	**2476**	**673**	**3074**
	2014 BMW i3					
M-Sim (SEVP)	422 (-20.7)	1873 (**10.8**)	127 (-17.0)	2407 (**16.7**)	493 (-8.7)	2829 (**12.4**)
M-Sim (FASTSim)	395 (**-25.8**)	1882 (11.4)	132 (-13.7)	2230 (8.1)	516 (-4.4)	2692 (7.0)
M-Sim (ADVISOR)	461 (-13.3)	1667 (-1.4)	143 (-6.5)	2151 (4.3)	535 (-0.9)	2660 (5.7)
ANL Test Data	**532**	**1690**	**153**	**2062**	**540**	**2516**
	2014 Smart EV					
M-Sim (SEVP)	294 (-5.8)	1563 (7.4)	77 (-11.5)	2265 (12.2)	321 (**13.8**)	2569 (13.8)
M-Sim (FASTSim)	308 (-1.3)	1384 (-4.9)	94 (8.0)	1831 (-9.3)	368 (**30.5**)	2223 (-1.6)
M-Sim (ADVISOR)	335 (7.4)	1319 (-9.3)	95 (9.2)	1882 (-6.8)	371 (**31.6**)	2252 (-0.3)
ANL Test Data	**312**	**1455**	**87**	**2019**	**282**	**2258**
	2015 Soul					
M-Sim (SEVP)	533 (-6.3)	1983 (4.5)	164 (-7.9)	2498 (3.7)	610 (-5.0)	3058 (4.3)
M-Sim (FASTSim)	501 (-12.0)	2024 (6.6)	162 (-9.0)	2499 (3.7)	614 (-4.4)	3095 (5.6)
M-Sim (ADVISOR)	529 (-7.0)	1931 (1.7)	164 (-7.9)	2492 (3.4)	609 (-5.1)	3112 (6.2)
ANL Test Data	**569**	**1898**	**178**	**2410**	**642**	**2931**
	2015 Spark					
M-Sim (SEVP)	454 (-2.6)	1732 (1.8)	143 (-2.7)	2113 (6.9)	532 (-0.7)	2591 (4.9)
M-Sim (FASTSim)	422 (-9.4)	1794 (5.5)	138 (-6.1)	2184 (10.5)	528 (-1.5)	2688 (8.8)
M-Sim (ADVISOR)	458 (-1.7)	1673 (-1.6)	142 (-3.4)	2155 (9.0)	528 (-1.5)	2683 (8.6)
ANL Test Data	**466**	**1701**	**147**	**1977**	**536**	**2471**
	2015 eGolf					
M-Sim (SEVP)	465 (-18.3)	2229 (**22.5**)	157 (-10.3)	2572 (**20.2**)	577 (-10.7)	3134 (**15.3**)
M-Sim (FASTSim)	548 (-3.7)	1966 (8.0)	192 (9.7)	2160 (1.0)	711 (10.1)	2748 (1.1)
M-Sim (ADVISOR)	543 (-4.6)	1850 (1.6)	196 (12.0)	2017 (-5.7)	651 (0.8)	2531 (-6.8)
ANL Test Data	**569**	**1820**	**175**	**2139**	**646**	**2717**
	2015 B-class					
M-Sim (SEVP)	624 (-5.6)	2213 (-5.7)	203 (-11.7)	2563 (-2.5)	752 (4.9)	3181 (-1.1)
M-Sim (FASTSim)	565 (-14.5)	2332 (-0.6)	195 (-15.2)	2621 (-0.3)	741 (3.3)	3259 (1.3)
M-Sim (ADVISOR)	620 (6.2)	2150 (-8.4)	207(-10.0)	2512 (-4.5)	750 (4.6)	3235 (0.6)
ANL Test Data	**661**	**2346**	**230**	**2629**	**717**	**3217**

Table 3-6. Net energy consumption comparison. Units are Wh and % error (underestimations in simulators are given as negative values).

	UDDS	HWFET	US06	UDDS	HWFET	US06
	2012 Leaf			**2013 Leaf**		
M-Sim (SEVP)	1494 (2.6)	2354 (-0.2)	2528 (-5.0)	1395 (8.9)	2198 (4.7)	2291 (4.3)
M-Sim (FASTSim)	1455 (-0.1)	2077 (-12.0)	2185 (-17.9)	1351 (5.5)	1949 (-7.2)	2051 (-6.6)
M-Sim (ADVISOR)	1344 (-7.7)	2091 (-11.4)	2232 (-16.2)	1238 (-3.4)	1986 (-5.4)	2108 (-4.0)
ANL Test Data	1456	2359	2662	1281	2100	2196
	2012 MiEV			**2013 Focus EV**		
M-Sim (SEVP)	1259 (1.5)	2085 (3.5)	2164 (-2.4)	1668 (12.2)	2556 (12.5)	2663 (10.9)
M-Sim (FASTSim)	1160 (-6.5)	1777 (-11.8)	1881 (-15.2)	1598 (7.5)	2222 (-2.2)	2318 (-3.5)
M-Sim (ADVISOR)	1151 (-7.2)	1874 (-7.0)	1993 (-10.1)	1395 (-6.1)	2124 (-6.5)	2283 (-4.9)
ANL Test Data	1240	2015	2217	1486	2271	2401
	2014 BMW i3			**2014 Smart EV**		
M-Sim (SEVP)	1451 (**25.3**)	2280 (**19.4**)	2336 (**18.2**)	1269 (11.0)	2188 (13.3)	2248 (13.8)
M-Sim (FASTSim)	1487 (**28.4**)	2098 (9.9)	2176 (10.1)	1076 (-5.9)	1737 (-10.1)	1855 (-6.1)
M-Sim (ADVISOR)	1206 (4.1)	2008 (5.2)	2125 (7.5)	984 (-13.9)	1787 (-7.5)	1881 (-4.8)
ANL Test Data	1158	1909	1976	1143	1932	1976
	2015 Soul			**2015 Spark**		
M-Sim (SEVP)	1450 (9.1)	2334 (4.6)	2448 (6.9)	1278 (3.5)	1970 (7.7)	2059 (6.4)
M-Sim (FASTSim)	1523 (14.6)	2337 (4.7)	2481 (8.4)	1372 (11.1)	2046 (11.8)	2160 (11.6)
M-Sim (ADVISOR)	1402 (5.5)	2328 (4.3)	2503 (9.3)	1215 (-1.6)	2013 (10.0)	2155 (11.4)
ANL Test Data	1329	2232	2289	1235	1830	1935
	2015 eGolf			**2015 B-class**		
M-Sim (SEVP)	1764 (**41.0**)	2415 (**23.0**)	2557 (**23.5**)	1589 (-5.7)	2360 (-1.6)	2429 (-2.8)
M-Sim (FASTSim)	1418 (13.3)	1968 (0.2)	2037 (-1.6)	1767 (4.9)	2426 (1.1)	2518 (0.7)
M-Sim (ADVISOR)	1307 (4.5)	1821(-7.3)	1880 (-9.2)	1530 (-9.2)	2305 (-3.9)	2485 (-0.6)
ANL Test Data	1251	1964	2071	1685	2399	2500

Table 3-7. Summary of initial M-Sim simulator net energy consumption comparison results.

Simulator	Highest Under-estimation	Highest Over-estimation	Number of tests where optimum result achieved
SEVP	-5.7%	41.0%	9
FASTSim	-17.9%	28.4%	8
ADVISOR	-16.2%	11.4%	13

3.4.3 Regenerative Braking Model Analysis

The initial M-Sim results show significant overestimation of the regenerative energy for the US06 drive cycle in three vehicle models. namely the 2012 version of

the Leaf, the 2012 MiEV and the 2014 Smart EV. As noted in Table 3-5, the regenerative energy in these vehicles is calculated with a relatively low error in both the UDDS and HWFET drive cycles. There are several potential error sources for the regenerative energy consumption issue including the tractive effort model and the brake model.

3.4.3.1 Regenerative Energy Error based on Tractive Effort Model

The tractive effort model in the SEVP is based on the coast-down coefficients while the other two simulators use the standard kinematic equation approach for tractive effort modelling. The regenerative energy is a function of the tractive effort and when the tractive effort is overestimated, this results in lower levels of regenerative energy and vice versa, when the tractive effort is underestimated.

This tractive effort dependency can be seen in the SEVP simulator result for the Smart EV in the US06 drive cycle, where a significant overestimation of the tractive effort, as indicated by the overestimated motoring energy result, reduced the regenerative energy result compared to the two other simulators. However, the tractive effort model results in the other two vehicles show good agreement to the ANL test results for motoring energy consumption. This indicates that the tractive effort model is not the source of the regenerative energy error in these three vehicles.

3.4.3.2 Regenerative Energy Error based on Brake Model

The powertrain models in FASTSim and ADVISOR incorporate brake models based on vehicle speed. Removing these component models in M-Sim shows limited impact on regenerative energy values, seen in all three types of drive cycle. With the brake model removed in these three vehicles, the regenerative energy increased by amounts ranging from 5.2% to 6.4% in the UDDS, 0.6% to 1.7% in the HWFET, and 2.2% to 2.8% in the US06 regenerative energy results. These existing brake models are mainly impacting low speed, low regenerative energy braking events, typically found in urban driving environments.

The SEVP simulator does not contain a brake model and assumes 100 % regenerative braking. A comparison of the ANL measurements with the SEVP simulator output was carried out to determine if a brake model was required. Figure 3-11 presents this comparison of the regenerative energy for a section of US06. Figure

3-11(a) shows the regenerative energy in the 2012 Leaf and Figure 3-11(b) shows the regenerative energy in the 2013 Leaf. The 2012 Leaf test results indicate that there was a limit to the regenerative energy in this vehicle. This limit does not appear to be a speed related function as implemented in the ADVISOR and FASTSim models. It is also not peak power limited, as assumed in the 2014 version of the SEVP simulator. Similar limits in regenerative energy were seen in the 2012 MiEV and 2014 Smart EV comparison. In the 2013 Leaf, the regenerative energy limits appear to have been removed.

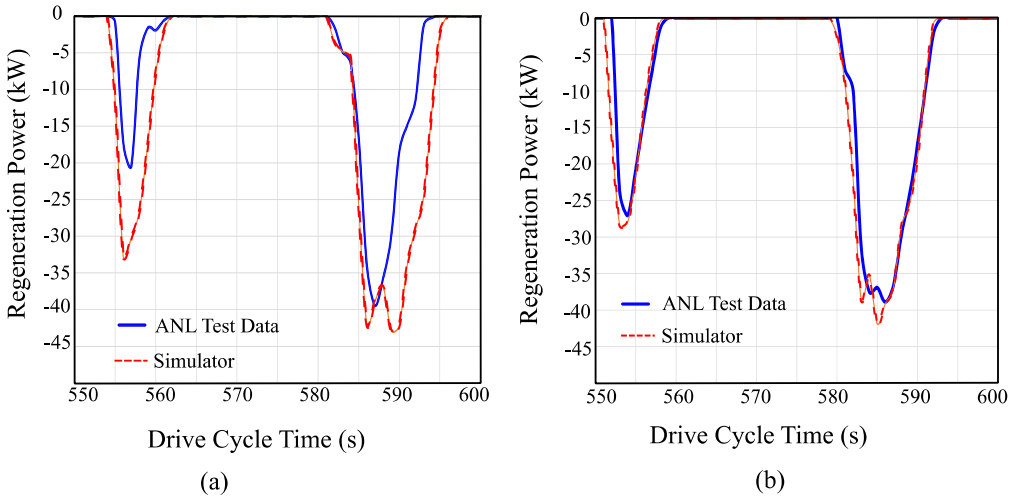

Figure 3-11. Response in 2012 Leaf and 2013 Leaf in US06.

3.4.3.3 New Proposed Brake Model for 2012 Leaf, MiEV and Smart EV

Clearly, a new regenerative brake model is needed for these three vehicles that significantly reduces the regenerative energy in the US06. Currently, as the SEVP simulator without a brake model provides good estimates of regenerative energy in the UDDS and HWFET drive cycles, the new proposed brake model must have no or only a minor impact in these drive cycles. A comparison of the test measurements and the simulator values during braking events showed that the regenerative energy was not a simple function of either speed, or a braking power or braking energy but it could be related to the deceleration rate of the vehicle.

With low deceleration rates, 100% of the braking energy is applied to the motor shaft and recovered as regenerative energy. As the deceleration rate increases, a higher portion of the braking energy is applied to the friction brakes at the wheels, leaving a

reduced portion available at the motor shaft for regenerative energy. The proposed brake model for the three vehicles splits the braking power between friction brakes and regenerative brakes based on the deceleration rate of the vehicle.

A simple third-order polynomial implemented this regenerative braking fraction Reg_{ach} to acceleration a relationship, using coefficients derived by model experimentation as shown in Figure 3-12 (a). The SEVP simulator outputs with this new brake model are shown in Figure 3-12 (b) for the 2012 Leaf. With the proposed brake model implemented, a good correlation is shown between the ANL test data and SEVP simulation outputs. This brake model was incorporated into all three simulators in M-Sim, with the 2012 Leaf and the MiEV, using the same polynomial coefficients

$$Reg_{ach} = 0.014a^3 - 0.076a^2 + 0.0024a + 1 \tag{3.9}$$

The Smart EV proposed brake model required a different set of coefficients, given as

$$Reg_{ach} = 0.0075a^3 - 0.04a^2 + 0.0024a + 1 \tag{3.10}$$

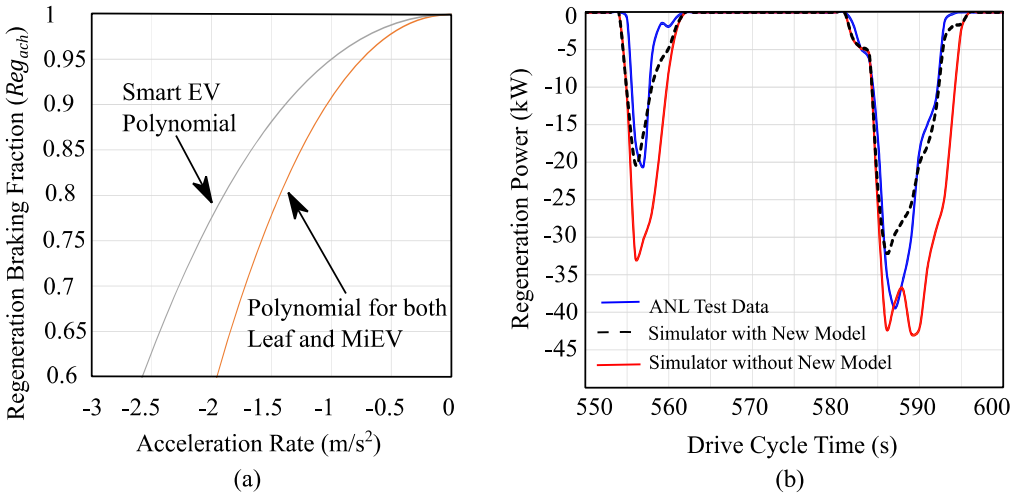

Figure 3-12. New brake model based on deceleration rates. (a) Regenerative braking fraction based on the deceleration rate relationship for the three vehicles (b) US06 regenerative energy in 2012 Leaf with and without proposed braking model.

Table 3-8 presents the regenerative energy in the simulators with the new braking model implemented. These results show a 50% reduction in US06 regenerative energy in both the 2012 Leaf and MiEV, while a 22% reduction was visible in the

Smart EV results. A 10% reduction was recorded in both the UDDS and HWFET drive cycles for the 2012 Leaf and MiEV. A 4% reduction in the UDDS and a 5% reduction in the HWFET was seen in the Smart regenerative energy results.

Further experimentation is required to improve this braking model by increasing its impact in the US06 and decreasing its impact in both the UDDS and HWFET drive cycles. As this model is only required in older model vehicles, no further regenerative modelling work was carried out in this study.

Table 3-8. Comparison results with new proposed regenerative braking model. (All regenerative energy units are Wh).

	UDDS		HWFET		US06	
	Old Model	**New Model**	**Old Model**	**New Model**	**Old Model**	**New Model**
	2012 Leaf					
M-Sim (SEVP)	539 (3.3)	509 (-2.5)	169 (5.0)	156 (-3.1)	621 (**53.7**)	458 (13.4)
M-Sim (FASTSim)	526 (0.8)	472 (-9.6)	180 (11.8)	163 (1.2)	669 (**65.6**)	473 (17.1)
M-Sim (ADVISOR)	553 (5.9)	506 (-3.1)	182 (13.0)	166 (3.1)	656 (**62.4**)	476 (17.8)
ANL Test Data	**522**		**161**		**404**	
	2012 MiEV					
M-Sim (SEVP)	406 (5.7)	383 (-0.3)	119 (2.6)	110 (-5.2)	457 (**27.3**)	334 (-7.0)
M-Sim (FASTSim)	408 (6.3)	366 (-4.7)	132 (13.8)	120 (3.4)	497 (**38.4**)	347 (-3.3)
M-Sim (ADVISOR)	411 (7.0)	374 (-2.6)	128 (10.3)	128 (10.3)	479 (**33.4**)	337 (-6.1)
ANL Test Data	**384**		**116**		**359**	
	2014 Smart EV					
M-Sim (SEVP)	294 (-5.8)	297 (-4.8)	77 (-11.5)	74 (-14.9)	321 (**13.8**)	282 (0.0)
M-Sim (FASTSim)	308 (-1.3)	296 (-4.9)	94 (8.0)	89 (2.3)	368 (**30.5**)	306 (8.5)
M-Sim (ADVISOR)	335 (7.4)	329 (5.4)	95 (9.2)	90 (3.4)	371 (**31.6**)	311 (10.3)
ANL Test Data	**312**		**87**		**282**	

3.4.4 SEVP Motoring Energy Overestimation

According to the initial M-Sim comparison results, the SEVP simulator significantly overestimates the motoring energy consumption in all drive cycles of two vehicles, namely the BMW i3 and the eGOLF. Overestimation of motoring energy consumption in vehicle simulators can result from either excessive loss in the powertrain component models and/or an overestimation of the tractive effort required by the vehicle.

The SEVP powertrain contains only three component models, namely a transmission model, a motor model and an inverter model. As the same transmission model was used in all three simulators in M-Sim, it was eliminated as the error source

in the SEVP simulator. A comparison of the power loss in the ADVISOR's combined motor-inverter model with the total power losses in the SEVP's motor and inverter models showed a good correlation between these component models. The ADVISOR simulator does not significantly overestimate the motoring energy consumption for these vehicles. This analysis identified the tractive effort model in the SEVP simulator as the source of the simulator error.

3.4.4.1 Tractive Effort Analysis-Source of Coast-down Coefficients

There is a clear difference in the tractive effort models of the three simulators: FASTSim and ADVISOR determine the tractive effort using selected vehicle parameters as noted in (3.2), while SEVP uses coast-down test coefficients as noted in (3.3). There are two sources for these coast-down coefficients: (i) the values published annually by the EPA; and (ii) dynamometer derived values from ANL using the test vehicles. The M-Sim validation was based on the ANL coast-down coefficients. The alternative EPA coefficients only resulted in minor changes in the motoring energy consumption in these two vehicles, ranging from -2.4% (eGOLF UDDS result) to +2.6% (BMW i3 US06). This eliminated the source of the coast-down coefficients as the cause of the motoring energy overestimation in the eGolf and BMW i3.

3.4.4.2 Tractive Effort Analysis-Acceleration Calculation Method

A detailed examination of the code for all three simulators identified a second difference with potential to impact the tractive effort model outputs. FASTSim and ADVISOR both defined the legislative drive cycle speed in one second intervals as the speed the vehicle must reach at the end of each interval, as shown in Figure 3-13(a). The SEVP simulator defined the drive cycle speed as the speed obtained at the midpoint in each interval.

All three simulators use the speed at the midpoint of each interval for the calculation of the tractive effort, as shown in Figure 3-13(a). This results in an average speed value for each interval being used in the tractive effort calculation in both the ADVISOR and FASTSim simulators. In the SEVP simulator, as the drive cycle speed was assumed to be reached at the midpoint of each interval, the speed used for tractive effort calculation will be higher than in the other two simulators, when the vehicle is accelerating, and lower when the vehicle is decelerating. The impact of the highlighted

differences in the drive cycle interval speed definition is shown in Figure 3-13(b), as increased motoring power in acceleration and reduced regenerative energy.

The calculation difference is predominantly visible in drive cycles that involve a high number of acceleration/deceleration events such as the UDDS and US06 drive cycles. When the SEVP simulator was modified to use the same speed definitions as the other two simulators, the motoring energy overestimation reduced in all drive cycles, but the average reduction was only -3.5%.

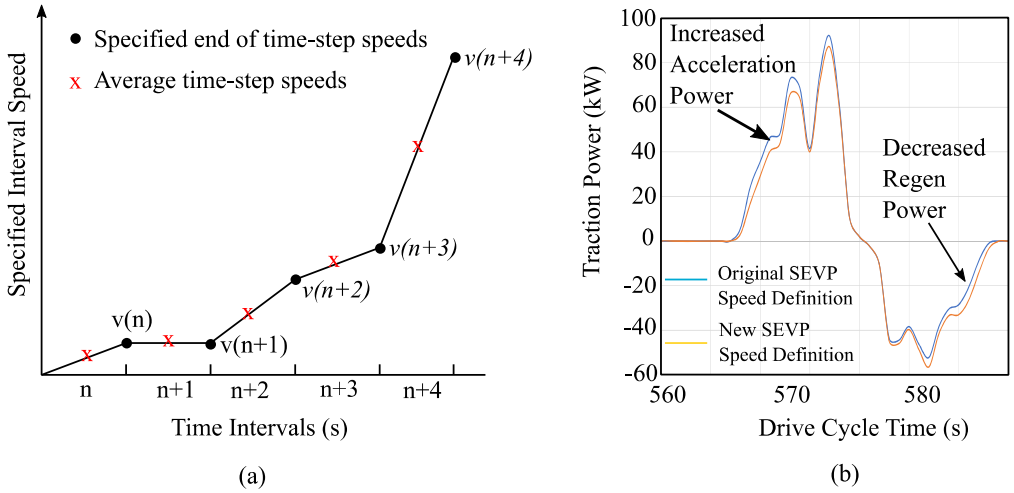

Figure 3-13. (a) Drive cycle time step speed definition and (b) impact on traction power in SEVP of assuming drive cycle speed is achieved at midpoint instead of at the end of the time step.

3.4.4.3 Tractive Effort-Alternative Calculation Procedure

For both the BMW i3 and the eGolf, the positive tractive effort energy required for motoring was combined with the negative tractive effort energy recovered during braking to get a net traction effort energy requirement for each drive cycle. When the net tractive effort energy is divided by the ANL measured net energy consumption in a drive cycle, the average powertrain efficiency required for a given drive cycle is obtained. In the SEVP simulator, the net tractive effort energy was first calculated using the ANL coast-down coefficients and using the new averaged interval speeds. Then it was recalculated using the standard equations used in the ADVISOR and

FASTSim simulators. The resultant net tractive effort energies and the required powertrain efficiencies are presented in Table 3-9.

This analysis shows that the required powertrain efficiencies of the BMW i3 would need to be 73% in the UDDS, 93% in the HWFET and 88% in the US06 to achieve the measured ANL net battery energy consumption. The optimum powertrain efficiencies observed across all three simulators to achieve best accuracy were approximately 60% in the UDDS and 80% in the other two drive cycles. The corresponding eGOLF required powertrain efficiencies were 85% (UDDS), 103% (HWFET) and 91% (US06).

As illustrated in Table 3-9, when the standard equation tractive effort calculation method of ADVISOR and FASTSim is used instead of the coast-down coefficients in the SEVP simulator, the required powertrain efficiency decreases significantly.

Table 3-9. Net tractive effort energy (Wh) and required powertrain efficiency (%).

	UDDS		**HWFET**		**US06**	
	Net Traction	**Powertrain Efficiency**	**Net Traction**	**Powertrain Efficiency**	**Net Traction**	**Powertrain Efficiency**
	2015 BMW i3					
SEVP (coast-down)	840	(72.5)	1780	(93.2)	1732	(87.7)
SEVP (Std. equations)	662	(57.2)	1444	(75.6)	1480	(74.9)
ANL Net Energy	**1158**		**1909**		**1976**	
	2015 eGolf					
SEVP (coast-down)	1069	(85.5)	2032	(103.5)	1890	(91.3)
SEVP (Std. equations)	691	(55.2)	1413	(71.9)	1409	(68.0)
ANL Net Energy	**1251**		**1964**		**2071**	

Table 3-10 summarises the impact on the net energy consumption in these two vehicles when : (i) the SEVP simulator uses the same end of interval definition of drive cycle speed as the other simulator and uses the average interval speed in the tractive effort calculation and (ii) uses the standard equation calculation method for tractive effort calculation. The previously observed significant overestimations in the BMW i3 and eGolf are then transformed to slight underestimations, using the standard equation tractive effort calculation equations.

Table 3-10. Net energy consumption estimation errors in SEVP simulator with different tractive effort calculation methods.

Tractive Effort Method	BMW i3			eGolf		
	UDDS	HWFET	US06	UDDS	HWFET	US06
Coast-down coefficients (initial)	25.3%	19.4%	18.2%	41.0%	23.0%	23.5%
Coast-down coefficients (ave. speed)	15.8%	18.6%	12.1%	30.5%	22.1%	16.6%
Standard Equations (ave. speed)	0.2%	0.3%	-1.1%	-0.7%	-11.3%	-7.7%

There is insufficient test data to identify why the coast-down coefficients produced results that were too high in these two vehicles. This study has shown that the use of the coast-down coefficients in vehicle simulators does not necessarily guarantee an accurate tractive effort estimation. However, the simulator comparison results summarised in Table 3-11 show that the SEVP simulator does provide the greatest number of accurate net energy consumption values when the coast-down method is used for the tractive effort calculation. The benefits of the coast-down method are enhanced when the two vehicles with least accurate coast-down coefficients are removed from this study giving a total of 24 tests instead of 30. The SEVP provides the best estimates of net energy consumption in 14 of the 24 tests.

Table 3-11. Simulator comparison based on number of tests where the optimum result is achieved.

Simulator	Initial Conditions	Redefined SEVP Vehicle Speeds	SEVP using Std equations for tractive effort	Exclude BMW i3 and eGolf tests
SEVP	9	15	9	14
FASTSim	8	7	9	6
ADVISOR	13	8	12	4

3.4.5 FASTSim Simulator Analysis

The FASTSim simulator results show a drive cycle dependency energy consumption pattern, with significantly lower powertrain efficiency in the UDDS drive cycle compared to that observed in the HWFET or US06 drive cycles. A typical FASTSim powertrain efficiency in the UDDS drive cycle is approximately 50%, while the equivalent SEVP efficiency is 65%. If the wheel slip and bearing friction model is excluded from the ADVISOR powertrain, its powertrain efficiency in the UDDS drive cycle is also in the 61% to 65% range.

Analysis of the FASTSim results for the ten vehicles shows that there is a correlation between the power-to-weight ratio (PWr) of the vehicle and the powertrain efficiency in the UDDS drive cycle. The highest powertrain efficiencies in FASTSim occur in vehicles with low PWr values due to the motor model used. This correlation results from the polynomial method used to estimate the losses in the motor-inverter model.

A normalised version of the polynomial is shown in Figure 3-11. As previously stated in Section 3.2.5.2, default efficiency values are applied at defined normalised output power operating points. A minimum efficiency of 30% occurs for operating powers near 0%, output power, and a user-defined peak efficiency occurs at 65% of the rated output power. The UDDS powertrain efficiency issue can be understood by examining the impact of the normalised loss curve for three of the test vehicles and their rated powers, the MiEV (49 kW), the 2013 Leaf (80 kW) and the BMW i3 (125 kW).

Traction effort in the UDDS drive cycle is largely determined by the mass of the vehicles, comprising 1304 kg (PWr 38), 1489 kg (PWr 53) and 1443 kg (PWr 87) respectively. The average motor output powers, in the UDDS drive cycle, for these three vehicles are 5.6 kW, 6.3 kW and 6.2 kW, respectively. As shown in Figure 3-11, the low PWr of the MiEV results in an average FASTSim motor-inverter efficiency of 80.5% while the higher PWr of the BMW i3 has an efficiency of only 72% in this FASTSim model.

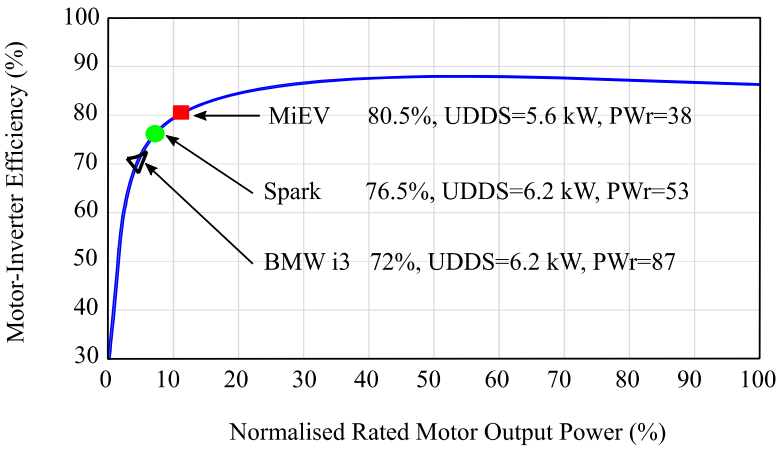

Figure 3-14. FASTSim motor-inverter efficiency with minimum 30% limit.

Increasing the minimum motor-inverter efficiency in FASTSim to 60% and the peak efficiency to 93% has the effect of lowering the efficiency difference in the UDDS cycle as shown in Figure 3-15. However, this results in an almost constant efficiency value in the motor-inverter model for most of the operating points of the BEV.

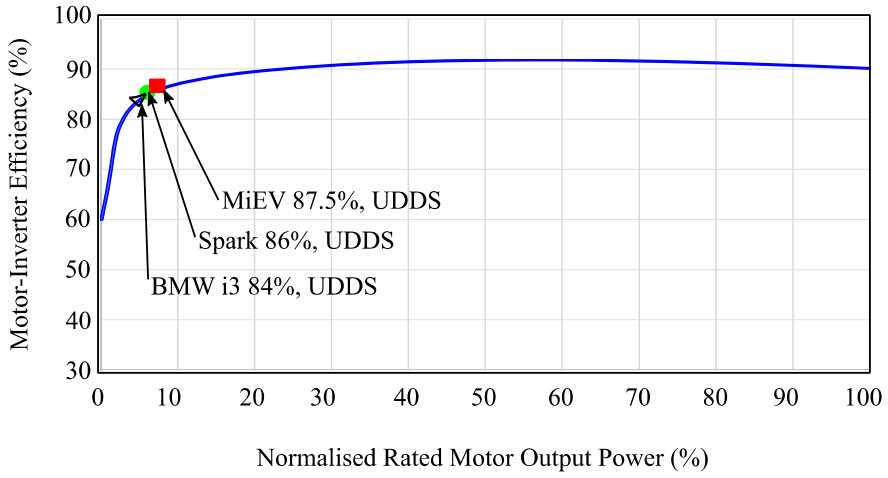

Figure 3-15. FASTSim motor-inverter efficiency with minimum 60% limit.

This analysis indicates that the polynomial approach in FASTSim for the motor-inverter loss model cannot be modified to accurately represent the ORNL efficiency map of a motor-inverter component, shown previously in Figure 3-6(a).

3.4.6 Impacts of P_{aux}, A_f, C_{rr} and Wheel Model on Results

The M-Sim provided the opportunity to simultaneously test the sensitivity of parameter changes across the three simulators. The four parameters investigated were, (i) auxiliary power levels, (ii) SAE frontal area profile factor, (iii) rolling resistance coefficient and (iv) the wheel slip and bearing friction model.

3.4.6.1 Impact of magnitude selected for constant load P_{aux}

The initial validation of the M-Sim assumed a constant auxiliary 200 W load at the battery terminals in all three simulators, as there was no published data on this

parameter. The actual value of auxiliary power was estimated using the high voltage battery power output when the vehicle was at zero speed. The UDDS drive cycle was used for this analysis as it contains a combined 259 s (19% of total time) of zero speed intervals. This analysis was conducted on all three UDDS tests carried out in the typical vehicle test schedule.

The impact of increasing the auxiliary power by 100 W, from 200 W to 300 W, is to increase the UDDS net energy consumption by 2.3% to 3.3%, with the smallest percentage increases recorded in the vehicles with the largest mass (kerb weight). The UDDS has a duration of 1370 s and the impact of the increased auxiliary power is lower in the shorter HWFET (765 s) at 0.9% to 1.2% and in the US06 (600 s) at 0.6% to 0.9%. Similar percentage changes were seen in all three simulators.

The M-Sim was retested with the average values of the actual auxiliary power levels derived from the ANL test data. Table 3-12 summarises the changes in the net energy consumption observed when actual P_{aux} values are applied. Significant changes of 4.6% to 7.3% were observed in the net energy consumption for the UDDS drive cycle for three test vehicles.

Table 3-12. Changes in net energy consumption when actual values of P_{aux} are applied.

Vehicle	ANL Tests P_{aux}	Changes in Net Energy Consumption (%)		
	Ave.	UDDS	HWFET	US06
Leaf 2012	224	0.6	0.2	0.2
Leaf 2013	400	**5.9**	2.0	1.5
MiEV	85	-3.5	-1.2	-0.9
Focus	380	**4.6**	1.7	1.2
BMW i3	190	-0.3	-0.1	-0.1
Smart	238	1.3	0.4	0.4
Soul	155	-1.3	-0.4	-0.3
Spark	435	**7.3**	2.8	2.0
eGolf	175	-0.7	-0.3	-0.2
B-class	280	1.8	0.7	0.6

With the actual auxiliary power included, the SEVP simulator achieved the closest net energy consumption values in 10 of the 24 tests (BMW i3 and eGolf excluded). The ADVISOR simulator achieved the closest net energy estimate result in 8 tests and the FASTSim simulator in 6 tests.

3.4.6.2 Impact of A_f Calculation

The SAE frontal area profile factors are commonly used in vehicle simulators to estimate the frontal area of a vehicle using the published vehicle's width and height dimensions. The default BEVs in ADVISOR and FASTSim use a profile factor of 0.8 and this factor was also applied to these simulators in M-Sim to determine the tractive effort associated with aerodynamic drag. The SEVP simulator uses the coast-down coefficients to estimate aerodynamic drag and is not included in this sensitivity analysis.

The profile factor was increased to 0.85 and percentage change in net energy consumption in each cycle was recorded. The typical UDDS net energy consumption increased by between 1.2% to 1.7%, HWFET net energy consumption by between 2.5% to 3.5% and US06 net energy by between 2.9% to 3.8%. This change improved the net energy consumption in six vehicles where ADVISOR and FASTSim had previous underestimated their energy consumption.

3.4.6.3 Impact of Selected C_{rr}

The rolling resistance coefficient C_{rr} is considered as a constant in both ADVISOR and FASTSim simulators. The M-Sim default C_{rr} value of 0.008 is a compromise between the 0.005 claimed for some BEV tyres and a typical C_{rr} value of 0.011 standard radial tyres [33].

The C_{rr} coefficient is a function of vehicle mass, tyre pressure and vehicle speed. The relationship with speed can be modelled as either a linear or a quadratic function. For this parameter sensitivity analysis, a linear function of C_{rr} to vehicle given in [34], was adapted for an average timestep speed v in m/s and is given as

$$C_{rr} = 0.008\left(1 + \frac{v}{44.704}\right) \tag{3.11}$$

A large impact on the net energy consumption, in the ADVISOR and FASTSim simulators in M-Sim, was observed with this parameter change. The UDDS energy consumption increased in the range of 9.6% to 11.1%; the HWFET energy consumption by 13% to 16.6% and the US06 energy consumption by 10% to 14%. The parameter change resulted in overestimation of net energy consumption in 22 out of 30 tests in FASTSim and 25 tests out of 30 in ADVISOR. In general, the increase

in net energy consumption appears to be too high in the UDDS and HWFET cycles using this linear variation of C_{rr}.

3.4.6.4 Impact of Wheel Model in Simulator

The final parameters to be analysed were the parameters of the wheel slip and bearing friction model in ADVISOR. Both SEVP and FASTSim simulators do not have a wheel model.

When the model is removed, the net energy reduced by -7.1% to -8.9% (average -7.7% reduction) in the UDDS drive cycle, by -5.5% to -7.0% (average -6.1% reduction) in the HWFET drive cycle and by -5.1% to -6.6% (average -5.7% reduction) in the US06 drive cycle. Most of this reduction relates to the removal of the bearing friction torque loss. The removal of the slip loss coefficient only resulted in a reduction of -1.4% in the net energy of the UDDS drive cycle, -0.5% reduction in the HWFET drive cycle and -1.6% reduction in the US06 drive cycle. Removing the complete component model from ADVISOR increased the underestimation of net energy in seven of the ten vehicles tested.

3.4.6.5 Summary of Impacts Analysed

This sensitivity analysis shows that: (i) accurate net energy consumption in city driving conditions, such as the UDDS drive cycle, requires an accurate estimate of the auxiliary power requirement; (ii) the variation of C_{rr} does not appear to be linear with speed and is lower than the doubling of the C_{rr} value at speeds of 161 kmph as predicted using (3.11); (iii) while both ADVISOR and FASTSim use the same equations (3.2) to calculate the vehicle's tractive effort, the high energy impact of the wheel slip and bearing friction model is only found in the ADVISOR powertrain. Removing this model increases the underestimation, indicating that the standard tractive effort equations as given in (3.2) will underestimate the energy consumption in the majority of BEVs.

3.5 Conclusions

In this chapter, three BEV powertrain simulators were analysed by combining their design methodologies into a single M-Sim MATLAB file. The results show that it is possible to replicate complex simulator powertrain models into a simple backward-facing approach, for BEV analysis. The educational advantage of this plug-and play simulator model is the in-depth understanding of the factors governing the energy consumption in BEV designs that allow a direct comparison of powertrain component models. Results show that the simplified parametric equations used for the SEVP motor-inverter models can achieve net energy consumption results that are comparable to both industry-standard simulators. The largest source of BEV simulation error is likely to occur from incorrect tractive effort determination. Testing a higher number of vehicles has highlighted that the use of coast-down coefficients to model traction effort does not guarantee improved precision in energy consumption estimation. The standard equation approach of (3.2) allows considerable flexibility to customise the parameters by experimentation, yielding educational value.

The M-Sim testing identified three issues that applied to all three simulators. First, the high impact of a relatively low change in auxiliary power during city driving conditions makes it very difficult to achieve high accuracy in energy consumption estimation without published data on this parameter for each vehicle. Second, the regenerative models, based on a speed function, have very little impact on the net energy consumption and in older BEV models, they should be replaced with a model based on acceleration rate. The latest versions of BEV designs achieve close to 100% regenerative braking. Third, vehicles with low PWr require a simulator with powertrain component limits and the implementation of these limits requires both backward-facing and forward-facing calculation paths to estimate achieved vehicle speed in each timestep of the drive cycle.

The M-Sim testing identified that the simple power-polynomial approach to modelling the motor-inverter losses in the BEV powertrain, as implemented in the FASTSim simulator, oversimplifies the efficiency of a typical BEV motor and results in excessive losses in city driving conditions. Generating the polynomial with a higher minimum efficiency improved the simulator's accuracy but leads to a component model that approaches an oversimplified constant-efficiency model. The SEVP motor-

inverter models with parametric equations, produce an efficiency map that better correlates to the measured ORNL data than the FASTSim polynomials.

Chapter 4 reviews and develops battery models for BEVs that can be integrated into vehicle simulators to widen their application areas and improve their education value for electrical engineering studies.

3.6 References.

[1] Argonne National Laboratory, Energy Systems Division, “Downloadable Dynamometer Database.” [Online]. Available: https://www.anl.gov/es/downloadable-dynamometer-database. [Accessed: 10-Jul-2020].

[2] K. Davis and J. G. Hayes, "Analysis of electric vehicle powertrain simulators for fuel consumption calculations," *2016 Int. Conf. on Electrical Systems for Aircraft, Railway, Ship Propulsion and Road Vehicles & Int. Transportation Electrification Conf. (ESARS-ITEC)*, Toulouse, 2016, pp. 1-6, doi: 10.1109/ESARS-ITEC.2016.7841414.

[3] J. Van Roy, N. Leemput, S. De Breucker, F. Geth, P. Tant, and J. Driesen, “An availability analysis and energy consumption model for a Flemish fleet of electric vehicles,” *Eur. Electr. Veh. Congr. EEVC*, Brussels, Belgium, 2011, pp. 1–12.

[4] R. Maia, M. Silva, R. Araújo and U. Nunes, "Electric vehicle simulator for energy consumption studies in electric mobility systems," *2011 IEEE Forum on Integrated and Sustainable Transportation Systems*, Vienna, 2011, pp. 227-232, doi: 10.1109/FISTS.2011.5973655.

[5] Y. Chen, G. Wu, R. Sun, A. Dubey, A. Laszka, and P. Pugliese, “A review and outlook of energy consumption estimation models for electric vehicles,” published online (https://arxiv.org/abs/2003.12873), arXiv.2003.12873V2 [eess.SY], 28 March 2020.

[6] K. Liu, T. Yamamoto, and T. Morikawa, “Impact of road gradient on energy consumption of electric vehicles,” *Transp. Res. Part D Transp. Environ.*, vol. 54, pp. 74–81, July 2017, doi: 10.1016/j.trd.2017.05.005

[7] X. Wu, D. Freese, A. Cabrera, and W. A. Kitch, “Electric vehicles’ energy consumption measurement and estimation,” *Transp. Res. Part D Transp. Environ.*, vol. 34, pp. 52–67, January 2015, doi: 10.1016/j.trd.2014.10.007.

[8] M. Amrhein and P. T. Krein, "Dynamic simulation for analysis of hybrid electric vehicle system and subsystem interactions, including power electronics," *IEEE Transactions on Vehicular Technology*, vol. 54, no. 3, pp. 825-836, May 2005, doi: 10.1109/TVT.2005.847231.

[9] C. C. Chan, A. Bouscayrol and K. Chen, "Electric, hybrid, and fuel-cell vehicles: Architectures and modeling," *IEEE Trans. on Vehicular Technology*, vol. 59, no. 2, pp. 589-598, Feb. 2010, doi: 10.1109/TVT.2009.2033605.

[10] C. Dépature, S. Jemeï, L. Boulon, A. Bouscayrol, N. Marx, and S. Morando, "IEEE VTS Motor Vehicles Challenge 2017 - energy management of a fuel cell/battery vehicle," *2016 IEEE Vehicle Power and Propulsion Conf. (VPPC)*, Hangzhou, 2016, pp. 1-6, doi: 10.1109/VPPC.2016.7791701.

[11] C. Depature, S. Pagerit, L. Boulon, S. Jemei, A. Rousseau and A. Bouscayrol, "IEEE VTS Motor Vehicles Challenge 2018 - energy management of a range extender electric vehicle," *2017 IEEE Vehicle Power and Propulsion Conf. (VPPC)*, Belfort, 2017, pp. 1-6, doi: 10.1109/VPPC.2017.8330993

[12] C. Marmaras, E. Xydas, and L. Cipcigan, “Simulation of electric vehicle driver behaviour in road transport and electric power networks,” *Transp. Res. Part C Emerging Technologies*, vol. 80, pp. 239–256, July 2017, doi: 10.1016/ j.trc.2017.05.004.

[13] B. Luin, S. Petelin, and F. Al-Mansour, “Microsimulation of electric vehicle energy consumption,” *Energy*, vol. 174, pp. 24–32, 1 May 2019, doi: 10.1016/ j.energy.2019.02.034

[14] C. Fiori, K. Ahn, and H. A. Rakha, “Power-based electric vehicle energy consumption model: Model development and validation,” *Appl. Energy*, vol. 168, pp. 257–268, 15 April 2016. doi: 10.1016/j.apenergy.2016.01.097

[15] T. Markel, A Brooker, T. Hendricks, V. Johnson, K. Kelly, B. Kramer, M.O’Keefe, S. Sprik, and K.Wipke, “ADVISOR : a systems analysis tool for advanced vehicle modeling,” *J. Power Sources,* vol. 110, no. 2, pp. 255–266, 22 August 2002, doi: 10.1016/S0378-7753(02)00189-1.

[16] A. Brooker, J. Gonder, L. Wang, E. Wood, S. Lopp, and L. Ramroth, “FASTSim : A model to estimate vehicle efficiency , cost and performance,” *SAE World Congress and Exhibition*, Detroit, MI., USA, 2015, pp.1-12, doi: 10.4271/2015-01-0973

[17] J.G. Hayes, R.P.R. de Oliveira, S. Vaughan and M. G. Egan, "Simplified electric vehicle power train models and range estimation," *2011 IEEE Vehicle Power and Propulsion Conf.(VPPC)*, Chicago, IL, 2011, pp. 1-5, doi: 10.1109/ VPPC.2011.6043163.

[18] United States Environmental Protection Agency, *Annual certification data for Vehicles, Engines and Equipment*, [Online]. Available: https://www.epa.gov/compliance-and-fuel-economy-data [Accessed: 10-Jul-2020].

[19] J. G. Hayes and K. Davis, "Simplified electric vehicle powertrain model for range and energy consumption based on EPA coast-down parameters and test validation by Argonne National Lab data on the Nissan Leaf," *2014 IEEE Transportation Electrification Conf. and Expo (ITEC)*, Dearborn, MI, 2014, pp. 1-6, doi: 10.1109/ITEC.2014.6861831.

[20] J. G. Hayes, "Simplified electric vehicle models for use in undergraduate teaching and research," *2014 IEEE Energy Conversion Congress and Exposition (ECCE)*, Pittsburgh, PA, 2014, pp. 1271-1277, doi: 10.1109/ECCE.2014.6953547.

[21] AVL List GmbH, “AVL Cruise” [Online]. Available: https://www.avl.com/cruise. [Accessed: 10-Jul-2020].

[22] Argonne National Laboratory , “Autonomie”, [Online]. Available: https://www.autonomie.net/. [Accessed: 10-Jul-2020].

[23] *Road Load Measurement and Dynamometer Simulation using Coastdown Techniques*, J1263, SAE International, 2010.

[24] Argonne National Laboratory, Energy Systems Division, “Downloadable Dynamometer Database.” [Online]. Available: https://www.anl.gov/es/downloadable-dynamometer-database. [Accessed: 10-Jul-2020].

[25] A. Brooker, K. Haraldsson, T. Hendricks, V. Johnson, K. Kelly, B. Kramer, T. Markel, M. O’Keefe, S. Sprik, K. Wipke, M. Zolot, *ADVISOR Documentation*, Available: http://adv-vehicle-sim.sourceforge.net/ [Accessed 25-Nov-2020].

[26] J. Larminie and J. Lowry, *Electric Vehicle Technology Explained*, 1st ed. Chichester, West Sussex, UK: Wiley, 2003.

[27] K. Michaelis, B. R. Höhn, and M. Hinterstoißer, “Influence factors on gearbox power loss,” *Ind. Lubr. Tribol.*, vol. 63, no. 1, pp. 46–55, 2011, doi: 10.1108/00368791111101830

[28] A. Grunwald, B. James, “System approach to consider efficiency, NVH, and durability in the optimization of an electric all wheel drive gearbox,” *Vehicle Concept Modelling in Automotive Sector,* Brussels, 2011.

[29] T. Hofman and C. H. Dai, "Energy efficiency analysis and comparison of transmission technologies for an electric vehicle," *2010 IEEE Vehicle Power*

and Propulsion Conf.(VPPC), Lille, 2010, pp. 1-6, doi: 10.1109/ VPPC.2010.5729082.

[30] L. A. M. Van Dongen, "Efficiency characteristics of manual and automatic passenger car transaxles," *SAE Trans.*, vol. 91, pp. 2498-2509, January 1982.

[31] T. A. Burress, "Benchmarking of competitive technologies 2012 Nissan LEAF," Oak Ridge National Laboratory (ORNL), Presentation at US DOE Hydrogen and Fuel Cell Peer Evaluation Meeting, May 2012.

[32] R. Abousleiman and O. Rawashdeh, "Energy consumption model of an electric vehicle," *2015 IEEE Transportation Electrification Conf. and Expo (ITEC)*, Dearborn, MI, 2015, pp. 1-5, doi: 10.1109/ITEC.2015.7165773.

[33] R. Bosch GmbH, *Bosch Automotive Handbook*, 10th ed., Chichester, West Sussex, UK: Wiley, 2018.

[34] T. D. Gillespie, *Fundamentals of Vehicle Dynamics*, 1st ed., Warrendale, PA, USA: Society of Automotive Engineers, 1992.

4 BATTERY MODELLING

As identified in Chapter 2, electrical circuit simulation with the simplified electric vehicle powertrain (SEVP) model requires a comprehensive battery model. In this chapter the Li-ion battery models are expanded as equivalent-electrical-circuits (EEC), consisting of a voltage-source model coupled to an internal-impedance network model. The voltage-source models are developed using battery electric vehicle (BEV) discharge test data from INL. Four existing battery models, Matlab, Tremblay, Log-Linear-Exponential and Polynomial models, are compared to the INL test data. Then, based on this test data, a new simplified empirical Li-ion voltage-source model is proposed. It is shown that the steady-state performance of voltage-source models enables a virtual fuel gauge for a BEV simulator to be constructed. Next, the dynamic performance of the Li-ion battery models, with two different internal-impedance models, is tested and validated utilising dynamometer test data from ANL. Finally, an adaptation of the battery models is proposed to factor in a capacity reduction over the lifetime of the vehicle, implemented by a basic ageing model, derived from the battery warranty conditions. This Chapter is an expanded version of an IEEE ECCE conference paper, published in 2020 [1].

4.1 Introduction

Battery modelling is a vast and complex research topic, covering numerous battery chemistries, with non-linear characteristics and with changes in these characteristics as a function of time or as a function of environmental conditions. Comprehensive reviews of all aspects of battery models can be found in [2], [3]. The modeling approach is highly dependent on the application area for the battery model. Battery models in electric vehicles can be classified by the modelling approach taken, e.g. electrochemical, mathematical, and EEC models; or by the end application requirement such as state-of-charge (SOC) and state-of-health (SOH) estimations and battery-management-systems (BMS) development. The high-fidelity physics-based electrochemical models can produce accurate results but are not suitable for real-time applications due to their long simulation times. Mathematical models, in the form of analytical or stochastic models, can provide fast and accurate results when modelling the dynamic changes with the battery. EEC battery models are suitable when the battery is a component of a larger electrical circuit system simulation. The required lifetime of batteries in BEV applications is in excess of 10 years. The development of accurate BEV battery pack models is impeded by the difficulty in measuring internal battery parameter changes over this lifetime and the rapid change in battery technology in BEV applications [4]-[6].

The study of battery models in vehicle simulators has a narrower focus and tends to consider either models constructed as ideal power sources or as EEC models. Vehicle simulators that are principally concerned with the calculation of the energy consumption, typically adopt an ideal power source as a battery model. These models do not consider the change in voltage associated both with the charge/discharge power levels and with the level of charge remaining in the battery. Vehicle simulators such as FASTSim [7], SEVP [8] and VT_CPEM [9] utilise ideal power sources as battery models. These approaches do not provide the electrical circuit data required for electrical simulation of the BEV powertrain components and for identifying the performance constraints of the vehicle.

The alternative EEC models represent the battery as a charge-dependent voltage source with an internal-impedance network modelled as either a single resistor or as a more complex Thevenin circuit. Two widely used vehicle simulators, Advisor [10] and Autonomie [11], provide a variety of EEC models for vehicle batteries. However, EEC

battery models require detailed battery information for BEVs which is difficult to obtain because of the proprietary nature of BEV battery technologies. Fortunately, INL and the Centre for Evaluation of Clean Energy Technology has carried out battery testing on a wide range of hybrid-electric vehicles (HEVs) and BEVs in Phoenix, Arizona [12]. A sample of the INL published test data is presented in Figure 4-1.

Manufacturer: AESC	Rated Pack Energy/Capacity: 24.0 kWh/66.2 Ah
Type: Lithium-ion	Min / Max Cell Voltage: 2.50/4.20 V
Number of Cells: 96	Pack Mass/Volume: 290.3 kg / 350.6 L
Nominal Cell/System Voltage: 3.8/360V	Thermal Management:Passive

(a) Battery Pack Specification

Test Number	Vehicle Odometer (miles)	Date of Test	Measured Average Capacity (Ah)	Measured Average Energy Capacity (kWh)	30 s Discharge Power Capability at 80% DOD (kW)	10 s Charge Power Capability at 20% DOD (kW)
Begining-of-Life (BOL)	493	2/14/2014	67.1	24.6	233.3	60.9
ICD 1	5,154	5/10/2014	64.4	23.6	223.2	67.7
ICD 2	15,326	4/22/2015	56.2	20.6	103.5	83.6
ICD 3	24,039	8/15/2016	49.4	17.9	NA	85.6

(b) Battery Test Results Summary

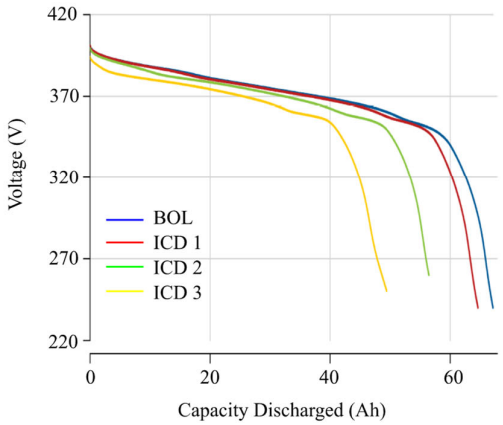

(c) Static Capacity Test Results

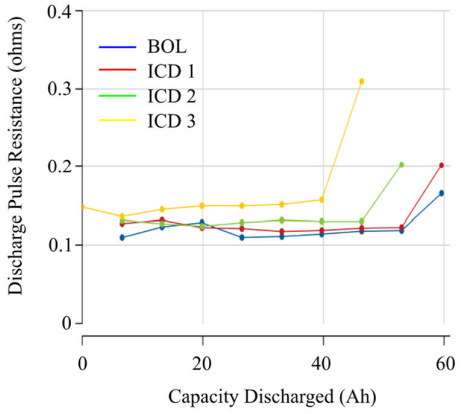

(d) 30 s Discharge Resistances

Figure 4-1. Sample of Published INL Data on 2013 Nissan Leaf Battery Pack [12].

In addition to their published test data, INL provided this research study with detailed battery test data files in Excel file format that enabled the reproduction of the discharge curves observed in Figure 4-1(c). The test data covers eight versions of BEVs as summarised in Table 4-1. For each version of vehicle, up to four different battery packs were repeatedly tested at intervals based on odometer readings. An

insight into the 2015 version of Tesla batteries can also be gained as Tesla provided the powertrain components to one of the vehicles in this study, the Mercedes B-class.

Table 4-1. Vehicles and battery packs [12].

Vehicle Manufacturer	Version	Year	Electrode	Series Cells	Battery Manufacturer
Ford	Focus EV	2013	LMO	86	LG Chem
Nissan	Leaf	2013	LMO	96	AESC
Smart	Fortwo	2014	LMO	93	ACCmotive
BMW	i3	2014	NMC	96	SDI
Chevrolet	Spark	2015	NMC	96	LG Chem
Volkswagen	e-Golf	2015	NMC	88	Sanyo
Kia	Soul	2015	NMC	96	SK
Mercedes	B-class	2015	NCA	84	Tesla

Periodic test data recorded at various odometer readings, starting with a beginning of life (BOL) test after 640 km, provide some understanding of the effect of ageing on battery pack capacity and of how this ageing impacts a battery model. ANL dynamometer tests [13] on these vehicles provides the data on the dynamic response of the batteries required to select the internal network component values. ANL testing also provides the operational voltage limits imposed by the battery management systems in each BEV. Combining the INL test data with the results of an examination of the dynamometer test data, for the same vehicles, provides comprehensive insights into Li-ion battery pack operational specifications as shown in Table 4-2.

Table 4-2. BEV Battery pack operational specifications [12],[13].

Parameter		Focus	Leaf	Fortwo	BMW i3	Spark	e-Golf	Soul	B-class
Rated Energy	(kWh)	23	24	17.6	18.8	18.4	24	27	28
Rated Capacity	(Ah)	75	66.2	52	60	52	75	75	93
*640 km Capacity Test	(Ah)	74.8	66	52.2	59.9	50.8	73.9	85.4	113.3
*6400 km Capacity Test	(Ah)	71.6	62.2	51	58.2	49.1	70.7	82.9	109.6
*19300 km Capacity Test	(Ah)	67.1	54.2	49.7	55.1	46.8	67.8	76.5	106.2
Maximum Voltage	(V)	359	400	388	391	396	359	411	341
Minimum Voltage	(V)	262	291	283	289	293	268	289	253
*Pack Resistance R_{BP}									
discharge	(mΩ)	85	130	175	130	130	80	100	125
charge	(mΩ)	65	100	140	110	100	70	70	120
Cells in series		86	96	93	96	96	88	96	84
Maximum cell voltage	(V)	4.17	4.17	4.17	4.07	4.13	4.08	4.28	4.06
Minimum cell voltage	(V)	3.05	3.03	3.04	3.01	3.05	3.05	3.01	3.01
Nominal cell voltage	(V)	3.7	3.7	3.7	3.7	3.7	3.7	3.7	3.6
Average vehicle consumption, E_{VEH} (Wh/km)		178	175	148	162	151	174	159	178

*Averaged test values for up to four battery packs tested by INL for each vehicle version.

The chapter is organized as follows: Section 4.2 reviews various options for EEC battery model development: Section 4.3 validates four empirical battery voltage modelling techniques with the INL test data and proposes a new generic Li-ion voltage model: Section 4.4 presents the conversion of a battery voltage model to a virtual fuel gauge for a vehicle simulator: Section 4.5 evaluates the impact of the choice of internal network on the dynamic performance of the battery models in HEVs and BEVs: Section 4.6 proposes an adaptation of the battery model, to include a reduced fully-charged battery capacity due to battery ageing which then allows simulation over the vehicle's lifetime: The study conclusions are presented in Section 4.7.

4.2 Equivalent Electrical Circuits for Battery Models

In EEC models, the battery terminal voltage is a non-linear function of the battery's capacity where the capacity is frequently normalized to a state-of-charge (SOC) value or a depth-of-discharge (DOD) value. The terminal voltage also depends on the voltage drop across the internal network. As the battery ages, the battery capacity reduces, or fades, which alters the open-circuit-voltage (OCV) relationship to the original rated battery capacity. This section reviews the battery terminal voltage function and the choices for the internal networks for EEC models. The model is adapted for reduced battery capacity over the lifetime of the vehicle in Section 4.5.

The OCV-to-capacity relationship is largely dependent on the battery's chemistry. For BEV and HEV applications, the dominant battery chemistry is Li-ion. But Li-ion battery technology is not homogenous and an analysis of the structure of the BEV Li-ion batteries by INL shows that their cathodes were made from either nickel-manganese-cobalt (NMC), lithium-manganese-dioxide (LMO) or nickel-cobalt-aluminium (NCA). Figure 4-2 illustrates the significant differences in the discharge voltage profiles for various Li-ion batteries. Even within a subcategory of Li-ion such as LMO types, significant differences can be seen in the voltage profiles as shown in Figure 4-2(a) for the Leaf, Focus and Fortwo vehicles. For comparability, normalised discharge curves are presented in Figure 4-2(b).

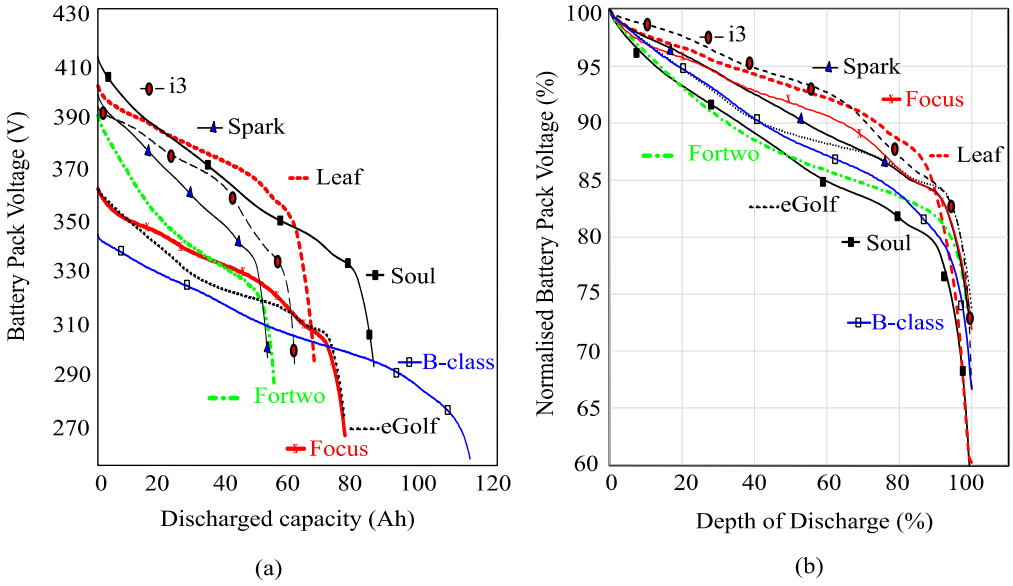

Figure 4-2. Discharges profiles (a) BOL test result values and (b) normalised test values.

The characteristics of each of these discharge profiles can be classified by defining three zones on the discharge profiles as shown in Figure 4-3. The voltage profile is typically generated during a constant-current discharge test, with a test current i_T equal to either one third of the *C* rate of the battery for INL testing of BEVs, or equal to the *C* rate for the INL testing of the lower capacity HEV's battery packs.

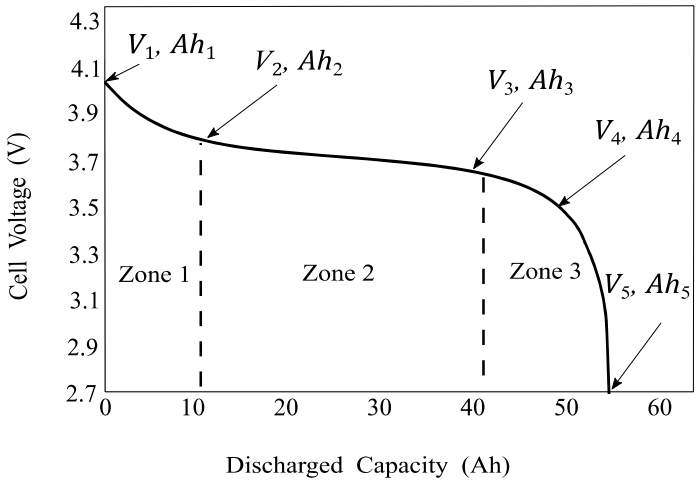

Figure 4-3. Li-ion cell voltage profile zone classification.

As discussed in [14], an initial activation polarization voltage drop is modelled using an exponential or a logarithmic equation in Zone 1; Zone 2 shows an ohmic quasi-linear voltage drop, while a concentration polarization voltage drop is characterized by an exponential decrease in terminal voltage as the battery is fully discharged in Zone 3. The knee point on the discharge curve is defined by the battery terminal voltage, V_4 , and by the ampere-hour (Ah) discharged capacity, Ah_4.

The choice of function to model the battery voltage profile depends on the application of the battery within the vehicle. Simple linear voltage functions can characterize the OCV to capacity profile in some alternative-fueled vehicles such as HEVs and fuel cell electric vehicles (FCEV), where the battery is a secondary energy source, typically with low energy capacities [15]. In such vehicles, the battery has a short-term dynamic role in vehicle operation, charging at high *C* rates during regenerative braking and discharging at equally high *C* rates as the vehicle accelerates. The lifetime of the battery is extended by limiting the operating SOC range to the quasi-linear region (Zone 2 of Figure 4-3) of the profile. With a limited operational

range from 20% to 80% SOC, a linear equation can be used to represent the OCV-capacity relationship in these vehicles [8],[14].

However, in a BEV, the battery is the sole energy source and the maximum driving range is achieved by utilising the full capacity of the battery which effectively means operating in all three zones of Figure 4-3. The BEV battery OCV-capacity profile may be represented as a look-up table (LUT), as a higher-order polynomial, or as a set of equations, with one equation for the dominant electrochemical process at each stage of a discharge [16]-[18]. In high-level simulators such as ADVISOR and Autonomie, all their battery models' OCV-DOD profiles are implemented using LUTs.

Once the OCV-capacity relationship is established, the choice of internal impedance network determines the dynamic performance of the model. Figure 4-4 illustrates two possible models for the internal network: (a) a single resistor R_{INT} and (b) a Thevenin circuit.

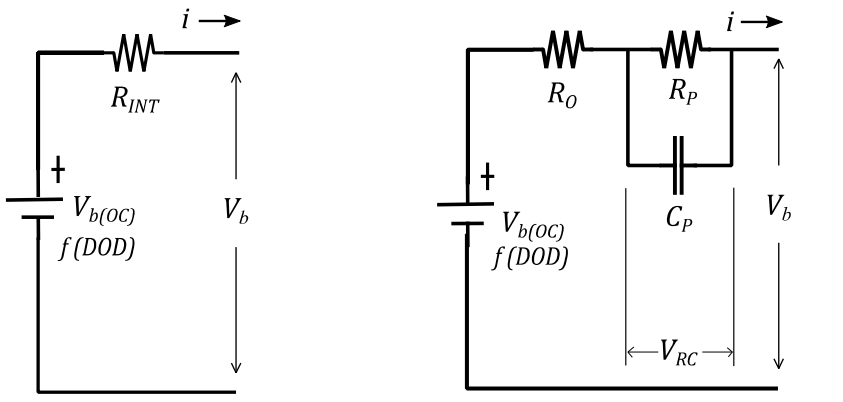

(a) Simple resistor internal impedance.

(b) Thevenin circuit internal impedance.

Figure 4-4. Battery model with (a) R_{INT} and (b) Thevenin internal networks.

In simple EEC models, the internal voltage drop is modelled as a single resistance R_{INT} which can either have a fixed value or a variable value that is a function of the battery condition. Battery testing shows that R_{INT} varies with SOC [19], with temperature, and with battery age [20], which implies reduced accuracy in estimating the internal voltage drop with models utilizing fixed R_{INT} values. But in vehicle simulators, the choice of fixed or variable value R_{INT} is somewhat dependent on the type of vehicle being simulated. For HEV and FCEV simulations, short-duration high *C* rate current pulses result in relatively high voltage drops across the internal network.

These internal voltage drops represent a significant portion of the operating voltage range (Zone 2 of Figure 4-3). High accuracy in modelling the internal network of the battery is required in these vehicles. In contrast, BEV batteries have higher nominal voltages (360 V-370 V), with capacities that are 10 to 50 times higher than HEV batteries. These higher capacities result in current pulses with lower *C* rates. The internal voltage-drop in a BEV battery, under most driving conditions, is relatively small compared to the BEV operating voltage range. Under these circumstances, a fixed-value R_{INT} may provide sufficient accuracy for BEV applications [21]-[23]. This dependency of internal circuit choice on vehicle type is examined further in Section 4.5.1

Figure 4-5 illustrates the voltage drop profile produced during standard Hybrid Pulse Power Characterization (HPPC) tests on batteries [24], [25]. The HPPC test involves discharging the battery using a high-power constant-current pulse. The terminal voltage is measured before and during the pulse to estimate the internal impedance of the battery. The Thevenin circuit of Figure 4-4(b) produces a time-dependent non-linear internal voltage-drop that is consistent with HPPC test results. The time-dependent voltage-drop results from an initial low polarization resistance for charge near the electrodes and is followed by a gradual increase in polarization resistance as the surface charge is depleted. This time-dependent voltage-drop can be modelled using Thevenin circuits which include an ohmic resistance R_o due to the resistance of the ohmic contacts in the battery, connected in series with parallel-connected resistor-capacitor (RC) components. The parallel components comprise a polarization resistance R_P due to chemical polarization, and a polarization capacitor, C_P. This Thevenin circuit provides a first-order response at the battery terminals. Higher-order responses are achieved by adding further parallel RC networks in series with R_o [26],[27]. The calculation of the internal network component values is determined by a HPPC test which measures the voltage change when a constant amplitude current pulse, with a duration of between 10 to 30 seconds, is discharged from the battery [28], [29]. The transient response measured determinates the polarization components R_P, C_P. The simple model resistor R_{INT} is the sum of R_o and R_P estimated from the long-duration current pulse as shown in Figure 4-5.

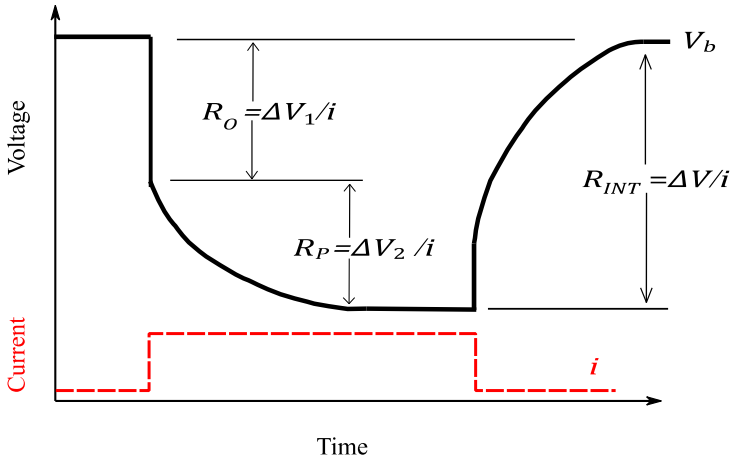

Figure 4-5. Characteristic HPPC discharge current pulse to estimate internal resistance.

The EEC battery models in the Advisor and Autonomie vehicle simulators utilize both types of internal networks. Each Advisor battery model uses LUTs to vary the internal network component values based on the battery SOC. Autonomie implements similar battery models to Advisor and it further includes an additional Thevenin circuit model called a Partnership-for-a-New-Generation-of-Vehicles (PNGV) model [30]. Several studies of low energy capacity batteries, under high *C* rate current conditions, opt for a Thevenin circuit internal network in their battery models [16], [31]. The dynamic performance of the EEC battery models for the eight vehicles tested by INL is discussed in Section 4.5 of this chapter.

4.3 Empirical Li-ion Battery Voltage Models

This section investigates various battery models. Four well-known models are validated against the INL test data in terms of R^2 value and rms error voltage per cell. An enhancement is proposed for the Tremblay model to improve its accuracy. A novel simplified generic model is proposed for use in vehicle simulators. All of the models are evaluated under steady-state constant-current discharge conditions in this section.

4.3.1 MATLAB Simple Generic Battery Voltage Model

The 2017b version of MATLAB provides a simple generic battery model [32]. The model is defined by the nominal battery voltage V_{nom}, one point on the discharge profile and the battery's SOC. The MATLAB model determines the battery terminal voltage V_b using

$$V_b = V_{nom}\left[1 - \left(\frac{\alpha_{mat}(1 - SoC)}{\left(1 - \beta_{mat}(1 - SoC)\right)}\right)\right] - R_{INT}i \tag{4.1}$$

where α_{mat} and β_{mat} are curve-fit constants selected to fit the defined discharge data point, and i is the discharge current. As the procedure assumes that V_b is zero when the SOC is zero, it follows that the sum $\alpha_{mat} + \beta_{mat} = 1$. The maximum battery voltage of the Matlab model is the specified nominal battery voltage. The sharp curve at the knee voltage is realised with high values of β_{mat} , but this also results in a near constant battery voltage above the knee-voltage point. This model is plotted in Figure 4-6 in a comparison with INL discharge curve data on the Chevy Spark BEV. As can be seen, this battery model resulted in large errors.

These errors result from (i) the large difference between the nominal (3.7 V) and the maximum voltages (up to 4.28 V) in BEV Li-ion cells, and (ii) the modelling assumption that the battery voltage is zero at 0% SOC (100% DOD). As the resulting voltage profile does not perform well in comparison to the INL test voltage profiles, the MATLAB model was not appraised further in this study. The latest version of MATAB has replaced this simple battery model with a generic battery model based on the Tremblay model [33].

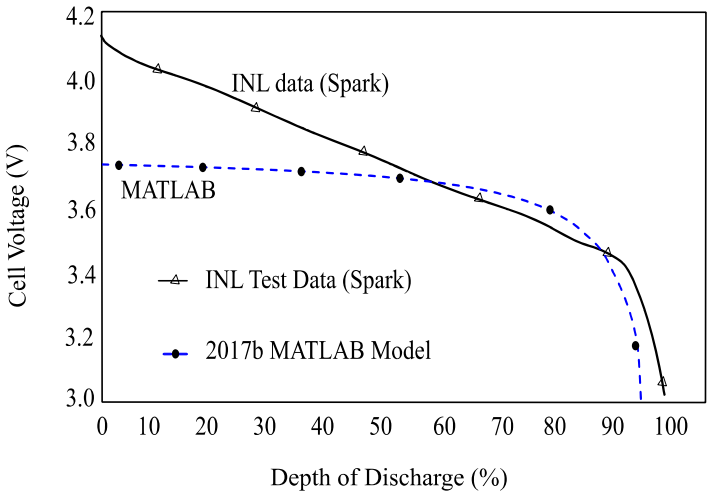

Figure 4-6. 2017b MATLAB model comparison with Chevy Spark discharge data from INL.

4.3.2 Tremblay Battery Voltage Model

The Tremblay battery model [34], [35] is widely referenced in the literature [21], [36]-[38] and is based on Shepherd's equation for battery discharge voltage estimation [39]. The resultant battery voltage is determined using

$$V_b = E_O + A_{tre}e^{(-B_{tre}Ah_x)} - K_{tre}\left[\frac{Ah_{FC}}{(Ah_{FC} - Ah_x)}\right] - R_{INT}i \tag{4.2}$$

where E_O is a derived battery voltage constant, A_{tre} and B_{tre} are empirical constants selected to define the initial exponential voltage drop, K_{tre} is an empirical constant relating the quasi-linear ohmic voltage drop, Ah_{FC} is the fully-discharged capacity (Ah), and Ah_x is the discharged capacity (Ah), from the fully-charged state, at any specified point x. Figure 4-7 illustrates the parameters of the Tremblay equation. The empirical constants are determined from the discharge curve in Figure 4-7; A_{tre} is the voltage drop from V_1 to V_2 while B_{tre} is given as $3/Ah_2$. The value of K_{tre} is derived by assuming $V_b = V_1$ at $t = 0$ and subtracting the known $V_b = V_3$ from V_1. Once K_{tre} is derived, E_O is then determined by substitution. This procedure results in a voltage-source discharge with a Zone 1 exponential voltage drop given by the $A_{tre}e^{(-B_{tre}Ah_x)}$ term, with a relatively flat Zone 2 and with a Zone 3 voltage drop given by the $Ah_{FC}/(Ah_{FC} - Ah_x)$ term.

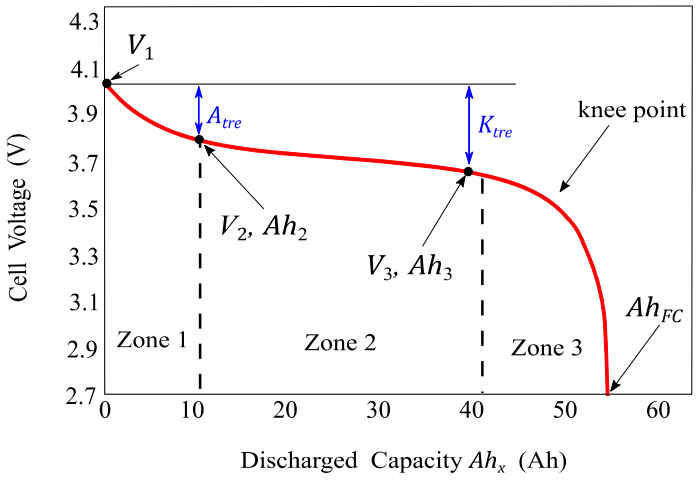

Figure 4-7. Tremblay model parameters.

A standard Tremblay model with parameters, calculated using the previously described procedure, and a "Modified-Tremblay" model, calculated with a modified procedure, are both plotted in Figure 4-8 in a comparison with INL discharge curve data on the Chevy Spark BEV. The Tremblay battery model results in a voltage-discharged capacity relationship with a long flat Zone 2 region, as seen in Figure 4-8, and had a very high roll-off above the knee voltage. Low R^2 values were achieved which ranged from 0.403 to 0.881 and the typical rms voltage error was high (0.25 V/cell, equivalent to a 6.8 % error). Given that the operational voltage range from minimum to maximum cell voltage is 3 V to 4.13 V, a 0.25 V modelling error is equivalent to a very high 23% error for this operational-voltage range.

4.3.2.1 Modified Tremblay Model

This error in the standard Tremblay model is now reduced by modifying the Tremblay coefficient calculation procedure. The adapted model is shown in Figure 4-8 as a "Modified-Tremblay" model. This modified version of the Tremblay model achieved improved R^2 values, ranging from 0.739 to 0.967 and typical rms voltage errors of 0.08 V/cell.

The improvement is best explained by a further detailed examination of the terms in the original Tremblay model. In (4.2), the influence of the $A_{tre}e^{(-B_{tre}Ah_x)}$ term on the voltage profile is restricted to the initial activation polarization region as $A_{tre} = (V_1 - V_2)$ and $B_{tre} = 3/Ah_2$. The second term $K_{tre}[Ah_{FC}/(Ah_{FC} - Ah_x)]$ is

required to model both the ohmic quasi-linear and the concentration polarization voltage drops. Increasing the value of K_{tre} improves the quasi-linear voltage drop but results in a premature knee point occurring at a higher battery voltage. In the Modified-Tremblay, the influence of the first term is extended into the quasi-linear region by redefining the coefficients as $A_{tre} = (V_1 - V_3)$ and $B_{tre} = 2/Ah_3$.

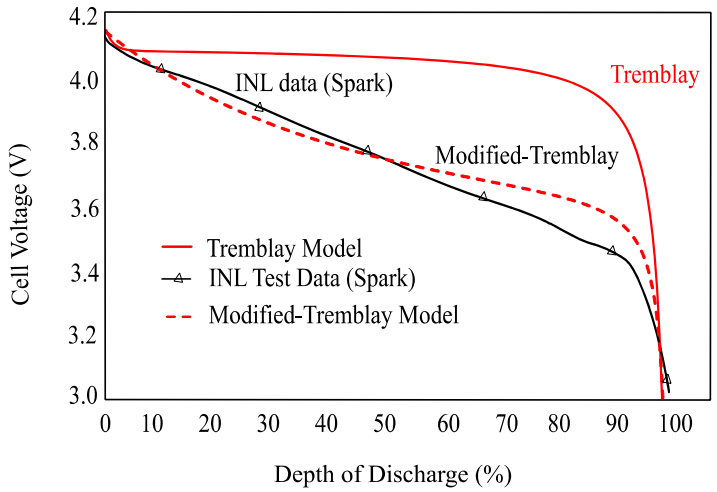

Figure 4-8. Tremblay model and Modified-Tremblay model comparison with Chevy Spark discharge test data from INL.

From this analysis it appears that the Tremblay battery model can benefit from the inclusion of an additional term when used to model BEV Li-ion batteries. This new term is required for the quasi-linear voltage drop seen in Zone 2 of Figure 4-3. In addition, as the Tremblay procedure only utilizes three discharge curve points, all of which are located above the knee voltage, it underestimates the capacity by approximately 2% SOC. For example, a minimum 3 V cell-voltage is reached at 98 % DOD instead of 100 % DOD.

4.3.3 Log-Linear-Exponential Model

A novel Li-ion battery model termed a log-linear-exponential (LLE) was introduced in [14]. The LLE model requires measurements at all five points from the voltage profile shown in Figure 4-3. The structure of the LLE model assigns an equation term to the voltage drop in each zone of the discharge profile. The resultant equation is given as

$$V_b = V_r^o - C_{LLE}\, log_e(DoD_x) - D_{LLE}(DoD_x) - F_{LLE}e^{(G_{LLE}[DoD_x - DoD_3])} - R_{INT}i \quad (4.3)$$

where V_r^o is the open-circuit reversible voltage, DoD_x is the depth of discharge as a percentage at any specified point x on the discharge curve, DoD_3 is the depth of discharge at point V_3 in Figure 4-3, and C_{LLE}, D_{LLE}, F_{LLE} and G_{LLE} are empirical constants. The minimum value of DoD_x must be limited to 0.5% in (4.3) to prevent a log_e function error. The first term $C_{LLE}\, log_e(DoD_x)$ estimates the voltage drop in the initial activation polarization region (Zone 1) of the profile. The second term, $D_{LLE}(DoD_x)$is required to model the ohmic quasi-linear voltage drop in Zone 2. The $F_{LLE}e^{(G_{LLE}[DoD_x - DoD_3])}$ term estimates the concentration polarisation voltage drop in Zone 3.

The empirical constants are calculated in a defined order, starting with the logarithmic voltage drop empirical constant C which is determined by

$$C_{LLE} = \frac{[V_1 - V_2]}{log_e(DoD_2/DoD_1)} \quad (4.4)$$

based on V_1 being approximated as the voltage at 0.5% DOD (DoD_1). By slightly offsetting the DoD_1 from 0% to 0.5%, a potential division by zero error is avoided in (4.4). The quasi-linear drop coefficient D_{LLE} is then evaluated using

$$D_{LLE} = \frac{[V_r^o - C_{LLE}\, log_e(DoD_3) - R_{INT}i - V_3]}{DoD_3} \quad (4.5)$$

The exponential voltage drop on the voltage profile requires two coefficients G_{LLE} and F_{LLE} which are determined using

$$G_{LLE} = \frac{log_e\left(\frac{V_r^0 - C_{LLE}\, log_e(DoD_5) - D_{LLE}(DoD_5) - R_{INT}i - V_5}{V_r^0 - C_{LLE}\, log_e(DoD_4) - D_{LLE}(DoD_4) - R_{INT}i - V_4}\right)}{(DoD_5 - DoD_4)} \quad (4.6)$$

and

$$F_{LLE} = [V_r^0 - C_{LLE}\, log_e(DoD_4) - D_{LLE}(DoD_4) - R_{INT}i - V_4]e^{(G_{LLE}[DoD_3 - DoD_4])} \quad (4.7)$$

The parameters DoD_1, DoD_2, DoD_3, DoD_4 and DoD_5 are the depths of discharge (%) at points Ah_1 to Ah_5 on Figure 4-3. The resulting discharge curve has three distinct zones, with very low cross-interference between the equation terms.

This LLE model is plotted in Figure 4-9 in a comparison with INL discharge curve data for the Nissan Leaf, BMW i3 and Mercedes B-class BEVs. The model parameter values and model comparison results for all eight vehicles in the study are provided in Table 4-3. The LLE model coefficients in Table 4-3 combined with the number of series cells per battery pack given in Table 4-1, enables the voltage profiles of the complete battery packs in all eight vehicles to be modelled.

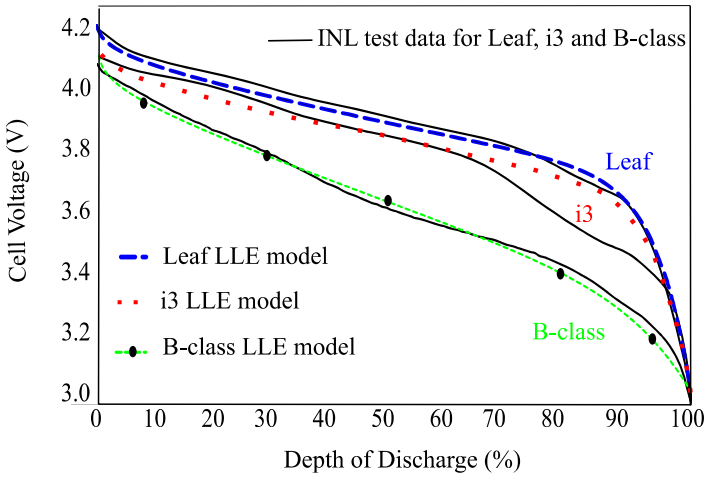

Figure 4-9. Comparison of LLE models for Leaf, BMW i3 and B-class batteries with discharge test data from INL for these vehicles.

Table 4-3 Coefficients for LLE battery cell voltage models

Vehicle	V_1^0	C_{LLE}	D_{LLE}	F_{LLE}	G_{LLE}	R^2	Error*
Focus	4.20	0.033	0.005	0.012	0.193	0.986	0.04
Leaf	4.19	0.037	0.003	0.049	0.179	0.988	0.03
Fortwo	4.21	0.067	0.005	0.0002	0.451	0.991	0.03
i3	4.10	0.02	0.004	0.002	0.176	0.943	0.06
Spark	4.15	0.018	0.006	0.010	0.374	0.997	0.02
eGolf	4.11	0.046	0.005	0.003	0.532	0.987	0.02
Soul	4.29	0.106	0.004	0.008	0.391	0.991	0.03
B-class	4.11	0.024	0.007	0.018	0.132	0.994	0.02

* rms voltage error values given as volts per cell

As presented in Table 4-3, the LLE battery model achieves a good correlation to the INL discharge data, with R^2 values of 0.943 to 0.997 and results in a low rms voltage error of 0.03 V/cell, equivalent to less than 1 % error (3 % operational-voltage range error) in seven of the eight vehicles. As illustrated in Figure 4-9, the discharge profile of the BMW i3 has a characteristic fourth zone (between 70 % to 90 % DOD) which is not captured by the three terms of the LLE model. In this vehicle, a higher rms voltage error of 0.06 V/cell, equivalent to a 1.6 % error (or 5.5 % operational-voltage range error) is recorded.

The Tremblay model establishes the open-circuit voltage to capacity relationship with the actual measured battery capacity while the LLE model establishes this relationship with a normalised capacity. The advantage of the normalised capacity approach is presented in Section 4.4 where the battery voltage profile is used as a fuel gauge in a vehicle simulator.

4.3.4 Polynomial Models

Polynomial models for batteries using curve-fitting procedures are often presented in the literature [16],[18], [27],[40]. In this study, a curve-fit procedure is directly applied to the INL voltage test data that had been recorded at a *C*/3 test current i_T. The lowest-order polynomial to provide a good fit to the battery pack discharge curve was a fifth-order polynomial model of the form given by

$$V_b = a_5(DoD_x)^5 + a_4(DoD_x)^4 + a_3(DoD_x)^3 + a_2(DoD_x)^2 + a_1(DoD_x) + a_0 - R_{INT}(i - i_T) \quad (4.8)$$

These 5th order polynomial models are plotted in Figure 4-10 in a comparison with INL discharge curve data for the Nissan Leaf, Ford Focus and Mercedes B-class BEVs. The coefficients of each polynomial to replicate a cell voltage of the battery pack are provided in Table 4-4. The R_{INT} values in Table 4-4 represent the equivalent combined cell resistance when the battery pack is represented as a single string of cells. The actual cell resistance in vehicles such as the B-class, which has 3696 cells arranged in 44 paralleled strings, is significantly higher.

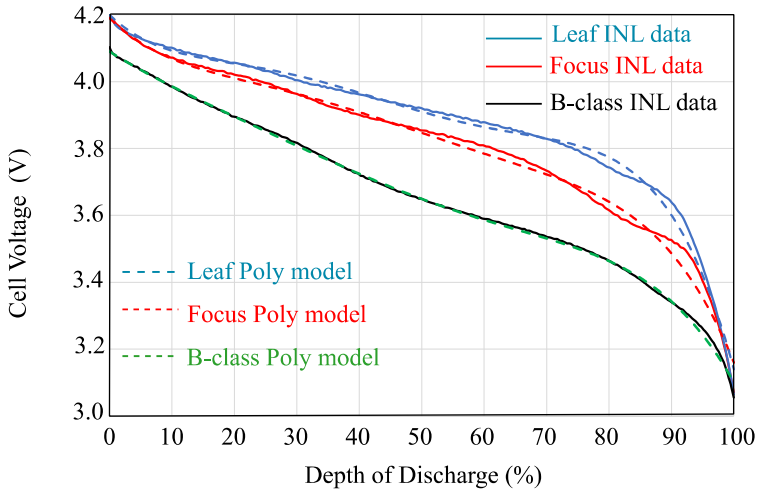

Figure 4-10. Comparison of polynomial models for Leaf, Focus and B-class batteries with discharge test data from INL for these vehicles.

Table 4-4 Higher-order polynomial coefficients for the eight battery packs

Vehicle	Cell R_{INT} (mΩ)	*Fifth-Order Polynomial Coefficients*						*Curve-Fit Results*	
		a_5	a_4	a_3	a_2	a_1	a_0	R^2	*V error**
Focus	0.99	-11.06	24.84	-20.86	7.87	-1.82	4.19	0.992	0.021
Leaf	1.35	-17.80	38.24	-29.63	9.94	-1.81	4.20	0.994	0.017
Fortwo	1.88	-10.50	21.87	-16.44	6.18	-2.16	4.21	0.996	0.014
BMW i3	1.35	-4.48	9.09	-7.08	2.32	-0.76	4.10	0.989	0.025
Spark	1.35	-15.85	35.07	-27.30	8.86	-1.78	4.16	0.995	0.018
e-Golf	0.91	-8.45	16.15	-10.59	3.43	-1.45	4.10	0.992	0.018
Soul	1.04	-19.52	44.97	-37.14	13.42	-2.94	4.32	0.997	0.017
B-class	1.49	-5.46	10.20	-6.58	2.04	-1.19	4.09	0.999	0.007

* rms voltage error values given as volts per cell

The polynomial models achieved the highest R^2 values ranging from 0.989 to 0.999 and the lowest rms voltage error. A typical error value was 0.02 V/cell, equivalent to 0.5% error based on the nominal cell voltage or 1.7% error over the operational-voltage range. These results are consistent with the results reported in several studies [40], [41]. Similar to the LLE models, the polynomial models were developed based on a normalised capacity to open-circuit voltage relationship.

4.3.5 Proposed Generic Li-ion Battery Voltage Model

The INL discharge tests show significant differences in the voltage-charge profiles for the battery packs of the eight vehicles. As is shown in Figure 4-2, the voltage profile shape is not specific to the cathode chemistry. These differences negate the possibility of a single empirical model for all eight BEVs and therefore for high accuracy models, a custom empirical model, such as a polynomial model, is required for each BEV. However, when test data is not available, such as during the concept design stage for a new vehicle, BEV simulation would benefit from a simplified generic Li-ion battery model, based on a minimum number of battery parameters.

In this study, an empirical generic Li-ion battery model is proposed based on eight observed characteristics in the INL test data. The voltage profile of this model is determined from the first three common discharge test characteristics observed in the INL test data:

1) The initial logarithmic drop in battery voltage, shown as Zone 1 in Figure 4-3, is significantly reduced and is quasi-linear, possibly limited by the battery management system to prevent over-heating during charging [42]. This voltage drop will be excluded in the proposed generic model.
2) The discharge voltage in six of the eight BEVs tested has a relatively linear characteristic in the range from 0% to 90% DOD. The exceptions are the Smart Fortwo and the e-Golf which have a slight logarithmic characteristic in this range.
3) The quasi-linear zone is followed by an exponential decreasing battery voltage and 100% discharged capacity is reached at a relatively high cell voltage. Typically, this minimum cell voltage is at 70% to 80% of the nominal cell voltage.

The proposed generic model's voltage to normalised capacity relationship is expressed as a linearly decreasing voltage function from 0% DOD to 90% DOD, followed by an exponentially decreasing voltage function from 90% DOD to 100% DOD. This relationship is presented in equation form as

$$V_b = V_{cell-max} - A_{gm}(DoD_x) - B_{gm}e^{[-C_{gm}(1-DoD_x)]} - R_{INT}i \quad (4.9)$$

where $V_{cell-max}$ is the voltage of a fully-charged cell, A_{gm} is the quasi-linear zone slope in volts per % DOD, B_{gm} is the additional voltage drop required from the exponential function to achieve the minimum cell voltage at 100% discharged capacity and C_{gm} is an empirical value to achieve a good representative voltage curve in Zone 3. Chen [31] proposes an experimentally derived value of 35 for C_{gm} and this is adopted here for the generic model as it provides a reasonably good fit to the INL data.

Figure 4-11 illustrates the two voltage drop terms of (4.9) for the generic model. Three additional observations from the INL test data are used to derive the model parameters $V_{cell-max}$, A_{gm} and B_{gm} .

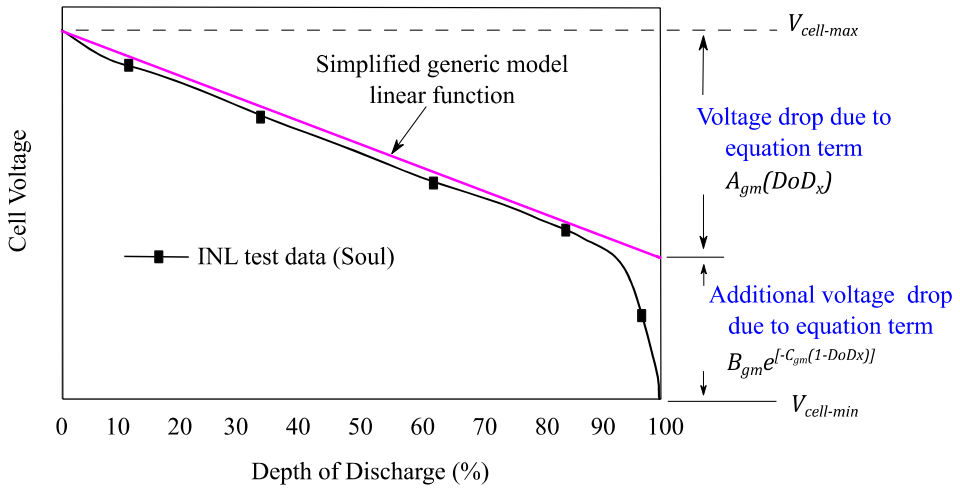

Figure 4-11. Generic battery model voltage drops.

4) As shown in Table 4-2, the maximum cell voltages $V_{cell-max}$ ranged from 4.28 V (Soul) to 4.06 V (B-class). The resultant mean value of the measured maximum cell voltages, during a *C*/3 discharge, is 4.13V. This average cell terminal voltage value includes an average internal voltage drop of 0.03 V. The adjusted mean value of the maximum open-circuit cell voltage of 4.16 V is used for $V_{cell-max}$ in (4.9).

5) The observed voltage at end of the quasi-linear zone, which occurred at 90% DOD in INL tests, is approximately 16% lower than $V_{cell-max}$ for two out of the three Li-ion chemistries tested and approx. 20% lower than

$V_{cell-max}$ for the NCA cathode found in the B-class. This equates to a cell voltage 3.49 V for a $V_{cell-max}$ of 4.16 V. Based on these voltages, the slope of the drop, A_{gm} parameter in (4.9), is 0.0075 V per 1% DOD. This equates to a total voltage drop from this term of 0.75 V at 100% DOD.

6) The B_{gm} parameter value in (4.9) depends on the minimum cell operating voltage $V_{cell-min}$. From Table 4-2, the mean value of the minimum cell voltages in the INL test data is 3.03 V and this value is used in the generic model for $V_{cell-min}$. The operating range cell voltage drop is 4.16 V minus 3.03 V which equates to 1.13 V. When the linear voltage drop is subtracted from this value, the additional voltage drop required from the exponential function is 0.38 V. This equates to the B_{gm} parameter value in (4.9).

Inserting these values into (4.9) provides a generic Li-ion battery model voltage profile given by

$$V_b = 4.16 - 0.75(DoD_x) - 0.38e^{[-35(1-DoD_x)]} - R_{INT}i \tag{4.10}$$

The final generic model parameter to be estimated for a cell voltage profile is R_{INT}. An examination of the INL published data provides an estimate of a generic value for Li-ion cells. These cell resistance values are based on an assumed single string battery pack.

7) The measured beginning-of-life (BOL) test discharge resistance values for the eight battery packs R_{BP} ranged from 0.08 Ω to 0.16 Ω per pack or an R_{INT} of 0.9 mΩ to 1.9 mΩ per cell. This equates to an average cell resistance R_{INT} of 1.3 mΩ for the generic model.

The simple average R_{INT} values of 1.3 mΩ per cell for the generic model, assumes that the battery pack total resistance R_{BP}, which is the product of R_{INT} and the number of cell in the string N_{series}, is independent of all other battery specifications. However, analysis of the INL test data showed some variation of the R_{BP} values with both the battery capacity and with the cathode structure of the Li-ion battery. This analysis resulted in defining an empirical conversion factor $K_{cathode}$, measured in ΩAh, that relates the cell resistance to the cathode type and cell Ah capacity Ah_{rated}. The equivalent cell resistance R_{INT} in the generic model is estimated by

$$R_{INT} = \frac{K_{cathode}}{Ah_{rated}} \tag{4.11}$$

where $K_{cathode}$ is estimated from the INL data to be 85 mΩAh for LMO, 75 mΩAh for NMC and 140 mΩAh for NCA cathodes.

Both the simple average value and the cathode-capacity dependent value of R_{INT} for the generic model are compared to the INL test data in Table 4-5. As the INL published data is for the pack resistance R_{BP}, for this comparison, both estimates of R_{INT} are converted to their equivalent R_{BP} values with a multiplication by N_{series} .

Table 4-5 Comparison of generic Li-ion pack resistance estimations methods.

Vehicle	Cathode Type	Series Cells	INL data R_{BP} (mΩ)	Rated capacity (Ah)	(averaged values) R_{BP} (mΩ)	(4.11) R_{BP} (mΩ)	(averaged values) Error (%)	(4.11) Error (%)
Focus	LMO	86	85	75	112	97	32	14
Leaf	LMO	96	130	66.2	125	123	-4	-5
Fortwo	LMO	93	175	52	121	152	-31	-13
i3	NMC	96	130	60	125	120	-4	-8
Spark	NMC	96	130	52	125	138	-4	6
e-Golf	NMC	88	80	75	114	88	42	10
Soul	NMC	96	100	75	125	96	25	-4
B-class	NCA	84	125	93	109	126	-13	8

As shown in Table 4-5, the simple average resistance approach results in large underestimations (-31%) and overestimations (42%) for the R_{BP} values of the battery packs studied. The cell resistance estimated by (4.11) shows a better agreement to the INL R_{BP} values and a reduced error range of -13% to 14%.

A generic Li-ion battery pack model also requires an estimate of N_{series}. The nominal cell voltages $V_{cell-nom}$, published by INL, are 3.6 V the B-class which is the only BEV with an NCA cathode, and 3.7 V for all the other BEVs. For a BEV simulation with a required nominal system voltage of the battery pack $V_{sys-nom}$, the required number of cells in series is given by

$$N_{series} = \frac{V_{sys-nom}}{V_{cell-nom}} \tag{4.12}$$

While the generic model's R_{BP} values, calculated using (4.11), reduce the error in the estimation of this parameter, the literature shows that cell resistance is also dependent on multiple other factors including SOC value, cell temperature and age of cell. The values obtained from (4.11) are based on a very small sample size of battery packs and further research is required to investigate if battery pack resistance can be estimated with reasonable accuracy based just on the cathode type and rated Ah capacity.

The simple generic model is plotted in Figure 4-12 in a comparison with INL discharge curve data for all the eight vehicles in this study. The comparison is made based on the normalised cell capacity of an equivalent single string battery pack.

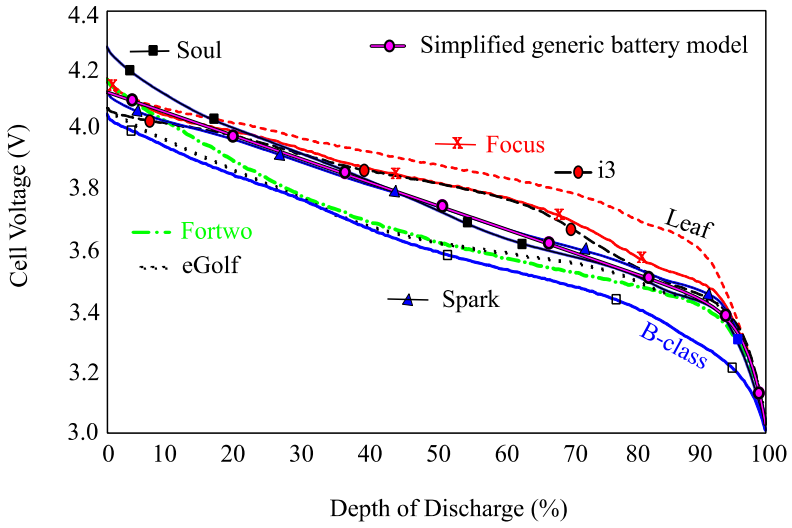

Figure 4-12. Comparison of generic model voltage profile to INL test data.

The generic model achieves R^2 values ranging from 0.935 to 0.999. The typical rms voltage error was 0.075 V/cell which is equivalent to 2% error or a 6.9% operational-voltage range error. The model provides the best correlation to Li-ion with NMC cathodes. As shown in Figure 4-12, this model underestimates the Leaf battery (LMO cathode) voltage by a rms voltage error of 0.125 V/cell and overestimates the B-class battery (NCA cathode) voltage by a rms error voltage of 0.12 V/cell.

A comparison of the proposed generic Li-ion model with both the Tremblay and Modified-Tremblay models is shown in Table 4-6. All three models use just two equation terms to shape the voltage profile of the battery model. The Tremblay model focuses on modeling the Zone 1 and Zone 3 voltage drops of Figure 4-3. In contrast, the generic model does not consider the Zone 1 voltage drop and concentrates on estimating the voltage drops in Zone 2 and Zone 3. With the highest R^2 values and lowest voltage error results highlighted in Table 4-6, it is evident that the generic model provides improved accuracy for most of the tested battery packs. The error in the e-Golf and B-class is reduced if the measured maximum cell voltage values of 4.08 and 4.06 respectively, are used in (4.10) instead of the INL averaged value of 4.16 V.

Table 4-6 Comparison of generic, Tremblay and Modified-Tremblay model results.

Vehicle	**R^2**			**Error (rms volts per cell)**		
	Generic	***Tremblay***	***Modified-Tremblay***	***Generic***	***Tremblay***	***Modified-Tremblay***
Focus	0.981	0.761	0.818	0.063	0.24	0.13
Leaf	0.935	0.881	0.895	0.125	0.33	0.94
Fortwo	0.965	0.561	0.939	0.091	0.52	0.07
i3	0.972	0.572	0.85	0.051	0.25	0.13
Spark	0.999	0.475	0.739	0.019	0.26	0.09
e-Golf	0.972	0.403	0.967	0.092	0.3	0.06
Soul	0.992	0.46	0.861	0.037	0.4	0.11
B-class	0.991	0.749	0.945	0.12	0.33	0.08

4.4 Virtual Fuel Gauge based on Battery Pack Voltage

The five reviewed models determine the open-circuit voltage (OCV) during steady-state operation by implementing either an actual or a normalised battery capacity. Both approaches were examined to evaluate their capability to establish a virtual fuel gauge in a vehicle simulator.

The INL battery pack testing was repeated at specific odometer readings. As shown for the B-class BEV in Figure 4-13(a), the capacity reduces as the battery ages. This alters the OCV with actual capacity relationship, requiring an updated voltage-source model as the battery ages. When the reduced capacity is normalized to 100% DOD as in Figure 4-13(b), the voltage to normalised capacity relationship does not significantly change as the battery ages.

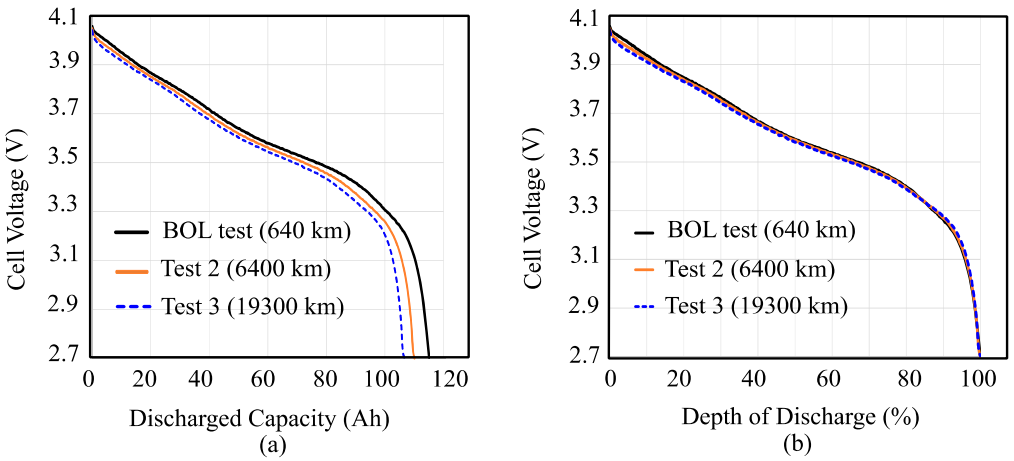

Figure 4-13. B-class cell discharge voltage as a function of (a) actual capacity and (b) normalised capacity over time.

The B-class cell, with its NCA cathode, showed a relatively low level of capacity fade (6%) in the INL tests. The highest capacity fades were observed in the Leaf (LMO cathode) with 26% after 38,000 km over 800 days, and in the Soul (NMC cathode) with 8.4% after 19,428 km over approximately 600 days. Figure 4-14 shows the voltage to capacity relationships of Li-ion cells in these vehicles. As shown in Figure 4-14 (b) and Figure 4-14 (d), the voltage to normalised capacity relationships in these cells do not significantly change as the battery ages. The reduced capacity with ageing must still be determined, for example during battery charging, but the normalised fuel capacity to battery pack voltage allows a virtual fuel gauge to be constructed, as shown in Figure 4-15.

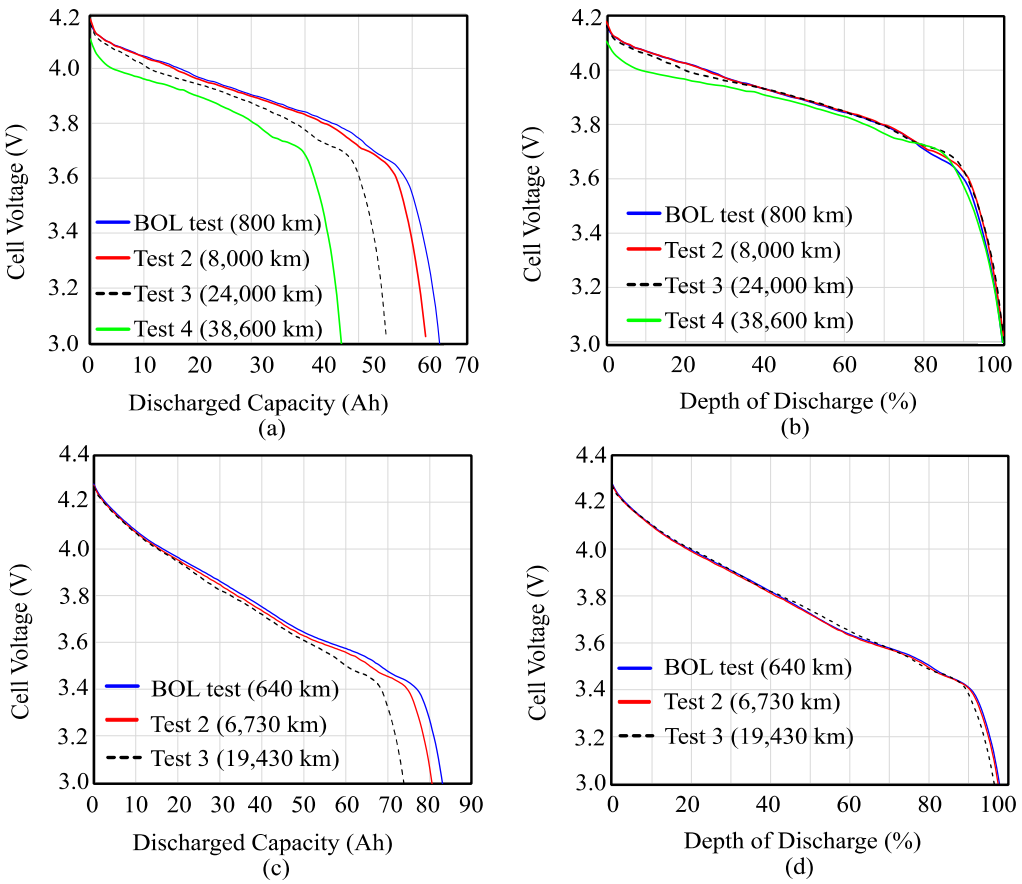

Figure 4-14. Leaf cell discharge voltage as a function of (a) actual capacity and (b) normalised capacity, and Soul cell discharge voltage (c) actual capacity and (d) normalised capacity.

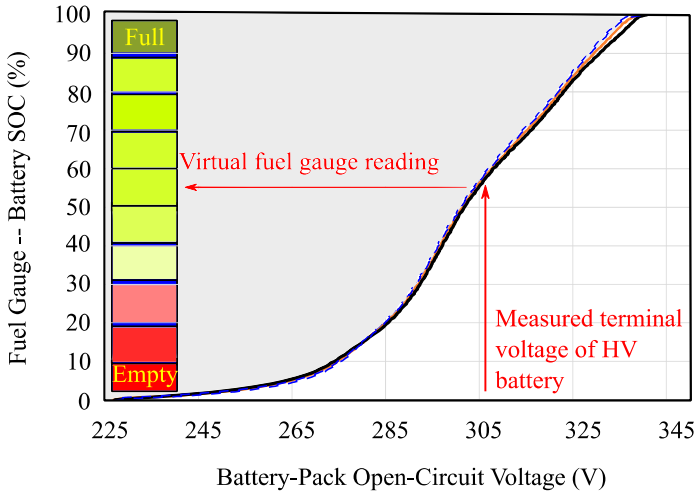

Figure 4-15. Virtual fuel gauge based on normalised capacity.

4.5 Dynamic Battery Models in BEVs and HEVs

Each of the empirical battery voltage models requires an internal-impedance network to function as a battery model within a vehicle simulator. The lowest computational option for the simulator is achieved by representing this network as a single resistance value rather than as a Thevenin circuit. Within the literature, the dynamic performance of HEV battery cells is typically modelled by Thevenin circuits [3],[43],[44]. However, the literature does not report whether the complexity of the Thevenin circuit is required for the lower dynamic-performance requirements of BEV battery packs. This study examines the impact of both internal network options on the dynamic performance of the battery model for a BEV application.

The cell single resistance value R_{INT} or the battery pack single resistance value R_{BP} can be determined from the HPPC test R_{BP} values provided by INL as illustrated in Figure 4-1. The resistance values were measured at discrete SOC levels from approximately 10% SOC to 90% SOC. The HPPC testing is performed during both full-discharge and full-charge tests. The average measured R_{BP} values in each vehicle are given in Table 4-2. The value of this resistance in a battery varies with (i) operational mode (charge or discharge), (ii) battery age, (iii) DOD, and (iv) temperature. The resistance values were slightly higher when discharging compared to charging, e.g. in the BMW i3 the discharge resistance is approximately 130 mΩ while the charge resistance is approximately 110 mΩ. There is insufficient INL test data to accurately model the increase in resistance as the battery aged. The INL resistance measurements show increased values as the battery discharges rise above 80% DOD. A modified version of the Chen model [31] for the increase in cell resistance with ageing provides a good estimation of this R_{INT} to DOD relationship which is determined by

$$R_{INT}(DoD_x) = R_{AVE} + A_R e^{[B_R(1-DoD_x)]} \tag{4.13}$$

where R_{AVE} is the average INL test resistance values up to 80 % DOD, A_R and B_R are curve-fit coefficients. Values of $A_R = 0.2$ and $B_R =$ -0.15 were selected as they provided the best correlation to the limited data points published by INL. As this change in R_{INT} is only observed in the final 20% of the remaining battery capacity, it is proposed not to implement this function in the basic SEVP simulator as the increased

accuracy in voltage drop estimation would negate the computational advantage of using the simple R_{INT} model.

As INL do not publish the battery terminal voltage profile during a HPPC test (Figure 4-4), the estimation of the values of the polarizing resistor R_P and capacitor C_P for Thevenin internal networks required an additional data source. In separate testing, ANL tested the eight vehicles in this study on a dynamometer and measured the battery terminal voltages and currents at 100 ms intervals during various legislative drive-cycle tests [13]. ANL published their test data in the form of Excel files. The method used to derive the Thevenin parameters from the ANL data comprised applying the measured currents to the battery model and then adjusting the component values until the model output voltages matched the ANL measured voltages. As this analysis was based on a complete battery pack rather than on individual cells, the resulting Thevenin circuit parameters R_{0_BP} , R_{P_BP} and C_{P_BP} are valid only for the battery pack dynamic validation. The derived battery pack Thevenin circuit values are presented in Table 4-7. These parameters can be adjusted to their equivalent cell parameters R_0 , R_P and C_P if the dynamic performance of individual cells is required.

Table 4-7. Derived Thevenin circuit parameters for battery pack models from ANL data.

Vehicle	R_{0_BP}(mΩ)	R_{P_BP} (mΩ)	C_{P_BP} (F)
Focus	55	30	165
Leaf	75	55	90
Fortwo	75	100	50
i3	50	80	90
Spark	55	75	95
e-Golf	50	30	165
Soul	40	60	115
B-class	85	40	175

Figure 4-16 presents a comparison of the voltage from a battery model with a single internal resistance R_{BP} and the voltage from a battery model with a Thevenin circuit internal-impedance to the measured ANL voltages. The difference in the dynamic responses between those battery models is evident in Figure 4-16. The ANL measured voltages show a time-dependent voltage drop that is especially obvious

during the constant-current discharge pulse in the time period from 22 s to 24 s. While the battery discharge current is constant, the terminal voltage shows a characteristic slope associated with a time-dependent increase in polarisation resistance. The amplitude of the current pulse is equivalent to a 2 C current for this battery. For illustration purposes only, a dc offset of approximately 2 V was introduced into the battery models for Figure 4-16 to clearly display the measured and model outputs in this figure. The battery model with a simple R_{BP} internal network over-estimated the internal voltage drop and displayed a constant voltage drop during the constant current discharge pulse. In contrast, the dynamic response of the battery model with a Thevenin circuit provided a model output voltage profile that matches the ANL test voltage profiles as seen in Figure 4-16.

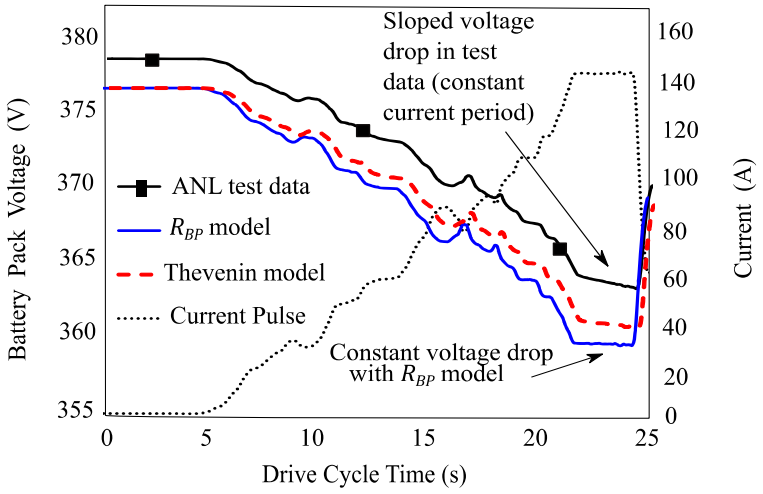

Figure 4-16. R_{BP} and Thevenin models compared to ANL test data for the 2013 Leaf.

The Thevenin circuit is modelled in discrete time with sample period T_s. The voltage drop across the Thevenin circuit shown in Figure 4-4 has two terms; (i) the voltage drop across the ohmic resistance R_o which is calculated simply as $V_{R0} = iR_0$ and (ii) the voltage drop across the parallel RC circuit V_{RC}. In [24] the calculation of V_{RC} for any time-period k , is given as $V_{RC,k}$ and it is determined using

$$V_{RC,k} = V_{RC,k-1}e^{\left(-T_s/\tau\right)} + R_p\left(1 - e^{\left(-T_s/\tau\right)}\right)i_k \tag{4.14}$$

where $V_{RC,k-1}$ is the voltage drop in the previous period, τ is the time constant of the RC circuit and i_k is the battery current in period k.

The small difference in battery terminal voltages between the internal-impedance networks observed in Figure 4-16, prompted further analysis to establish why the Thevenin circuit is usually selected for battery models in vehicle simulators. As the literature on vehicle simulators focuses on the study of HEVs rather than BEVs, a comparison of the operating requirements of batteries in both types of vehicle is required. Battery specifications and operating parameters for a 2015 Honda Accord HEV Li-ion battery and a 2015 Kia Soul BEV battery are shown in Table 4-8 based on INL battery pack test data and on dynamometer data from ANL. While the range of battery currents are similar in both the HEV and the BEV, the rated Ah capacity of the HEV is less than 7% of the BEV capacity. The lower capacity HEV battery has an increased internal resistance and a reduced operational SOC range compared to the BEV battery.

Table 4-8. Comparison of 2015 Honda Accord HEV and 2015 Kia Soul BEV.

Parameters		***HEV***	***BEV***
Rated battery capacity	(Ah), [kWh]	5,[1.3]	75,[27]
Maximum pack voltage	(V)	285	399
Minimum pack voltage	(V)	231	288
Number of cells		72	96
Maximum cell voltage	(V)	3.95	4.16
Minimum cell voltage	(V)	3.2	3.0
Average discharge pack resistance	(mΩ)	200	100
Operational SOC maximum limit	(%)	70	97.5
Operational SOC minimum limit	(%)	20	5
Maximum pack current	(A)	213	260
Minimum pack current	(A)	-178	-162

While the rated HEV battery capacity is provided in Table 4-8, the usable capacity may be lower. As illustrated in Figure 4-17, ANL test data on the Honda Accord HEV battery shows that the usable capacity, over the specified voltage range of 231 V to 285 V, is approximately 2.5 Ah. Lower usable capacity means that the battery terminal voltage in a HEV is dependent on both the voltage drop across the internal-impedance and on the change in the open-circuit voltage with a change in capacity.

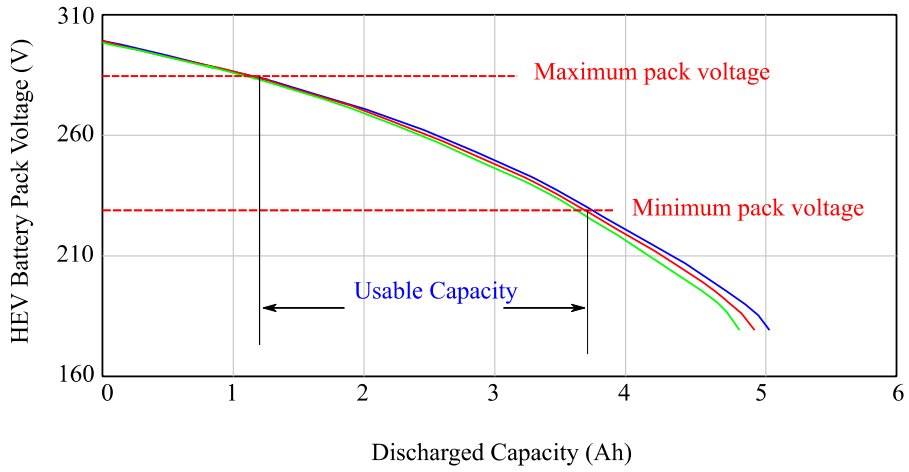

Figure 4-17. INL discharge test for Honda Accord HEV combined with operating voltage limits derived from ANL dynamometer tests [12], [13].

Using the INL test data, the Accord battery voltage profile was modelled using a second-order polynomial instead of a typical fifth-order polynomial due to the restricted operational SOC range of the HEV. The model was validated with both types of internal-impedance networks. The Thevenin circuit component values were determined using ANL dynamometer data. The results of the validation test are presented in Figure 4-18.

In the drive cycle test shown in Figure 4-18, the HEV accelerates during the time period 9 s to 12.5 s. This acceleration event results in an open-circuit voltage drop of approximately 6 V due to the battery capacity discharge as seen from the change in the battery voltage before (266 V) and after (260 V) the current pulse. The measured terminal voltage drop during the discharge current of 213 A, equivalent to a 42.6 *C* rate, is approximately 22.5 V (266 V to 243.5 V). Even in this low capacity HEV battery, this test result shows that the internal impedance is the dominant source of the battery voltage drop during high current discharges.

When a simple R_{BP} internal-impedance model is implemented, the battery model estimates a voltage drop of 45 V (266 V to 221 V) and the battery model voltage is lower than the permissible minimum battery operating voltage level of 231 V. In this HEV, the over-estimated voltage drop of 22.5V using the simple R_{BP} model represents

approximately 41.5% of the narrow operating voltage range. When the Thevenin internal impedance is used, the voltage reduces from 266 V to 239 V which represents an overestimation of only 4.5 V or 8% of the operating voltage range. This improved response explains why the simple R_{BP} model is not the preferred choice in the literature for HEV simulation.

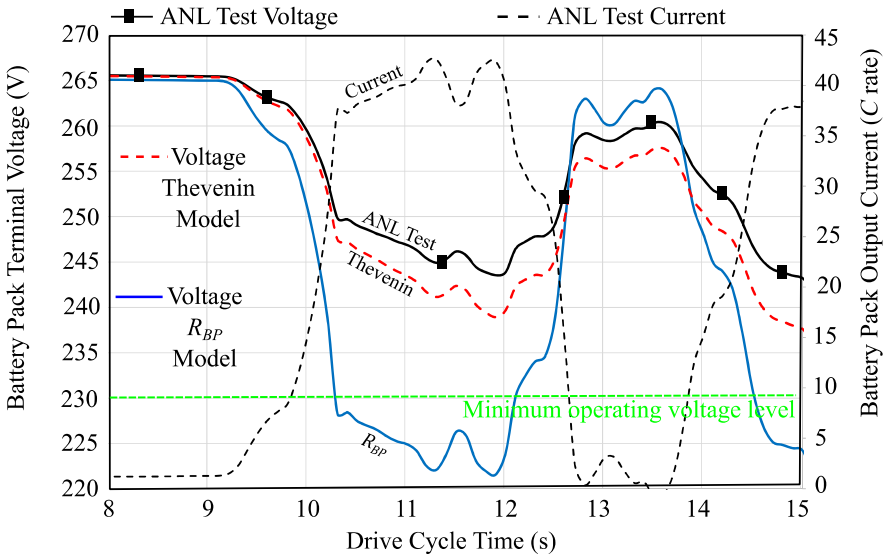

Figure 4-18. R_{BP} and Thevenin models compared to ANL data for the 2015 Honda Accord HEV.

Figure 4-19 shows the comparison of both battery models to the ANL dynamometer data for the Kia Soul BEV. In an equivalent acceleration test to that performed with the HEV, the BEV battery current approaches a far lower 3 *C* rate. The voltage drop, due to the change in battery capacity for this acceleration event, was not detected in the BEV testing due to significantly higher battery capacities in these vehicles. With these conditions, as shown in Figure 4-19, the R_{BP} network overestimates the voltage drop by up to 15 V. However, this overestimation represents only 7.5% of the wide operating voltage range of a BEV battery and it does not impact vehicle simulation until the battery is nearly fully discharged, at greater than 95% DOD. The Thevenin internal impedance has a significantly lower overestimated voltage drop but it has a higher computational load during the simulation.

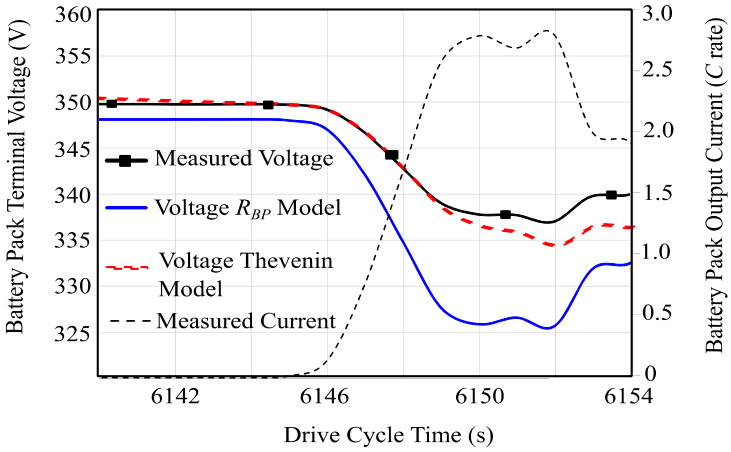

Figure 4-19. R_{BP} and Thevenin models compared to ANL data for the 2015 Kia Soul BEV at very high current outputs due to vehicle acceleration.

Further analysis of the ANL test data for the Soul BEV over several drive cycles showed that the average discharge *C* rate was less than 0.5 *C*. Both types of internal impedance circuit battery models were implemented to simulate BEV operation over drive cycles with battery currents up to 1.4 *C*. The voltage-drop differences between both internal networks under these conditions were less than 5V as shown in Figure 4-20. From this analysis we can conclude that the simple R_{BP} internal-impedance network provides sufficient accuracy in vehicle simulation of BEVs for lower power but the Thevenin impedance is required in drive cycles that require near-full power dynamic output from the battery.

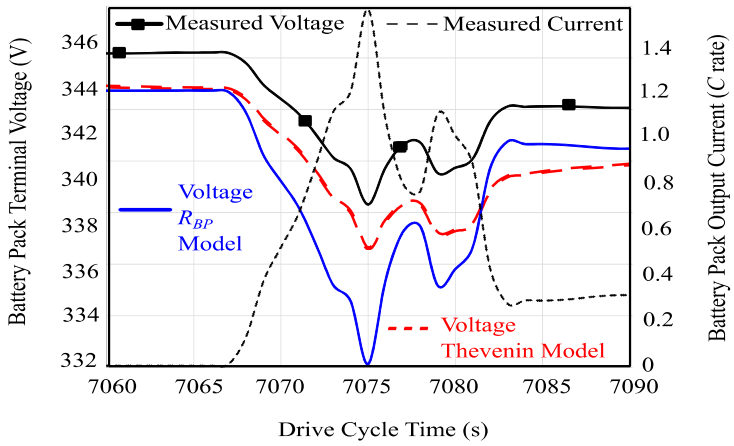

Figure 4-20. R_{BP} and Thevenin models compared to ANL data for the 2015 Kia Soul BEV at levels of current output up to 1.4 *C*.

4.6 Adapting the Battery Models for Lifetime Testing

Accurate range estimation of a BEV, at any stage in its lifetime, requires a battery model based on the available fully charged battery capacity value Ah_{FC} at that instant in its lifetime. The value of this parameter reduces as the battery ages, as was previously shown in Figures 4-13(a), Figure 4-14(a) and Figure 4-14(b) for the short time timespan between the first and last INL tests, which was typically less than two years. When the reduced Ah_{FC} is normalized to 100% DOD, the voltage-DOD relationship does not significantly change as the battery ages. This demonstrates that an empirical battery model that incorporates an ageing model to estimate the reduced capacity may remain valid over the lifetime of the vehicle. In this study, the limited battery ageing data was analysed to see if a simplified empirical battery ageing model could be formulated. Recent reported improvements in Li-ion battery lifetime performance suggests that any ageing model based on 2015 data is likely to require modifications for any future research studies [4]-[6]. Nonetheless, the educational value of the current research is; (i) the provision of factors that can impact battery ageing when constructed in battery packs, and (ii) the relationship between battery ageing and warranty periods.

As with most rechargeable battery types, the ageing loss percentage Q_{loss} of a Li-ion battery is largely determined by two major factors, namely (i) calendar ageing loss percentage Q_{loss_cal} when the battery is neither charging nor discharging and (ii) cycle-life ageing loss percentage Q_{loss_cyc} during battery operation. These three ageing parameters are related as shown by

$$Q_{loss} = Q_{loss\_cal} + Q_{loss\_cyc} \tag{4.15}$$

Known factors that impact calendar ageing include ambient temperature, the chemical structure of the cathode, and the SOC level when the battery is not operating. The dominant impact factor is ambient temperature and this is modelled using the power law relationship known as the Arrhenius equation [45], [46]. The general form of Q_{loss_cal} calendar capacity loss % is given as

$$Q_{loss\_cal} = A_{CAL} e^{\left(-E_A/RT\right)} t^x \tag{4.16}$$

where A_{CAL} is a pre-exponential coefficient determined using test data, E_A is the activation energy in J/mol, R is the universal gas constant in J/mol K, T is the ambient temperature in K, t is time in days, and x is the power law value which is commonly assigned a value of 0.5 [18], [41], [45]. The characteristic curve of this equation shows a high rate of capacity fade during the early life of the battery, followed by slower capacity reduction rates with time.

Cycle ageing is also affected by numerous factors including cycle depth ΔSoC, number of cycles, charge and discharge current levels, average SOC during the discharge/charge cycle and ambient temperature. The contribution of each individual cycle ageing factor is difficult to define as there are inter-dependencies between the factors. For instance, the impact of ΔSoC on battery lifetime cannot be calculated in isolation as ambient temperature and the average SOC value during each cycle should also be considered. In addition to this multi-dimensional array of input factors on cycle ageing, an ageing model requires a full history of the battery operation. In the absence of an operational history, simpler cycle ageing models are proposed in the literature which either assume a reduced number of factors or combine factors to represent cycle ageing by a reduced parameter equation. For example, the number of cycles and ΔSoC can be combined and represented as an Ah-throughput parameter. The number of performable cycles for a given ΔSoC is typically defined by means of a Woehler diagram [47]. An example of a Woehler diagram is presented in Figure 4-21.

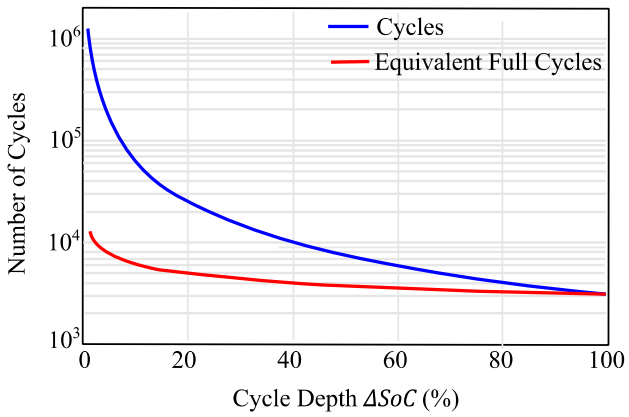

Figure 4-21. A sample of a Woehler diagram [47].

The combination of the ΔSoC of all the cycles produces a lifetime achievable Ah-throughput value and that lifetime Ah-throughput value increases with lower values of cycle ΔSoC. A typical Li-ion lifetime achievable Ah-throughput to ΔSoC relationship is given by

$$Ah_{LIFE} = Ah_{100\%DoD}\left(\frac{1}{\Delta SoC}\right)^{z} \tag{4.17}$$

where Ah_{LIFE} is the lifetime achievable Ah-throughput based on cycle depths of ΔSoC, $Ah_{100\%DoD}$ is the published battery lifetime Ah-throughput value where all the cycles involve fully discharging the battery and the coefficient z can have a value of 1 or greater [14],[27],[48],[49]. The combined impacts of Ah-throughput and temperature on cycle ageing can then form a reduced parameter cycle ageing model using an Arrhenius equation, expressing Q_{loss_cyc} the cycle capacity loss % as

$$Q_{loss\_cyc} = A_{CYC}e^{(-E_A/RT)}(Ah_{LIFE})^{y} \tag{4.18}$$

where A_{CYC} is a pre-exponential coefficient and y is the power law exponent. Both A_{CYC} and y may be derived by applying curve-fit procedures to battery lifetime test data.

The ageing models of (4.16) and (4.18) allow the estimation of the capacity fade. The coefficients of these equations would usually be determined from detailed ageing test data using regression techniques. The INL ageing data includes insufficient data points to estimate the ageing model coefficients using regression and when published Li-ion ageing model coefficients [45] were applied to the models, the resultant capacity fade was much higher than the recorded fade for seven of the eight BEVs. In the absence of detailed test data for ageing, an alternative approach for the estimation of the ageing model coefficients based on BEV warranties is proposed in this study.

BEV manufacturers typically offer an 8-year (2920 days) or 100,000 mile (160,000 km) warranty for their batteries. The proposed ageing estimation method assumes that the warranty-specified capacity fade (30 %) is evenly split between calendar and cycle ageing. The pre-exponential coefficient A_{CAL} for the calendar ageing model in (4.16) is calculated based on a Q_{loss_cal} of 15% after 8 years (2,920

days) and assuming a worst-case ambient temperature of 35ºC for the warranty calculation. The resulting A_{CAL} coefficient is given by

$$A_{CAL} = 15/\left[e^{(-E_A/RT)} \times 2920^{0.5}\right] \tag{4.19}$$

where E_A is assumed as 24,500 J/mol and R is the universal gas constant of 8.314 J/mol K. This equation gives an A_{CAL} value of 3968 for all of the vehicles in the INL study.

The cycle ageing pre-exponential coefficient can be derived by also setting Q_{loss_cyc} =15% for an Ah-throughput value equivalent to 100,000 miles (160,000 km) and assuming the same worst-case ambient temperature of 35ºC. From (4.17), the worst-case Ah-throughput for a warranty calculation occurs when ΔSoC =100%. The cycle ageing pre-exponential coefficient A_{CYC} is then calculated using

$$A_{CYC} = 15/\left[e^{\left(-E_A/RT\right)} \times \left(\frac{160000 \times E_{VEH}}{V_{sys-nom}}\right)^{0.55}\right] \tag{4.20}$$

where E_{VEH} is the vehicle's average consumption in Wh/km recorded during the INL BEV tests as noted in Table 4-2. The lifetime Ah-throughput is calculated by dividing E_{VEH} by the nominal system voltage $V_{sys-nom}$ and multiplying by the warranty travel distance as shown in (4.20). The derived ageing coefficients, together with the relevant INL test data parameters, are presented in Table 4-9.

Table 4-9. Ageing model parameters based on an 8-year, 160,000 km warranty and INL test data.

Vehicle	A_{CAL}	A_{CYC}	$V_{sys-nom}$	E_{VEH}
Focus	3968	404	318	178
Leaf	3968	440	355	175
Fortwo	3968	401	344	148
BMW i3	3968	388	355	162
Spark	3968	403	355	151
e-Golf	3968	305	326	174
Soul	3968	461	355	159
B-class	3968	391	302	178

With these warranty-derived coefficients, the ageing model over-estimated capacity fade in five of the eight vehicles but showed a higher underestimated fade in

the remaining three vehicles, which suggested that additional ageing factors are required. Further analysis identified two possible factors that may contribute to the error in the capacity fade estimation: (i) the lack of battery calendar data before the BOL test at 640 km and (ii) the impact of the pack cooling system on battery ageing.

The rate of calendar ageing is plotted in Figure 4-22. The lack of data before the first BOL test is significant as the calendar ageing model (4.16) predicts a high rate of ageing during the early lifetime of the battery.

An ageing model validation requires the time period between battery manufacture and the INL BOL test date to offset this early calendar ageing. In this study, the calendar period before the BOL test is assumed to be 45 days. The percentage calendar ageing capacity loss for this period is then offset from the predicted capacity loss at INL testing dates. For instance, if (4.16) estimates the calendar ageing loss as 2% after 45 days, 4.5% after 365 days, then the 45 days calendar loss is adjusted to 2%-2%=0% for the BOL test and adjusted to 2.5% for the 365-day test. Using this adjustment method, the ageing model capacity fade profiles match (within 2%) the INL test data ageing profiles for the liquid-cooled battery packs in the Focus, BMW i3 and SPARK, but the ageing model still underestimates (by up to 9%) the capacity fade in the air-cooled battery pack of the Leaf.

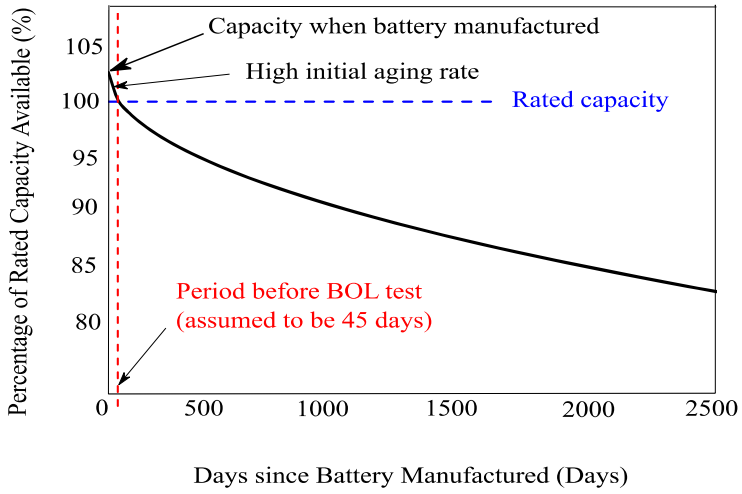

Figure 4-22. Ageing model adjustment for pre-BOL test period calendar ageing.

The impact of the battery pack cooling system is evident in the INL tests where the three air-cooled batteries have higher rates of capacity fade than the liquid-cooled batteries. The highest capacity fade was recorded in the passively air-cooled battery pack of the Leaf (26% after 38,600 km, 800 days) and the lowest fade in the active-liquid-cooled battery pack of the B-class, (6% after 19,300 km, 400 days). In addition to active liquid-cooling, the reduction in capacity fade in the B-class may result from its NCA cathode, which leads to less pronounced calendar capacity fade at high temperatures compared to the Manganese based cathodes [45].

A cooling system adjustment factor is proposed that multiplies the value of A_{CYC}, calculated using (4.20), by a factor value of 1 for liquid-cooling and up to 2.5 for air-cooling systems. Table 4-10 contains the capacity comparison (measured versus ageing model capacities at 6,400 km and 19,300 km).

Table 4-10. Warranty based ageing model comparison to INL data.

Vehicle	***Multiplier***	***at 6400 km***		***at 19300 km***	
		Actual	***[Model]***	***Actual***	***[Model]***
Focus	1	71.4	[72.1]	67.5	[67.8]
Leaf	2.5	62.3	[60.4*]	52.9	[54.6 *]
Fortwo	1	50.3	[50.3]	49.2	[48.8]
BMW i3	1	57.3	[57.3]	54.2	[53.1]
Spark	1	49.2	[49.3]	46.6	[45.3]
e-Golf	1.5	71.0	[71.3*]	66.5	[67.6 *]
Soul	2	81.2	[79.0*]	74.4	[74.2 *]
B-class	1	108.1	[108.5]	104.2	[104.1]

*cooling system multiplier applied values

The proposed simplified ageing model, with these two adjustment factors, estimated the capacity in all eight vehicles (19,300 km test) with a maximum error of 1.7 Ah and an average error of 0.78 Ah. The study limitations included: (i) A data source which is limited to a small number of vehicles: (ii) All the vehicles operated in one geographical area with relatively high ambient temperatures and (iii) The impact of driving style could not be assessed due to a lack of data. Further investigation is required but these exploratory results show promise as a simple battery ageing model.

4.7 Conclusions

In this study, the review of four existing battery models showed that only the LLE models and the higher-order polynomial models accurately represent the voltage-capacity profiles of the INL tested BEV Li-ion battery packs. A summary of LLE model coefficients and higher-order polynomial battery model coefficients for eight commercially available BEVs are provided in the chapter.

The commonly used Tremblay battery model was shown to result in significant voltage errors. A proposed change in the calculation procedure for this model resulted in a significant improvement in the modelling results. The standard Tremblay model focuses on capturing Zone 1 and Zone 2 of an actual battery voltage-capacity profile while the INL test data shows that Zones 2 and 3 are dominant for Li-ion battery packs.

For concept vehicles, where battery test data may not available, the developed generic Li-ion battery model (4.10) provided realistic battery output voltages for BEV simulators. The generic model consists of a linear OCV-DOD relationship in the range of 0-90% DOD, followed by an exponentially decreasing voltage for the final 10% of battery capacity. In contrast to the Tremblay model, the generic model was based on averaged voltage INL measurements and focused on Zones 2 and Zone 3 of the voltage-capacity profile.

The impact of battery capacity fade, associated with battery ageing, was considered for a lifetime model of the vehicle. The advantage of a battery model based on a normalised capacity to voltage relationship was shown to mitigate this negative impact. A further advantage of this battery modelling approach was to provide a virtual fuel gauge for a vehicle simulator.

For dynamic performance of a vehicle, the choice of internal-impedance circuit was shown to determine the dynamic response of the battery model. Comparing the battery models to dynamometer data from ANL showed that a Thevenin circuit for the internal-impedance model was vital for HEV simulation to avoid simulation error with the narrow operating voltage range as shown in Figure 4-14. For BEV simulation, the simpler R_{INT} internal-impedance provided good accuracy when the drive cycle does not involve highly dynamic events that require near-full output battery power. Except for high precision battery voltage modelling, the wide operating voltage range of the BEV battery pack minimises the need for a more complex Thevenin circuit.

For BEV range estimation over a vehicle's lifetime, an empirical battery ageing model, with coefficients derived from the BEV battery warranty conditions is proposed. This ageing model provided capacity-fade trends compatible with the observed trends in the INL tests. Applying this ageing model when normalizing the battery capacity results in a voltage-DOD profile model that is tentatively valid over the lifetime of the vehicle. The ageing model indicates a possible relationship between the battery pack cooling system and the capacity fade of the battery.

Adding these comprehensive EEC battery models to the SEVP model extends the ability of this vehicle model beyond energy consumption estimation. While these battery models improve the SEVP as an electrical circuit simulator, an IPM traction motor model is required to complete the powertrain circuit. This motor model is developed and reported in Chapter 5.

4.8 References.

[1] K. Davis and J. G. Hayes, " Comparison of lithium-ion battery pack models based on test data from Idaho and Argonne national laboratories," *2020 IEEE Energy Conversion Congress and Exposition (ECCE)*, Detroit, IL, 2020.

[2] A. Fotouhi, D. J. Auger, K. Propp, S. Longo, and M. Wild, "A review on electric vehicle battery modelling : From Lithium-ion toward Lithium – Sulphur," *Renew. Sustain. Energy Rev.*, vol. 56, pp. 1008–1021, April 2016. doi.org/10.1016/ j.rser.2015.12.009

[3] A. Shafiei, A. Momeni and S. S. Williamson, "Battery modeling approaches and management techniques for Plug-in Hybrid Electric Vehicles," *2011 IEEE Vehicle Power and Propulsion Conf. (VPPC),* Chicago, IL, 2011, pp. 1-5, doi: 10.1109/ VPPC.2011.6043191.

[4] BBC News, "Tesla battery supplier CATL says new design has one million-mile lifespan" [Online], Available: www.bbc.com/news/technology-52966178. [Accessed: 27-Jul-2020].

[5] Y. Ding, Z. P. Cano, A. Yu, J. Lu and Z. Chen, "Automotive Li-ion batteries: current status and future perspectives". *Electrochemical Energy Reviews*, *2*(1), pp.1-28, Mar 2019, doi.org/10.1007/s41918-018-0022-z

[6] F. Wu, J. Maier and Y. Yu, "Guidelines and trends for next-generation rechargeable lithium and lithium-ion batteries", Chemical Society Reviews, 49(5), pp.1569-1614, 2020, DOI: 10.1039/c7cs00863e.

[7] A. Brooker, J. Gonder, L. Wang, E. Wood, S. Lopp, and L. Ramroth, "FASTSim : A model to estimate vehicle efficiency, cost and performance," in *SAE World Congress and Exhibition*, Detroit, MI., USA, 2015, pp.1-12, doi:10.4271/2015-01-0973

[8] K. Davis and J. G. Hayes, "Analysis of electric vehicle powertrain simulators for fuel consumption calculations," *2016 Int. Conf. on Electrical Systems for Aircraft, Railway, Ship Propulsion and Road Vehicles & Int. Transportation Electrification Conf. (ESARS-ITEC)*, Toulouse, 2016, pp. 1-6, doi: 10.1109/ESARS-ITEC.2016.7841414.

[9] C. Fiori, K. Ahn, and H. A. Rakha, "Power-based electric vehicle energy consumption model: Model development and validation," *Appl. Energy*, vol. 168, pp. 257–268, 15 April 2016. doi.org/10.1016/j.apenergy.2016.01.097

[10] V. H. Johnson, “Battery performance models in ADVISOR,” *J. Power Sources*, vol.110, pp. 321–329, 22 August 2002, doi.org/10.1016/S0378-7753(02)00194-5.

[11] Argonne National Laboratory, “Autonomie”, [Online]. Available: https:// www.autonomie.net/. [Accessed: 10-Jul-2020].

[12] Idaho National Laboratory, Advanced Vehicles, “Library Alphabetical.” [Online]. Available: https://avt.inl.gov/content/pubs-az. [Accessed: 10-Jul-2020]

[13] Argonne National Laboratory, Energy Systems Division, “Downloadable Dynamometer Database.” [Online]. Available: https://www.anl.gov/es/ downloadable-dynamometer-database. [Accessed: 10-Jul-2020].

[14] J. G. Hayes and G. A. Goodarzi, *Electric Powertrain:Energy Systems, Power Electronics and Drives for Hybrid, Electric and Fuel Cell Vehicles, 1*st ed., Chichester, West Sussex, UK: Wiley, 2018, pp. 40-48.

[15] Argonne National Laboratory, “HEV test page at ANL.” [Online]. Available: https://www.anl.gov/es/hybrid-electric-vehicle-testing. [Accessed: 18-Jun-2019].

[16] R. C. Kroeze and P. T. Krein, "Electrical battery model for use in dynamic electric vehicle simulations," *2008 IEEE Power Electronics Specialists Conf.(PESC)*, Rhodes, 2008, pp. 1336-1342, doi: 10.1109/ PESC.2008.4592119.

[17] L. Lavigne, J. Sabatier, J. M. Francisco, F. Guillemard, and A. Noury, “Lithium-ion open circuit voltage (OCV) curve modelling and its ageing adjustment,” *J. Power Sources*, vol. 324, pp. 694–703, 30 August 2016, doi.org/10.1016/ j.jpowsour.2016.05.121.

[18] T. Mesbahi, N. Rizoug, P. Bartholomeüs, R. Sadoun, F. Khenfri and P. Le Moigne, "Dynamic model of Li-ion batteries incorporating electrothermal and ageing aspects for electric vehicle applications," in *IEEE Transactions on Industrial Electronics*, vol. 65, no. 2, pp. 1298-1305, Feb. 2018, doi: 10.1109/ TIE.2017.2714118.

[19] M. Einhorn, F. V. Conte, C. Kral and J. Fleig, "Comparison, selection, and parameterization of electrical battery models for automotive applications," in *IEEE Transactions on Power Electronics*, vol. 28, no. 3, pp. 1429-1437, March 2013, doi: 10.1109/TPEL.2012.2210564.

[20] A. Guha and A. Patra, "State of health estimation of lithium-ion batteries using capacity fade and internal resistance growth models," in *IEEE Transactions on Transportation Electrification*, vol. 4, no. 1, pp. 135-146, March 2018, doi: 10.1109/TTE.2017.2776558.

[21] R. T. Doucette and M. D. McCulloch, “Modeling the prospects of plug-in hybrid electric vehicles to reduce CO_2 emissions,” *Applied Energy*, vol. 88, no. 7, pp. 2315–2323, July 2011. doi.org/10.1016/j.apenergy.2011.01.045.

[22] E. A. Grunditz and T. Thiringer, "Characterizing BEV powertrain energy consumption, efficiency, and range during official and drive cycles from Gothenburg, Sweden," in *IEEE Transactions on Vehicular Technology*, vol. 65, no. 6, pp. 3964-3980, June 2016, doi: 10.1109/TVT.2015.2492239.

[23] G. Park, S. Lee, S. Jin, and S. Kwak, “Expert systems with applications integrated modeling and analysis of dynamics for electric vehicle powertrains,” *Expert Syst. Appl.*, vol. 41, no. 5, pp. 2595–2607, April 2014, doi.org/10.1016/j.eswa.2013.10.007

[24] A. Rahmoun and H. Biechl, “Modelling of li-ion batteries using equivalent circuit diagrams,” *Electrical Review (Prz. Elektrotechniczny)*, vol. 2, no. 7, pp. 152–156, January 2012.

[25] H. He, R. Xiong, H. Guo, and S. Li, “Comparison study on the battery models used for the energy management of batteries in electric vehicles,” *Energy Convers. Manag*., vol. 64, pp. 113–121, December 2012, doi.org/10.1016/j.enconman.2012.04.014

[26] H. He, R. Xiong, and J. Fan, “Evaluation of lithium-ion battery equivalent circuit models for state of charge estimation by an experimental approach,” *energies*, vol. 4, pp. 582–598, 29 March 2011, doi.org/10.3390/en4040582

[27] Y. Cao, R. C. Kroeze and P. T. Krein, "Multi-timescale parametric electrical battery model for use in dynamic electric vehicle simulations," in *IEEE Transactions on Transportation Electrification*, vol. 2, no. 4, pp. 432-442, Dec. 2016, doi: 10.1109/TTE.2016.2569069.

[28] *Secondary lithium-ion cells for the propulsion of electric road vehicles-Part 1: Performance testing*, IEC62660-1–2011, 2011.

[29] J. P. Christophersen, “Battery Test Manual for Electric Vehicles, Revision 3,” Idaho National laboratory, INL/EXT-15-34184, June 2015.

[30] Idaho National Laboratory, “PNGV battery test manual”, US Department of Energy, DOE/ID-10597, February 2001.

[31] M. Chen and G. A. Rincon-Mora, "Accurate electrical battery model capable of predicting runtime and I-V performance," in *IEEE Transactions on Energy Conversion*, vol. 21, no. 2, pp. 504-511, June 2006, doi: 10.1109/TEC.2006.874229.

[32] MATLAB, “MATLAB R2017b Simple battery model.” [Online]. Available: Simscape/Power Systems/Simscape Components/Sources /Battery. [Accessed: 23-Jul-2019].

[33] MATLAB, “MATLAB Generic battery model.” [Online]. Available: Simscape/Power Systems/Simscape Components/Sources /Battery. [Accessed: 22-Jun-2020].

[34] O. Tremblay, L. Dessaint and A. Dekkiche, "A generic battery model for the dynamic simulation of hybrid electric vehicles," *2007 IEEE Vehicle Power and Propulsion Conf. (VPPC)*, Arlington, TX, 2007, pp. 284-289, doi: 10.1109/VPPC.2007.4544139.

[35] O. Tremblay and L. Dessaint, “Experimental validation of a battery dynamic model for EV applications,” *World Electr. Veh. J.*, vol. 3, pp. 289–298, July 2009, doi.org/10.3390/wevj3020289.

[36] S. Bhide and T. Shim, "Novel predictive electric Li-ion battery model incorporating thermal and rate factor effects," in *IEEE Transactions on Vehicular Technology*, vol. 60, no. 3, pp. 819-829, March 2011, doi: 10.1109/TVT.2010.2103333.

[37] S. M. Mousavi G. and M. Nikdel, “Various battery models for various simulation studies and applications,” *Renew. Sustain. Energy Rev.*, vol. 32, pp. 477–485, April 2014, doi.org/10.1016/j.rser.2014.01.048.

[38] Y. Zhang, S. Lyden, B. A. L. de la Barra and M. E. Haque, "Optimization of Tremblay's battery model parameters for plug-in hybrid electric vehicle applications," *2017 Australasian Universities Power Engineering Conf. (AUPEC)*, Melbourne, VIC, 2017, pp. 1-6, doi: 10.1109/AUPEC.2017.8282405.

[39] C. M. Shepherd, “Design of primary and secondary cells,” *J. Electrochem. Soc.*, vol. 112, pp. 657–664, 1965, doi.org/10.1149/1.2423659

[40] N. Kim, A. Rousseau and E. Rask, "Parameter estimation for a lithium-ion battery from chassis dynamometer tests," in *IEEE Transactions on Vehicular Technology*, vol. 65, no. 6, pp. 4393-4400, June 2016, doi: 10.1109/ TVT.2015.2495322.

[41] R. Spotnitz, "Simulation of capacity fade in lithium-ion batteries," *J. Power Sources*, vol. 113, no. 1, pp. 72–80, 1 January 2003, doi.org/10.1016/S0378-7753(02)00490-1.

[42] J. McDowall, "Understanding lithium technology," in *Battcon*, Marco Island, FL, USA: 2008, pp. 1–10.

[43] J. Nadeau, M. R. Dubois, A. Desrochers and N. Denis, "Ageing estimation of lithium-ion batteries applied to a three-wheel PHEV roadster," *IEEE Vehicle Power and Propulsion Conference (VPPC)*, Beijing, 2013, pp. 1-6, doi: 10.1109/VPPC.2013.6671663.

[44] J. Remmlinger, M. Buchholz, M. Meiler, P. Bernreuter, and K. Dietmayer, "State-of-health monitoring of lithium-ion batteries in electric vehicles by on-board internal resistance estimation", *J. Power Sources*, vol. 196*,* no.12, pp.5357-5363, 15 June 2011, doi.org/10.1016/j.jpowsour.2010.08.035.

[45] J. Wang, P. Liu, J. Hicks-Garner, E. Sherman, S. Soukiazian, M. Verbrugge, H. Tataria, J. Musser and P. Finamore. "Cycle-life model for graphite-LiFePO 4 cells," *J. Power Sources*, vol. 196, no. 8, pp. 3942–3948, 15 April 2011, doi.org/ 10.1016/j.jpowsour.2010.11.134.

[46] M. Dubarry, N. Qin, and P. Brooker, "Calendar aging of commercial Li-ion cells of different chemistries – A review," *Curr. Opin. Electrochem.*, vol. 9, pp. 106–113, June 2018, doi.org/10.1016/j.coelec.2018.05.023

[47] D. Magnor and D. Uwe Sauer, "Concept of a battery aging model for Lithium-ion batteries considering the lifetime dependency," in *Proc. European Photovoltaic Solar Energy Conf.*, Hamburg, Germany, 2009, pp. 1–7.

[48] J. E. Harlow, X. Ma, J. Li, E. Logan, Y. Liu, N. Zhang, L. Ma, S. L. Glazier, M. E. Cormier, M. Genovese, S. Buteau, A. Cameron, J. E. Stark and J. R. Dahn, "A wide range of testing results on an excellent lithium-ion cell chemistry to be used as benchmarks for new battery technologies," *J. Electrochem. Soc.*, vol. 166, no. 13, pp. 3031–3044, 6 September 2019, doi: 10.1149/2.0981913jes.

[49] M. Ecker, N. Nieto, S. Kabitz, J. Schmalstieg, H. Blanke, A. Warnecke, D. Uwe Sauer, “Calendar and cycle life study of Li(NiMnCo)O2-based 18650 lithium-ion batteries,” *J. Power Sources*, vol. 248, pp.839-851, 2014, doi.org/10.1016/ j.jpowsour.2013.09.143

5 IPM MOTOR MODEL

A surface-mounted permanent magnet motor (SPM) was used in Chapter 2 for the development of the simplified electric vehicle powertrain (SEVP) simulator. However, the machine of choice in battery electric vehicles (BEVs) is the interior-permanent-magnet (IPM) synchronous motors. The IPM is a cross between a SPM and a reluctance machine.

In this chapter, an IPM motor model is developed that: (i) converts the output torque and speed requirements from the motor into input phase voltages and currents; (ii) estimates the motor's efficiency at each operating point; (iii) estimates the motor parameters using finite element analysis (FEA) software; (iv) validates the FEA models with test data from Oak Ridge National Laboratory (ORNL); (v) at each torque output, the IPM model identifies the speed at which the motor switches from maximum torque-per-amp (MTPA) mode to maximum-torque-per-volt (MTPV) mode; and (iv) the IPM model also incorporates the available dc voltage from the battery model, as described in Chapter 4, to dynamically alter the electrical performance of the IPM motor model.

The proposed IPM model shows a good correlation to test data for an IPM motor, published by Oakridge National Laboratory, and used in the 2004 version of the Toyota Prius. However, the model validation highlights that significant differences do exist, possibly due to the six-step operation used in the Prius motor testing.

This model development procedure resulted in the creation and documentation of a range of IPM finite element models for IPM motors rated from 50 kW to 165 kW. This research material provides a valuable resource for undergraduate teaching and for post-graduate research purposes.

5.1 Introduction

Permanent magnet synchronous machines (PMSM) are the preferred choice for the traction motor of a BEV due to their very high-power densities and high efficiencies. The classification of a PMSM is primarily based on the permanent-magnet (PM) topology implemented on the rotor. The two principle classes are: (i) SPM, where arc-shaped magnets are adhesively bonded to the surface of the rotor laminations, and (ii) IPM, where the PM's are embedded within the rotor laminations. The SPM topologies are easier to manufacture but have a lower constant power speed range (CPSR) that limits their maximum speed. Their CPSR is limited by the adhesive strength of the magnet bonding compounds and by the ability to provide sufficiently high phase currents during high-speed flux weakening operation.

The literature on IPM synchronous motors provides complex electrical circuit models to describe the torque-to-current relationships [1]-[7]. The complexity results from the non-linearities and the interdependencies between some of the motor parameters [8]-[10]. The SEVP model was primarily designed for energy loss estimation with a low computational load in a vehicle simulator [11]. The high complexity of existing IPM models is not compatible with this low computational modelling goal.

Within the family of PM synchronous motor designs, the SPM motor requires a less-complex electrical circuit model and its performance is similar to the IPM motor, in low to medium speed applications. In addition, the fundamental sources of energy loss do not differ significantly between the SPM and IPM motors. As outlined in Chapter 2, the SPM motor model implemented in the SEVP model required further simplifications such as (i) assuming high-speed operation without flux weakening and (ii) high-torque operation without magnetic saturation. While these simplifications were shown in Chapter 2 to have only minor impacts on the model in energy consumption estimation, the accuracy of this motor model in electrical circuit simulation can be enhanced.

The challenge addressed in this chapter is to replace the simplified SPM model with an IPM motor model that captures the torque-generating ability for BEV applications. The incorporation of maximum limits for the input phase voltage and input phase current in the model is required for accurate electrical circuit simulation. A simplified IPM model that features these functions provides an electrical

engineering educational resource for IPM studies, as well as a low-computational vehicle simulator model.

Modelling of IPM motors requires construction and operational performance data which is generally not published by vehicle manufacturers. Fortunately, the U.S. Department of Energy's (DOE) FreedomCAR and Vehicle Technologies (FCVT) program supported ORNL to research a range of hybrid-electric vehicle (HEV) and BEV technologies. ORNL benchmark tested vehicles from Toyota, Lexus, Honda and Nissan, and they published a series of very detailed technology benchmarking reports [12]-[16]. These ORNL reports contained the specifications of five IPM motors designed for HEV operation, four motors by Toyota\Lexus and one motor by Honda. The Honda motor is excluded from this analysis due to its low power and torque ratings which means that the motor is not suitable for BEV applications. ORNL also published some technical details of the 2012 Nissan Leaf IPM motor in the form of presentation slides [17].

As previously mentioned, the motor parameters necessary for an IPM model cannot be easily estimated from published motor data. Building test rigs and measuring these parameters on prototype motors for IPM motor performance characterisation is costly, time-consuming and complex. A widely used alternative method of studying these motors is to examine the motors' magnetic design using FEA models. The comprehensive construction details of the IPM motors within the ORNL reports provided the basis for developing this study's FEA motor models. The free-to-download FEA software package, FEMM, was selected to enable widespread applicability of any IPM models developed [18]. As FEMM offers only 2D model analysis, an alternative modelling method, involving post-processing of the FEA outputs in MATLAB or Excel, was necessary to implement simple rotor magnet skew designs, such as that found in the Leaf motor.

This chapter is organized as follows: Section 5.2 explains the principle differences in the operation of SPM and IPM motors; Section 5.3 outlines the development of FEA models for IPM motors and the testing procedures for these models; Section 5.4 presents the validation results on the developed FEA models. Section 5.5 describes the development of the IPM model using the FEA derived motor parameters. Section 5.6 reviews the validation results of the IPM model. The study conclusions are presented in Section 5.7. Additional modelling results are contained in Appendix C.

5.2 Differences between SPM and IPM Motors

In the simplified, non-saturated SPM motor model of the SEVP, the electromagnetic torque T_r and rms phase current I_{ph} are related by a constant torque constant k as shown by

$$T_r = 3kI_{ph} \tag{5.1}$$

As outlined in Chapter 2, the model is structured within a reference frame comprising direct and quadrature (dq) axes. The d-axis is the magnetic axis of the PMs and the q-axis represents the magnetic axis from the combined three phase currents. In a dq motor model, the phase current I_{ph} is subdivided into two per-phase rms axis currents, I_d and I_q. The dq model represents the torque output equation for a three-phase SPM or IPM motor with p poles as

$$T_r = 3\frac{p}{2}\left[\psi_d I_q - \psi_q I_d\right] \tag{5.2}$$

where ψ_d and ψ_q are the d-axis and q-axis flux linkages. The axes' flux linkages can be converted to a PM flux linkage ψ_{pm}, a d-axis inductance L_d, and a q-axis inductance L_q to give

$$T_r = 3\frac{p}{2}\left[\psi_{pm} I_q + \left(L_d - L_q\right) I_d I_q\right] \tag{5.3}$$

As the PM flux linkage is related to the motor constant k value by

$$k = \frac{p}{2}\psi_{pm} \tag{5.4}$$

a simplified motor torque output equation is provided by

$$T_r = 3kI_q + 3\frac{p}{2}\left(L_d - L_q\right) I_d I_q \tag{5.5}$$

Equation (5.5) shows that the electromagnetic torque output from SPM and IPM motors is the combination of the permanent-magnet torque term $T_{pm} = 3kI_q$ and a

synchronous-reluctance torque term $T_{sr} = 3\frac{p}{2}(L_d - L_q)I_d I_q$. The value of T_{sr} depends on the difference in the *d*- and *q*-axis inductance values. Idealised models of SPM motors represent these designs with only T_{pm}, hence their torque output is given by (5.1). This simplification may be understood by an examination of the axis inductances.

5.2.1 Axis Inductances

In [19], a simplified estimate of an axis pole-pair inductance is made using

$$L_{pole-pair} = 2\frac{\mu_o N_{coil}^2 \pi r l_{mot}}{l_{gap} p} \tag{5.6}$$

where N_{coil} is the turns per coil, r is the radius at the midpoint of the stator-rotor airgap, l_{mot} is the rotor length and l_{gap} is the effective width of the low permeability sections in the magnetic path of the relevant axis. Figure 5-1 illustrates the differences in the magnetic gap lengths for each axis in both SPM and IPM motors.

Figure 5-1(a) illustrates one pole of an eight-pole SPM motor. As the permeability of each PM is close to 1, the value of l_{gap} in the *d*-axis is the combination of the PM thickness and the small physical airgap between the rotor and stator. This results in a large value of l_{gap} and a corresponding low value of inductance L_d. From Figure 5-1(a), it is clear that the value of l_{gap} is approximately the same in both *d*- and *q*-axes resulting in low values of L_d and L_q that are approximately equal in an SPM motor. From (5.5), a simple SPM motor is modelled with no reluctance torque output as L_d is equal to L_q.

The equivalent IPM motor, as shown in Figure 5-1(b), has a large value of l_{gap} in its *d*-axis but a considerably smaller value in its *q*-axis. This results in a low value of L_d and a high value of L_q in this IPM motor. From (5.5), the IPM motor produces significant reluctance torque output during flux weakening when the I_d current has negative values.

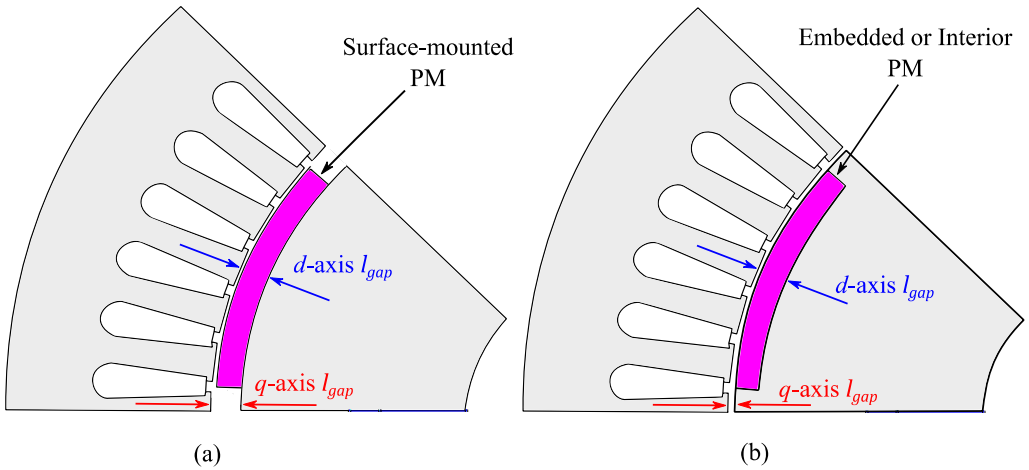

Figure 5-1. Magnetic gap differences for axis inductances for (a) SPM and (b) IPM motors.

5.2.2 IPM Rotor Topologies

Arc-shaped magnets, used in the IPM design shown in Figure 5-1(b), are expensive to manufacture and alternative IPM rotor topologies that use lower-cost rectangular shaped magnets are more commonly found in HEV and BEV designs. A range of PM rotor topologies are illustrated in Figure 5-2. The choice of topology impacts peak torque output, cogging torque, PM demagnetisation, mechanical stress and torque segregation between magnetic or reluctance torque. In general, topologies with thicker magnets such as in Figures 5-2(b), (e) provide improved demagnetisation performance and suffer less from mechanical stress. Double-layer magnetic configurations such as the delta-shaped topology in Figure 5-2(c), the double V-shaped topology in Figure 5-2(d) or the VU topology in Figure 5-2(f), have lower *d*-axis inductances that result in higher levels of reluctance torque. The delta-shaped topology in Figure 5-2(c) provides the highest torque output for operation below the rated or base speed but it requires high levels of flux weakening above this rated speed which can limit its CPSR. A comprehensive list of the attributes of each PM topology is provided by various research studies published in the literature [20]-[24]. Three of the IPM motors in this study have V-shaped PM topologies and two motors have delta-shaped PM topologies.

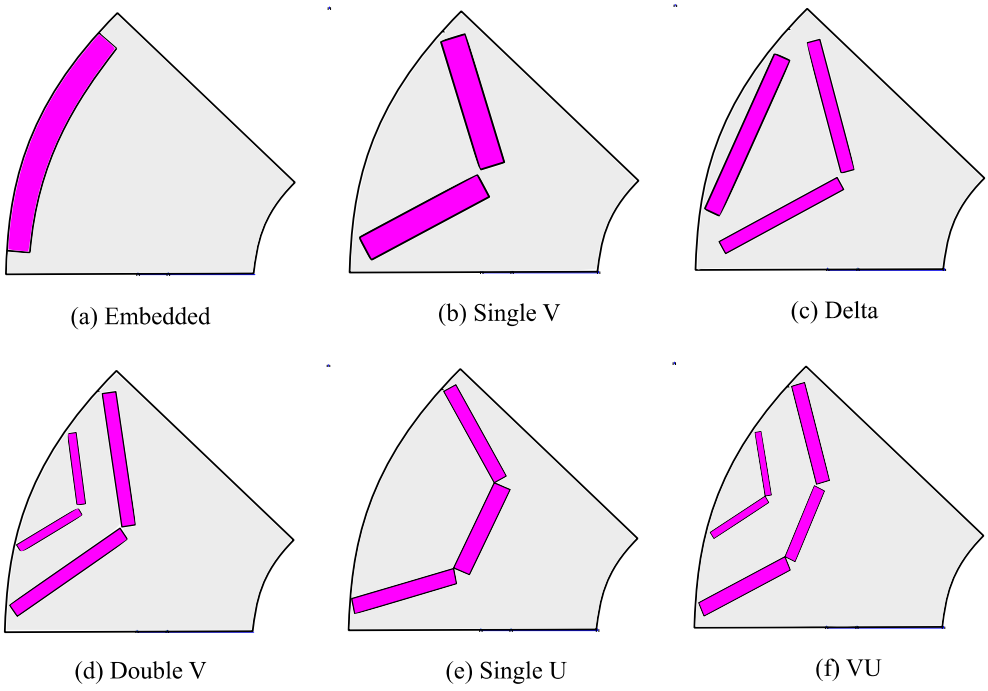

Figure 5-2. Various PM rotor topologies for IPM motors.

5.2.3 Advanced IPM Motor Models

Based on (5.5), the theoretical torque outputs from an IPM motor are illustrated in Figure 5-3. In an SPM motor, optimum torque generation is achieved when the phase current is vector-controlled to be in phase with the back-emf. As shown in Figure 5-3, this mode of operation in an IPM motor does not achieve maximum torque output. MTPA operation in an IPM motor occurs when operating with phase advance angles greater than 90° and this mode is achieved with negative values of I_d. In a SPM motor, negative I_d is only associated with flux-weakening operation or MTPV operation above rated speed. Conversely, in an IPM motor, a negative I_d value is a requirement for below-the-rated-speed operation to achieve maximum torque output and it is an above-rated-speed requirement for flux-weakening operation. One of the complexities in developing an IPM motor model comes from the difficulty in

determining the required phase advance angle, as this angle is a function of system efficiency, the output torque required and the operating speed of the motor [25]-[28].

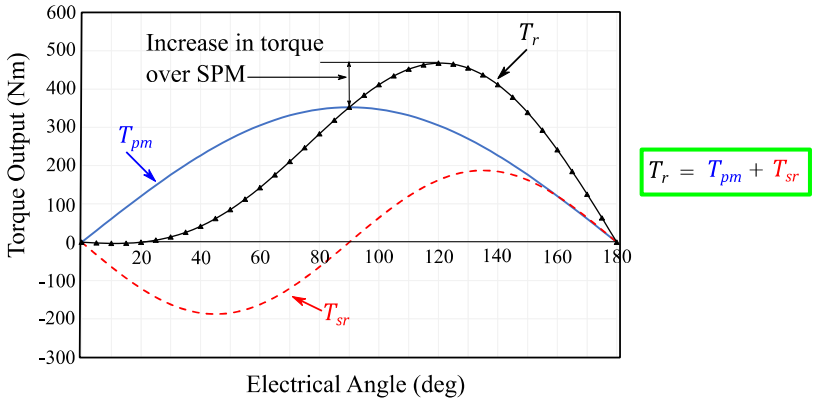

Figure 5-3. Theoretical torque outputs from an IPM motor.

5.2.3.1 Operation within Phase Current and Voltage Limits

The *dq* equivalent per-phase circuit diagrams for an IPM motor are shown in Figure 5-4. The relationship between the input phase current and the *dq* axis current is

$$I_{ph}^2 = I_d^2 + I_q^2 \tag{5.7}$$

and the corresponding voltage relationship is

$$V_{ph}^2 = V_d^2 + V_q^2 \tag{5.8}$$

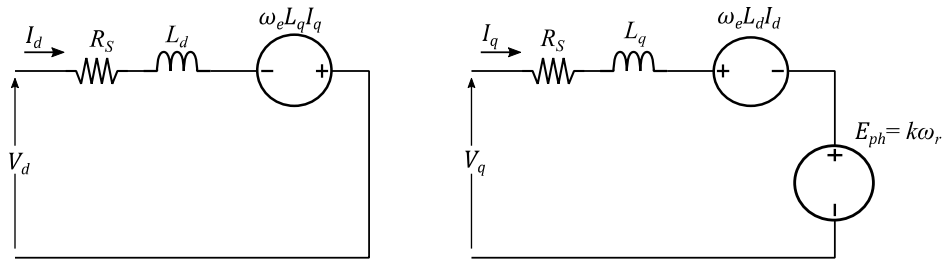

(a) *d*-axis equivalent electrical circuit (b) *q*-axis equivalent electrical circuit

Figure 5-4. IPM motor equivalent circuits in *dq* reference frame.

Derived from the equivalent circuit, the *dq* axis voltages are represented by the voltage drops across each component. For steady-state analysis, the dynamic voltage drops across L_d and L_q are assumed to be zero and by representing the angular electrical frequency ω_e by its equivalent rotor speed ω_r, the resultant phase voltage is calculated by

$$V_{ph}^2 = \left(R_S I_d - \left(\frac{p}{2}\right)\omega_r L_q I_q\right)^2 + \left(R_S I_q + \left(\frac{p}{2}\right)\omega_r L_d I_d + k\omega_r\right)^2 \tag{5.9}$$

Simplifying this equation, by neglecting the small voltage drops across R_S and rearranging the remaining parameters in terms of the axis currents I_d, I_q gives

$$\left(\frac{V_{ph}}{\left(\frac{p}{2}\right)\omega_r L_q}\right)^2 = \left(I_q\right)^2 + \left(\left(\frac{L_d}{L_q}\right)I_d + \frac{k}{\left(\frac{p}{2}\right)L_q}\right)^2 \tag{5.10}$$

For motor operation with a specified maximum phase current and a maximum phase voltage, (5.7) and (5.10) represent constraints on the allowable axis currents. These constraints are presented in Figure 5-5. When these are drawn in a *dq* reference frame diagram, the maximum phase current imposes an axis current constraint represented as a circular phase current limit boundary. The maximum phase voltage imposes further axis current constraints represented by a set of speed-dependent ellipses.

Based on (5.10), the calculation of the axis current constraints due to the maximum phase voltage requires knowledge of the internal parameters k, L_d and L_q of the motor. As the motor speed increases, this voltage-dependent constraint restricts the I_q current range and the torque output becomes increasingly dependent on the synchronous-reluctance torque T_{sr} produced by the negative I_d current.

The voltage limits in Figure 5-5 are drawn based on the assumption that the three relevant motor parameters k, L_d and L_q are constant for all values of I_d and I_q. However, the literature on IPM motor design represents both the *d*-axis and the *q*-axis inductances as more complex parameters due to the effects of saturation in IPM motors. This saturation leads to two impacts; (i) a change in axis inductance due to a change in its corresponding axis current; for instance, a change in L_q due to a changing

value of I_q; (ii) cross-magnetisation effects between the two axes, such as a change in L_q due to a change in I_d.

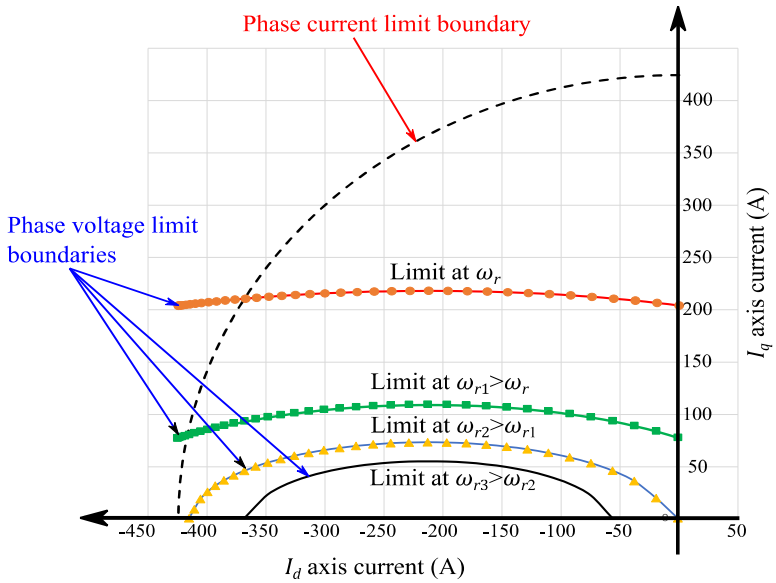

Figure 5-5. Phase current and voltage limits shown in *dq* reference frame.

5.2.3.2 Impacts of Cross-Magnetisation on Torque and Voltage

Cross-magnetisation occurs as the magnetic paths of the *d*-axis and the *q*-axis share common sections in the rotor and stator. As the magnetic properties of these shared sections are altered by one axis current, the inductance value of the second axis also changes. In [8], this cross-magnetisation is represented by two addition motor inductances, L_{dq} and L_{qd}. The change in *d*-axis inductance due to a change in the *q*-axis is defined as

$$L_{dq} = \frac{\Delta\psi_d}{\Delta I_q} \qquad \text{with a constant } I_d \tag{5.11}$$

where $\Delta\psi_d$ represents the change in the *d*-axis flux linkage due to a change ΔI_q in the value of I_q while I_d is kept constant. The second cross-magnetising inductance is defined as

$$L_{qd} = \frac{\Delta\psi_q}{\Delta I_d} \qquad \text{with a constant} \quad I_q \tag{5.12}$$

where $\Delta\psi_q$ represents the change in the q-axis flux linkage due to a change ΔI_d in the value of I_d while I_q is kept constant.

As previously mentioned, the magnetic saturation results in a dependence of ψ_d on I_d and ψ_q on I_q. Combining this saturation, with the cross-magnetisation, results in L_{dq} and L_{qd} values that are simultaneously dependent on the values of both axis currents. In [8], the torque equation for the IPM motor is modified from (5.5) to incorporate these cross-magnetisation inductances and is given as

$$T_r = \frac{3}{2}\frac{p}{2}\left[\psi_{pm,d} i_q - \psi_{pm,q} i_d + \left(L_d - L_q\right) i_d i_q + \left(L_{dq} i_q^2 - L_{qd} i_d^2\right)\right] \tag{5.13}$$

where $\psi_{pm,d}$ is the PM flux linkage in the d-axis, $\psi_{pm,q}$ is the PM flux linkage in the q-axis, i_q is the peak q-axis current and i_d is the peak d-axis current. As in [8], if the value of $\psi_{pm,q}$is assumed to be relatively small and the axis currents are converted to their per-phase rms equivalent values, the torque of an IPM motor is given as

$$T_r = 3kI_q + 3\frac{p}{2}\left[\left(L_d - L_q\right) I_d I_q + \left(L_{dq} I_q^2 - L_{qd} I_d^2\right)\right] \tag{5.14}$$

In addition to impacting the torque equation, the cross inductances also impact the voltage equation of the motor. The addition of these cross-inductance voltage drops changes (5.9) to

$$V_{ph}^2 = \left[R_S I_d - \left(\omega_e\left(L_q I_q + L_{qd} I_d\right)\right)\right]^2 + \left[R_S I_q + \left(\omega_e\left(L_d I_d + L_{dq} I_q\right)\right) + k\omega_r\right]^2 \tag{5.15}$$

where the angular frequency ω_e is defined as

$$\omega_e = \left(\frac{p}{2}\right)\omega_r \tag{5.16}$$

5.2.3.3 Flux Weakening in an IPM Motor

As the speed in an IPM motor increases, the back-emf voltage $k\omega_r$ and each axis voltage increases, assuming constant values of I_d and I_q. When the maximum phase voltage is reached, higher motor speeds are only possible by reducing the voltage drops across the inductances by an amount equal to the increase in the back-emf. As previously explained in Chapter 2, an increase in the negative value of I_d is required to achieve the voltage reduction required.

In an SPM motor, an increase in the negative value of I_d has no impact on the torque output. However, in an IPM, the reluctance torque is dependent on the value of I_d and any increase in this current for flux-weakening operation results in an increase in torque output unless the I_q current is simultaneously decreased to maintain a constant torque output. This interdependency between voltage control and torque control makes the flux-weakening process more complex in an IPM motor. In addition to this interdependency, magnetic saturation further complicates the process. Any change in an axis current results in a change in values of both axis inductances and cross inductances values. In Section 5.5, the IPM motor model developed addresses all of these interactions.

Equations (5.14) and (5.15) are applied to develop an IPM motor model for a simulator. The next section presents the methods used to build an FEA motor model which establishes the required motor parameters for these equations.

5.3 FEA Model Development

A summary of the design specification parameters of five IPM motors is provided in Table 5-1. The use of HEV motors in this BEV motor study is justified as the four HEV motors have peak torque levels of 200-400 Nm and power output levels of 80 -125 kW consistent with the observed levels in BEVs [29].

Table 5-1. Summary details of IPM motors modelled.

Parameters	**Units**	**Prius04 (HEV)**	**Prius10 (HEV)**	**Leaf (BEV)**	**Camry (HEV)**	**LS600h (HEV)**
Peak Power	kW	50	60	80	105*	165**
Peak Torque	Nm	400	207	280	207	300
Max Speed	rpm	6,000	13,500	10,390	14,000	10,230
Voltage Range	Vdc	200-500	200-650	250-400	250-650	288-650
Source Vehicle		2004 Prius	2010 Prius	2012 Leaf	2007 Camry	2008 LS600h

* ORNL testing of Camry limited to approx. 60 kW due to cooling issues.

** ORNL testing of LS600h limited to approx. 106 kW due to test setup at facility.

Motor performance characterisation requires the identification of two key traits of the motor, the back-emf constant k established using a no-load spin test and the phase-current torque output relationship established using locked-rotor tests. Additional testing is required to establish motor efficiency, typically accomplished by estimating ohmic losses in the windings and iron losses in the core.

The comprehensive construction details of the IPM motors in the ORNL reports provided the basis for developing FEA motor models. The free-to-download FEA software package, FEMM, was selected to enable widespread availability of any models developed [18]. The motor performance test results published in the ORNL reports then allowed the customisation of the material properties of the FEA models to replicate their performance in the models.

5.3.1 Dimensional Construction of FEA Model

The FEA model development began by using the dimensional data in the ORNL reports to draw the stator and rotor structures in FEMM. Few details of the Leaf motor are available in the ORNL publications. However, the motor designs can be approximated using other references [17],[30],[31]. Despite FEMM's simple drawing tools, complex shapes such as stator winding slots, as shown in Figure 5-6, can be implemented by utilizing the symmetry of the shapes involved. As these motor designs are symmetrical, only one of the eight motor poles is required for each FEA model.

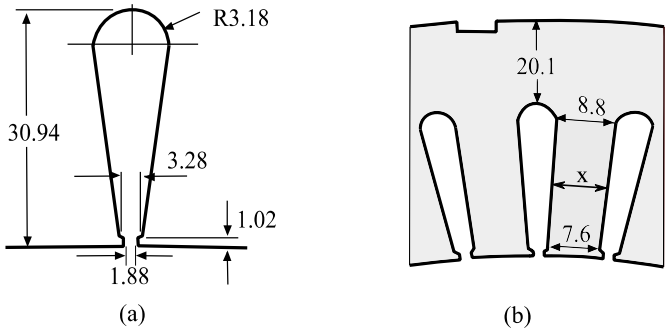

Figure 5-6. Stator slot details for (a) Camry and (b) LS600h.

The dimensional data extracted from various ORNL reports is summarised in Table 5-2. In addition, this table contains winding details for the motors. A review of the stator construction details showed a significant number of common characteristics between the designs.

Table 5-2. Construction details of five IPM machines.

Parameters	Units	Prius04	Prius10	Leaf	Camry	LS600h
Rated power	kW	50	60	80	105	165
Max. speed	rpm	6000	13500	10890	14000	10230
DC voltage range	V	200-500	200-650	250-400	250-650	288-650
Rated torque	Nm	400	207	280	207	300
Number of poles	#	8	8	8	8	8
PM configuration		V-shape	V-shape	Delta	V-shape	Delta
Stator length	mm	84	50.8	151	60.7	135.4
Stator OD	mm	269	264	200	264	200
Stator ID	mm	161.9	161.9	131	161.9	130.86
Stator slots	#	48	48	48	48	48
Airgap	mm	0.73	0.73	0.5	0.73	0.89
Rotor length	mm	83.6	50.165	151	62	135.9
Rotor OD	mm	160.5	160.4	130	160.5	129.1
Rotor ID	mm	111	51	NA	105	53
Rotor slew		No	No	Yes	No	No
Wire size	AWG	20	20	20	20	20
Turns per coil	#	11	11	8	14	7
Coils in series	#	8	8	2	4	4
Coils in parallel	#	0	0	4	2	2
Phase resistance	Ω	0.077	0.077	0.00567	0.023	0.0225
PM (V-shape) quantity	#	16	16	288	16	32
PM length	mm	83.1	49.3	8.36	60.6	66.4
PM width	mm	18.9	17.88	28.9	19.1	18.7
PM thickness	mm	6.5	7.16	3.79	6.6	3.05
	Additional Leaf and LS600h PM magnet details for top part of Delta					
PM (top) quantity	#	-	-	144	-	16
PM length	mm	-	-	8.34	-	66.4
PM width	mm	-	-	21.3	-	18.7
PM thickness	mm	-	-	2.29	-	3.05
Lam thickness	mm	0.305	0.305	NA	0.31	0.28

5.3.1.1 Rotor Designs

The rotor designs are characterized by the configuration of their PMs. The two types of PM configurations found in the motors of this study are illustrated in Figures 5-7 and 5-8. The PM configuration on the 2004 Prius, 2010 Prius and Camry is a "V-shape" topology. In Figure 5-7, the 2010 Prius and Camry rotor designs are shown to be identical apart from their internal diameters. The Leaf and LS600h motors have a "Delta-shape" PM configuration as illustrated in Figure 5-8. The rotor stack length is approximately equal to the length of the PM in both Prius motors and in the Camry motor. In the LS600h motor, two PMs are used over the length of its rotor and the Leaf motor uses eighteen PMs over the length of its rotor. In addition, the Leaf motor includes a mid-rotor skew of 3.75° mechanical degrees in the alignment of these magnets. The skew is implemented in the 2D FEA software by initially modelling half the motor length and then modifying the FEA results in post-processing software to obtain the full-length results.

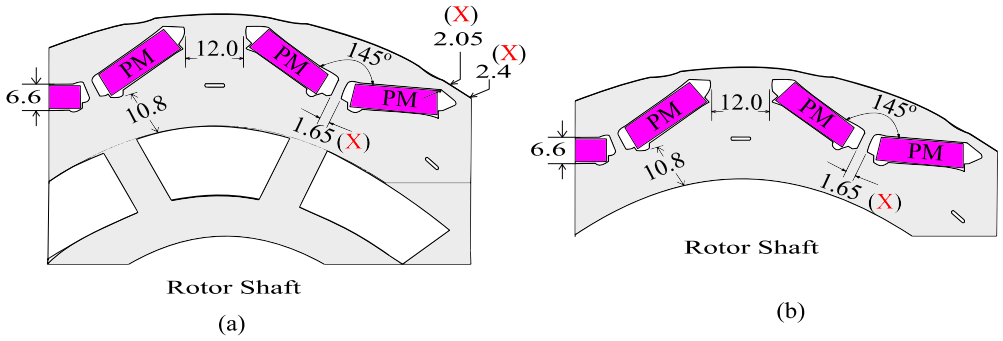

Figure 5-7. V-shaped PM configurations in (a) 2010 Prius and (b) Camry.

When drawing the FEA motor models, there are a number of critical dimensions which are marked with an "X" in Figures 5-6 (b), 5-7 and 5-8 (a). In the stator designs, the width of the teeth determines the current value at which saturation takes place, which in turn leads to changes in the values of L_d and L_q. In the rotor design, oversizing the narrow flux bridges results in lower torque outputs from the models. The minimum q-axis dimension, given as 12mm in Figure 5-7. and as 6.75mm in Figure 5-8 (a), determines the reluctance torque available at the maximum currents.

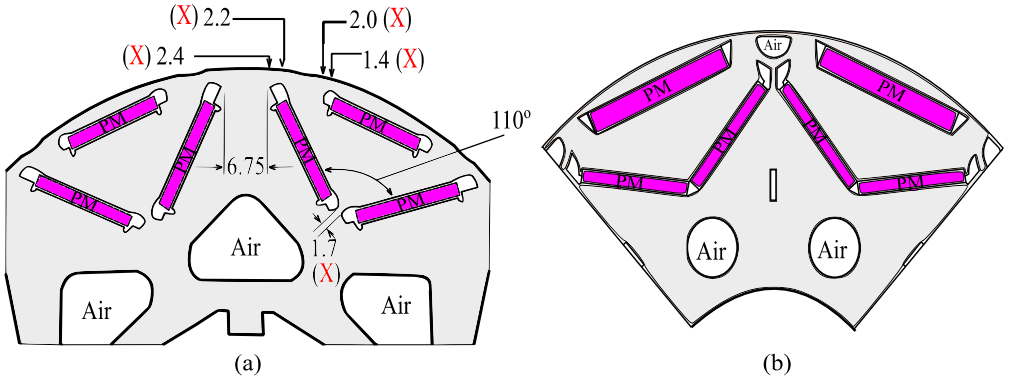

Figure 5-8. Delta-shaped PM configurations in (a) 2008 LS600h and (b) 2012 Leaf.

5.3.2 FEA Model Material Properties

Once a dimensionally precise representation of the motor is achieved in the FEA software, the accuracy of the model in determining motor performance characteristics principally depends on specifying the properties of the PMs. The PMs require a high remanent flux density B_r for torque production as well as a high intrinsic coercivity H_{cJ} to prevent the stator winding currents from demagnetizing the PMs.

The ORNL reports state that in the Prius, Camry and LS600h, the HEV motors use neodymium-iron-boron (NdFeB) magnets. ORNL tested the PM properties and their test results match several products offered by NdFeB manufacturers, such as Hitachi [32] and Arnold [33]. In the ORNL report on the 2010 Prius, the Hitachi Neomax PM range is mentioned as a potential magnet for this IPM Motor. The B-H characteristics of the Neomax F-series, at 20°C, are shown in Figure 5-9. Research by [31] concludes that the PMs used in the Leaf motor are similar to a PM from the Arnold N28AH product range.

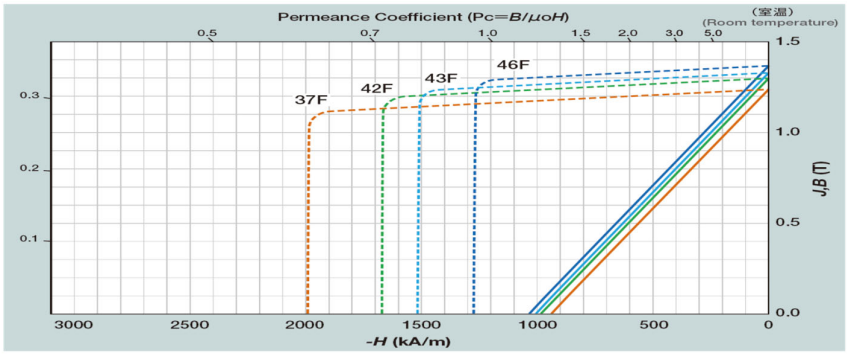

Figure 5-9. Hitachi NMX F-series Permanent Magnets at room temperature [32].

Typically, the temperature coefficients of these commercial PMs are quoted as -0.12 %/ºC for B_r and -0.393 %/ºC for H_{cJ}. ORNL tests on the PMs over a wide temperature range, as shown in Figure 5-10, confirm these temperature coefficients. The temperature coefficients are required to adapt the published magnetic values to match the operating temperature of the rotor under load. The FEMM software model for a PM is achieved by converting the B_r value to a coercivity H_{cB} value using

$$B_r = \mu_0 \mu_r H_{cB} \tag{5.17}$$

where μ_0 is the permeability of free space ($4\pi \times 10^{-7}$), μ_r is the relative permeability value and the coercivity H_{cB} has units of kA/m (1kOe=79.577 kA/m). The B_r has units of Tesla, where 10 kG equals 1 T. The default FEMM μ_r value for sintered NdFeB is 1.05 and this value was applied in all of the motor models in this study.

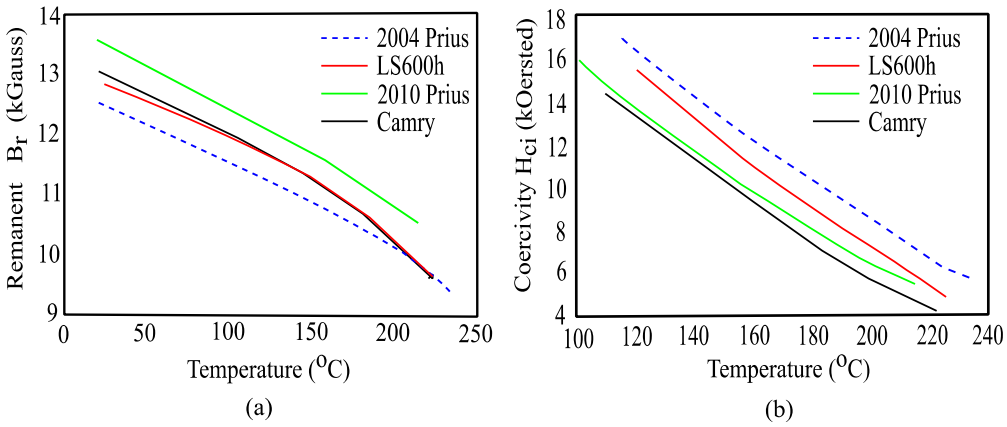

Figure 5-10. (a) Remanent flux densities B_r and (b) Intrinsic coercivities H_{ci} of PM

Rotor temperatures are extremely difficult to measure directly. The ORNL measurements of the stator winding temperatures in the Leaf were used to approximate the operating temperatures of the PM during motor back-emf or locked-rotor performance testing [17]. As shown in Figure 5-11, the stator temperatures varied from 60°C to 135°C and it is reasonable to assume that the rotor temperatures will be slightly higher than the reported stator temperatures.

The PM selection approach followed in this study assumed that ORNL back-emf testing was performed at low rotor temperatures and the FEA model PM's properties were selected to achieve the same back-emf performance as ORNL reported. The temperature coefficients of these PMs were then applied to their H_{cB} values for locked-rotor testing, using the chart in Figure 5-11 as a guide to the expected rotor temperatures.

Following the building of the FEA models, software code was required to simulate each of the physical tests normally conducted to characterise the performance of these motors. This code allows control of the relative movement between the stator and rotor in the model. As each simulation test may involve multiple modifications to the FEA model as it is rotated, it is common practice to use a separate supervisory software package to control the FEA software. These simulation test techniques are outlined in the next section.

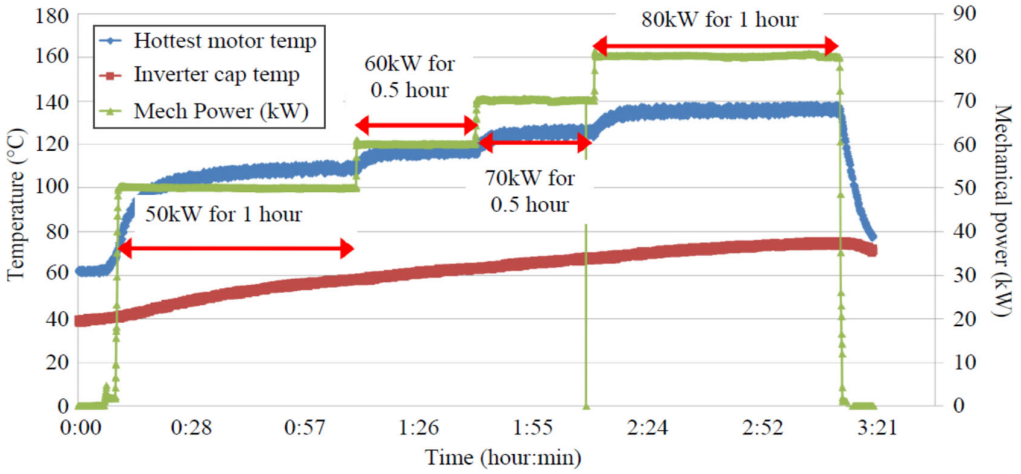

Figure 5-11. ORNL stator winding temperatures for the Leaf motor [17].

5.3.3 FEA Techniques for Motor Characterisation

Characterisation of the IPM motor requires establishing (1) the back-emf of the motor, (2) the synchronous *dq* axis inductances and cross-magnetisation inductances, (3) the locked-rotor torques with respect to electrical angle and (4) the motor losses. The techniques used to identify each of these parameters are outlined in the following sections, with sample test software provided in Appendix C.

5.3.3.1 Back-EMF

The back-emf of the motor is determined from the pole-pair flux-linkages ψ_{pole_pair} of each phase in the FEA model. These pole-pair flux linkages must then be converted to pole flux linkages ψ using the number of coils in series Z_{ser} divided by the number of parallel paths Z_{leg}, as determined by

$$\psi = \psi_{pole\_pair} \times \frac{Z_{ser}}{Z_{leg}} \tag{5.18}$$

In the model, as the rotor position changes relative to the stator, the back-EMF may be estimated by recording each phase-winding's flux-linkages, with all of the phase currents set to zero, using

$$e = -\frac{d\psi}{dt} = -\frac{d\psi}{d\theta}\frac{d\theta}{dt} = -\omega_e \frac{d\psi}{d\theta} \tag{5.19}$$

where e is the phase to neutral back-EMF, ψ is one phase winding pole flux linkage and ω_e is the electrical angular speed of the rotor [8].

In FEMM, small incremental changes in the rotor position with respect to the stator, may be automated using a scripting software called LUA or by using MATLAB. LUA commands rotation of the FEA model rotor components by a fixed angle and then completes the model by redrawing the airgap boundary lines between the stator and the rotor. This technique results in slow simulation speeds when a large number of rotor positions are required for a test. The LUA script only provides a reduced instruction set and has limited ability to manipulate the simulation test results into useful charts and diagrams. An alternative technique, called the moving-band or the sliding-band technique [34], achieves very similar results at higher simulation speeds as it does not involve the redrawing of the model at each step. The implementation of this technique in FEMM requires a higher-level supervisory software package such as MATLAB. The vast instruction-set of MATLAB also provides for post-processing of the simulation test results for motor characterisation. In this study, the sliding-band technique, controlled by MATLAB, was used extensively to characterise the five motors.

5.3.3.2 Determination of Inductances

Estimation of the *d*-axis and the *q*-axis inductances is based on the three-phase winding flux-linkages ψ_a, ψ_b, ψ_c, at two specific rotor positions: (i) at zero electrical degrees, θ = 0° where *q*-axis current is zero, and (ii) at ninety electrical degrees , θ = 90° where *d*-axis current is zero. The phase flux linkages are converted to *d*-axis and *q*-axis flux linkages using

$$\psi_d = \frac{2}{3}\left[\psi_a \cos(\theta) + \psi_b \cos\left(\theta - \frac{2\pi}{3}\right) + \psi_c \cos\left(\theta + \frac{2\pi}{3}\right)\right] \tag{5.20}$$

$$\psi_q = \frac{2}{3}\left[-\psi_a \sin(\theta) - \psi_b \sin\left(\theta - \frac{2\pi}{3}\right) - \psi_c \sin\left(\theta + \frac{2\pi}{3}\right)\right] \tag{5.21}$$

Simulation testing must be performed over the full range of motor currents to fully characterise magnetic saturation that results from high current operation. The axis inductance values for a range of currents, required for torque calculations in (5.5) or in (5.14), can then be extracted using

$\theta = 0°$, $$\psi_d = \psi_{pm,d} + L_d I_d \tag{5.22}$$

$\theta = 90°$, $$\psi_q = \psi_{pm,q} + L_q I_q \tag{5.23}$$

where $\psi_{pm,d}$ is the d-axis PM flux linkage and $\psi_{pm,q}$ is the q-axis PM flux linkage, both measured when the phase current is zero and $\theta = 90°$.

Cross-magnetisation inductances are simultaneously estimated during the axis inductance tests. For instance, when $\theta = 90°$ the change in ψ_d for a given change in I_q, allows L_{dq} to be estimated using (5.11). Similarly, when $\theta = 0°$ the change in ψ_q for a given change in I_d, allows L_{qd} to be estimated using (5.12).

5.3.3.3 Locked-Rotor Torques

As shown in Figure 5-3, operation of the motor at MTPA requires establishing the optimum electrical angle for torque production at each value of phase current. During locked-rotor testing, a dc test current $I_{test-dc}$, equivalent to $\sqrt{2}I_{ph}$, is supplied into a single-phase winding and this current is assumed to split evenly between the other two phase windings. The rotor section of the model is turned in small increments, from 0° electrical to 180° electrical, and the torque is measured at each increment to establish the optimum electrical angle for MTPA operation. This procedure is repeated at several $I_{test-dc}$ amplitudes to establish the function of the phase current to torque relationship. In addition, the torques recorded at an electrical angle of 90° permit the visualisation of any possible magnetic saturation at high currents and of the resultant variation in motor parameter k using

$$T(90°) = 3k\frac{I_{test-dc}}{\sqrt{2}} = 3kI_q \tag{5.24}$$

5.3.3.4 Motor Losses

Based on a specific torque/speed requirement of the motor, FEMM models can estimate the associated losses in the motor. The calculation of total motor losses requires estimation of the following losses; the ohmic losses which are also known as copper or winding losses; the core losses, comprising hysteresis and eddy current losses in the magnetic core; the proximity losses and the magnet losses.

In IPM motors, the ohmic losses occur in the stator windings while the core losses are distributed between the stator and rotor. In a 2D FEMM model, the stator resistance value is estimated only on the length of the copper in the stator slots and the end-turn length must be added to estimate the resistance for a full winding length [35]. The ORNL reports provided average phase winding resistance values. The ohmic losses are a function of the amplitudes of the phase currents and winding temperatures.

The core losses are typically calculated using the Steinmetz equation and may be estimated using the frozen permeability method as the rotor completes a 360-degree mechanical rotation [36]. These losses are a function of the motor speed, the phase advance angle, and the flux density B in the iron due to the magnitude of the phase currents. The iron loss is calculated using

$$P_{core} = k_h f B^2 + k_e f^2 B^2 + k_\alpha f^2 B^2 \tag{5.25}$$

where k_h is the iron hysteresis loss coefficient, k_e is the eddy current loss coefficient, k_α is proximity loss coefficient and f is the electrical frequency of the motor at a given motor speed. In this study, the proximity loss is assumed to be zero and the hysteresis and eddy current coefficients are assumed in [35] to be k_h = 143 and k_e = 0.53. The flux density is calculated for each element of the mesh in the FEA model. The loss in each mesh element of the FEA model is then summed to estimate the total iron loss in the motor. The MATLAB code for this calculation is included in Appendix C.

The modelling techniques outlined in this Section were applied to all five IPM motor models. The results obtained are summarised in the next section.

5.4 Validation of FEA Models for IPM Motors

The characterisation results presented in this section are mainly from the 2004 Prius HEV IPM motor and the 2012 Nissan Leaf BEV IPM motor. The 2004 Prius motor was chosen as the ORNL published data on this motor contain the greatest level of operational details useful for FEA model validation. The Leaf motor was chosen as it represents the only BEV IPM motor tested by ORNL. The three other HEV motors were also characterised and a summary of their validation results is provided in Appendix C. Simulation results for back-emf, inductance, locked-rotor torques, and motor losses are presented next.

5.4.1 Back-EMF

The rms values of the back-emf from all five vehicles, over the speed range of 0 to 10,000 rpm, are presented in Figure 5-12. This diagram shows the general correlation between the ORNL test measurements and the FEA model results for all five motors. The high values of the back-emfs indicate that flux weakening is required in all of these motors when operating at high speed. For instance, the Leaf motor is required to operate with a minimum battery voltage of 250V which is equivalent to a maximum input rms phase voltage V_{ph} of 102.5Vrms based on SVM operation in the inverter (m = 1.15).

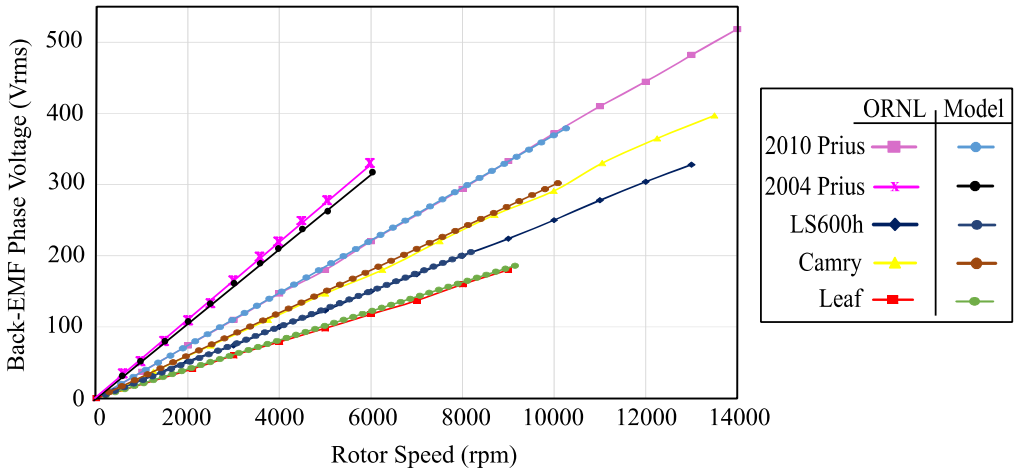

Figure 5-12. Back-emf results for all five IPM motors studied.

As the back-emf cannot exceed the input phase voltage when motoring, flux-weakening is required in the Leaf motor at all speeds greater that 5,000 rpm for this no-load torque test condition. At higher torques, the additional voltage drops across the axis inductances and stator resistances result in a requirement for flux weakening at speeds less than 5,000 rpm.

5.4.2 Inductance

The phase winding flux linkage simulation values were converted to inductances using the procedure outlined in Section 5.3.3.2. Figure 5-13 presents the axis inductance values in the 2004 Prius and Leaf IPM motors. A large change in *q*-axis inductance is associated with the magnetic saturation that occurs at high *q*-axis currents is present, and it is shown in Figure 5-13(a) for the 2004 Prius and in Figure 5-13(b) for the 2012 Leaf. The *d*-axis inductance shows little variation with *d*-axis current due to the low permeability of the PMs. The 2004 Prius inductance values are in agreement with the *q*-axis value of 5 mH and *d*-axis value of 1.7 mH stated in the ORNL report [12]. Validation of the inductance changes with current and the inductance values of the other four motors was not possible, as ORNL did not publish this data.

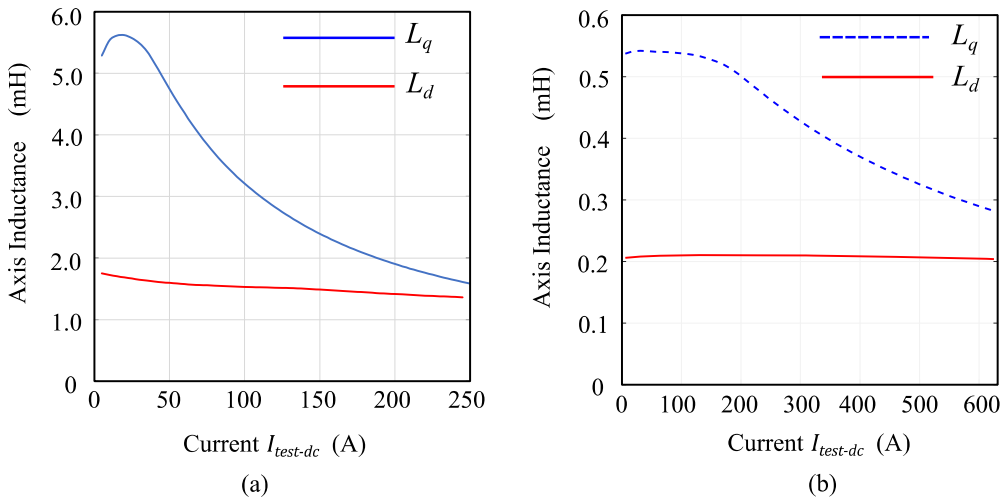

Figure 5-13. Axis inductances (a) 2004 Prius and (b) 2012 Leaf.

The measured cross-magnetisation inductances are displayed in Figure 5-14. Consistent with the literature, the V-shaped PM topology of the 2004 Prius shows higher levels of cross-magnetisation than the delta PM topology of the Leaf.

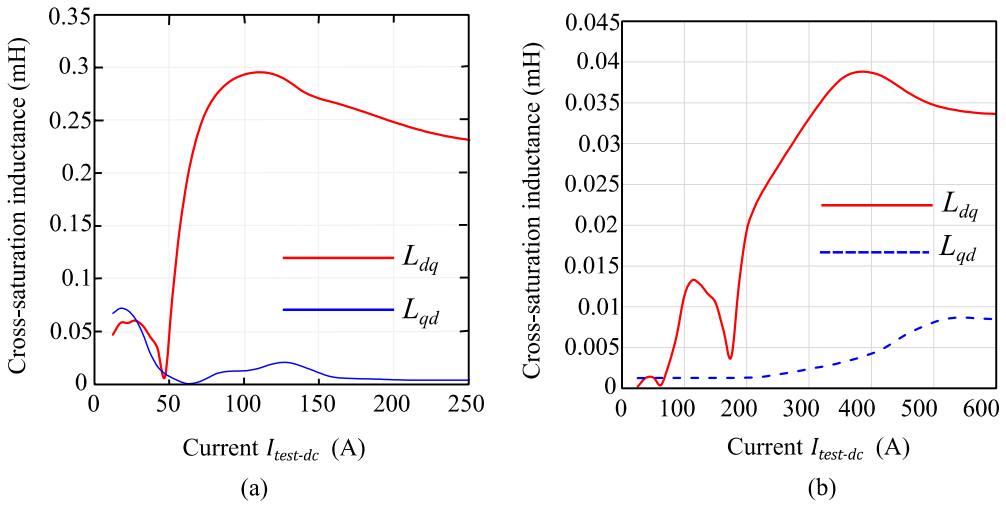

Figure 5-14. Cross-magnetisation inductances (a) 2004 Prius and (b) 2012 Leaf.

5.4.3 Locked-Rotor Torques

Assuming that the H_{cB} value of the PM was adjusted to a reasonable rotor test temperature, the FEMM models achieved good agreement with the ORNL locked rotor test results. In Figure 5-15, the ORNL torque measurements are compared to the FEMM model outputs for the 2004 Prius and the Leaf motors.

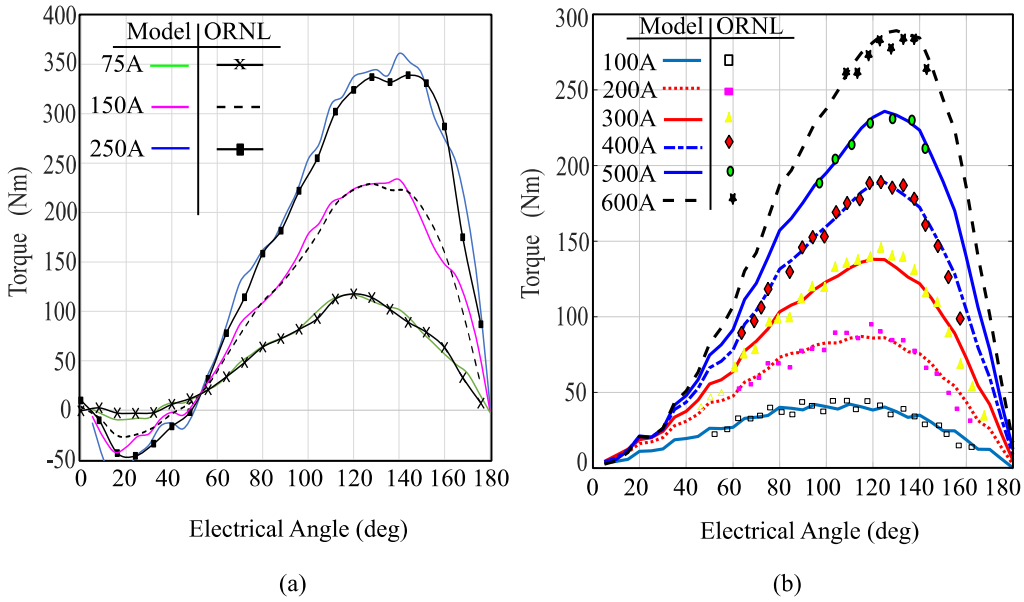

Figure 5-15. Locked-rotor results for (a) 2004 Prius and (b) Leaf.

A comparison of the torque measured with and without a skew is shown in Figure 5-16. The FEMM model's torque results for the Leaf were adjusted to implement the skew in the PMs on the rotor. The skewed torque result was achieved by estimating the torque in FEMM for one half of the rotor length, then summing this data with the equivalent 15° electrical rotated values, to obtain the full rotor length torques.

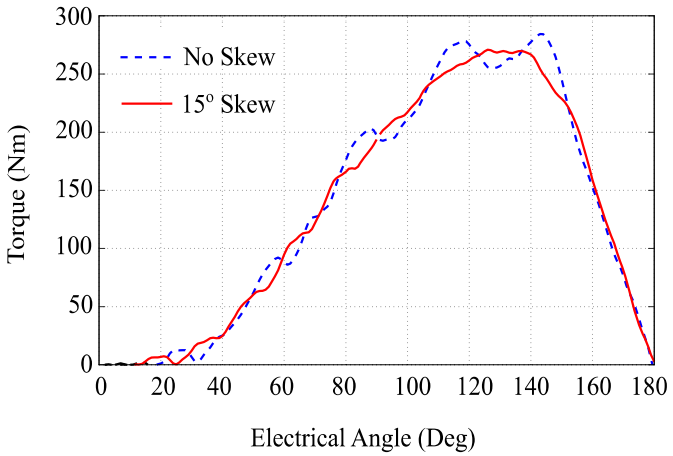

Figure 5-16. LEAF model torque outputs with and without a skew.

It is clear from these locked-rotor torque results of all five motors that MTPA operation is achieved over a range of electrical angles extending from 100° to 140°, with the largest phase advances necessary to achieve high-torque outputs.

5.4.4 Motor Losses

Estimation of both ohmic and core losses over the full range of torque and speed values is required for validation of the motor losses. The ohmic losses in the motor are dependent on the phase current amplitude. The phase current amplitude is in turn dependent on: (i) the required output torque, as seen by the locked-rotor torques; (ii) the required motor speed, in that flux weakening can require increased phase current for a constant torque output as the speed increases; (iii) core and friction losses. The FEA model does not provide sufficient results to estimate the phase current at every speed. Validation of the ohmic losses was conducted after the development of an IPM motor electrical model, reported in Section 5.5 and is therefore presented in Section 5.6.

The results of the core loss tests using the FEMM model of the Leaf are presented in Figure 5-17. The core losses obtained from the FEMM models at various dc test currents and a fixed electrical angle of 130° are presented in Figure 5-17 (a). As expected, the iron losses increase with increases in motor speed and with increases in phase current. The impact of increasing the phase advance angles is shown in Figure 5-17(b) where a constant dc test current of 620A was applied at a phase advance angle range of 130° to 155°. Increasing the phase advance angle weakens the PM magnetic field and results in a reduction in flux density, leading to a slight reduction in iron losses for the same phase current.

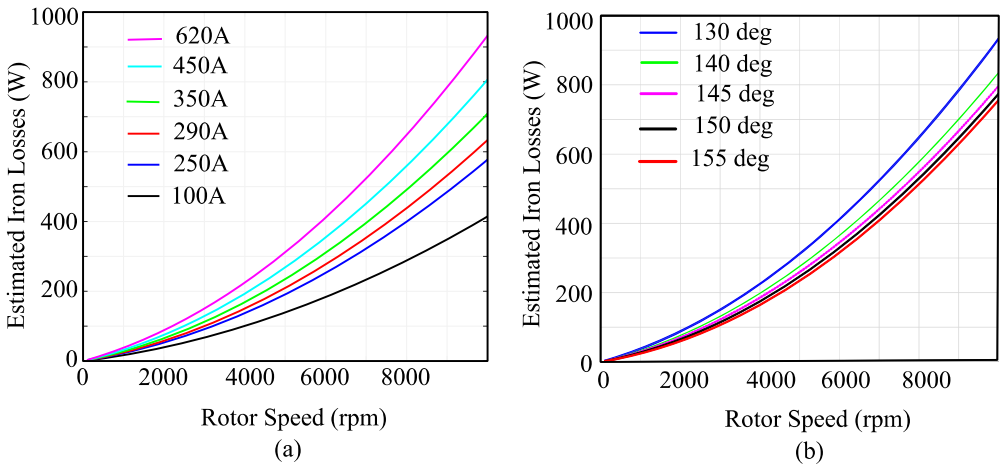

Figure 5-17. Leaf iron losses at (a) various $I_{test-dc}$ at a fixed phase angle of 130° and (b) phase angles with a fixed $I_{test-dc}$ of 620A.

As with the ohmic losses, the core loss results show that validation is only possible when an electrical motor model identifies the phase current and the phase advance angles required at each torque and each speed operating point. The combined motor losses are validated in Section 5.6 based on a comparison between the ORNL motor efficiency map and the efficiency of the IPM motor model at specific operating points.

5.5 Proposed IPM Motor Model Based on FEMM Results

The procedure to convert the FEA model characterisation results into an IPM motor model for a vehicle simulator is outlined in Figure 5-18. The three principle sections of this procedure are explained in Sections 5.5.1 to 5.5.3. The software structure of the model is then explained in Section 5.5.4.

In a backward-facing vehicle simulator such as the SEVP, the IPM motor must convert the rotor torque T_r and speed ω_r requirements into input rms phase voltages V_{ph} and currents I_{ph}. During MTPA motor operation, the locked-rotor results establish the relationship between the torque and the individual axis currents, I_d and I_q. In this mode, the phase voltage is not constrained by the available battery voltage and the phase voltage during MTPA operation is estimated using either (5.9) or (5.15).

In MTPV mode, the rotor speed is a critical parameter in determining the phase current required for a given torque. In this mode, the MTPA relationships between phase current and torque are no longer valid as these phase currents would result in excessive phase voltages at the higher speeds. For a model operating in MTPV mode, the phase current must simultaneously satisfy the torque equation of (5.5) or (5.14) and the voltage equation of (5.9) or (5.15).

The requirements to operate in both MTPA and MTPV modes, resulted in: (i) MTPA operation using curve-fit equations, based on the FEA model locked-rotor-torque to phase-current relationships; (ii) MTPV operation using the standard equations for torque and voltage, and then deriving the phase current amplitude and phase angle required using an iterative software process.

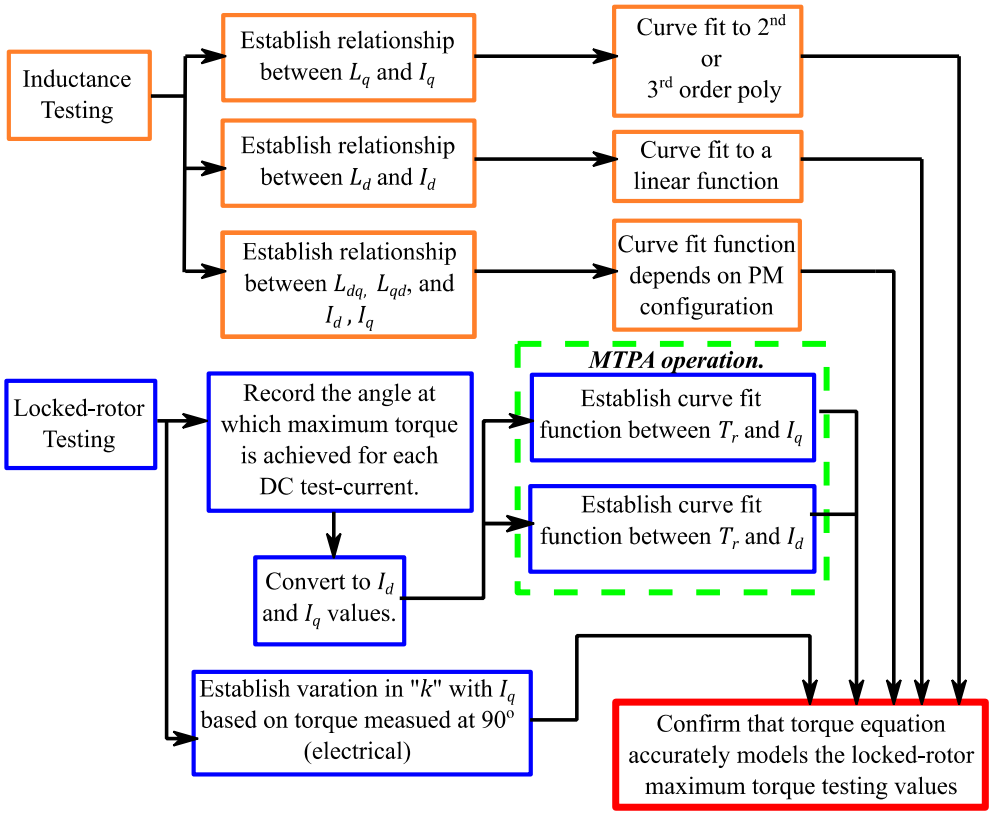

Figure 5-18. Procedure to convert FEA model results to an IPM motor model for a simulator.

5.5.1 Inductance Parameters for IPM Motor Model

The axis inductances were shown in the FEA models to be a function of their respective axis currents. In the IPM model, the L_q inductance is represented as a piecewise function consisting of a third-order polynomial equation at high I_q currents and a fixed L_q value at lower I_q currents. The L_d inductance is represented as a simple linear function of I_d. The low values of the cross inductances were initially represented as simple linear functions of the phase current.

5.5.2 Determination of Machine Constant *k*

The machine constant parameter k was derived from the FEA locked-rotor results at an electrical angle of 90°and the results for two IPM motors are shown in

Figure 5-19. As reluctance torque is zero at this angle, the output torque is given by (5.1). The dc test current in the locked-rotor test was divided by the $\sqrt{2}$ to give the rms phase currents. The results, as presented in Figure 5-19(a) for the 2004 Prius and Figure 5-19(b) for the Leaf, show that k is not constant. The variation in k is captured in the IPM model as a piecewise function consisting of a linear equation for the roll-off values of k at high I_q currents and a fixed k limit at lower currents. Parameter k as a function of I_q is taken to be zero at 90°.

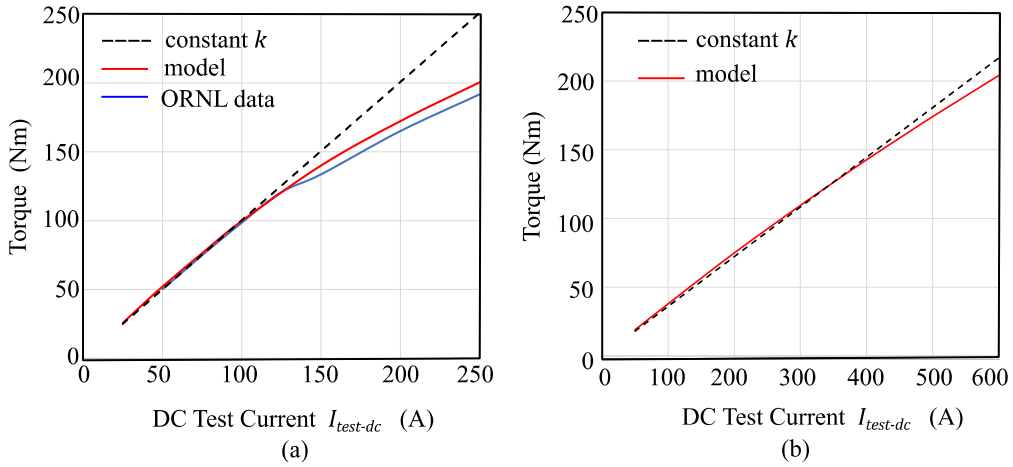

Figure 5-19. Torque at 90° for (a) 2004 Prius and (b) Leaf.

5.5.3 Determination of Optimum Electrical Angle for MTPA

The MTPA procedure involved recording the peak torque value for each dc test current value as well as the electrical angle at which this peak torque was achieved. The combined phase current and electrical angle was then split into equivalent axis currents I_d and I_q. Plotting these axis currents with respect to the torque enabled two curve-fit polynomials to be established that defined the relevant axis current in terms of torque output. The MTPA operating profiles shown in Figure 5-20 were derived for a range of torque outputs by estimating the values of I_d and I_q by means of polynomials and the electrical angle using

$$\frac{I_q}{I_d} = \frac{\left(I_{test-dc}/\sqrt{2}\right) Sin\theta}{\left(I_{test-dc}/\sqrt{2}\right) Cos\theta} = Tan\theta \tag{5.25}$$

The torque peaks observed in the FEA model at an electrical angle of 140° for the 2004 Prius were not considered in the development of the MTPA profile as these peaks were not observed in the ORNL test data.

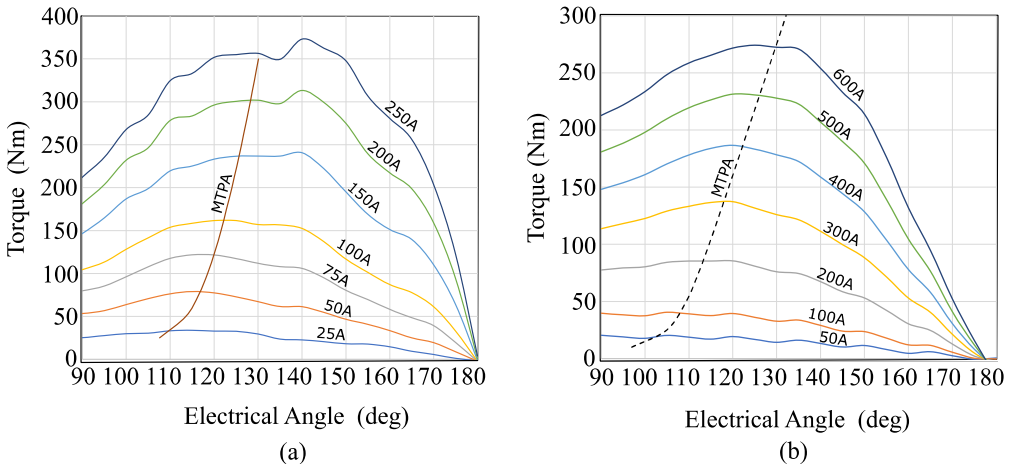

Figure 5-20. MTPA profiles for (a) 2004 Prius and (b) Leaf.

5.5.4 Structure of IPM Motor Model.

The flowchart structure of the IPM motor model is outlined in Figure 5-21. The model has three inputs: (i) a rotor torque T_r estimated from the vehicle's motive force requirement; (ii) an angular rotor speed ω_r based on the drive cycle schedule for a given time period; and (iii) the available dc voltage V_{BP} from the battery model based on its state of charge during this time period. The flowchart is colour coded, with the orange colour identifying the processes required for MTPA operation and the blue and green coloured processes representing the additional processes required for MTPV operation.

The model first checks that the required T_r is within the rated torque limit $T_{r(rated)}$ and within the rated power limit $P_{r(rated)}$. The model initially assumes that

MTPA operation is possible and based on the T_r required, calculates both axis currents using the polynomials determined from the locked-rotor FEA model tests. The axis currents then permit an approximation of the inductance values using the relationships determined in Section 5.5.1. Based on space-vector modulation of the inverter devices, the available battery voltage is converted to a maximum possible phase voltage $V_{ph(max)}$ using an assumed modulation index of m =1.15.

At this stage, the initial assumption of MTPA operation is checked by calculating the phase voltage V_{ph} using (5.15) based on the required output motor speed ω_r and the derived inductance values. If V_{ph} is less than $V_{ph(max)}$, then MTPA operation is possible and the model calculates the power losses associated with the stator resistance, core, friction and windage. If V_{ph} is greater than $V_{ph(max)}$, then MTPA operation is not possible and the model switches to MTPV operation.

For a model with minimal computational load, it would be desirable in MTPV mode, to have a fixed equation or set of equations that determine the axis currents for a given set of $V_{ph(max)}$, T_r and ω_r values. Such equations could not be determined due to the interdependency of the axis inductances on the axis current amplitudes. Instead, two simple active software loops were implemented to establish the axis currents required to operate at $V_{ph(max)}$ in MTPV mode while maintaining the torque output at T_r.

The outer voltage loop, coloured blue in Figure 5-21, begins by increasing the negative I_d current by a small increment to enable flux-weakening operation. Any change in I_d requires the inductances associated with this parameter to then be recalculated. As I_d also contributes to the torque output in an IPM motor, the model enters an inner torque loop, coloured green in Figure 5-21, to check if the torque remains at the required T_r value.

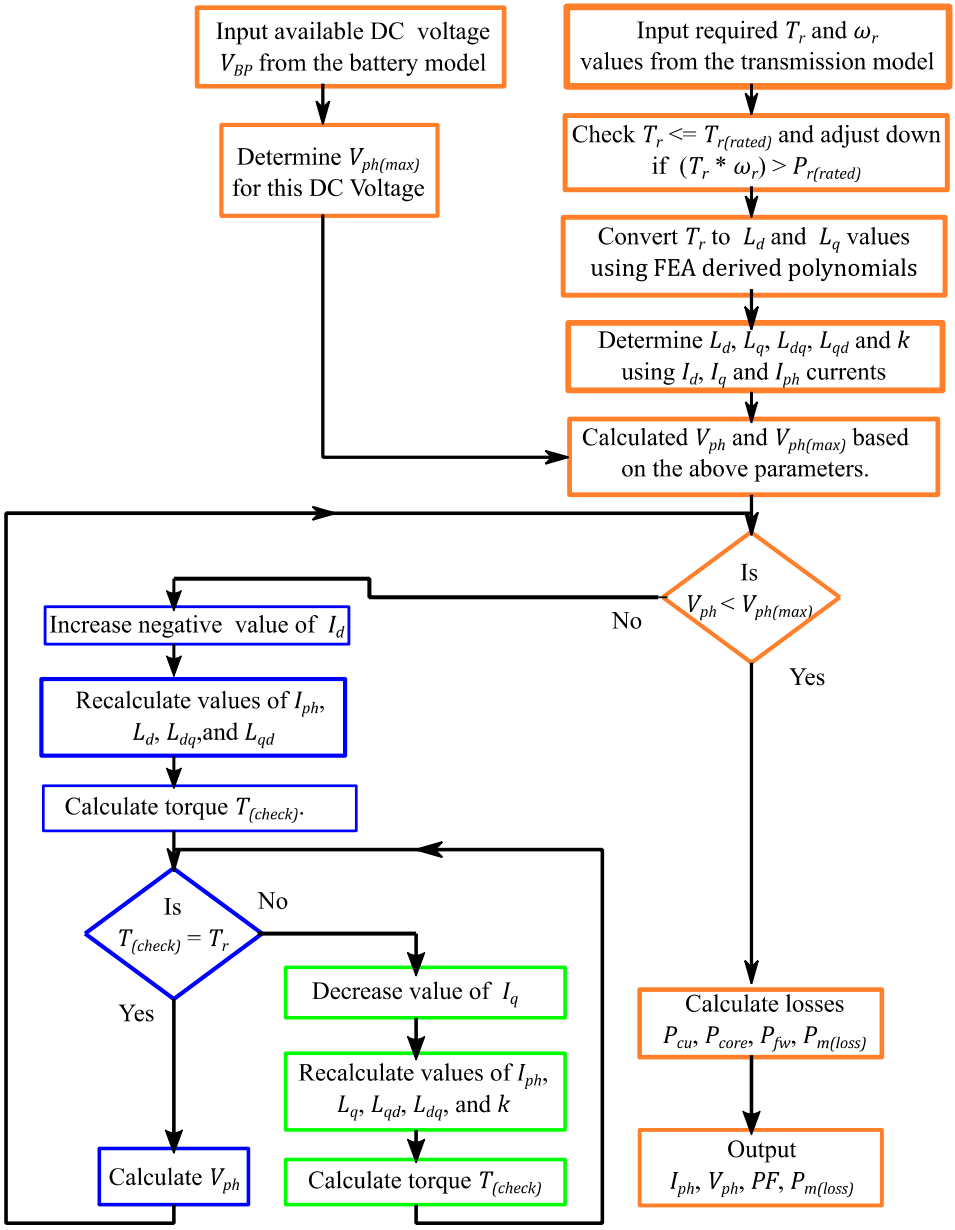

Figure 5-21. Flowchart structure of the proposed IPM motor model.

The torque $T_{(check)}$ is calculated using (5.14) with the new I_d and the previous I_q. If $T_{(check)}$ is greater than T_r, then the value of I_q is reduced by a small increment. All inductances associated with I_q are then recalculated and the $T_{(check)}$ value is re-estimated. Further reductions in I_q are implemented in this inner loop until $T_{(check)}$ equals T_r. At this stage, the V_{ph} in the outer loop is again calculated and checked

against the value of $V_{ph(max)}$. Both loops are implemented using simple "WHILE" statements.

When the loop values of I_d and I_q limit the phase voltage to $V_{ph(max)}$ and maintain the torque at T_r, they are used to calculate the motor losses.

5.5.5 Outputs from IPM Motor Model

The model phase and *dq* axis voltages at the rated power condition for the 2004 Prius are shown in Figure 5-22(a). The corresponding currents are provided in Figure 5-22(b). In the low speed MTPA region, the phase voltage rises while the phase current is approximately constant at this rated torque output. In the higher speed MTPV region, the phase voltage remains constant in the model and the phase current decreases with lower torque outputs in this constant power region.

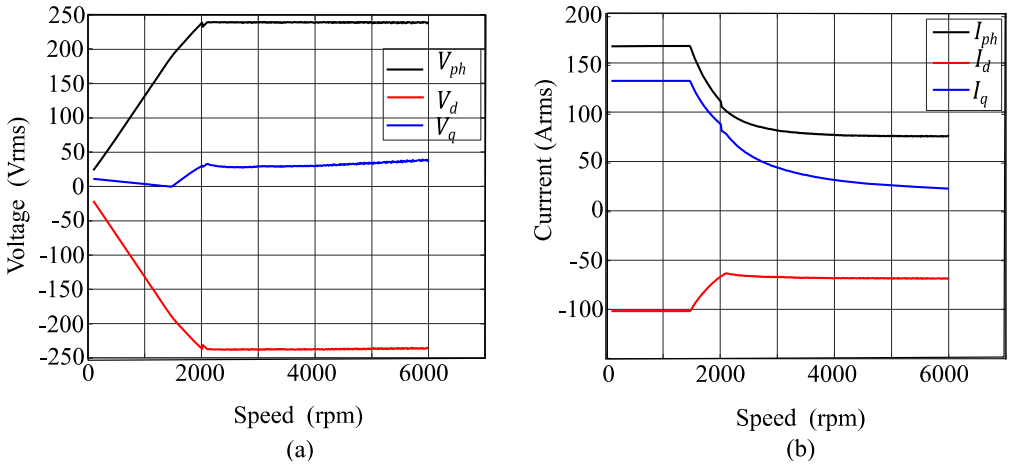

Figure 5-22. 2004 Prius IPM motor model phase and axis (a) voltages, (b) currents.

The distribution of power losses at the rated condition is presented in Figure 5-23(a) and the torque segregation over the full speed range is shown in Figure 5-23(b). When operating at rated condition, the ohmic losses dominate during high-torque, low-speed operation and they drop to reach parity with the core losses near maximum speed. The torque output is evenly split between PM and reluctance torques during MTPA operation. In MTPV mode, the reluctance torque dominates as the phase angle increases.

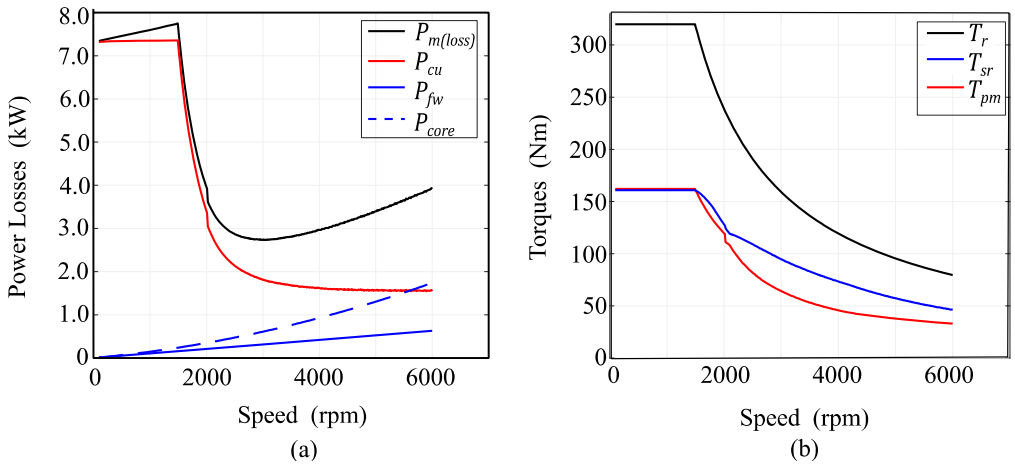

Figure 5-23. 2004 Prius IPM motor model at rated condition (a) power losses, (b) torque segregation.

Operating this active IPM motor model over the full speed and torque ranges of the 2004 Prius highlights the complexity of attempting to derive a phase current amplitude and current advance angle using static equation approaches. In Figure 5-24(a), the change of operating mode from MTPA to MTPV is evident by the increase in current advance angle with speed. The phase angle in MTPA mode is dependent on the torque output and is independent of the motor speed. In MTPV mode, the phase angles converge as the model limits the torque output based on the rated power of the motor. The phase angle increases with speed to achieve the flux-weakening operation described in Section 5.2.3.3.

In Figure 5-24(b), a reduction in the battery voltage from 500 Vdc to 350 Vdc in 50 Vdc increments, is shown to impact the speed at which MTPV operation begins. Based on Figure 5-24, the model demonstrates that the speed at which the change occurs from MTPA to MTPV operation is dependent on both the required torque value T_r and on the available battery voltage V_{BP}.

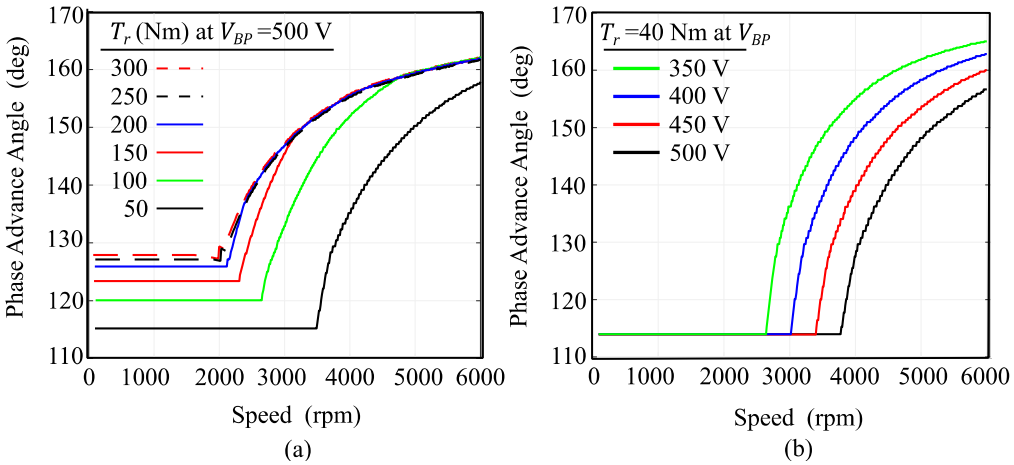

Figure 5-24. Phase advance dependent on (a) Torque output and (b) Battery voltage.

5.6 Model Validation

The IPM motor model was validated with the test data from the tables included in Appendix B of the 2004 Prius report from ORNL [12]. This is the only report from ORNL that provides the sufficiently detailed electrical test data needed to validate a model. The validation results are presented here for three torque levels; a low driving torque of 50 Nm; a mid-rated torque of 150 Nm; a maximum available torque/power output at each speed in the ORNL tests. The IPM model was compared to the ORNL test data in terms of efficiency, rms phase voltage and rms phase current.

5.6.1 Model Validation at Low Torque Output

A low torque output of 50 Nm was selected as a model validation condition as this torque level is commonly observed for BEV testing over a wide range of drive cycles [37]. This torque level in the 2004 Prius IPM motor is not power limited over the full ORNL testing speed range of 500 rpm to 6,000 rpm. The model efficiency validation results are presented in Figure 5-25 (a) and the sources of the power losses in the model are presented in Figure 5-25 (b).

The efficiency results, as presented in Figure 5-25(a), show a good correlation between the ORNL data and the IPM model. Further research is required to identify potential sources of the power loss at near maximum motor speed in the ORNL tests as the IPM model overestimates the efficiency in this region by 3.7%. Given the low torque output requirement, the ohmic losses in the model as shown in Figure 5-25 (b), are relatively low. The high back-emf of this motor prevents sinusoidal modulation as the speed increases and leads to six-step operation at higher motor speeds. This mode of modulation results in harmonic-rich operation and the losses associated with these harmonics are not factored-in to the core losses of the proposed IPM model.

In other IPM motor studies, the harmonics due to the distorted airgap flux distribution (as a result of the saturated flux-bridges on the rotor), have been shown to cause higher iron losses at high motor speeds [38],[39]. The simple FEA model developed in this study, assumes sinusoidal input currents, and does not include core-loss models for the higher-frequency harmonics. The resistance of the windings also increases with these harmonics due to the skin-effect and this leads to higher copper losses at high speeds [40].

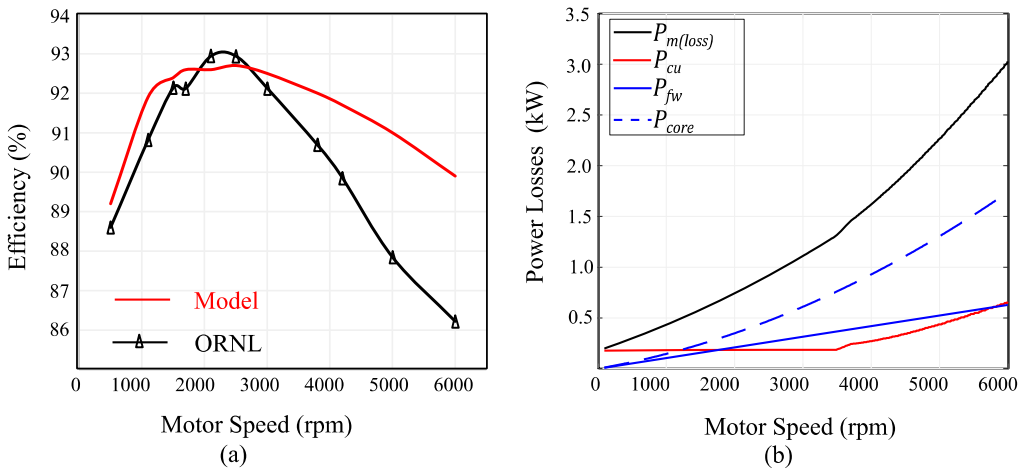

Figure 5-25. Validation results for IPM 2004 Prius motor model at a torque output of 50 Nm:

(a) efficiency and (b) distribution of power losses in model.

The model validation results for the phase voltages and phase currents are illustrated in Figure 5-26. When operating in the low speed MTPA region, the rms phase voltage results, as presented in Figure 5-26(a), showed significantly higher voltages in the ORNL data compared to the IPM model voltages. An analysis of the IPM motor models in [38],[41] indicates that the phase voltage output should include two additional voltage drops associated with (i) the PWM harmonics, when operating below base speed, and (ii) the harmonics associated with the non-uniform airgap flux distribution at all speeds. Additionally, the developed model is based on the dc winding resistance, instead of the ac resistance value that is referenced in other machine design studies [40],[42]. The voltage drop associated with the ac cables from the inverter to the motor, is also not incorporated into the IPM motor model [25]. Access to the ORNL test current and voltage waveforms would be required to adapt the motor model to eliminate these potential sources of the phase voltage differences.

When operating in the higher speed MTPV region, both the model and ORNL test data limit the phase voltage to 240 Vrms. Based on a 500 Vdc supply to the inverter, a 240 Vrms output requires six-step operation. Partial compatibility with these ORNL test conditions is achieved in the IPM model by modifying the assumed SVM modulation index of m=1.15 to m =1.37. This change improves the rms phase voltage output from the model but does not include the losses associated with the harmonics resulting from overmodulated six-step operation.

The phase current validation results as presented in Figure 5-26(b), show a slight underestimation in the MTPA mode and a large underestimation in MTPV mode. The MTPV phase current underestimation in the model are partially explained by an overestimation of motor efficiency at higher speeds, as displayed in Figure 5-26(a) and a delay in entering MTPV mode, as illustrated in Figure 5-26(b). The validation results at this 50 Nm torque output are summarised in Table 5-3.

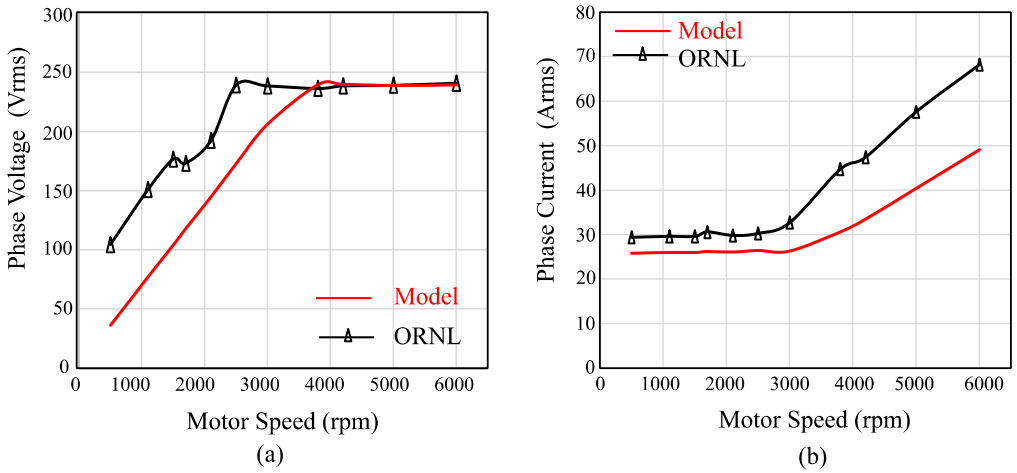

Figure 5-26. Validation results for IPM 2004 Prius motor model at a torque output of 50 Nm

(a) Phase voltages, (b) Phase currents.

Table 5-3. Validation results 2004 Prius model operating at 50 Nm output.

		ORNL Test Data			IPM Model Data		
Torque (Nm)	Test speed (rpm)	Efficiency (%)	V_{ph} (Volts rms)	I_{ph} (Amps rms)	Efficiency (%)	V_{ph} (Volts rms)	I_{ph} (Amps rms)
49.9	503	88.6	104.5	29.4	89.2	36.2	25.8
50.1	1,102	90.8	150.9	29.6	91.9	77.0	26.0
49.9	1,504	92.1	176.5	29.6	92.4	104	26.0
50.3	1,703	92.1	173.1	30.6	92.6	118	26.2
49.7	2,106	92.9	192.5	29.8	92.6	144.9	26.1
50.3	2,504	92.9	239.2	30.3	92.7	173	26.4
50	3,004	92.1	238.4	32.7	92.5	206.2	26.3
49.8	3,804	90.7	236.3	44.7	92.0	239.5	30.6
50.3	4,204	89.8	238.4	47.4	91.7	239.8	33.5
50.1	5,004	87.8	238.9	57.6	91.0	238.8	40.4
49.4	6,005	86.2	240.7	68.2	89.9	239.3	49.1

5.6.2 Model Validation at Mid-rated Torque Output

A medium torque output was selected as a further model validation condition as this torque level was observed in ORNL testing of all five models where maximum efficiency was achieved. The efficiency validation results are presented in Figure 5-27(a) and the sources of the power losses in the model are presented in Figure 5-27 (b). This torque level in the 2004 Prius motor is only available for the ORNL testing speed range of 500 rpm to 2,500 rpm due to the 50 kW power limit of this motor.

The efficiency results as presented in Figure 5-27(a) show a good agreement between the ORNL data and the IPM model.

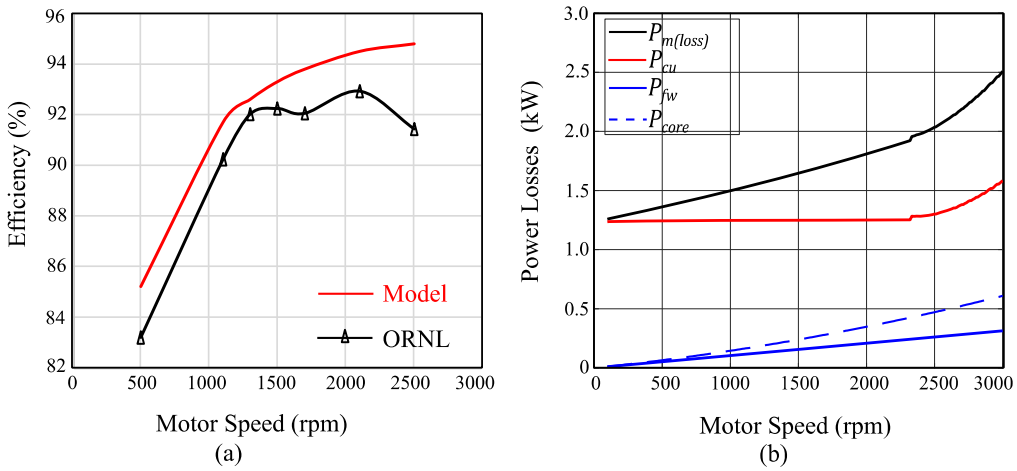

Figure 5-27. Validation results for IPM 2004 Prius motor model at a torque output of 150 Nm

(a) efficiency, (b) distribution of power losses.

The model validation results for the phase voltages and phase currents are illustrated in Figure 5-28. Similar to the validation at 50 Nm output, the rms phase voltage results, as presented in Figure 5-28(a), shows that the model voltages are significantly lower than the measured voltages in the ORNL tests. The phase current validation results as presented in Figure 5-28(b), show a slight underestimation in the MTPA mode.

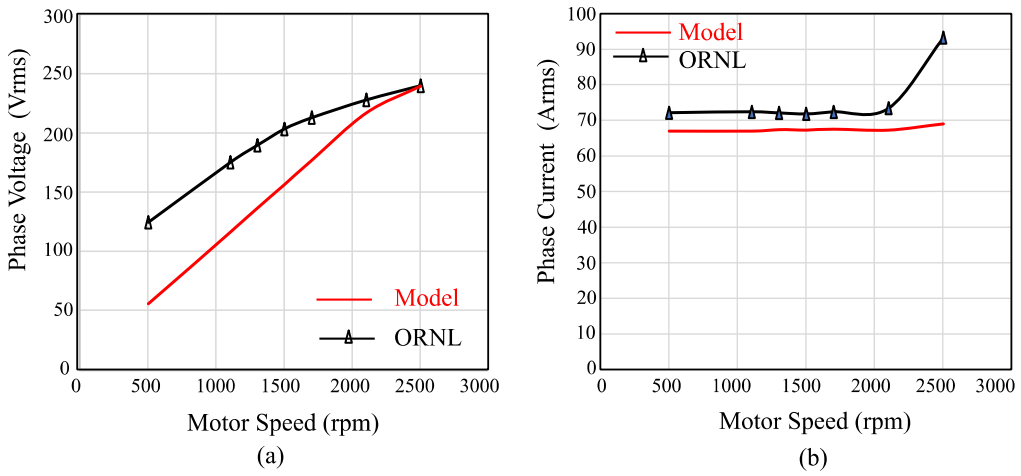

Figure 5-28. Validation results for IPM 2004 Prius motor model at a torque output of 150 Nm

(a) phase voltages, (b) phase currents.

The validation results for a torque output of 150 Nm are summarised in Table 5-4.

Table 5-4. Validation results of IPM 2004 Prius motor model operating at 150 Nm output.

		ORNL Test Data			IPM Model Data		
Torque (Nm)	Test speed (rpm)	Efficiency (%)	V_{ph} (Volts rms)	I_{ph} (Amps rms)	Efficiency (%)	V_{ph} (Volts rms)	I_{ph} (Amps rms)
148.8	503	83.2	124.4	72.2	85.2	55.5	67.0
148.4	1,106	90.2	175.2	72.4	91.7	116.2	67.0
149.3	1,305	92.0	189.5	72.1	92.6	136.6	67.4
148.9	1,503	92.2	203.3	71.8	93.3	156.4	67.3
149.4	1,704	92.1	212.9	72.4	93.8	177	67.5
148.8	2,105	92.9	227.9	73.4	94.5	217	67.3
149	2,504	91.4	239.9	93.2	94.8	239.6	69.0

5.6.3 Model Validation at Maximum Torque\Power Output

IPM motor model validation results when operating at maximum available torque, for a range of speeds, are presented in Figure 5-29 and in Figure 5-30. The model's estimated efficiency is illustrated in Figure 2-29(a) and shows a good correlation to the ORNL data up to speeds of 2,000 rpm. When operating at maximum

or rated torque, the power losses in this speed range are dominated by the ohmic losses in the windings as illustrated by Figure 2-29(b). The efficiency overestimation in the model increases to 6.3% at a speed of 4,200 rpm before reducing to a 3.7% overestimation at a speed of 6,005 rpm.

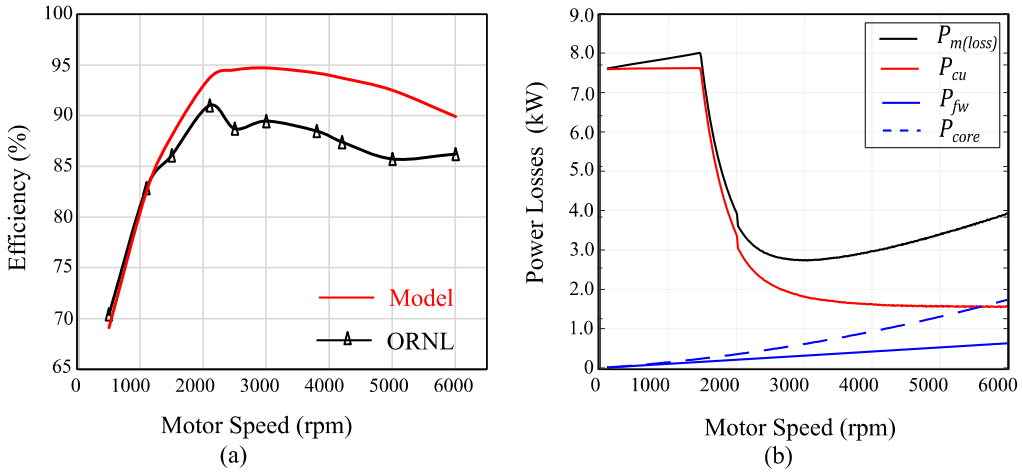

Figure 5-29. Validation results for IPM 2004 Prius motor model at peak torque output

(a) Efficiency, (b) Distribution of power losses.

The model validation results for the phase voltages and phase currents are illustrated in Figure 5-30. The model's rms phase voltages are in agreement with the ORNL tests values in the speed range of 2,100 rpm to 6,005 rpm, as presented in Figure 5-30(a). The phase currents are in agreement with ORNL data for speeds below 2,100 rpm. At a speed of 2,500 rpm, the ORNL data shows a significant increase in current which could be associated with a rapid change in phase advance angle. The change in phase current in the model is less pronounced. More detailed data on the operating mode of the ORNL controller is required to investigate the discrepancies in the phase currents during high-speed operation.

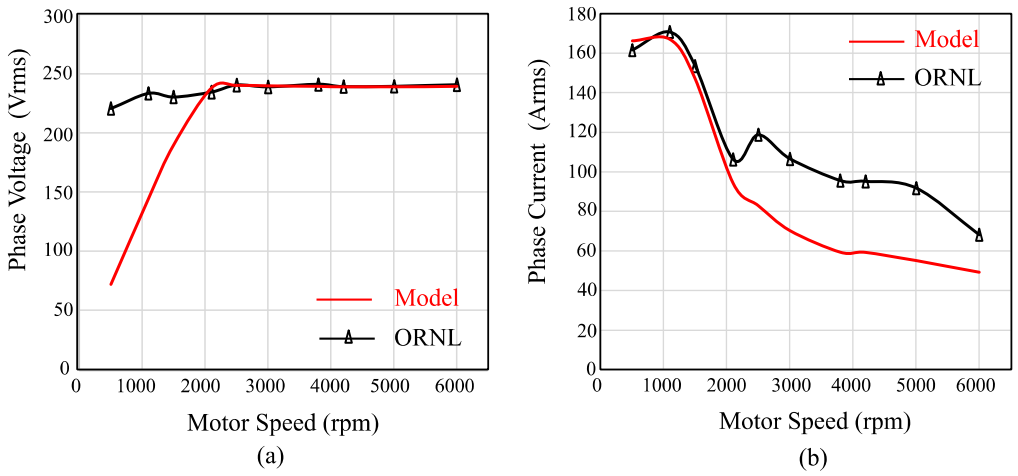

Figure 5-30. Validation results for IPM 2004 Prius motor model at a peak torque output

(a) Phase voltages, (b) Phase currents.

The validation results for this maximum torque \ power output of 324 Nm \ 50 kW are summarised in Table 5-4.

Table 5-5. Validation results at maximum available torque.

		ORNL Test Data			IPM Model Data		
Torque (Nm)	Test speed (rpm)	Efficiency (%)	V_{ph} (Volts rms)	I_{ph} (Amps rms)	Efficiency (%)	V_{ph} (Volts rms)	I_{ph} (Amps rms)
323	508	70.4	220.5	161.6	69.1	71.9	166.2
329.6	1,103	82.8	233.3	170.7	82.5	144.5	167
295.8	1,504	86.1	230.3	153.5	88.0	190	146.9
208.4	2,106	91.0	234.5	106.3	93.7	237.9	94.2
178.7	2,505	88.7	240.4	118.7	94.5	240	82.9
139	3,005	89.5	238.9	106.6	94.7	239.7	70.3
98.6	3,804	88.5	241	95.6	94.2	239.3	59.4
89.4	4,204	87.4	239.1	95.2	93.7	238.9	59.2
69.9	5,005	85.7	239.4	91.8	92.5	238.9	55.1
49.4	6,005	86.2	240.7	68.2	89.9	239.3	49.2

5.7 Conclusions.

The developed IPM motor models aid in understanding the drive requirements for the operation of an IPM motor over its full torque-speed range for a BEV traction motor. In particular, the models identified the requirement for flux weakening over the full speed range of the IPM motor. Below the base-speed, flux weakening is necessary to achieve the maximum torque output and to operate in MTPA mode. In this speed range, the optimum phase advance angle value is shown to increase with the torque required. Above base-speed, flux weakening is required to operate in MTPV mode with a limited battery voltage. The IPM motor models showed that the assumed linear relationship between the phase currents and torque in the simple DC motor is not valid in IPM motors. The high levels of magnetic saturation and cross-magnetisation found in IPM motors leads to complex non-linear relationships between the phase currents and both the electromagnetic and the reluctance torque outputs. Accurate simplification through linearization of these complex relationships is a non-trivial task.

The FEA models enabled the characterisation of the motor parameters required to develop the combined electrical and power loss IPM motor models. The locked-rotor testing of the FEA model established the phase current and optimum phase advance angle required for each torque output during MTPA operation. The IPM model implemented a simple iterative process to estimate the phase current and phase advance angle during MTPV operation. The IPM model's phase voltage result are lower than the values observed in the ORNL data and this error requires further research as it also impacts the phase current and the phase advance angle. Adding a new inductive element in both the *d*-axis and *q*-axis equivalent circuits to represent the harmonics of the airgap flux distribution, as seen in [38], is potential solution to this voltage error.

The IPM motor model structured with two relatively simple iteration loops enables the model to function as both an energy consumption model and an electrical circuit model in a BEV powertrain. The iteration loops can be implemented in most software environments using "While" functions. The model achieves a smooth transfer from MTPA to MTPV operation and also limits torque output based on the rated power of the motor. Further improvements in the model requires research into the low phase voltage estimates during MTPA operation and the inclusion of harmonic losses in the core losses as the motor approaches maximum speed output.

An indirect positive outcome of this IPM machines operating-characteristics-study, is a set of FEA models for traction motors for EVs. These simple machine models provide a further valuable educational resource to develop engineering skills in undergraduate studies. While the FEA software used does not provide the precision needed for IPM motor design for commercial applications, its reduced design parameter requirements and minimal instruction set, make it an ideal tool for educational applications. When students are tasked with a new motor development exercise, the dataset of typical commercial IPM parameters gathered in this study, provides the student with a realistic starting point in terms of the possible physical size to power output ratio. This dataset includes the following: (i) typical winding wire gauges and airgap lengths; (ii) typical diameters and length of stators and rotors to achieve a given power and torque output specification; (iii) and types of PM used in commercial IPM motor designs. The dataset also provides students with a starting library of realistic material properties to simulate their initial designs. The models can then be used to explore the effects of d-axis and q-axis inductances, the back-emf speed constant, the impact of rotor temperature on torque output, motor cogging-torques, magnetic saturation in motor designs and the impact of skewing the rotor magnets on torque output.

5.8 References

[1] T. M. Jahns, "Flux-weakening regime operation of an interior permanent-magnet synchronous motor drive," in *IEEE Transactions on Industry Applications*, vol. IA-23, no. 4, pp. 681-689, July 1987, doi: 10.1109/TIA.1987.4504966

[2] M. S. Toulabi, J. Salmon and A. M. Knight, "Concentrated winding IPM synchronous motor design for wide field weakening applications," in *IEEE Transactions on Industry Applications*, vol. 53, no. 3, pp. 1892-1900, May-June 2017, doi: 10.1109/TIA.2017.2650985.

[3] L. Sepulchre, M. Fadel, M. Pietrzak-David and G. Porte, "MTPV flux-weakening strategy for PMSM high speed drive," in *IEEE Transactions on Industry Applications*, vol. 54, no. 6, pp. 6081-6089, Nov.-Dec. 2018, doi: 10.1109/TIA.2018.2856841.

[4] T. J. E. Miller, M. Popescu, C. Cossar and M. McGilp, "Performance estimation of interior permanent-magnet brushless motors using the voltage-driven flux-MMF diagram," *IEEE Transactions on Magnetics*, vol. 42, no. 7, pp. 1867-1872, July 2006, doi: 10.1109/TMAG.2006.874512.

[5] Z. Xu and M. F. Rahman, "Direct torque and flux regulation of an IPM synchronous motor drive using variable structure control approach," in *IEEE Transactions on Power Electronics*, vol. 22, no. 6, pp. 2487-2498, Nov. 2007, doi: 10.1109/TPEL.2007.909208.

[6] S. Lee, Y. Jeong, Y. Kim and S. Jung, "Novel analysis and design methodology of interior permanent-magnet synchronous motor using newly adopted synthetic flux linkage," in *IEEE Transactions on Industrial Electronics*, vol. 58, no. 9, pp. 3806-3814, Sept. 2011, doi: 10.1109/TIE.2010.2093479.

[7] M. A. Rahman and P. Zhou, "Analysis of brushless permanent magnet synchronous motors," in *IEEE Transactions on Industrial Electronics*, vol. 43, no. 2, pp. 256-267, April 1996, doi: 10.1109/41.491349.

[8] S. T. Lee, T. A. Burress and L. M. Tolbert, "Power-factor and torque calculation with consideration of cross saturation of the interior permanent magnet synchronous motor with brushless field excitation," 2009 *IEEE Int. Electric Machines and Drives Conf.*, Miami, FL, 2009, pp. 317-322, doi: 10.1109/IEMDC.2009.5075224.

[9] B. Stumberger, G. Stumberger, D. Dolinar, A. Hamler and M. Trlep, "Evaluation of saturation and cross-magnetization effects in interior permanent-magnet synchronous motor," *IEEE Transactions on Industry Applications*, vol. 39, no. 5, pp. 1264-1271, Sept.-Oct. 2003, doi: 10.1109/TIA.2003.816538.

[10] K. Yamazaki and M. Kumagai, "Torque analysis of interior permanent-magnet synchronous motors by considering cross-magnetization: variation in torque components with permanent-magnet configurations," *IEEE Transactions on Industrial Electronics*, vol. 61, no. 7, pp. 3192-3201, July 2014, doi: 10.1109/TIE.2013.2278508.

[11] J. G. Hayes and K. Davis, "Simplified electric vehicle powertrain model for range and energy consumption based on EPA coast-down parameters and test validation by Argonne National Lab data on the Nissan Leaf," *2014 IEEE Transportation Electrification Conf. and Expo (ITEC)*, Dearborn, MI, 2014, pp. 1-6, doi: 10.1109/ITEC.2014.6861831.

[12] R. H. Staunton, C. W. Ayers, L. D. Marlino, J. N. Chiasson, and T. A. Burress, “Evaluation of 2004 Toyota Prius hybrid electric drive system interim report”, Oak Ridge National Lab. (ORNL), ORNL/TM-2006/423, May 2006.

[13] R. H. Staunton, T. A. Burress, and L. D. Marlino, “Evaluation of 2005 Honda Accord hybrid electric drive system”, Oak Ridge National Laboratory (ORNL), ORNL/TM-2006/535, September 2006.

[14] T. A. Burress, C. L. Coomer, S. L. Campbell, L. E. Seiber, L. D. Marlino, R. H. Staunton, J. P. Cunningham, “Evaluation of the 2007 Toyota Camry hybrid synergy drive system,” Oak Ridge National Laboratory (ORNL), ORNL/TM-2007/190, April 2008.

[15] T. A. Burress C. L. Coomer, S. L. Campbell, A. A. Wereszczak, J. P. Cunningham, L. D. Marlino, L. E. Seiber, H. T. Lin, “Evaluation of the 2008 Lexus LS 600H hybrid synergy drive system,” Oak Ridge National Laboratory (ORNL), ORNL/TM-2008/185, January 2009.

[16] T. A. Burress, S. L. Campbell, C. L. Coomer, C. W. Ayers, A. A. Wereszczak, J. P. Cunningham, L. D. Marlino, L. E. Seiber, H. T. Lin, “Evaluation of the 2010 Toyota Prius hybrid synergy drive system,” Oak Ridge National Laboratory (ORNL), ORNL/TM-2010/253, March 2011.

[17] T. A. Burress, “Benchmarking of Competitive Technologies 2012 Nissan LEAF,” Oak Ridge National Laboratory (ORNL), Presentation at US DOE Hydrogen and Fuel Cell Peer Evaluation Meeting, May 2012.

[18] Finite Element Method Magnetics, “FEMM software download,” [Online]. Available: http://www.femm.info/wiki/HomePage. [Accessed: 10-Jul-2020]

[19] J. G. Hayes and G. A. Goodarzi, *Electric Powertrain:Energy Systems, Power Electronics and Drives for Hybrid, Electric and Fuel Cell Vehicles,* 1st ed., Chichester, West Sussex, UK: Wiley, 2018, pp. 256.

[20] G. Choi and T. M. Jahns, "Demagnetization characteristics of permanent magnet synchronous machines," *IECON 2014 - 40th Annual Conference of the IEEE Industrial Electronics Society*, Dallas, TX, 2014, pp. 469-475, doi: 10.1109/IECON.2014.7048542.

[21] X. Liu, H. Chen, J. Zhao and A. Belahcen, "Research on the performances and parameters of interior PMSM used for electric vehicles," *IEEE Transactions on Industrial Electronics*, vol. 63, no. 6, pp. 3533-3545, June 2016, doi: 10.1109/ TIE.2016.2524415.

[22] Y. Yang, S. M. Castano, R. Yang, M. Kasprzak, B. Bilgin, A. Sathyan, H. Dadkhah, A. Emadi, "Design and comparison of interior permanent magnet motor topologies for traction applications," *IEEE Transactions on Transportation Electrification*, vol. 3, no. 1, pp. 86-97, March 2017, doi: 10.1109/TTE.2016.2614972.

[23] A. Wang, Y. Jia and W. L. Soong, "Comparison of five topologies for an interior permanent-magnet machine for a hybrid electric vehicle," *IEEE Transactions on Magnetics*, vol. 47, no. 10, pp. 3606-3609, Oct. 2011, doi: 10.1109/ TMAG.2011.2157097.

[24] D. Yu, X. Y. Huang, Y. T. Fang and J. Zhang, "Design and comparison of interior permanent magnet synchronous traction motors for high speed railway applications," *2017 IEEE Workshop on Electrical Machines Design, Control and Diagnosis (WEMDCD)*, Nottingham, 2017, pp. 58-62, doi: 10.1109/ WEMDCD.2017.7947724.

[25] B. Gallert, G. Choi, K. Lee, X. Jing and Y. Son, "Maximum efficiency control strategy of PM traction machine drives in GM hybrid and electric vehicles," *2017 IEEE Energy Conversion Congress and Exposition (ECCE)*, Cincinnati, OH, 2017, pp. 566-571, doi: 10.1109/ECCE.2017.8095833.

[26] T. Inoue, Y. Inoue, S. Morimoto and M. Sanada, "Mathematical model for MTPA control of permanent-magnet synchronous motor in stator flux linkage synchronous frame," in *IEEE Transactions on Industry Applications*, vol. 51, no. 5, pp. 3620-3628, Sept.-Oct. 2015, doi: 10.1109/TIA.2015.2417128.

[27] S. Sue and C. Pan, "Voltage-constraint-tracking-based field-weakening control of IPM synchronous motor drives," in *IEEE Transactions on Industrial Electronics*, vol. 55, no. 1, pp. 340-347, Jan. 2008, doi: 10.1109/TIE.2007.909087.

[28] Y. Si, C. Liu, Z. Zhang, Y. Liu, M. Wang and Q. Lei, "A novel interior permanent magnet synchronous motor drive control strategy based on off-line calculation and curve fitting," 2020 *IEEE Applied Power Electronics Conference and Exposition (APEC)*, New Orleans, LA, USA, 2020, pp. 253-258, doi: 10.1109/APEC39645.2020.9124292.

[29] EVSpecifications, "EVSpecifications, News and Comparisons." [Online]. Available: www.evspecifications.com. [Accessed: 10-Jul-2020].

[30] Y. Sato, S. Ishikawa, T. Okubo, M. Abe, K. Tamai, "Development of high response motor and inverter system for the Nissan Leaf electric vehicle," *SAE Technical Paper*, no. 2011-01-0350, 2011, doi: 10.4271/2011-01-0350.

[31] R. Yang, "Electrified vehicle traction machine design with manufacturing considerations," PhD. dissertation, Dept. of Mech. Eng., McMaster University, Hamilton, Ontario, 2016.

[32] Hitachi Metals America Ltd, "Permanent magnet catalog." [Online]. Available: https://www.hitachimetals.com/materials-products/permanent-magnets/neodymium.php [Accessed: 10-Jul-2020]

[33] Arnold Magnetic Technologies "Neodymium Iron Boron Magnets." [Online]. Available: http://www.arnoldmagnetics.com/products/neodymium-iron-boron-magnets/ [Accessed: 10-Jul-2020]

[34] D. Meeker, "Sliding band motion model for electric machines." [Online] Finite Element Method Magnetics. Available: www.femm.info/wiki/SlidingBand. [Accessed: 10-Jul-2020].

[35] D. Meeker, "Rotating Losses in a surface mount permanent magnet motor." [Online] Finite Element Method Magnetics. Available: www.femm.info/ wiki/ SPMloss. [Accessed: 10-Jul-2020].

[36] J. A. Walker, D. G. Dorrell and C. Cossar, "Flux-linkage calculation in permanent-magnet motors using the frozen permeabilities method," in *IEEE Transactions on Magnetics*, vol. 41, no. 10, pp. 3946-3948, Oct. 2005, doi: 10.1109/TMAG.2005.854973.

[37] G. Choi and T. M. Jahns, "Design of electric machines for electric vehicles based on driving schedules," *2013 Int. Electric Machines & Drives Conf.*, Chicago, IL, 2013, pp. 54-61, doi: 10.1109/IEMDC.2013.6556192.

[38] M. Fasil, C. Antaloae, N. Mijatovic, B. B. Jensen and J. Holboll, "Improved dq-axes model of PMSM considering airgap flux harmonics and saturation," in *IEEE Transactions on Applied Superconductivity*, vol. 26, no. 4, pp. 1-5, June 2016, Art no. 5202705, doi: 10.1109/TASC.2016.2524021.

[39] K. Yamazaki and Y. Seto, "Iron loss analysis of interior permanent-magnet synchronous motors-variation of main loss factors due to driving condition," in *IEEE Transactions on Industry Applications*, vol. 42, no. 4, pp. 1045-1052, July-Aug. 2006, doi: 10.1109/TIA.2006.876080

[40] K.S. Cha, J.W. Chin, S.H. Park, Y.H Jung, E.C. Lee, M.S. Lim, “Design method for reducing AC resistance of traction motor using high fill factor coil to improve fuel economy of eBus”. *IEEE/ASME Transactions on Mechatronics*. 2021 Jan 26, doi:10.1109/TMECH.2021.87715513054798.

[41] L. Chang, T. M. Jahns and R. Blissenbach, "Estimation of PWM-Induced Iron Loss in IPM Machines Incorporating the Impact of Flux Ripple Waveshape and Nonlinear Magnetic Characteristics," in *IEEE Transactions on Industry Applications*, vol. 56, no. 2, pp. 1332-1345, March-April 2020, doi: 10.1109/TIA.2019.2961074.

[42] L. Stoyanov, V. Lazarov, Z. Zarkov, E. Popov, “Influence of skin effect on stator windings resistance of AC machines for electric drives”. 2019 *IEEE 16th Conference on Electrical Machines, Drives and Power Systems (ELMA)* 2019 Jun 6 (pp. 1-6), doi: 10.1109/ELMA.2019.8771551

6 ENERGY MANAGEMENT STRATEGY FOR A FUEL CELL ELECTRIC VEHICLE

This chapter presents a novel energy management strategy (EMS) which outperforms the published strategies developed for an international technology challenge, *IEEE Vehicular Technology Society (VTS) Motor Vehicles Challenge 2017*. The objective of the strategy is to minimise the cost of ownership of a low-power (15 kW) fuel cell-battery electric vehicle. Both the fuel consumption cost and power sources degradation costs are combined to represent the total cost of ownership. The simple adaptive rule-based strategy optimises the fuel cell (FC) operation during low-traction power operation and switches to battery charge-sustaining operation for high traction power operation. This minimises fuel consumption and increases the lifetimes of the fuel cell and of the battery. The strategy is then compared with the EMS of a fuel cell vehicle (FCEV), the 2015 Toyota Mirai, and the challenge vehicle model is modified to capture the updated learnings from the Mirai. Finally, a cost-benefit analysis for a plug-in fuel cell vehicle (PFCV) is considered in order to improve FC lifetimes and to reduce costs for short drive cycles. The contents of this chapter were published in the IET journal of Electrical Systems in Transportation in 2019 [1].

6.1 Introduction

The objective of this chapter is to develop an optimised rules-based EMS for the FCEV model shown in Figure 6-1 which was provided in the *IEEE VTS Motor Vehicles Challenge 2017* [2], while also modifying the model based on the 2015 Toyota Mirai FCEV, and considering a plug-in FCEV option. This was the first VTS challenge to develop an EMS for a FCEV within a limited development time and 48 participants from 14 countries each developed an EMS. The second VTS challenge

(2018) required the development of an EMS for a plug-in hybrid electric vehicle (PHEV), while the 2019 challenge involves an EMS for a locomotive application.

Fuel cell electric vehicles (FCEV) are hybrid-electric vehicles (HEV) with a FC as the primary power source for the traction drive [3],[4]. The FC is a low-voltage source and requires a boost converter at the FC output to increase the dc link voltage at the input to the traction drive, thereby reducing the inverter and motor losses in the traction drive system [5]. The FC is a unidirectional power source, and so requires secondary power sources, such as batteries and/or supercapacitors, to absorb regenerative braking energy [6]. The dynamic response of a FC has, until recently, been regarded as slow which has resulted in these secondary power sources providing power to the traction motor during vehicle acceleration to improve the performance of the vehicle [7]-[9].

An EMS controls the power sharing between the primary and secondary power sources in the FCEV. The complexity of the EMS and the controllability of each power source depends on the configuration of the power sources in the FCEV. The simplest configuration, shown in Figure 6-1, uses a battery or a supercapacitor directly connected to the boost converter output. In this configuration, battery power equates to the difference between the traction power and the FC output power. The EMS can directly control the FC power output while also indirectly controlling the battery power during steady-state operation. If the dynamic power response of the FC is limited, the EMS typically provides the average traction power requirement while minimising hydrogen (H_2) fuel consumption by optimising the operating point of the FC [10]. Note that a bidirectional dc-dc typically interfaces the battery to the dc link in high-power vehicles such as the Toyota Mirai [11].

The price premium associated with new zero-carbon emission vehicles such as an FCEV, can be a barrier to their adoption by consumers. Research studies show that if a total cost of ownership (COO) approach is applied to these vehicles, then the lower fuel costs [12],[13] or the higher resale values [14] can offset the purchase price premium during the initial years of ownership (typically a three-year period). Life-cycle-cost analysis studies [15] are conducted over a longer time period and in these studies, the degradation of a major power source such as the battery or the FC, can result in high replacement costs. These replacement costs can negate the lower fuel costs in the initial years of operation. Development of an EMS in a HEV design, using an internal combustion engine (ICE) as the primary power source, tends to focus on

minimizing fuel consumption but the significance of power-source replacement costs to the real operating costs of these vehicles is rarely mentioned. Given that a FC vehicle has two power sources with degradation rates higher than the ICE of a conventional vehicle, minimising the degradation rates must be a critical operating strategy for this vehicle. This leads to the concept of developing an EMS based on minimising COO costs rather than just minimising fuel consumption.

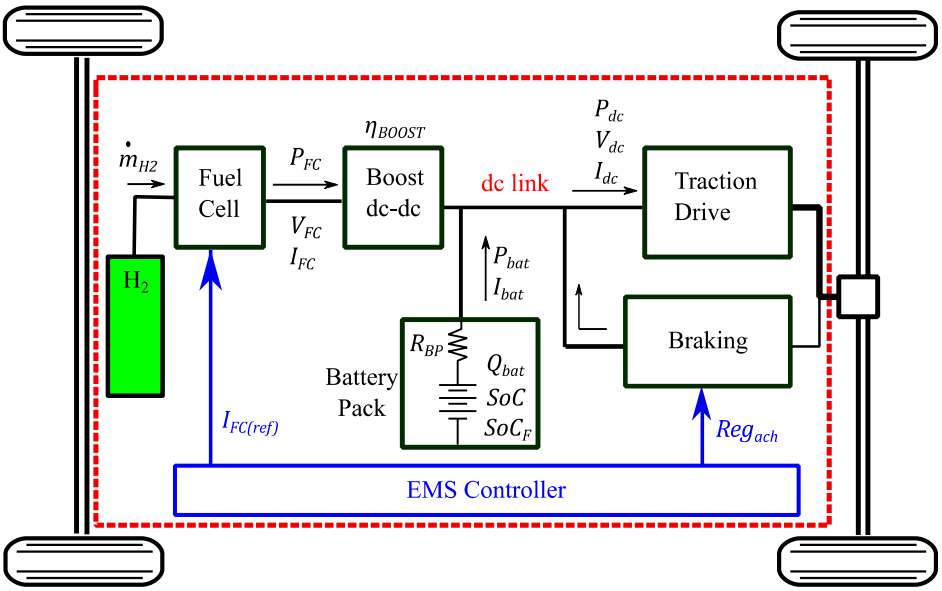

Figure 6-1. FCEV model configuration for the VTS challenge.

The 2017 challenge scoring was based on the total COO, which comprise the combined costs associated with H_2 fuel consumption, FC degradation, battery degradation as well as a battery recharge cost to restore the battery to 100% state of charge (SOC) at the end of each drive cycle. The EMS can only control the FC output current I_{FC} within a range of 0 to 400 A, and the regenerative-braking distribution factor Reg_{ach} within a specified range of 0 to 0.5. All the costs in this paper are reported in US dollars ($) as this was the currency required in the challenge.

This paper presents an optimised rules-based EMS for the challenge model which outperforms the published strategies for this challenge. The authors provide an overview of EMS development techniques and power source degradation mechanisms.

The EMS of the Toyota Mirai is explored based on the Argonne National Laboratory (ANL) test report [9]. The challenge vehicle model is modified to match the Mirai FC performance. Finally, a PFCV is considered as a viable option to reduce drive cycle costs and increase the FC lifetime.

The paper is organised as follows; EMS development techniques, FC degradation and battery degradation are reviewed in Section 6.2. Section 6.3 details the FCEV model provided in the challenge. Section 6.4 describes the experimental tests and offline optimisations to develop the proposed EMS. Section 6.5 presents the Simulink model of the new simple adaptive rule-based EMS. Section 6.6 examines the 2015 Toyota Mirai and the modifications to the challenge FCEV model. Section 6.7 is a cost-analysis of a PFCV configuration to reduce the total ownership costs for short drive cycles. Section 6.8 provides some concluding remarks.

6.2 EMS and Power Source Degradation

This section reviews the literature on EMS development in HEV designs and on operating conditions that impact degradation in both FC and batteries. A brief review of other studies on EMS for FCEV is also included.

6.2.1 EMS Development Techniques

The objective of an EMS is to specify the operating levels for each of the power sources in a HEV or FCEV to minimise a particular quantity, e.g. the fuel consumption of the vehicle over a given drive cycle. The system optimisation problem is usually specified with numerous system constraints such as the dynamic operational limits of individual system components. The techniques used to solve this problem may be classified as model-based optimisation or rule-based optimisation.

Model-based optimisation tends to be computationally complex and requires long computational times. Model-based techniques are difficult to implement for real-time control of power sources as they also require prior knowledge of the complete drive cycle to determine an optimum global solution. The most frequently referenced model-based optimisation techniques are Dynamic Programming (DP), Pontryagins Minimum Principle (PMP), and Equivalent Consumption Minimisation Strategies (ECMS) [16]-[18].

DP yields an optimised global solution for a cost function provided the time horizon of the problem is fixed, and provided that simple mathematical models of the system can be formulated [19]. The optimised solution is found by defining possible system states for each time-period interval within local and global system constraints. Starting at the final system state, the costs associated with transitioning between all possible states in a time interval to all possible states in the previous time interval are calculated. This reverse-time calculation method is repeated until the costs of transitioning from all the previous possible states to the current state are calculated. By determining the sum of all possible path costs from the starting interval state to the final interval state, it is then possible to determine the operating state at each interval, which results in the minimum overall path costs. As the DP technique has prior knowledge of the complete drive cycle, it can provide a global optimised solution. This solution may be used to benchmark less computationally intensive, real-time control

strategies over the same drive cycle. PMP is a numerical solution method that also determines an optimal global solution using an iterative technique, called the shooting method. PMP is described in Chapter 6 of [19].

ECMS is a computationally less intensive technique which determines local, rather than global, optimisation solutions. When the objective of the EMS is to minimise fuel consumption, the ECMS process assigns a fuel consumption value to the power associated with each source in the HEV. For a primary source, the efficiency map of the power converter (ICE or FC) will determine the fuel consumption. For a secondary source, such as the battery, the electrical power must be converted to equivalent fuel-flow rates using equivalence factors. The main challenge with ECMS is the selection of these equivalence factors as they will vary with power-flow direction (charge or discharge), with the efficiencies of components in the power path, and with the source of the charge power (primary source or regenerative braking). Ideally, they can only be optimised if the future driving conditions are known; for example, if in some future period of the drive cycle, significant regenerative braking energy is available, then using electrical energy now will have little impact on fuel consumption because this electrical energy will not be replenished by the primary-sources' fuel.

Simpler EMS techniques involve the development of rules to govern the source power levels. These rules can be based on: (i) heuristics or engineering experience, (ii) offline-optimisation of individual components (local minima) to determine maximum component efficiency conditions, and (iii) optimisation of the complete vehicle system in a defined state, e.g. braking, battery-charging, high-acceleration, urban-driving or highway-driving. The success of a rule-based EMS depends on many factors including the level of engineering expertise available, the accuracy of the component models, the ability of the EMS to quickly identify the operating state based on the available feedback signals, and the ability to convert expertise into rules using techniques such as fuzzy logic controllers (FLC) [20].

6.2.2 Review of EMS Development for FCEV

EMS development for FC vehicles is a recent field of study and existing literature is limited in scope. The literature focuses on FCEV EMS development which minimises fuel consumption and maximises the range. In this chapter, minimising the

COO is the objective of the EMS and this requires a study of the literature for the causes of degradation in both power sources.

Optimisation using model-based techniques for real-time applications has led some researchers to overcome the requirement for prior knowledge, by initially optimising using multiple sets of the legislative drive cycles. The resulting optimised strategies are then correlated to specific driving characteristics, e.g. urban driving (low speed with frequent stop-starts), highway driving (constant high-speed), or aggressive driving (high speed with rapid acceleration and deceleration). Real-time control can then be achieved as the EMS selects an optimised control-set based on the current driving characteristics. The control-set selection can be achieved using lookup tables, fuzzy logic or simple rule-based controllers. This technique was applied in EMS development for the Chevy Volt PHEV [21] and achieved the minimum fuel consumption in the 2018 VTS challenge. Optimised control-sets for a FCEV, developed using DP, are presented in [22].

Other studies that implement model-based optimisation techniques include [23], where PMP is applied to a series-HEV to minimise fuel consumption, and the computational time is reduced by utilising probability distributions for future traction demands. In [24], minimisation of the fuel consumption and battery degradation are the dual objectives which are resolved using PMP for a parallel-HEV. The PMP is implemented online using an ECMS and the results indicate that to maximise the battery lifetime, the SOC range must be limited. As shown in [25], prioritising the battery-lifetime leads to a load-following strategy for the FC.

Rule-based strategies are more widely implemented than model-based strategies in the literature. A review of the ten best scoring EMS in the 2017 VTS challenge, shows that most utilised rule-based strategies [26] and achieved optimised results similar to the benchmark DP model-based strategy developed by the challenge organisers. Using DP, the optimal COO result for the 32.6 km challenge drive cycle is \$1.612. The winner of the challenge [27] achieves a trip cost of \$1.624 using a rule-based battery charge-sustaining (CS) strategy implemented using a simple proportional-integral (PI) loop controller. The challenge runner-up also implemented a rule-based CS strategy with the FC current specified using one of seven FC operating states [22]. These operating states are defined by the SOC and the traction power. The third-place finisher uses a look-up table (LUT), which is indexed by the traction power and the actual SOC [28]. The LUT values are established by offline optimisation of

the total cost equations specified in [2] and assume steady-state operation, with the FC polarisation curve approximated as a linear function of FC current. This cost optimisation identifies elliptical power-sharing relationships between the two power sources, dependent on traction power and SOC. While this real-time optimisation method specifies the FC operating output once the FC switches on, it does not specify the optimum FC switch-on criteria. Battery-only operation, for the initial part of the challenge drive cycle, results in a total cost of $1.647 for this EMS. The authors of this paper also contributed an EMS to the challenge and achieved a fifth-place finish, with a total trip cost of $1.656. Our EMS was also rule-based with some offline-optimisation of the FC (combined H_2 consumption, FC degradation and dc-dc converter efficiency). As with the EMS presented in [28], our EMS has a FC switch-on at 70% SOC but based on the challenge model, this results in high battery degradation costs.

Other rule-based strategies for FC vehicles include a research study by Yue et al. [29] who developed an EMS that controls the FC output and reduces the degradation of the battery. They employ a FLC that uses thirty-six rules to set the FC current to one of nine possible levels. The input parameters are traction demand, battery SOC and battery remaining useful life, which has been estimated using prognostics. This EMS achieves a 4.75% reduction in battery degradation but does not specify the change in FC fuel economy or the impact on FC degradation to achieve this reduction. Hames et al [10] tested four fuel-saving control strategies in a FCEV with both battery and supercapacitor (SCAP) secondary power sources. While their strategies incorporated both battery and SCAP min\max SOC values as constraints, the level of power source degradation is not evaluated. An ECMS is proposed as the optimum strategy based solely on achieving the minimum hydrogen consumption over a given drive cycle. Two control strategies for a FCEV are presented in [30]: one to minimise fuel consumption by maximising the utilisation of the battery and SCAP power sources; the other for reduced battery degradation by utilising the SCAP to supply the high-current pulses to the traction drive and to receive high-current pulses during regenerative braking. While the latter strategy in [30] lowers battery degradation, the impact of each control strategy on FC degradation is not presented in their paper. In stop-go driving conditions, their study demonstrated that H_2 consumption increases significantly (173%) when the reduced battery degradation strategy is employed. An adaptive FLC EMS is proposed for a low-power FCEV in

[31] and focuses on optimising the powertrain control rather than utilising a fuel minimisation strategy. This EMS adapts to three load conditions (braking, normal driving and max power driving) by adjusting the FC power output and the FC dynamic-response rate for load changes to maintain the battery SOC at a reference value.

6.2.3 Power Source 1 - FC Degradation

An understanding of the root causes of FC degradation during normal vehicle operating conditions is necessary in order to optimise the durability of a FC. FC operation is usually explained as a steady-state energy conversion process where hydrogen is provided to the anode and oxygen (O_2) to the cathode. At suitable temperatures, the hydrogen splits into hydrogen ions, which migrate to the cathode via a membrane, and into electrons which flow in an external circuit. Wastewater results when the hydrogen ions react with the O_2 at the cathode. The output power is determined by controlling the flow rates of each gas based on the stoichiometric ratio for this reaction. The balance of plant (BOP) controls the steady-state gas flow requirements and the removal of wastewater. In steady-state benign conditions, FC stack lifetimes of more than 25,000 hours are possible [32].

Under dynamic conditions, such as found in vehicle applications, process control is considerably more complex. As the power demand varies, the BOP must quickly adjust the gas flow rates to match the new power demand. An additional vehicle FC issue is that air needs to be pumped to meet the O_2 requirement at the cathode. Under high-power conditions, the BOP must be designed to flow a high volume of air to the cathode. A study by Pei et al. [32] summarises four vehicle operating conditions which may result in FC degradation, namely, load-cycling operation, stop-start operation, high-power operation and low current operation (idling). Accelerated lifetime testing of a FC stack from a bus [33] showed that 56% of the FC degradation was due to load-cycling and 33% due to stop-start operating. This study derived performance deterioration rates of 0.0000593 % per cycle for large-range load-cycling, 0.00196% per cycle for stop-start cycling, 0.00126 % per hour for idling operation time and 0.00147% per hour for high-power operation. The reduced FC lifetime, when operating under such dynamic conditions, can be as low as one-tenth of the lifetime under steady-state conditions.

Studies of FC degradation in vehicles [34]-[36] show that the principal FC stack degradation mechanisms are membrane dehydration and incorrect stoichiometric ratios due to flooding in the gas flow channels. For example, during idling operation, the maintaining of membrane hydration is difficult due to the low levels of wastewater available, and so micro-cracks may form on the dehydrated membrane. During high-power operation, waste-water flooding in the air channels can cause non-uniform power generation and lead to excessive temperatures within the stack. The degradation found under stop-start conditions results from incorrect gas conditions at one, or at both electrodes. When the FC has been off for a time, air from the cathode side can migrate to the anode side. At start-up, the FC open-circuit voltage can only be developed when the H_2 fuel has displaced any leaked air at the anode. In the absence of H ions, O_2 in the air oxidises with the carbon structure which supports the platinum catalyst particles at the cathode. Carbon dioxide (CO_2) or carbon monoxide (CO) is formed and the catalyst is lost as its carbon structure degrades. A similar condition can occur when the H_2 fuel flow is shut off. The greatest challenge for the BOP equipment for load-cycling conditions is maintaining the humidity at both the anode and the cathode sides of the membrane while simultaneously controlling the stack temperature. The high number of these cycles during vehicle operation can result in a significant deterioration of the stack output voltage within a relatively short period of time (1,000-3,000 h), despite the fact that degradation associated with each individual load cycle is low. FC degradation due to air pollutants and to wastewater freezing in cold ambient temperatures, can be minimised by good BOP design.

6.2.4 Power Source 2 - Battery Degradation

Modelling of battery degradation is achieved using physically based electrochemical models which require detailed information about the internal chemical construction or by using semi-empirical or empirical models that establish degradation relationships using experimental test data. The complex electrochemical models have been shown to provide the best degradation estimates [37], but the simpler empirical models are easier to integrate into vehicle simulators and are used in this study. The two battery types used in FCEV are Nickel Metal-Hydride (NiMH) and Lithium-ion (Li-ion). As Li-ion is the dominant battery technology in vehicles, this paper will

review degradation mechanisms in this battery type, although the 2015 Toyota Mirai FCEV features a NiMH battery. Battery degradation is associated with a loss of usable capacity (capacity fade) and with an associated increase in the internal series resistance which restricts the power output (power fade) of the battery.

Battery degradation can be classified as either calendar degradation or as cycle degradation. Calendar degradation refers to the loss of capacity over time when the battery is neither charging nor discharging. Ambient temperature is the main impact factor in calendar degradation across all battery chemistries and the degradation rate is modelled using a power law relationship known as the Arrhenius equation. This equation states that degradation rates increase as ambient (battery) temperatures increase and is valid for Li-ion chemistries. It is not applied to sub-zero ambient temperatures applications as the electrochemical degradation mechanism for Li-ion is different at these temperatures [38]. The general form of this Arrhenius equation for battery degradation, is given as

$$Q_{loss\_cal} = A_{CAL} e^{\left(\frac{-E_A}{RT}\right)} \cdot t^x \tag{6.1}$$

where Q_{loss_cal} is the percentage battery capacity loss, A_{CAL} is a curve-fitting coefficient determined using test data, E_A is the battery cell activation energy in J/mol, R is the universal gas constant in J/mol K, T is the ambient temperature in K, t is the test time period which is usually specified in days due to the long-time constant associated with calendar degradation and x is the power law value which is commonly assigned a value of 0.5 [39]. In addition to temperature, the rate for calendar degradation is dependent on the battery SOC. For Li-ion batteries, increased calendar degradation occurs at very high (SOC>80%) values of SOC [40].

Cycle degradation rate is impacted by multiple operational parameters of the application. Examples of impact factors include depth of discharge (DOD), charge and discharge capacity *C* rate, ambient temperature and the number of load cycles. Cycle degradation can be compared to mechanical fatigue modelling [41] and it is difficult to establish individual parameter impacts on the degradation rate as the impact parameters are interlinked. One approach to simplify cycle degradation modelling [39], [42] is to combine the DOD and cycle-number parameters into a single Ampere-hour (Ah) throughput value $Ah_{100\%\mathrm{DoD}}$ and then to use regression analysis to relate

the temperature and *C* rate to experimental test data. This yields an empirical model for percentage capacity loss in the form of

$$Q_{loss\_cyc} = \left[(a_0T^2 + b_0T + c_0)e^{(d_0T + f_0(C_{rate}))} \times Ah_{100\%\text{DoD}}\right] + \left(k_0 e^{\left(\frac{-E_A}{RT}\right)} \times t^{0.5}\right) \tag{6.2}$$

where $a_0, b_0, c_0, d_0, f_0, k_0$ are the coefficients fitted to the test data. The validity of this approach is questionable as the Ah throughput of a battery is not constant but is a quadratic function of cycle DOD [43]. In [44] an effective Ah throughput is determined using severity maps. The severity map provides a degradation rate for each set of conditions (SOC, temperature, magnitude of current) in a given cycle and integrating these rates over time provides an effective lifetime Ah throughput value (Ah_{LIFE}). The complexity in modelling cycle degradation is further demonstrated by a study in Sweden [45], where the impact of battery current direction (charge or discharge) was tested and the cycle degradation is found to be higher when charging at high *C* rates compared to the equivalent degradation recorded when discharging at the same *C* rate. Alternative cycle degradation models for Li-ion batteries which are based on loss of active material or SEI layer growth are discussed in [37].

The increase in the battery pack series resistance R_{BP}, which results in power-fade, is modelled in [46] as

$$R_{BP}(\text{SOC}) = a_1 e^{(-b_1 SoC)} + R_{BP0} \tag{6.3}$$

where a_1, b_1 are coefficients fitted to the test data and R_{BP0} is the initial measured series resistance of a fully charged battery pack. This model results in a rapid increase in resistance as the SOC drops below 20%. Combining this model with the impact of high SOC on calendar degradation found in [40], minimum battery degradation occurs when the SOC is constrained in a range from 20% to 80%.

6.3 Fuel Cell Vehicle Model

The challenge vehicle parameters are presented in Table 6-1. The equations of the FCEV model are either published in [2], or else extracted by the authors from the Matlab\Simulink model provided by the challenge organisers. The vehicle specification is based on the 2009 model of the Tazzari-Zero EV [47].

Table 6-1. Vehicle model parameters [2].

Parameter	Symbols	Units	Value
Max traction power		kW	15
Max traction torque		Nm	2000
Vehicle mass	M	kg	698
Wheel radius		m	0.2865
Gear ratio	N_g		5.84
Frontal area	A_f	m^2	1.942
Drag coefficient	C_d		0.36
Rolling Resistance	C_{rr}		0.02
Fuel Cell max power		kW	16
Fuel Cell max current		A	400
Fuel Cell max voltage		V	60
Fuel Cell min voltage		V	40
Battery capacity	Ah_{RATED}	Ah	40
Battery max voltage		V	100.8
Battery min voltage		V	60

A vehicle's total motive force or tractive effort F_{te} is based on the vehicle speed and the acceleration requirements of the drive cycle

$$F_{te} = MgC_{rr} + 0.5\rho C_d A_f v^2 + Mgsin\theta_r + Ma \tag{6.4}$$

where the parameters are vehicle mass M in kg, frontal area A_f in m^2, drag coefficient C_d, tyre rolling-resistance coefficient C_{rr}, vehicle acceleration a in m/s^2, air density ρ (1.223 kg/m^3), gravity g (9.81 m/s^2), road grade θ_r, and the net relative air velocity v in m/s which is the combined vehicle and wind velocities. The regenerative braking distribution fraction, Reg_{ach}, is a fraction of this traction force and it is limited to a maximum of Reg_{ach}=0.5 in this front-wheel drive vehicle. A Reg_{ach}=0 represents no regenerative braking available in this vehicle.

The COO costs per drive cycle are calculated based on the fuel and the power source replacement costs presented in Table 6-2. These costs are based on US Department of Energy system target costs for 2020.

Table 6-2. Fuel costs and component replacement costs [2].

Parameter		Units	Value
FC replacement cost	FC_{cost}	$	600
Battery replacement cost	BAT_{cost}	$	640
H_2 fuel cost	$H_{2\,cost}$	$/g	0.0035

The H_2 mass flow rate $\dot{m}_{H2}$ with units in g/s, is given as a linear equation:

$$\dot{m}_{H2} = (a_2 I_{FC} + b_2) \times 0.08988/60 \tag{6.5}$$

where a_2 and b_2 are the experimentally validated coefficients of the FC model (shown in Table 6-3) and I_{FC} is the FC output current. The FC output voltage, V_{FC} is modelled using a polynomial relationship to FC output current:

$$V_{FC} = c_2(I_{FC})^3 + d_2(I_{FC})^2 + f_2 I_{FC} + k_2 \tag{6.6}$$

where c_2, d_2, f_2 and k_2 are the FC coefficients shown in Table 6-3.

Table 6-3. FC model coefficients [2].

Coefficient	Value
a_2	0.52488
b_2	15.835
c_2	-6.7791e-07
d_2	0.00044927
f_2	-0.11913
k_2	59.124

The dc-dc boost converter efficiency η_{BOOST} is given as:

$$\eta_{BOOST} = -0.0095 I_{FC} + 95 \tag{6.7}$$

The degradation of the FC Δ_{FC} at time t is a combination of the number of start-stop events N_{SWITCH} and a quadratic function of the operational power of the FC:

$$\Delta_{FC}(t) = \Delta_{SWITCH} N_{SWITCH} + \int_0^t \delta(t) \tag{6.8}$$

where the operating-power degradation function is

$$\delta(t) = \frac{\delta_0}{3600}\left(1 + \frac{\alpha}{P_{FC-NOM}^2}[P_{FC}(t) - P_{FC-NOM}]^2\right) \tag{6.9}$$

Parameter Δ_{SWITCH} is a start-stop event FC degradation coefficient, δ_0 and α are FC operating-power degradation coefficients, and all of the coefficient values are provided in Table 6-4. Parameter P_{FC-NOM} is the nominal power of the FC, which has a specified value of 6 kW for this FCEV.

Table 6-4. FC degradation coefficients [2].

Coefficient	Value
Δ_{SWITCH}	$2.5\text{x}10^{-4}$
δ_0	$0.5\text{x}10^{-4}$
α	4

FC degradation has a significant impact on the EMS development and is high for drive cycles with frequent FC start-stop events due to the high value of Δ_{SWITCH}. This FC degradation model captures two of the four vehicle operating conditions [32] reported in the literature. The impact of load-cycling and idling are not represented in the model equations. Load-cycling is severely restricted by the slow dynamic response of the FC model to avoid this degradation condition.

Battery degradation Δ_{BAT} is determined using the magnitude of the battery current I_{bat}, SOC and the battery operational state, e.g. discharging ($I_{bat}>0$) or charging ($I_{bat}<0$). The battery degradation at time t is given as

$$\Delta_{BAT}(t) = \left(\frac{1}{Q_{LIFETIME}}\right)\int_0^t |F(\text{SOC})G(I_{bat})I_{bat}|\, dt \tag{6.10}$$

where

$$F(\mathrm{SOC}) = 1 + 3.25(1 - SoC)^2 \tag{6.11}$$

Parameter $Q_{LIFETIME}$ is the effective battery throughput [44] in ampere-seconds, calculated using the nominal battery capacity Q_{bat} of 40 Ah:

$$Q_{LIFETIME} = 15000 \times 3600 \times Q_{bat} \tag{6.12}$$

The degradation component $G(I_{bat})$ is dependent on the battery current and is determined using;

for $I_{bat} > 0$ (discharging)

$$G(I_{bat}) = 1 + 0.45\left(\frac{I_{bat}}{I_{RATED}}\right) \tag{6.13}$$

and for $I_{bat} < 0$ (charging)

$$G(I_{bat}) = 1 + 0.55\left(\frac{|I_{bat}|}{I_{RATED}}\right) \tag{6.14}$$

where I_{RATED} is the rated current of the battery (40 A for this vehicle). The ratio I_{bat} / I_{RATED} is the *C* rate value of the battery current. While the literature identifies temperature as a major battery degradation factor for both calendar and cycle degradation, it is not included in this model. Also, analysis of these two degradation model functions (Figure 6-2) shows a linear increase with *C* rate and a power law relationship with SOC, with minimum degradation occurring at 100% SOC. This SOC-degradation function conflicts with the literature, which shows a high SOC can lead to a high level of degradation [40]. In this vehicle model, operating the battery near to 100% SOC will reduce battery degradation costs. This degradation function, when combined with a challenge constraint which specified 100% SOC at the end of each drive cycle, greatly influenced the development of an EMS for this vehicle. However, this topic is revisited in Section 6.6.

The model recharges the battery using the FC. The recharging cost ($CHG) is calculated for the additional H_2 required, FC degradation, boost efficiency and battery degradation during the recharge operation. FC degradation costs are higher if the FC is off at the end of the drive cycle and must be switched-on again to meet the battery recharge requirement.

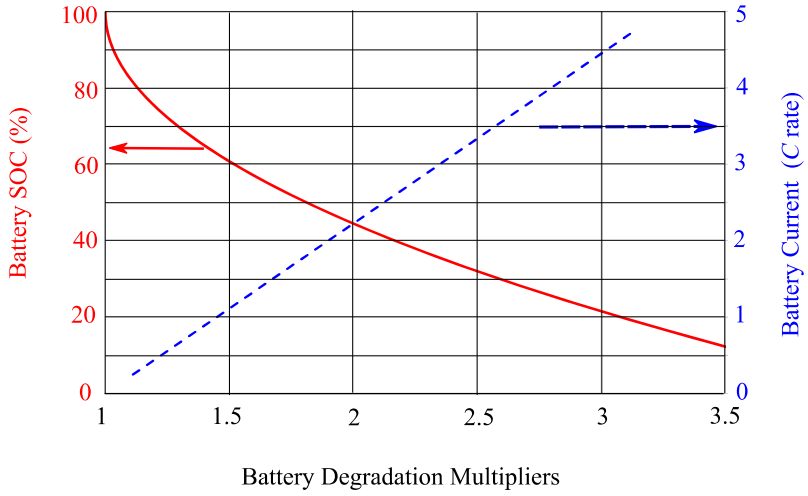

Figure 6-2. Battery degradation rate based on SOC and on discharge current amplitude.

The vehicle model provides two equations to calculate the recharging costs dependent on the FC status (on or off) and the SOC of the battery at the end of the drive cycle SoC_F.

FC on:

$$\$_{CHG} = -0.0286(SoC_F)^3 + 0.2527(SoC_F)^2 - 1.362(SoC_F) + 1.1376 \qquad (6.15)$$

FC off:

$$\$_{CHG} = -1.7987(SoC_F)^3 + 2.9842(SoC_F)^2 - 2.6188(SoC_F) + 1.4543 \qquad (6.16)$$

Total drive cycle costs ($\$_{TOT}$) are calculated by converting the degradation values to costs using the component replacement costs in Table 6-2. These costs are then summed with the fuel costs and recharging costs.

$$\$_{TOT} = FC_{COST}\Delta_{FC} + BAT_{COST}\Delta_{BAT} + H_{2\,COST}\int_0^t \dot{m}_{H2}\,dt + \$_{CHG} \qquad (6.17)$$

The FC model's dynamic response uses three rate-limiting components connected in series; a 6 A/s current rise limit for FC output currents < 150 A, a 20 A/s current rise limit for FC output currents >150 A and a 15 mHz low-pass filter. The significance of this slow FC dynamic response for EMS development is presented in Section 6.4.

6.4 EMS Development Strategy

The competition organisers provided the vehicle model with a simple rule-based EMS (referred to as the baseline-EMS in this chapter), which implements thermostat-type control of the FC. The FC starts when the battery SOC drops to 40% and operates at the maximum power output until the FC stops at an SOC of 70%. The initial braking strategy sets Reg_{ach} to zero, which implies no regenerative braking. Three drive cycles are provided as part of the vehicle simulation model. Two drive cycles are adapted versions (max. speed restricted to 85 kmph) of legislative vehicle test cycles: New European Drive cycle (NEDC) and the class 2 version of the Worldwide-harmonised Light-vehicle Test Procedure (WLTP). A third drive cycle (Urban) is based on a short (380 s) recorded journey by the University of Lille in a Tazzari-Zero vehicle. The challenge organisers used a fourth drive cycle, referred to as *VTS*TC in this chapter, with a 2,590 s duration, to score any EMS developed by the 2017 challenge participants.

As the duration of the challenge drive cycle is unknown to the challenge participants, model-based optimisation techniques such as DP and PMP could not be implemented for EMS development. Instead the approach followed is similar to ECMS, except that equivalent costs rather than equivalent fuel consumption are modelled. Each power source, FC and battery, was analysed in terms of the costs to provide 1 kWh to the input of the traction drive on the dc link.

The cost map ($/kWh) for the FC is developed using Matlab arrays as follows: a FC power-output relationship with I_{FC} is established when (6.6) is multiplied by a 0-400 A range of I_{FC} values. Equation (6.5) establishes the H_2 consumption at each power level, which can then be normalised to a fuel cost per kW at the FC output. FC degradation costs for each power level (neglecting the FC start-stop degradation costs) can be calculated using (6.9) and combined with the fuel costs. The boost converter efficiency (6.7) is applied to the combined costs at the FC output terminals in order to determine the cost per kWh at the dc link. These calculations are summarised in a FC cost map at various I_{FC} values in Figure 6-3. The optimised FC operating power level is impacted by both the boost converter efficiency and the FC degradation. When only fuel costs are considered, the optimised FC operating-level is at 244 A (11.46 kW) with a resulting cost per kWh of $0.237, shown as OPT-1 in Figure 6-3. When the FC degradation costs are included, the optimum operating-level shifts down to 184 A (8.87

kW) and the cost rises to \$0.249 /kWh, shown as OPT-2 in Figure 6-3. Finally, when the boost converter efficiency is also considered, the optimum operating-level reduces further to 172 A (8.34 kW) and results in a cost of \$0.263 /kWh, shown as OPT-3 in Figure 6.3. This analysis identifies a single optimum operating point and also shows the low variation in FC costs (less than \$0.01/kWh) in the I_{FC} range of 105 A (5.2 kW) to 275 A (12.5 kW), suggesting that a wide operating range is possible for the FC without incurring significant additional COO costs. The cost associated with FC degradation for each stop-start event is calculated using the FC replacement cost (Table 6-2) and the degradation coefficient Δ_{SWITCH} (Table 6-3). The high cost of \$0.15 per event advocates that the developed EMS must minimise the number of FC start-stop events in each drive cycle.

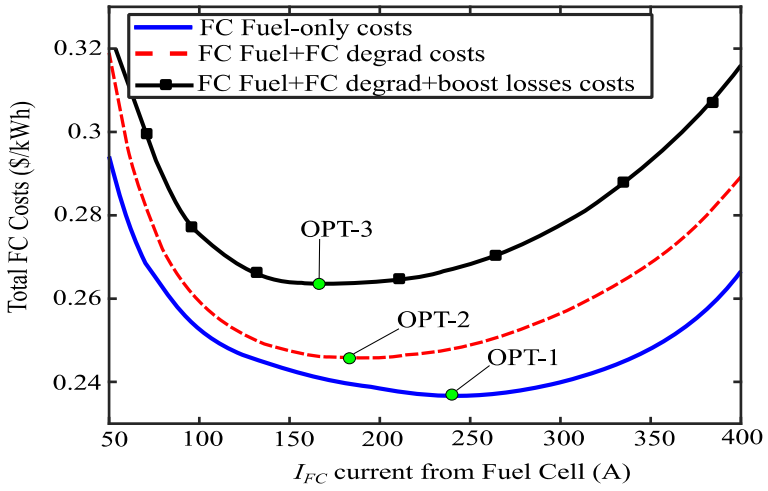

Figure 6-3. Offline optimisation of FC costs to provide 1 kWh at the dc link.

In this FCEV, the battery energy can only be recharged by the FC or by regenerative braking. For FC-supplied battery energy, the total costs for the battery to resupply 1 kWh of this stored energy back to the dc link, would be the combination of the recharge cost plus the discharge costs. The recharge cost is the sum of the previously calculated FC costs, internal energy loss in the series resistance, and the battery degradation costs during recharging. The discharge cost is the combined series-resistance energy loss costs and the battery degradation costs during discharge. As the battery degradation costs are dependent on both the SOC and the battery current direction (charging or discharging), a cost map for the battery has many dimensions which also depend on the rates of charging and discharging. In order to simplify the

cost calculation, the same current value is assumed for both charge and discharge battery currents. Using equations (6.10 to 6.14), a cost-map for 1 kWh provided by the battery at the dc link is shown in Figure 6-4.

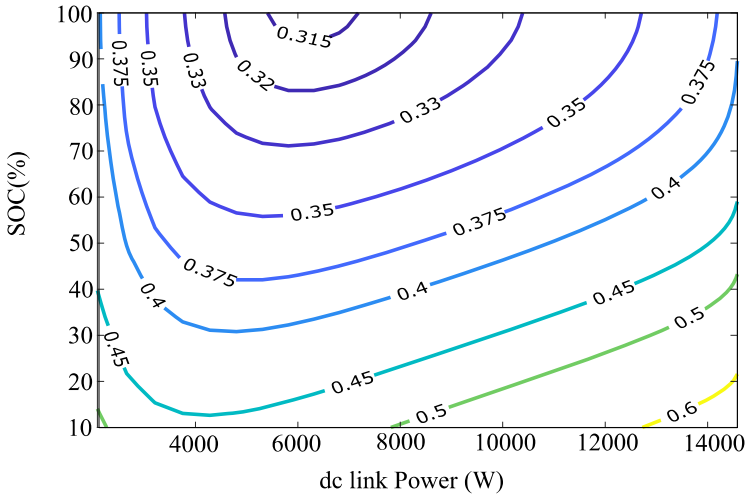

Figure 6-4. Offline optimisation of battery costs to provide 1 kWh at the dc link.

The map shows that battery operation at low SOC levels results in higher costs. When costs in Figure 6-4 are compared to the costs in Figure 6-3 for 1 kWh at the dc link, it is apparent that battery-only operation for this FCEV would result in significantly higher COO costs than FC-only operation. This cost map also identifies the FC output power required to minimise the recharging costs based on the battery SOC value.

Assuming steady-state operation, the offline equivalent-cost optimisation of the power sources (Figure 6-3 and Figure 6-4) suggests that FC-only operation should achieve minimum drive cycle costs. An EMS to achieve FC-only operation is a load-following strategy where the traction power demand at the dc link P_{dc} as shown in Figure 6-1, is converted to a FC current demand I_{FC}. This type of load-following strategy is possible with some advanced designs of FCEV, such as the Toyota Mirai [8]. However, the dynamic response of the FC stack in the challenge vehicle, is considerably slower than the dynamic power rates required by the traction drive.

Optimisation which includes component dynamic performance constraints is beyond the scope of this study, but experimentation using the Matlab-Simulink model provided useful insights into what might be achieved. For example, when a simple load-following EMS was developed for the FCEV, the results in Figure [6-5] show

that the FC is unable to track the traction power requirement. As the challenge did not allow participants to change the dynamic response, battery operation is required for the vehicle during acceleration and braking in each drive cycle. As the battery is directly connected to the dc link, an EMS has only limited control on the instantaneous battery power (and current) levels. Figure 6-5 also clarifies that the traction power requirements during acceleration are higher than the 16 kW available from the FC which also leads to a battery power requirement for peak traction loads.

Further experimentation with the vehicle model illustrates that the required traction energy, measured at the input of the traction drive P_{dc} is independent of the battery voltage value. With full regenerative braking (Reg_{ach} = 0.5), the traction energy requirement at the dc link is 2% lower for the NEDC and WLTP drive cycles, and is 11% lower on the Urban drive cycle. Using the baseline-EMS, model simulations show that the degradation costs for one FC start-stop event represents up to 24% of the COO costs for an Urban drive cycle.

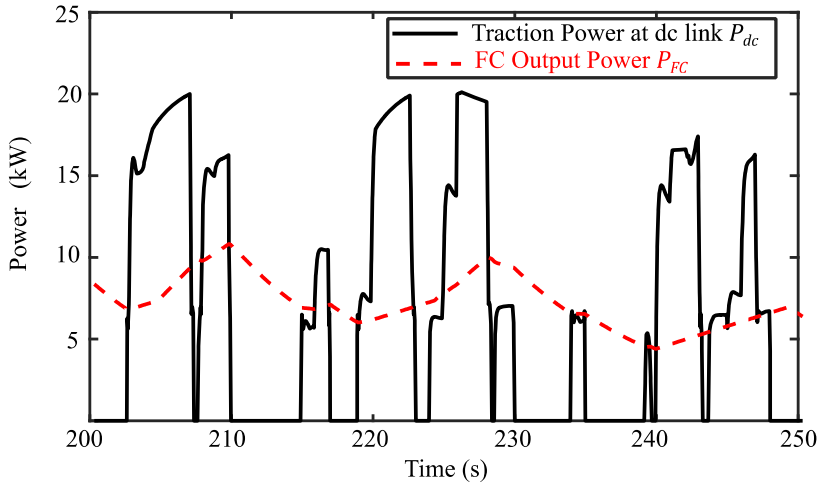

Figure 6-5. Dynamic response of the FC with a load-following strategy

The combination of the equivalent-cost analysis of the power sources and the experimentation with the vehicle model resulted in a set of optimising vehicle operating conditions which were used to develop a rule-based EMS. These conditions are as follows:

(i) Minimise the FC start-stop events per drive cycle to one event.

(ii) Maintain the battery SOC close to 100% while ensuring the FC is not turned off. FC is turned off only if the battery SOC reaches 100% or the FC output current drops below 10 mA.

(iii) Operate the FC close to its optimum power level for minimum COO costs ($P_{FC-OPT3}$ = 8.34 kW or $I_{FC-OPT3}$ = 172 A).

(iv) Reduce the traction energy requirement for H_2 fuel by maximising the recovered energy using a high regenerative braking distribution factor, Reg_{ach}= 0.5.

(v) Prioritise FC output over battery output for increasing traction power demands due to the lower equivalent costs associated with the FC power source.

In order to simultaneously meet the requirements of conditions (i) to (iv) with the slow power dynamics of a power plant, such as the FC, a safety margin must be incorporated into the EMS. Restricting the FC start-up until the battery SOC has dropped from 100% to 95% SOC provides a 5% SOC margin before the FC will be turned off again. Condition (i) can be achieved by linearly decreasing the FC power output as the battery approaches 100% so that FC turn-off conditions are not reached before the end of the drive cycle. A linearly decreasing regenerative braking distribution factor Reg_{ach} is applied when the battery SOC is higher than 98%. This prevents a regenerative braking event from recharging the battery to 100% which would result in the FC turning off. Condition (v) can be implemented by comparing the FC power output P_{FC} with the traction drive power P_{dc}: if the P_{dc} requirement increases, then P_{FC} is proportionally increased in response to the increasing traction demand. The EMS structure described can be implemented with the following six rules:

Rule 1: FC turned on when SOC<95%

Rule 2: SOC<95%, FC = $P_{FC-OPT3}$ (or $I_{FC-OPT3}$)

Rule 3: SOC>95%, FC = $k_p \times \Delta SoC \times I_{FC-OPT3}$

Rule 4: SOC<95%, $P_{dc} > P_{FC-OPT3}$, FC=$(1 + k_{sus}) \times I_{FC-OPT3}$

Rule 5: SOC<98%, Reg_{ach} = 0.5

Rule 6: SOC>98%, Reg_{ach} = $k_R \times$ 0.5

where k_p, k_{sus} and k_R are linearly decreasing proportional gains based on equations supplied in Section 6.5.

6.5 Results for New Optimised Challenge EMS

The newly developed EMS for this vehicle, EMS-1, is shown in Figure 6-6 and is a simplified version of the three previous EMS proposed by the authors [48]. The simple regenerative braking elements of the strategy given by rules 5 and 6, are not shown in Figure 6-6.

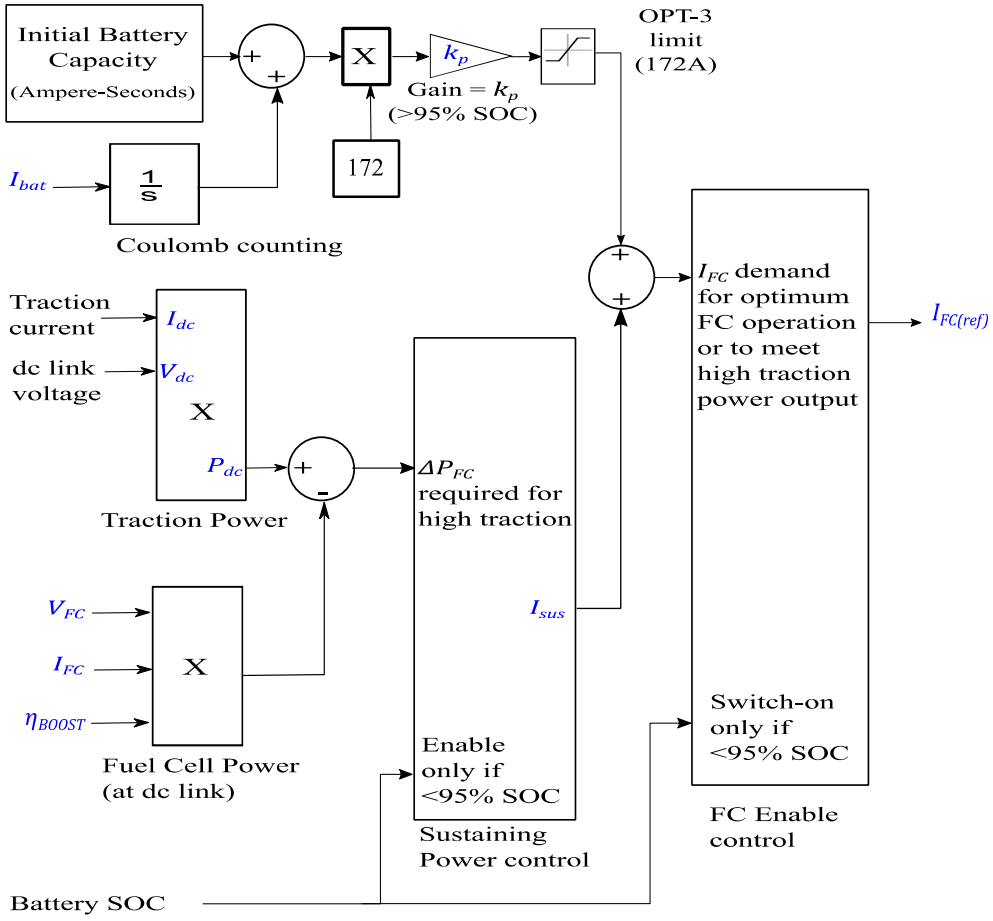

Figure 6-6. Simulink model implementation of EMS-1

The FC current demand $I_{FC(ref)}$ is zero until the FC is enabled. The FC turns on when the battery SOC drops to 95%. The battery recharging current demand is initially determined by converting the starting battery Ah value to an Ampere-second (As) value and this demand is updated each second, using the Coulomb counting method, as the vehicle completes the drive cycle. The maximum recharge current is set to the

optimum FC current level of 172 A. At 95% SOC and above, a proportion gain k_p automatically reduces the current demand below the maximum as given by

$$k_P = 1/(0.05 \times 3600 \times Q_{bat}) \tag{6.18}$$

If the battery SOC is below 95%, the FC will operate at its optimum power level of 8.34 kW (172 A) and primarily supply the traction drive requirement, P_{LINK}. Any surplus power will recharge the battery. The remaining components in EMS-1 only become operational when P_{dc} exceeds η_{BOOST} x 8.34 kW. In this condition, the FC power reaching the dc link is less than the traction drive power requirement, so the FC power is raised by calculating the power increase needed. This power increase is converted to a current-sustaining-demand value I_{sus} using a proportional gain (k_{sus}) value given by;

$$k_{sus} = \left(I_{FC(MAX)} - I_{FC-OPT3}\right)/\left(P_{FC(MAX)} - P_{FC-OPT3}\right) \tag{6.19}$$

where $I_{FC(MAX)}$ and $P_{FC(MAX)}$ are the FC maximum current of 400 A and FC maximum power of 16 kW, respectively.

The regenerative braking strategy keeps Reg_{ach} constant at 0.5 (Rule 5) and linearly reduces this factor using a proportional gain k_R when the battery SOC exceeds 98%.

$$k_R = 50(1 - SoC) \tag{6.20}$$

As per Rule 4, the sustaining circuit is only active while the SOC is less than 95%. The net effect of switching off the sustaining circuit and proportionally decreasing the battery recharge current demand, is that the charge-sustaining battery control keeps the SOC in the region of 97% as shown in Figure 6-7.

In the VTS challenge, the level of optimisation achieved by an EMS is evaluated by the minimisation of the COO costs over a drive cycle. For the *VTS*TC drive cycle, a benchmark cost of \$1.612 was established by the challenge organisers using DP optimisation. The proposed rule-based strategy, EMS-1, achieves a COO of \$1.592 in the *VTS*TC drive cycle. This is a 2% improvement on the challenge winner costs of \$1.624 and a 1% improvement on the benchmark DP optimisation costs.

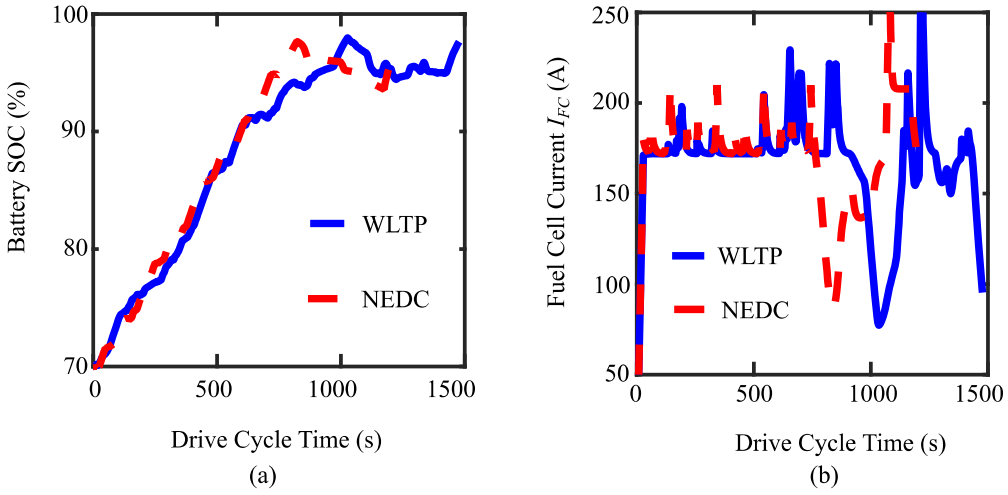

Figure 6-7. EMS-1 test results over WLTP and NEDC drive cycles (a) Battery SOC (b) I_{FC} .

The proposed EMS was also evaluated for the three other drive cycles provided with the challenge model. A comparison with the baseline-EMS performance in terms of COO costs and the impact on power source lifetimes are detailed in Table 6-5. In these evaluations, the vehicle starts the drive cycle with a battery at an initial SOC of 70%. The impact of this starting condition is that each drive cycle will have fixed recharging costs associated with the challenge requirement that the battery must be fully recharged at the end of a drive cycle. The recharging fixed costs include the H_2 fuel costs, the FC degradation cost for a start-stop event, as well as FC and battery operational degradation costs. For each drive cycle the energy required at the traction drive input can also be regarded as a fixed cost as an EMS cannot change this traction energy demand. The approximated fixed cost for the traction energy in Table 6-5, is calculated by assuming P_{dc} is to be provided only by the FC, operating at maximum efficiency ($0.2635 per kWh) and the battery discharge degradation costs are assumed to be zero.

Optimisation of the power sources using either model-based or rule-based EMS cannot achieve COO costs that are lower than the fixed drive cycle related costs. The results of simulations with the EMS-1 strategy show that COO costs are within 4% of these fixed costs. The EMS-1 strategy decreases COO costs by up to 29.5% when compared to the baseline-EMS for the WLTP drive cycle.

Table 6-5. Simulation results and analysis of fixed-cost impacts.

Parameter	Units	Urban	NEDC	WLTP
DC bus Traction Energy	Wh	576	1,610	2,098
Min cost of Traction Energy	$	0.152	0.424	0.553
FC start-stop degradation cost	$	0.15	0.15	0.15
Battery recharge cost (70% SOC)	$	0.298	0.298	0.298
Total fixed drive cycle costs	$	0.60	0.872	1.001
Drive cycle costs(baseline-EMS)	$	0.74	1.09	1.46
Drive cycle costs (EMS-1)	$	0.625	0.897	1.029
Cost reduction using EMS-1	$	15.5%	17.6%	29.5%
FC lifetime (baseline-EMS)	h	N\A[a]	1,104	1,205
FC lifetime (EMS-1)	h	394	1,196	1,441
Battery lifetime(baseline-EMS)	h	1,369	2,532	1,801
Battery lifetime (EMS-1)	h	2,305	6,031	6,860

[a] FC not operating in this drive cycle using baseline-EMS

Strategies can also be evaluated in terms of their impacts on power source lifetimes. EMS-1 improves the lifetime of both the FC and the battery. The FC operating times are shorter with the baseline-EMS but the higher power levels lead to higher levels of FC degradation and a lower FC lifetime. On the *VTS*TC, EMS-1 results in a FC lifetime of 2,299 hours and a battery lifetime of 5,465 hours. These are comparable to the DP optimised lifetime values of 2,447 hours for the FC and 4,703 hours for the battery.

6.6 Toyota Mirai Analysis and Model Modifications.

State-of-the-art mass produced FCEV designs include the Honda FCX Clarity [49], the Toyota Mirai [50], and the Hyundai Nexo [51]. Their power-source ratings differ from many of the low-power FC vehicles tested in EMS development studies. The commercial FCEV models are equipped with high power FC stacks, from 95 kW for the Nexo to 114 kW for the Mirai, to match the peak-power requirements of the vehicles. They also have advanced FC stack and BOP designs to improve gas flows and humidity controls, which result in higher dynamic power rates from the FC stack while significantly reducing the impacts of FC degradation [52]. For cost reasons, FCEV designs have the same powertrain configuration as existing high-volume HEV configurations, with the ICE and transmission system being replaced by a FC stack [53]. The EMS for these vehicles are not published in the literature but the basic rules of the operating strategy for the Toyota Mirai can be deduced from the tests carried out by ANL [9]. The condition for FC turn-on is when the DC bus power demand exceeds 5 kW. During normal driving conditions, the EMS controls the FC with a load-following strategy. During braking and when idling, the FC is turned off. As Toyota offer an 8 year /100,000 miles warranty for the Mirai, their EMS suggests that they have significantly reduced the FC degradation impacts associated with load-cycling and start-stop events using new stack and BOP designs.

The FC system efficiency, where the system includes the FC water pump, compressor, H_2 pump and the boost converter, has a peak efficiency of 63.7% at low output powers of approximately 10 kW. This is consistent with the vehicle power requirements for most drive cycles. FC degradation at high-power output is reduced by folding-back the peak FC power output after a period of approximately 30 s. The EMS maintains the battery SOC at a constant level of approximately 60%. This charge-sustaining level is consistent with the literature on battery degradation which identifies operating with a low-SOC of 20% or with a high-SOC of 80% as increasing the rate of battery degradation.

In this section, the challenge FCEV model is compared to the Mirai. The battery degradation equation (6.11) is replaced with an equation which is compatible with the Li-ion degradation mechanisms found in the literature and which reflects battery operation in typical HEV designs. The developed strategy, EMS-1, is modified to include the new battery degradation equation. The FC voltage and mass flow equations

are modified to achieve the higher efficiency of the Toyota Mirai FC stack. This new FC model is tested with the EMS-1 strategy.

6.6.1 Charge-sustaining at 60% SOC

In order to optimise the COO over a drive cycle, the challenge FCEV battery degradation model, as specified by (6.11), constrains EMS development to strategies with the battery operating at close to 100% SOC. A proposed alternative degradation model is specified in equation (6.21) and is plotted with the original degradation model in Figure 6-8.

$$F(\mathrm{SOC}) = 0.98 + 7e^{-10SoC} + e^{12(SoC-1.03)} \tag{6.21}$$

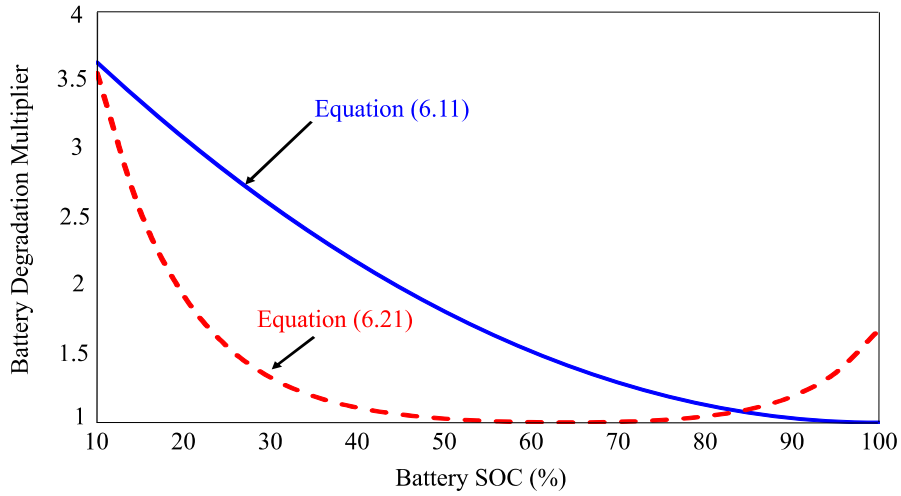

Figure 6-8. Battery degradation equation comparison.

This bathtub-curve-shaped model optimises battery operating in the range of 50% to 80% SOC. Modification of EMS-1 to minimise COO cost by applying this new battery degradation model involved changing; (i) FC turn-on from 95% to 60% SOC, (ii) sustaining circuit disable point from above 95% SOC to above 60% SOC, and (iii) the battery recharge current demand function to specify a linearly decreasing demand from optimum FC current to zero in the 5% SOC region above the target SOC value (60% in our tests). Implementation of these three parameter value changes achieved nearly identical *VTS*TC drive cycle combined costs for fuel, battery degradation and

FC degradation as had been achieved when operating at a charge-sustaining level of 95% SOC. The new COO cost for the *VTS*TC, without a recharge to 100% requirement, was $1.592 with an average battery SOC of 60%, compared to $1.586 for EMS-1 with an average battery SOC of 95%. The modified vehicle model allowed optimising strategies over a wider, more typical, range of battery SOC values.

6.6.2 Scaling the Mirai FC Stack

A scaled version of the Mirai FC stack is modelled by modifying equation (6.6) to reflect the improved current density of the Mirai FC [8] and the resulting FC polarisation curve is given by equation (6.22). The Toyota Mirai system efficiency test data in [9] can be used to derive a new FC mass flow equation (6.23).

$$V_{FC} = c_x - d_x \, log_e(I_{FC}) - f_x I_{FC} \tag{6.22}$$

$$\dot{m}_{H2} = [a_x (I_{FC})^2 + b_x I_{FC} + 2.7529] \times 0.08988/60 \tag{6.23}$$

The new FC polarisation curve coefficient values and the mass flow coefficients are specified in Table 6-6.

Table 6-6 New FC model coefficients based on Toyota Mirai.

Coefficient	Value
a_x	0.0005
b_x	0.4284
c_x	60
d_x	0.75
f_x	0.0172

Offline optimisation of the new FC model shows optimum FC efficiency occurs at 88 A (4.87 kW). Using the new FC model and incorporating the new optimum FC current into EMS-1, the combined costs for the *VTS*TC drive cycle were reduced from $1.59 to $1.19. The dynamic rate limits on the FC model had to be substantially increased to simulate the new model with the load-following strategy of the Mirai. The results for this strategy show a slight reduction in cost to $1.17. With both the EMS-1 and the load-following strategies, fuel consumption is the same but the load-following strategy reduced the degradation of the battery and increased the FC degradation.

6.7 PFCV Cost Analysis

Short Urban drive cycles lead to reduced FC lifetimes and have high fixed costs from FC degradation. The cost per kilometre ($/km), as shown in Table 6-7, reduces with increased drive cycle distance.

Table 6-7 Simulation results in $ per km

Parameter	Units	Urban	NEDC	WLTP	*VTSTC*
Distance	km	3.47	10.66	14.66	36.79
Cost (baseline-EMS)	$/km	0.113	0.076	0.069	0.074
Cost (EMS-1)	$/km	0.097	0.059	0.052	0.043

While the large 3.2 kWh battery in the FCEV has sufficient capacity to complete short drive cycles in battery-only mode, there is no cost-advantage as the FC is the only battery recharging source. An alternative PFCV configuration is proposed which incorporates an on-board battery charger, similar to the 3-6 kW chargers found in battery electric vehicles. Research by [54] argues that a PFCV design would also reduce driver anxiety associated with a single fuel-source vehicle.

The offline analysis to calculate an equivalent cost to provide 1 kWh to the dc link from a battery which is charged from an external supply, must include the local electrical tariffs, charger efficiency and battery degradation costs during discharging and charging. Electricity tariffs are highly dependent on regional factors and range from $0.10 to $0.33 per kWh (USA average $0.21 /kWh and UK average $0.22 /kWh) [55]. An analysis of battery charging test data for the Nissan LEAF (2013 model), shows the average charging efficiency is 89% when recharging the battery at power levels from 3 kW to 6 kW [56]. The charging battery degradation costs calculated using (5.10, 5.12, 5.14, 5.21) are shown in Figure 6-9. Using the new battery degradation model, battery discharge degradation costs can be minimised by restricting the battery-only (charge-depletion) operation of the vehicle to SOC values in the range of 50% to 80%. Assuming an on-board charger power rating of 4 kW and the specified battery-only SOC range, the average battery charging degradation cost is approximately $0.0225/kWh.

This PFCV model configuration, with the initial SOC set to 80%, costs $0.075 /km for the Urban drive cycle, assuming the highest electrical utility tariff of $0.33/kWh. This is a cost reduction of 22% compared to the FCEV operated using

EMS-1 for the Urban drive cycle. At the end of the drive cycle, the battery ΔDOD is 20% or 60% SOC.

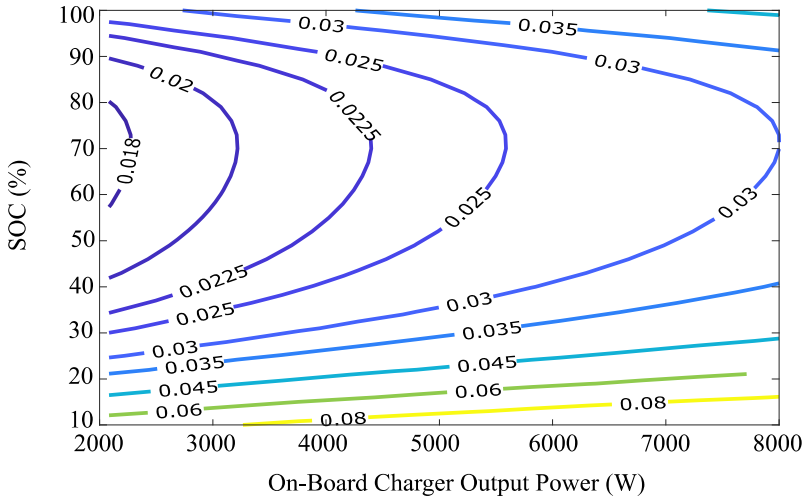

Figure 6-9. Battery charge degradation cost per kWh.

Over the longer NEDC drive cycle, the PFCV model cannot achieve battery-only operation within the 50-80% SOC range as the longer distance would result in a ΔDOD of 55%. Operating initially on battery-only until the ΔDOD is 30% and then switching to a charge-sustaining strategy, a cost reduction (compared to EMS-1 costs) is only achieved if the electrical tariff is less than $0.31/kWh. Further analysis and simulations of the PFCV model with the specified 3.2 kWh battery, show that COO costs are optimised if an on-board charger recharges the battery from an external supply for all journeys with distances up to 10 km. The PFCV strategy impacts the lifetime of both power sources. Battery lifetime in the PFCV is shorter than in the FCEV due to the increase in battery power needed to complete journeys. The calculated battery lifetime for Urban drive cycles is 2,182 hours, while NEDC type drive cycles achieve battery lifetimes of 2,665 hours. The advantage of the PFCV model is seen in increased FC lifetime for Urban drive cycles, from 394 h using EMS-1 in the FCEV to 1,200 hours in the PFCV.

6.8 Conclusions

This chapter reports on the development of an EMS for a fuel cell-battery HEV to meet the requirements of the 2017 VTS challenge. The developed EMS, (EMS-1), for low traction power, operates the FC at a maximum efficiency power level to provide the average traction power and any surplus FC power, is used to recharge the battery. For higher traction powers, EMS-1 implements a battery charge-sustaining strategy which allows the FC power output to increase linearly with traction power. The rule-based strategy is developed using offline optimisation in Matlab. EMS-1 achieves a drive cycle cost that is 2% lower than the winning challenge strategy while achieving prolonged lifetimes for both the FC and the battery.

The competition model is then modified to reflect the 2015 Toyota Mirai FCEV, and a new battery degradation model is proposed for the vehicle which allows a charge-sustaining strategy at the battery SOC level commonly used in HEV and FCEV designs.

Finally, the high cost for short drive cycles is addressed by proposing a PFCV design which reduces battery-only operation costs by recharging from a utility supply.

6.9 References

[1] K. Davis and J. G. Hayes, "Fuel cell vehicle energy management strategy based on the cost of ownership," *IET Electrical Systems in Transportation*, vol. 9, no. 4, pp. 226-236, 12 2019, doi: 10.1049/iet-est.2019.0021.

[2] C. Dépature, S. Jemeï, L. Boulon, A. Bouscayrol, N. Marx, and S. Morando, "IEEE VTS Motor Vehicles Challenge 2017 - energy management of a fuel cell/battery vehicle," *2016 IEEE Vehicle Power and Propulsion Conf. (VPPC)*, Hangzhou, 2016, pp. 1-6, doi: 10.1109/VPPC.2016.7791701.

[3] M. Ehsani, Y. Gao, S. Longo, and K. Ebrahimi, *Modern Electric, Hybrid Electric, and Fuel Cell Vehicles*, 3rd ed., Boca Raton, FL. USA: CRC Press, 2018, pp. 19-45.

[4] C. Mi, M. Abul Masrur, and D. Wenzhong Gao, *Hybrid Electric Vehicles Principles and Applications with Practical Perspectives*, 1st ed. Chichester, West Sussex, UK: Wiley, 2011.

[5] J. G. Hayes and G. A. Goodarzi, *Electric Powertrain:Energy Systems, Power Electronics and Drives for Hybrid, Electric and Fuel Cell Vehicles, 1*st ed., Chichester, West Sussex, UK: Wiley, 2018, pp. 40-48.

[6] S. Ahmadi, S. M. T. Bathaee, and A. H. Hosseinpour, "Improving fuel economy and performance of a fuel-cell hybrid electric vehicle (fuel-cell, battery, and ultra-capacitor) using optimized energy management strategy," *Energy Convers. Manag.*, vol. 160, pp. 74–84, 15 March 2018, doi: 10.1016/ j.enconman.2018.01.020

[7] G. Wang, Y.Yu, H. Liu, C. Gong, S. Wen, X. Wang, and Z. Tu, "Progress on design and development of polymer electrolyte membrane fuel cell systems for vehicle applications: A review," *Fuel Process. Technol.*, vol. 179, pp. 203–228, October 2018, doi: 10.1016/j.fuproc.2018.06.013.

[8] T. Yoshida and K. Kojima, "Toyota MIRAI fuel cell vehicle and progress toward a future hydrogen society," *Electrochemical Society Interface Mag.*, vol. 24, pp. 45–49, 2015, doi: 10.1149/2.F03152if.

[9] H. Lohse-Busch, M. Duoba, K. Stutenberg and S. lliev, "Technology assessment of a fuel cell vehicle : 2017 Toyota Mirai," Argonne National Laboratory (ANL), ANL/ESD-18/12, January 2018.

[10] Y. Hames, K. Kaya, E. Baltacioglu and A.Turksoy, "Analysis of the control strategies for fuel saving in the hydrogen fuel cell vehicles," *Int. J. Hydrogen Energy*, vol. 43, pp. 10810–10821, 7 June 2018, doi: 10.1016/ j.ijhydene.2017.12.150

[11] I. Alexa, S. D. Puscasu and A. Onea, "Dynamic programming for energy management of hybrid energy supply system of electric vehicles," *2018 IEEE Int. Conf. Automation, Quality and Testing, Robotics (AQTR)*, Cluj-Napoca, 2018, pp. 1-6, doi: 10.1109/AQTR.2018.8402752.

[12] K. Palmer, J. E. Tate, Z. Wadud and J. Nellthorp, "Total cost of ownership and market share for hybrid and electric vehicles in the UK , US and Japan," *Appl. Energy*, vol. 209, pp. 108–119, 1 January 2018, doi: 10.1016/ j.apenergy.2017.10.089.

[13] J. Hagman, S. Ritzen, J. J. Stier and Y. Susilo, "Total cost of ownership and its potential implications for battery electric vehicle diffusion," *Res. Transp. Bus. Manag.*, vol. 18, pp. 11–17, March 2016, doi: 10.1016/j.rtbm.2016.01.003

[14] E. A. Gilmore and L. B. Lave, "Comparing resale prices and total cost of ownership for gasoline, hybrid and diesel passenger cars and trucks," *Transp. Policy*, vol. 27, pp. 200–208, May 2013. doi: 10.1016/j.tranpol.2012.12.007

[15] S. Kara, W. Li, and N. Sadjiva, "Life cycle cost analysis of electrical vehicles in Australia," *Procedia CIRP*, vol. 61, pp. 767–772, 2017, doi: 10.1016/j.procir.2016.11.179

[16] N. Sulaiman, M. A. Hannan, A. Mohamed, P. J. Ker, E. M. Majilan and W. R. Wan Daud, "Optimization of energy management system for fuel-cell hybrid electric vehicles: Issues and recommendations," *Appl. Energy*, vol. 228, pp. 2061–2079, 15 October 2018, doi: 10.1016/j.apenergy.2018.07.087.

[17] J. J. Eckert, L. C. A. Silva, E. S. Costa, F. M. Santiciolli, F. G. Dedini and F. C. Correa, "Electric vehicle drivetrain optimisation," *IET Electr. Syst. Transp.*, vol. 7, no. 1, pp. 32–40, March 2017. doi: 10.1049/iet-est.2016.0022

[18] H. Li, A. Ravey, A. N.Diaye and A. Djerdir, "Equivalent consumption minimization strategy for hybrid electric vehicle powered by fuel cell, battery and supercapacitor," *IECON 2016 - 42nd Annual Conf. of the IEEE Industrial Electronics Society*, Florence, 2016, pp. 4401-4406, doi: 10.1109/ IECON.2016.7794047.

[19] S. Onori, L. Serrao, and G. Rizzoni, *Hybrid Electric Vehicles Energy Management Strategies*, 1st edn. SpringerBriefs in Control,Automation and Robotics, London, Uk: Springer-Verlag, 2016.

[20] S. H. Mahyiddin, M. R. Mohamed, Z. Mustaffa, A. C. Khor, M. H. Sulaiman, H. Ahmad and S. A. Rahman, "Fuzzy logic energy management system of series hybrid electric vehicle," *4th IET Clean Energy and Technology Conference (CEAT 2016)*, Kuala Lumpur, 2016, pp. 1-6, doi: 10.1049/cp.2016.1267.

[21] W. Lee, H. Jeoung, D. Park and N. Kim, "An adaptive energy management strategy for extended-range electric vehicles based on Pontryagin's Minimum Principle," *2018 IEEE Vehicle Power and Propulsion Conf. (VPPC)*, Chicago, IL, 2018, pp. 1-4, doi: 10.1109/VPPC.2018.8605042.

[22] Z. Chen, N. Guo, Q. Zhang, J. Shen and R. Xiao, "An optimized rule based energy management strategy for a fuel cell/battery vehicle," *2017 IEEE Vehicle Power and Propulsion Conf. (VPPC)*, Belfort, 2017, pp. 1-6, doi: 10.1109/VPPC.2017.8330991.

[23] J. M. Luján, C. Guardiola, B. Pla and A. Reig, "Analytical optimal solution to the energy management problem in series hybrid electric vehicles," *IEEE Transactions on Vehicular Technology*, vol. 67, no. 8, pp. 6803-6813, Aug. 2018, doi: 10.1109/TVT.2018.2821265.

[24] L. Serrao, S. Onori, A. Sciarretta, Y. Guezennec and G. Rizzoni, "Optimal energy management of hybrid electric vehicles including battery aging," *Proceedings of the 2011 American Control Conference*, San Francisco, CA, 2011, pp. 2125-2130, doi: 10.1109/ACC.2011.5991576.

[25] M. Carignano, V. Roda, R. Costa-Castelló, L. Valiño, A. Lozano and F. Barreras, "Assessment of energy management in a fuel cell/battery hybrid vehicle," *IEEE Access*, vol. 7, pp. 16110-16122, 2019, doi: 10.1109/ACCESS.2018.2889738.

[26] C. Depature, S. Jemei, L. Boulon , A. Bouscayrol , N. Marx , S. Morando and A. Castaings ,"Energy management in fuel-cell/battery vehicles: Key issues identified in the IEEE Vehicular Technology Society Motor Vehicle Challenge 2017," *IEEE Vehicular Technology Magazine*, vol. 13, no. 3, pp. 144-151, Sept. 2018, doi: 10.1109/MVT.2018.2837154.

[27] E. G. Amaya, H. Chiacchiarini, C. De Angelo and M. Asensio, "The energy management strategy of FC/battery vehicles winner of the 2017 IEEE VTS Motor Vehicles Challenge," *2017 IEEE Vehicle Power and Propulsion Conf. (VPPC)*, Belfort, 2017, pp. 1-6, doi: 10.1109/VPPC.2017.8330996.

[28] A. Serpi and M. Porru, "A real-time energy management system for operating cost minimization of fuel cell/battery electric vehicles," *2017 IEEE Vehicle Power and Propulsion Conference (VPPC)*, Belfort, 2017, pp. 1-5, doi: 10.1109/VPPC.2017.8330992.

[29] M. Yue, S. Jemei, R. Gouriveau and N. Zerhouni, "Developing a health-conscious energy management strategy based on prognostics for a battery/fuel cell hybrid electric vehicle," *2018 IEEE Vehicle Power and Propulsion Conf. (VPPC)*, Chicago, IL, 2018, pp. 1-6, doi: 10.1109/VPPC.2018.8604987.

[30] K. Kaya and Y. Hames, “Two new control strategies : For hydrogen fuel saving and extend the life cycle in the hydrogen fuel cell vehicles,” *Int. J. Hydrogen Energy*, vol. 44, no. 34, pp. 18967-18980, 12 July 2018, doi: 10.1016/j.ijhydene.2018.12.111

[31] J. Chen, C. Xu, C. Wu and W. Xu, "Adaptive fuzzy logic control of fuel-cell-battery hybrid systems for electric vehicles," *IEEE Transactions on Industrial Informatics*, vol. 14, no. 1, pp. 292-300, Jan. 2018, doi: 10.1109/TII.2016.2618886.

[32] P. Pei and H. Chen, “Main factors affecting the lifetime of Proton Exchange Membrane fuel cells in vehicle applications: A review,” *Appl. Energy*, vol. 125, pp. 60–75, 15 July 2014, doi: 10.1016/j.apenergy.2014.03.048.

[33] P. Pei, Q. Chang, and T. Tang, “A quick evaluating method for automotive fuel cell lifetime,” *Int. J. Hydrogen Energy*, vol. 33, no. 14, pp. 3829–3836, July 2008, doi: 10.1016/j.ijhydene.2008.04.048

[34] Y. Yu, H. Li, H. Wang, X. Yuan, G. Wang and M. Pan, “A review on performance degradation of proton exchange membrane fuel cells during startup and shutdown processes : Causes , consequences , and mitigation strategies,” *J. Power Sources*, vol. 205, pp. 10–23, 1 May 2012, doi: 10.1016/j.jpowsour.2012.01.059.

[35] G. Wang, F. Huang, Y. Yu, S. Wen and Z. Tu, “Degradation behavior of a proton exchange membrane fuel cell stack under dynamic cycles between idling and rated condition*,” Int. J. Hydrogen Energy,* vol. 3, no. 9, pp. 4471–4481, 1 March 2018, doi: 10.1016/j.ijhydene.2018.01.020.

[36] T. Zhang, P. Wang, H. Chen and P. Pei, “A review of automotive proton exchange membrane fuel cell degradation under start-stop operating condition,” *Appl. Energy*, vol. 223, pp. 249–262, 1 August 2018, doi: 10.1016/ j.apenergy.2018.04.049.

[37] X. Jin, A. P. Vora, V. Hoshing, T. Saha, G. M. Shaver, O. Wasynczuk and S. Varigonda, "Comparison of Li-ion battery degradation models for system design and control algorithm development," *2017 American Control Conference (ACC)*, Seattle, WA, 2017, pp. 74-79, doi: 10.23919/ACC.2017.7962933.

[38] J. Jaguemont, L. Boulon, P. Venet, Y. Dubé and A. Sari, "Lithium-ion battery aging experiments at subzero temperatures and model development for capacity fade estimation," *IEEE Transactions on Vehicular Technology*, vol. 65, no. 6, pp. 4328-4343, June 2016, doi: 10.1109/TVT.2015.2473841.

[39] J. Wang, J. Purewal, P. Liu, J. Hicks-Garner, S. Soukazian, E. Sherman, A. Sorenson, L. Vu, H. Tataria and M. W. Verbrugge, “Degradation of lithium ion batteries employing graphite negatives and nickel - cobalt - manganese oxide + spinel manganese oxide positives : Part 1 , aging mechanisms and life estimation,” *J. Power Sources*, vol. 269, pp. 937–948, December 2014, doi: 10.1016/j.jpowsour.2014.07.030.

[40] A. Brooker, J. Gonder, L. Wang, E. Wood, S. Lopp, and L. Ramroth, “FASTSim : A model to estimate vehicle efficiency , cost and performance,” *SAE World Congress and Exhibition*, Detroit, MI., USA, 2015, pp.1-12, doi:10.4271/2015-01-0973

[41] L. Serrao, S. Onori, and G. Rizzoni, “A novel model-based algorithm for battery prognosis,” *IFAC Proc.* , vol. 42, no. 8, pp. 923–928, 2009. doi: 10.3182/ 20090630-4-ES-2003.00152

[42] J. Wang, P. Liu, J. Hicks-Garner, E. Sherman, S. Soukiazian, M. Verbrugge, H. Tataria, J. Musser and P. Finamore, “Cycle-life model for graphite-LiFePO 4 cells,” *J. Power Sources*, vol. 196, no. 8, pp. 3942–3948, 15 April 2011, doi: 10.1016/j.jpowsour.2010.11.134.

[43] L. Serrao, Z. Chehab, Y. Guezennee and G. Rizzoni, "An aging model of Ni-MH batteries for hybrid electric vehicles," *2005 IEEE Vehicle Power and Propulsion Conf.(VPPC)*, Chicago, IL, 2005, pp. 8 pp.-, doi: 10.1109/VPPC.2005.1554536.

[44] V. Marano, S. Onori, Y. Guezennec, G. Rizzoni and N. Madella, "Lithium-ion batteries life estimation for plug-in hybrid electric vehicles," *2009 IEEE Vehicle Power and Propulsion Conf.(VPPC)*, Dearborn, MI, 2009, pp. 536-543, doi: 10.1109/VPPC.2009.5289803.

[45] E. Wikner, “Lithium ion battery aging : Battery lifetime testing and physics-based modeling for electric vehicle applications,” PhD. dissertation, Dept. of Elec. Eng., Chalmers University of Technology, Gothenburg, Sweden, 2017.

[46] M. Chen and G. A. Rincon-Mora, "Accurate electrical battery model capable of predicting runtime and I-V performance," *IEEE Transactions on Energy Conversion*, vol. 21, no. 2, pp. 504-511, June 2006, doi: 10.1109/TEC.2006.874229.

[47] Autoevolution, “Tazzari Zero 2009 Specification.” [Online]. Available: https://www.autoevolution.com/news/tazzari-zero-ev-video-photos-specs-5163.html. [Accessed: 10-July-2020].

[48] K. Davis and J. G. Hayes, "Energy management strategy development to minimize the operating costs for a fuel cell vehicle," *2017 IEEE Vehicle Power and Propulsion Conf. (VPPC)*, Belfort, 2017, pp. 1-6, doi: 10.1109/ VPPC.2017.8330990.

[49] M. Matsunaga, T. Fukushima, and K. Ojima, “Powertrain System of Honda FCX Clarity Fuel Cell Vehicle,” *World Electr. Veh. J.*, vol. 3, no. 4, pp. 820–829, 2009, doi: 10.3390/wevj3040820

[50] Toyota, “Toyota Mirai Specification.” [Online]. Available: https://www.toyota.com/mirai/assets/core/Docs/Mirai%20Specs.pdf. [Accessed: 10-Jul-2020].

[51] B. K. Hong and S. H. Kim, “Recent advances in fuel cell electric vehicle technologies of Hyundai,” *ECS Trans*., vol. 86, no. 13, pp. 3–11, 2018. doi: 10.1149/08613.0003ecst

[52] Y. Nonobe, "Development of the fuel cell vehicle Mirai," *IEEJ Trans. Electr. Electron. Eng.*, vol. 12, no. 1, pp. 5–9, January 2017, doi: 10.1002/tee.22328.

[53] T. Suzuki, "Fuel cell stack technology of Toyota," *ECS Trans.*, vol. 75, no. 14, pp. 423–434, 2016, doi: 10.1149/07514.0423ecst

[54] R. A. Fernandez, F. B. Cilleruelo, and I. V. Martinez, "A new approach to battery powered electric vehicles : A hydrogen fuel-cell-based range extender system," *Int. J. Hydrogen Energy*, vol. 41, pp. 4808–4819, 2 March 2016, doi: 10.1016/j.ijhydene.2016.01.035

[55] Statista, "Electricity prices around the world ", [Online] Available: www.statista.com/statistics/263492/electricity-prices-in-selected-countries/. [Accessed: 10-Jul-2020].

[56] Argonne National Laboratory, Energy Systems Division, "Downloadable Dynamometer Database." [Online]. Available: https://www.anl.gov/es/ downloadable-dynamometer-database. [Accessed: 10-Jul-2020].

7 CONCLUSIONS

This thesis has developed and validated a simplified electric vehicle powertrain (SEVP) simulator for battery electric vehicles (BEVs). When benchmarked against two widely-cited vehicle simulators, ADVISOR and FASTSim, the SEVP may be considered a comparable simulator for estimating instantaneous energy consumption in ten different vehicles. The development of more detailed electrical powertrain models, for both the Lithium-ion battery packs and for the traction IPM motor, extends the SEVP model application area to BEV electrical circuit powertrain simulation. With these complex component models included, the SEVP model is a valuable resource for teaching and research purposes. Future developments in the heavy-duty transportation sector are likely to require fuel cell electrical vehicle simulators and this requirement was recognised in this study by the development of an energy management strategy to minimise operating costs for fuel cell powered vehicles. The SEVP model offers reasonable accuracy and low computational load for a wide variety of mobility studies.

7.1 Thesis Summary

This section reprises the research topics presented in each chapter of the thesis. In Chapter 1, a basic introduction and an overview of the research topics of interest was presented, along with the thesis structure and objectives.

Chapter 2 presented a detailed description of the procedure, used in 2014 to develop the SEVP model for energy consumption estimations. This SEVP simulator, applied to the 2012 Nissan Leaf, was validated as an energy consumption model against the experimental test data published by the Argonne National Laboratory (ANL). Excellent correlation was demonstrated between the model predictions and the experimental data for range estimation and for energy consumption projections over a complete drive cycle. A deficiency in the SEVP model, related to energy consumption prediction for conditions that require HVAC power to control the passenger cabin temperature, was partly addressed in Chapter 2 by incorporating a simple third-order polynomial that related average HVAC power to outside ambient temperatures. Deficiencies in the motor model of the SEVP, such as the lack of consideration of flux weakening at high motor speeds and of magnetic saturation at high motor torques, were addressed. These deficiencies were addressed with relatively simple changes to the traction motor model and resulted in improved matching of the model's efficiency maps to the ORNL measured efficiency maps for these motors.

In Chapter 3, three BEV powertrain simulators were analysed by combining their design methodologies into a single M-Sim MATLAB file. The educational advantage of this plug-and play simulator model is the in-depth understanding of the factors governing the energy consumption in BEV designs. The simplified parametric equations of the SEVP motor-inverter models resulted in energy consumption estimates that are comparable to both of the industry-standard simulators. The M-Sim testing conducted in this study identified three issues that applied to all three simulators. First, the high impact of relatively low changes in auxiliary power during city driving conditions. This increases the difficulty in achieving high accuracy in energy consumption estimation, particularly when published data on this parameter for each vehicle is lacking. Second, the regenerative models, based on a speed function, have very little impact on the net energy consumption. In older BEV models, they should be replaced with a model based on acceleration rate. Third, the M-Sim testing identified that the simple power-polynomial approach to modelling the motor-inverter

losses in the BEV powertrain, as implemented in the FASTSim simulator, oversimplifies the efficiency calculation of a typical BEV motor and estimates excessive losses in city driving conditions.

Chapter 4 reviewed four existing battery models. This review showed that only two models, the LLE models and the higher-order polynomial models, accurately represent the voltage-capacity profiles of the Idaho National Laboratory (INL) tested BEV Li-ion battery packs. A summary of LLE model coefficients and higher-order polynomial battery model coefficients for eight commercially available BEVs are provided in this chapter. For concept vehicles, where battery test data may not available, the developed generic Li-ion battery model provided realistic battery output voltages for BEV simulators. The impact of battery capacity fade, associated with battery ageing, was considered for a lifetime model of the vehicle. A battery model based on a normalised capacity to voltage relationship was shown to mitigate the negative impact of capacity fade in battery voltage estimation. A further advantage of this battery modelling approach was to provide a virtual fuel gauge for vehicle simulators. The choice of internal-impedance circuit was shown to determine the dynamic response of the battery model. A comparison of battery models to dynamometer data from ANL showed that a Thevenin circuit model to represent the internal impedance, was vital for hybrid-electric vehicle (HEV) simulation. The time-dependent voltage drop across the Thevenin circuit avoided simulation errors due to the narrow operating voltage range in a HEV and this was shown in Figure 4-14. For BEV simulation, the simpler R_{INT} internal-impedance provided good accuracy when the drive cycle did not involve highly dynamic events that typically require near-full output battery power. Except for high precision battery voltage modelling, the wide operating voltage range of the BEV battery pack minimises the need for a more complex Thevenin circuit. For BEV range estimation over a vehicle's lifetime, an empirical battery ageing model, with coefficients derived from the BEV battery warranty conditions was proposed. This ageing model provided capacity-fade trends compatible with the observed trends in the INL tests. Applying this ageing model with normalizing the battery capacity, results in a voltage-capacity profile model that is, tentatively, valid over the lifetime of the vehicle. Further research on battery ageing is recommended as more data of BEV battery packs becomes available.

In Chapter 5, the proposed IPM motor models were developed to aid understanding of the electrical drive requirements for the operation of an IPM motor

over its full torque-speed range for a BEV traction motor. The resultant FEA models of these motors enabled the characterisation of the motor parameters. These parameters were then utilised to develop the combined electrical and power loss IPM motor models. The locked-rotor testing of the FEA model established the phase current and optimum phase advance angle for each torque output during MTPA operation. The IPM model implemented a simple iterative process to estimate the phase current and phase advance angle during MTPV operation. It achieved a smooth transfer from MTPA to MTPV operation and also limited torque output based on the rated power of the motor. An indirect positive outcome of this IPM machines operating-characteristics study is a set of educational FEA models for traction motors of EVs. These simple machine models provide a further valuable resource to develop engineering skills. While the FEA software used does not provide the precision needed for IPM motor design for commercial applications, its reduced design parameter requirements and minimal instruction set, make it an ideal tool for initial machine design or engineering educational applications. When students are tasked with a new motor development exercise, the dataset of typical commercial IPM parameters gathered in this study, provides the student with a realistic starting point in terms of the possible physical size to power output ratio. The dataset also provides a starting library of realistic material properties to simulate their initial designs. The models can then be used to explore the effects of *d*-axis and *q*-axis inductances, the back-emf speed constant, the impact of rotor temperature on torque output, motor cogging-torques, magnetic saturation in motor designs and the impact of skewing the rotor magnets on torque output.

In Chapter 6, the development of an EMS for a fuel cell-battery HEV to meet the requirements of the 2017 VTS challenge is presented. The developed rule-based EMS, (EMS-1), for low traction power, operated the FC at a maximum efficiency power level to provide the average traction power and any surplus FC power, was used to recharge the battery. For higher traction powers, EMS-1 implemented a battery charge-sustaining strategy which allowed the FC power output to increase linearly with traction power. EMS-1 achieved a drive cycle cost that is 2% lower than the winning challenge strategy while achieving prolonged lifetimes for both the FC and the battery. The competition model was then modified to emulate the 2015 Toyota Mirai FCEV, and a new battery degradation model was proposed for the vehicle which allowed the use of a charge-sustaining strategy at the battery SOC level, commonly

used in HEV and FCEV designs. Finally, the high cost for short drive cycles was addressed by proposing a PFCV design which reduced battery-only operation costs by recharging from a utility supply instead of recharging from the fuel cell.

7.1.1 Scalability of Developed Models

The SEVP models have been validated as energy consumption estimators for ten mid-sized BEVs in a number of legislative drive cycles. Expanding the scope of the SEVP simulator depends on the availability of vehicle coastdown parameters used to determinate the traction power. The EPA published coastdown parameters cover a limited range of vehicles, from small city vehicles to larger sport utility vehicles. Applying the SEVP to vehicles outside of this range, will require either translating the standard equations to equivalent coastdown coefficients or using the standard equations directly with the motor and inverter models of the SEVP. During the validation of the mid-sized vehicles in the M-Sim, the SEVP simulator tended to underestimate the energy consumption when standard equations were used for the traction power calculations. Further research is required to establish the appropriate relationship of C_{rr} with speed and the appropriate frontal-area profile factors to use for a given style of vehicle. A research study that equates the standard equations to the coastdown coefficients could allow the scalability of the SEVP models to estimate the energy consumptions of heavy-duty vehicles such as buses and trucks.

The Li-ion battery models developed were based on a range of capacities of approximately 16 kWh to 28 kWh and all these battery packs had an operating voltage range of approximately 250 V to 400 V. As the BEV market develops, faster charging of the vehicles is enabled by higher-power chargers, operating at higher voltages (800V). In addition, future battery technologies such as solid-electrolyte Li-ion batteries, as well as increased battery capacities seen in newer BEV designs, will have an impact on the battery models. Added to these changes are the improvements in battery ageing. All these changes will require re-validation of the proposed Li-ion battery pack models.

Future IPM motors models will need to consider newer motor manufacturing technologies such as hairpin windings and the voltage drops due to both PWM harmonics and airgap flux harmonics.

7.2 Thesis Contributions

This thesis has addressed gaps in the knowledge base for the understanding of the new technologies in the low carbon automotive transport sector.

Key contributions of this study include:

- A Simplified Electric Vehicle Powertrain Simulator including validation and benchmarked to other vehicle simulators. Instantaneous and cumulative energy consumption estimation from a low computational load simulator (operating in either Excel or MATLAB).
- Improved empirical battery models for electric vehicles that incorporate an ageing model. Including a simple generic Li-ion battery pack model.
- Development of finite element models for IPM modelling. The models allow complex motor designs to be demonstrated to undergraduate students.
- A proposed energy management strategy to optimise operating costs for fuel cell electric vehicles
- Identification of data sources useful for undergraduates and other researchers for future work in this area.

7.3 Future Work

Novel topics in powertrain modelling for the simulation EVs were explored in this thesis. As in any time limited project, the full potential of the models developed could not be scrutinised. This can be addressed in future work.

7.3.1 Planned Future Work

The SEVP research in Chapters 2 and 3 has been published at two peer reviewed IEEE conferences. A journal submission is planned that reports the combined structure of the basic SEVP for BEV energy consumption estimation in Chapter 2 with the comparison to two the industry-standard simulators in Chapter 3. The simple average HVAC power model will be included in this journal submission.

A second journal submission is planned that details electrical circuit simulation of a BEV powertrain and combines the new battery models of Chapter 4 with the proposed IPM models of Chapter 5.

7.3.2 Suggestions for Further Research

In Chapter 2, a preliminary review of the auxiliary loads, associated with the thermal requirements of maintaining a constant cabin temperature, identified a thermal time constant for the initial heating and cooling of the vehicle's cabin. Analysis highlighted the non-linear power output of the HVAC units. The heating and cooling requirements would appear to impact the achievable range of BEVs during short urban trips in sub-zero climates more severely. Further research is required to develop a simplified thermal model for the vehicle's cabin that can be incorporated into vehicle simulators.

The battery model proposed in Chapter 4 incorporated a simple ageing model based on temperature and energy throughput. Research related to the impact of fast charging on a battery shows increased ageing impact. Future research could incorporate this effect into improved battery models [1].

FEA models of IPM motors for HEVs and BEVs were developed in Chapter 5 based on the ORNL benchmark reports. Further research is required on these models to improve the energy loss models under high-speed MTPV conditions. Future studies

should consider the impact of skewed rotor designs on torque ripple [2]. In addition, the lack of induction motor models must be addressed as they are used in a number of BEVs [3]. The IPM model showed a good correlation to the 2004 Prius testing data showed a good correlation but there is room for improvement. Further validation of the IPM motor model is required using new data sets.

This study focused solely on the powertrain component models. These models assumed an average efficiency for the on-board battery charger when calculating the environmental impact or estimating the operating costs of these vehicles. As manufacturers advance the technology for self-driving vehicles, wireless battery charging is likely to be required. Research into the impact of all types of battery chargers is required. This research will enable better loss analysis for both grid-to-vehicle applications and for vehicle-to-grid applications [4].

7.4 References

[1] H. A. Serhan and E. M. Ahmed, "Effect of the different charging techniques on battery life-time: Review," *2018 International Conference on Innovative Trends in Computer Engineering (ITCE)*, Aswan, 2018, pp. 421-426, doi: 10.1109/ ITCE.2018.8316661.

[2] B. Bilgin, J. Liang , M. V. Terzic, J. Dong , R. Rodriguez, E. Trickett, and A. Emadi., "Modeling and Analysis of Electric Motors: State-of-the-Art Review," in *IEEE Transactions on Transportation Electrification*, vol. 5, no. 3, pp. 602-617, Sept. 2019, doi: 10.1109/TTE.2019.2931123.

[3] G. Sieklucki, "An Investigation into the Induction Motor of Tesla Model S Vehicle," *2018 International Symposium on Electrical Machines (SME)*, Andrychów, 2018, pp. 1-6, doi: 10.1109/ISEM.2018.8442648.

[4] M. Kesler, "Wireless Charging of Electric Vehicles," *2018 IEEE Wireless Power Transfer Conference (WPTC)*, Montreal, QC, Canada, 2018, pp. 1-4, doi: 10.1109/WPT.2018.8639303.

APPENDIX A

In this appendix, **A.1**, shows the procedure used to calculate CO_2 emissions in vehicles; **A.2** provides details of the ten vehicles used in this study; **A.3**, is a set of six figures that shows the torque-speed operating points for a Leaf BEV when completing a given drive cycle. The purpose of these figures is to show that the choice of drive cycle for simulator validation can influence the results. **A.4**, is included to provide a brief introduction to the *dq* reference frame for any reader that is not familiar with this analysis method.

A.1 Example CO_2 Calculation

This example calculates the CO_2 emissions from a petrol and from a diesel version of a passenger vehicle based on the measured fuel consumption for these vehicles.

Vehicle fuel consumption: 5.4 litres per 100 km (petrol), 3.9 litres per 100 km (diesel)

Fuel specifications:	Petrol C_8H_{12},	density
	Diesel $C_{12}H_{26}$,	density
Relative Atomic Masses:	Hydrogen	1 amu
	Carbon	12 amu
	Oxygen	16 amu

Combustion equation

$$C_xH_y + \left(x + \frac{y}{4}\right) O_2 = xCO_2 + \left(\frac{y}{2}\right) H_2O \quad \text{(A.1)}$$

Calculation procedure:

Step 1. calculate the mass of the fuel

Step 2. calculate the mass of the CO_2 emissions.

Step 3. Determine the CO_2 to fuel mass ratio

Step 4. Multiply this ratio by fuel consumption (grams fuel /km)

A.2 Specification of BEVs

Table A-1 Vehicle specifications

Vehicle Parameters	Units	BMWi3	FOCUS EV	LEAF 12	LEAF	MiEV	SMART	SOUL	SPARK	eGOLF	B-class
Max Motor Power	W	125000	106600	80000	80000	4900	55000	8100	85000	86000	132000
Max Motor Torque	Nm	250	250	280	280	178	130	285	443	270	340
Wheel Radius	m	0.3498	0.3284	0.316	0.316	0.285	0.2835	0.326	0.2922	0.316	0.317
Gear ratio		9.7	7.82	7.94	*8.19*	7.07	9.922	8.21	3.87	3.61	9.73
Rated Battery capacity	Wh	18800	23000	24000	24000	1600	17600	2700	19000	24000	28000
Mass of vehicle ANL	kg	1443	1790	1699	1498	1304	1050	1664	1432	1698	1926
***EPA** Mass of vehicle*		***1531***	***1754***	***1754***	***1644***	***1304***	***1077***	***1644***	***1474***	***1701***	***1928***
Coastdown Coeffi 'A'	*N*	105	162	183	142	95	108	113	104	185	142
***EPA** Coastdown 'A'*		***150***	***103***	***150***	***134***	***87***	***146***	***101***	***101***	***175***	***158***
Coastdown Coeff 'B'	*N/m/s*	6.6	5.168	-3.067	1.11	5.931	4.972	4.267	3.926	6.391	1.11
***EPA** Coastdown 'B'*		***3.443***	***3.629***	***0.615***	***0.709***	***4.33***	***-1.631***	***3.265***	***1.819***	***5.058***	***1.801***
Coastdown Coeff 'C'	*N/m^2/s^2*	0.26	0.337	0.562	0.395	0.286	0.344	0.368	0.277	0.221	0.395
***EPA** Coastdown 'C'*		***0.337***	***0.422***	***0.508***	***0.491***	***0.359***	***0.636***	***0.486***	***0.402***	***0.278***	***0.423***
Min Battery Voltage	V	335	270	250	250	310	300	295	288	305	246
Frontal Area	m^2	2.240	2.217	2.194	2.194	2.048	1.924	2.305	2.077	2.086	2.504
Drag coefficient (Cd)		0.29	0.295	0.29	0.28	0.3	0.34	0.35	0.33	0.27	0.28
Max vehicle speed	kmph	150	135	150	150	125	125	150	145	150	159
Max motor speed (rpm)	rpm	11000	8500	10000	10300	8250	11500	1000	5000	4535	13000
ANL test Auxiliary	W	190	380	224	400	85	238	155	435	175	280

A.3 Torque and Speed Operation Points in Drive Cycles

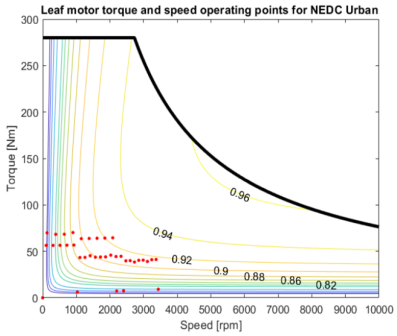

(a) Urban section of NEDC drive cycle

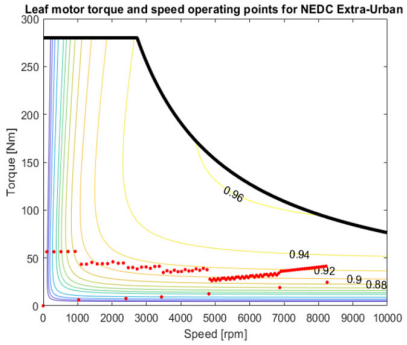

(b) Extra-urban section of NEDC drive cycle

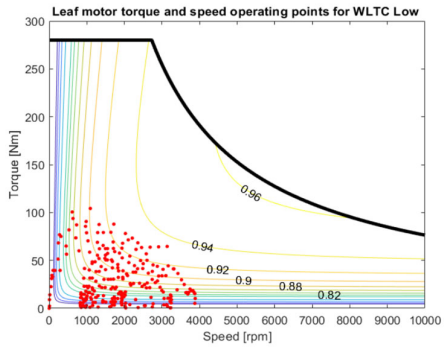

(c) Low section of WLTC drive cycle

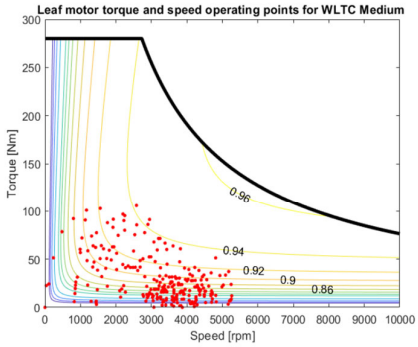

(d) Medium section of WLTC drive cycle

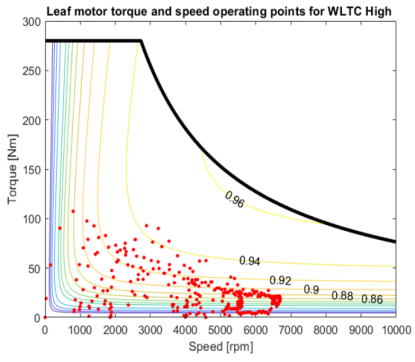

(e) High section of WLTC drive cycle

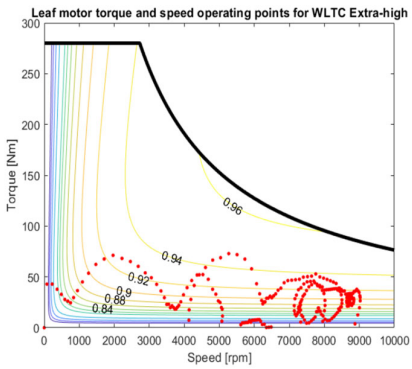

(f) Extra-high section of WLTC drive cycle

Figure A-1 Torque and speed operating points of the motor with different drive cycles.

A.4 Fundamentals of *dq* Reference Frame Analysis

The fundamentals of the *dq* reference frame are illustrated in Figure A-2. The *d*-axis is defined as the axis aligned to the magnetic field of the PM as shown in Figure A-2(a), while the *q*-axis is set at 90° (electrical) to the *d*-axis reference. The magnitude and direction of a phase current winding magnetic field depends on the amplitude and direction of the current in the stator windings as illustrated in Figure A-2(b) and (c) for a simple single winding motor. With the PM on the rotor and oriented as shown in Figure A-2(d), the winding magnetic field is aligned (0° electrical) with the PM field and it will strengthen the PM field. If the winding current is reversed, the winding magnetic field opposes the PM magnetic field (180° electrical, as shown in Figure A-2(e)) and the winding field has effectively weakened the PM excitation magnetic field. No electromagnetic torque is generated when the magnetic fields are aligned (Figure A-2 (d) and (e)).

In Figure A-2(f), both magnetic fields are orthogonal (at 90° to each other) and maximum electromagnetic torque is generated in this position. Superimposing the *dq* reference frame onto the magnetic axes of Figure A-2(f), the PM magnetic axis is aligned with the *d*-axis and the winding magnetic axis is aligned with the *q*-axis. With this alignment, the amplitude of the current in the stator winding is termed the i_q current and all of this phase current generates torque. The magnetic strength of the PM field can be represented by an equivalent *d*-axis current, i_d. With the PM at this 90° position, the phase current is not strengthening or weakening the PM magnetic field and the i_d component of the phase current is said to be zero. Advancing the rotor to the position shown in Figure A-2(h), the magnetic axes are no longer orthogonal or aligned and the stator winding current vector has both an i_d component and an i_q component as illustrated in Figure A-2(i).

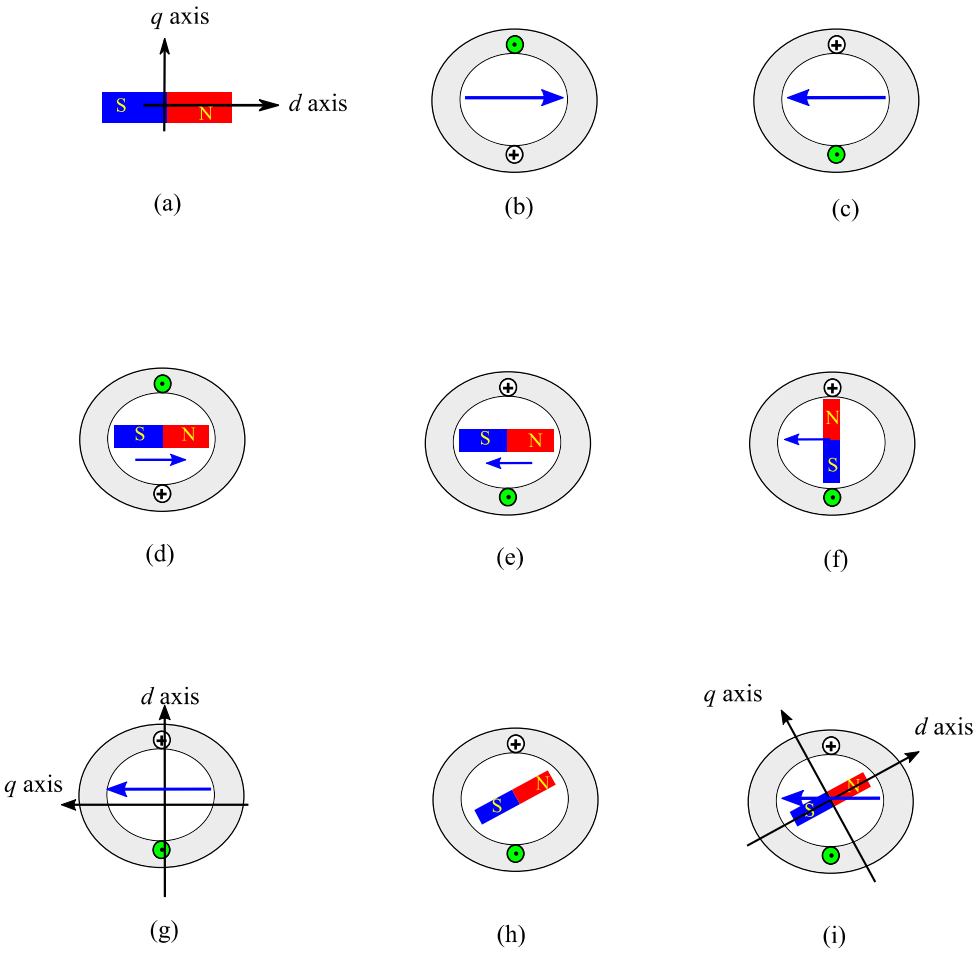

Figure A-2. *dq* reference frame and flux weakening.

An expanded version of Figure A-2(i) is presented in Figure A-3 to clarify the relative angles in the phase advance process. The i_q component of the phase current generates electromagnetic torque. As the winding magnetic field *d*-axis component opposes the PM flux, this is equivalent to a negative value of i_d causing flux weakening in the motor. The angle between the axis of the winding magnetic field and the q-axis is known as the current angle, γ. The electrical angle, θ , is the angle between the axis of the winding magnetic field and the *d*-axis. As the current angle or the electrical angle increases, the flux-weakening portion of the phase current (i_d) increases and the torque producing current (i_q) reduces.

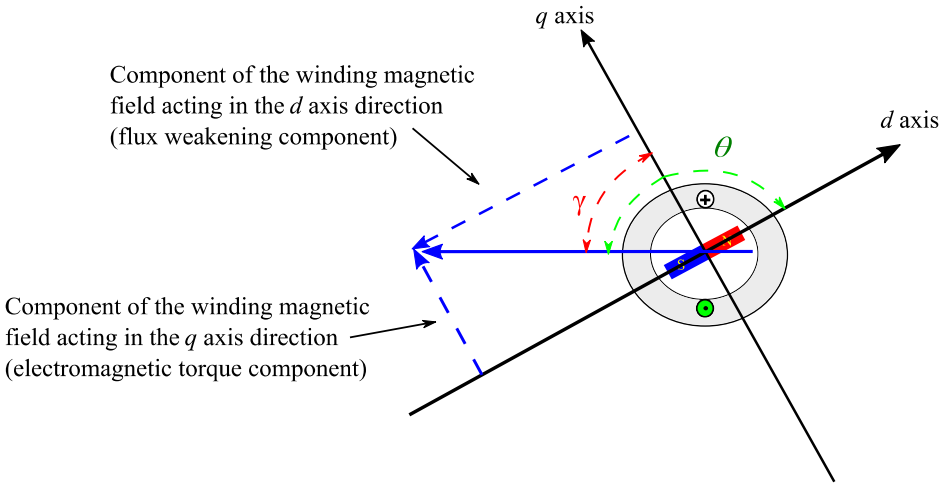

Figure A-3. Subdividing winding magnetic field into i_d and i_q components.

The amplitude of these two current components can be related back to an equivalent dc winding current I_{dc} and to the amplitude of the input rms phase current I_{ph} as shown by

$$I_{dc} = \sqrt{i_d^2 + i_q^2} = \sqrt{2} I_{ph} \tag{A.2}$$

The torque output, at each electrical angle (θ), is established with a locked rotor test of a motor. This testing is typically performed with a range of dc currents applied to one of the phases and this current can be transformed to the dq reference frame by

$$i_d = I_{dc}\, cos(\theta) \tag{A.3}$$

$$i_q = I_{dc}\, sin(\theta) \tag{A.4}$$

During normal motor operation, a three-phase ac supply voltage is applied to the three windings in the motor. The winding magnetic field axis is determined by the combination of the current amplitudes and directions in the three phase windings. If the relative position of the PM axis is known (θ known), a current transformation applied to the rms phase currents , I_{ph_A}, I_{ph_B}, I_{ph_C} establishes the equivalent i_d and i_q currents as shown by

$$i_d = \frac{2}{3}\left[\sqrt{2} I_{ph\_A}\, cos(\theta) + \sqrt{2} I_{ph\_B}\, cos\left(\theta - \frac{2\pi}{3}\right) + \sqrt{2} I_{ph\_C}\, cos\left(\theta + \frac{2\pi}{3}\right)\right] \tag{A.5}$$

$$i_q = \frac{2}{3}\left[-\sqrt{2} I_{ph\_A}\, sin(\theta) - \sqrt{2} I_{ph\_B}\, sin\left(\theta - \frac{2\pi}{3}\right) - \sqrt{2} I_{ph\_C}\, sin\left(\theta + \frac{2\pi}{3}\right)\right] \tag{A.6}$$

APPENDIX B

This appendix includes; **B.1**, a sample of an Excel file for a vehicle. This file is imported into the M-Sim MATLAB script to compare the three simulators. **B.2** a table of software authentication results for four vehicles that show the original simulators are accurately replicated by the M-Sim simulator. **B.3**, is one version of the M-Sim MATLAB scripts with numerous comments to aid understanding of the code structure as an educational resource.

B.1 Sample Vehicle Specification File for M-Sim

BMWi3	***Values transferred to Matlab***	*units*	
Mass of vehicle	1443	*kg*	
Max Motor Power output	125000	*W*	
Max Motor Torque output	250	*Nm*	
Wheel Radius	0.3498	*m*	
Gear ratio	9.7		
Rated Battery capacity	18800	*Wh*	
Coastdown Coefficient 'A'	105	*N*	
Coastdown Coefficient 'B'	6.6	*N/m/s*	
Coastdown Coefficient 'C'	0.26	*N/m^2/s^2*	
Min Battery Voltage	335	V	
Assumed Aux Power	200	W	
Assumed Battery Resistance	0.1	Ω	
Frontal Area	2.240	m	
Drag coefficient (Cd)	0.29		
Rolling Road Coefficient (Crr)	0.008		FASTSIm default value
Inertia (J)	3.26	assumed	FASTSIm default value
Battery efficiency	95.1%	assumed	FASTSIm default value
Gearbox efficiency	97.0%	assumed	FASTSIm default value
Peak Motor+Controller eff	89.0%		FASTSim poly calculation parameter
Motor efficiency	96.0%	assumed	only used for SEVP
Inverter efficiency	98.0%	assumed	only used for SEVP
Rated Battery capacity	85.0%	assumed	only used for SEVP
Motor power factor	0.9	assumed	only used for SEVP
x4	-7.47437E-08	(89% peak)	Motoring Poly Coeff FASTSim
x3	2.34357E-05	(89% peak)	Motoring Poly Coeff FASTSim
x2	-0.001816216	(89% peak)	Motoring Poly Coeff FASTSim
x	1.154016703	(89% peak)	Motoring Poly Coeff FASTSim
const	1.471512451	(89% peak)	Motoring Poly Coeff FASTSim
x4	8.32427E-08	(89% peak)	Braking Poly Coeff FASTSim
x3	-2.74121E-05	(89% peak)	Braking Poly Coeff FASTSim
x2	0.002562664	(89% peak)	Braking Poly Coeff FASTSim
x	0.822165235	(89% peak)	Braking Poly Coeff FASTSim
const	-1.096407029	(89% peak)	Braking Poly Coeff FASTSim
Top speed [mph]	93	mph	
Actual aux power	190	W	

B.2 Replicated Simulators in M-Sim Comparison Results.

Units [Wh]	LEAF12								
	UDDS			HWY			US06		
	Regen	*Motor*	*Net*	*Regen*	*Motor*	*Net*	*Regen*	*Motor*	*Net*
SEVP	538	2033	1495	169	2523	2354	620	3149	2529
M-Sim SEVP	539	2033	1494	169	2523	2354	621	3149	2528
FASTSim	526	1985	1459	179	2257	2078	665	2857	2192
M-Sim FASTSim	526	1985	1459	180	2257	2077	669	2855	2186
ADVISOR	553	1897	1344	182	2273	2091	653	2885	2232
M-Sim ADVISOR	553	1897	1344	182	2273	2091	654	2888	2234

Units [Wh]	LEAF13								
	UDDS			HWY			US06		
	Regen	*Motor*	*Net*	*Regen*	*Motor*	*Net*	*Regen*	*Motor*	*Net*
SEVP	463	1855	1392	143	2332	2189	538	2824	2286
M-Sim SEVP	465	1855	1390	143	2332	2189	539	2825	2286
FASTSim	452	1808	1356	152	2101	1949	574	2627	2053
M-Sim FASTSim	452	1808	1356	152	2101	1949	575	2628	2053
ADVISOR	481	1717	1236	154	2119	1965	565	2659	2094
M-Sim ADVISOR	480	1717	1237	154	2120	1966	565	2660	2095

Units [Wh]	MiEV								
	UDDS			HWY			US06		
	Regen	*Motor*	*Net*	*Regen*	*Motor*	*Net*	*Regen*	*Motor*	*Net*
SEVP	405	1665	1260	119	2204	2085	457	2621	2164
M-Sim SEVP	406	1665	1259	119	2204	2085	457	2621	2164
FASTSim	408	1571	1163	132	1909	1777	491	2399	**1908**
M-Sim FASTSim	408	1571	1163	132	1910	1778	497	2378	**1881**
ADVISOR	412	1561	1149	128	2002	1874	473	2469	1996
M-Sim ADVISOR	411	1561	1150	128	2002	1874	479	2472	1993

Units [Wh]	FOCUS EV								
	UDDS			HWY			US06		
	Regen	*Motor*	*Net*	*Regen*	*Motor*	*Net*	*Regen*	*Motor*	*Net*
SEVP	579	2051	1472	186	2505	2319	661	3196	2535
M-Sim SEVP	581	2052	1471	187	2505	2318	662	3196	2534
FASTSim	536	2140	1604	184	2407	2223	695	3015	2320
M-Sim FASTSim	536	2141	1605	184	2407	2223	695	3015	2320
ADVISOR	581	1974	1393	194	2318	2124	692	2979	2287
M-Sim ADVISOR	583	1978	1395	195	2319	2124	690	2976	2286

The power-limited motor of the MiEV results in performance limitations during high acceleration conditions in the US06 drive cycle. As the M-Sim powertrain models were designed without power limits, this vehicle was excluded from the comparison study.

B.3 M-Sim MATLAB Script

```
%Test Conditions. SEVP model using average time step speeds and  %actual recorded test speeds at Argonne used for tractive effort calculations %% written by Kevin Davis (July 2015)% Modified (December 2015 to add in four more vehicles)

%Initialisation section----------

clear variables; close all; clc;

% Excel Files Required - specify Auto type and Drive Cycle----------

% Auto required ----------

Auto='LEAF13'; % options for vehicles LEAF12, LEAF13, MiEV, FOCUS, BMWi3,

        %SMART,SOUL,SPARK

vehicle=xlsread(Auto,'B2:B34');  % vehicle parameters loaded except eff maps

mc_map_trq3=xlsread(Auto,'advisor','B2:U2'); % ADVISOR Motor torque range[Nm]

mc_map_spd3=xlsread(Auto,'advisor','A3:A22');% ADVISOR Speed range [rpm]

map_eff3=xlsread(Auto,'advisor','B3:U22');% ADVISOR Efficiency map [%]

% Drive Cycle required ----------

u=xlsread('61403016');  % Options for drive cycles UDDS, HWY, US06, NEDC

% UDDS          drive cycles are %61203033(LEAF12),  61402036(MiEV),   61403019(LEAF13), 61408016(FOCUS) %61505019(BMWi3),   61504017(SMART),  61506042(SOUL),     61508013(SPARK)

%HWY           drive cycles are %61203032(LEAF12),  61402035(MiEV),   61403012(LEAF13), 61408013(FOCUS) %61505021(BMWi3),   61504019(SMART),  61506044(SOUL),     61508015(SPARK)

%US06          drive cycles are %61203034(LEAF12),  61402037(MiEV),   61403016(LEAF13), 61408014(FOCUS) %61505020(BMWi3),   61504018(SMART),  61506043(SOUL),     61508014(SPARK)

 %read the US06 drive cycle speed value [m/s] from Excel     % file called US06.xls.

% Vehicle Parameters Required ----------

M=vehicle(1) ;  % Test weight in kg of vehicle (use curb weight plus 136kg   % if test weight is not known)  % conversion 1 [lbs] = 0.453592 [kg]

Prmax=vehicle(2);  % Max rotor power from electric motor , units [Watts}   % conversion 1 [hp] = 745.699872 [W]

Trmax=vehicle(3);  % Max rotor torque from electric motor , units [Nm}  % conversion 1 [ft lbs] = 1.35581795 [Nm]

Whrad=vehicle(4);  % Wheel radius [m]. Can be calculated from trye size. Example % 220/60R16 16 = wheel rim diameter in [inches], 220 = tyre   % width in [mm] and 60 = tyre depth given as a percentage of % width, so 60% of 220mm in this example.  % conversion 1 [inch] = 0.254 [m], 1 [mm] = 0.001 [m]

Gr=vehicle(5) ;    % Gear ratio. Also called Axle Ratio and Final Drive Ratio

Brated=vehicle(6);   % Rated(ie stated) high voltage (HV) battery capacity [Wh]

Acd=vehicle(7);    % Coast-down coefficient A. Units [N] EPA gives this in [lbs]
```

```
        % conversion 1[ibs] = 0.453592*9.80665 [N]
Bcd=vehicle(8);    % Coast-down coefficient B. Units [N/(m/s)]
%EPA gives this in [lbs/mph]      % conversion 1[ibs/mph] = 0.453592*9.80665/0.44704 [N/(m/s)]
Ccd=vehicle(9);    % Coast-down coefficient C. Units [N/(m^2/s^2)]
% EPA gives this in [lbs/mph^2] % conversion 1[ibs/mph^2]=0.453592*9.80665/(0.44704)^2
[N/(m^2/s^2)]
Bvolt=vehicle(10);  % Maximum value of the battery voltage [V]
Af=vehicle(13) ; % vehicle frontal area specified in meters squared
Cd=vehicle(14);
% Constants Assumed (taken from FASTSim veh_model worksheet, constants list)----------
g=9.81;    % gravity in [m/s^2]
rho=1.2;   % density of air [kg/m^3]
% Vehicle Parameters Assumed-----------------------------------------------------------------------------
Paux=vehicle(11)  ;    % assumes zero speed battery power is 200W
Bat_eff=vehicle(17);   % assumes battery efficiency of 91%
Inv_eff=vehicle(21);   % assume inverter (motor drive) efficiency of 98%
Mot_eff=vehicle(20);   % assumes motor efficiency of 97%
Gr_eff=vehicle(18) ;   % assumes gear efficiency of 97%
Bcap=Brated*vehicle(22);    % assumes only 85% of the battery capacity is usable
Mot_ph=vehicle(23);        % assumed motor power factor
R_batt=vehicle(12);    % assumes an internal battery efficiency of 0.1 [ohms]
J=vehicle(16)  ;         % total inertia of wheels plus rotating components
   % NOTE J is given per wheel in FASTSim but it is assumed
Jmot=0.01; % Motor inertia used in ADVISOR model only
Crr=vehicle(15); % Rolling road coefficient
x1m=vehicle(24); % reading motoring poly coeffients
x2m=vehicle(25);
x3m=vehicle(26);
x4m=vehicle(27);
x5m=vehicle(28);
x1b=vehicle(29); % reading Braking poly coeffients
x2b=vehicle(30);
x3b=vehicle(31);
```

```
x4b=vehicle(32);

x5b=vehicle(33);

%Motor and Controller loss parameters for SEVP----------------------------------------------------------

Pmot_max=Prmax/Mot_eff; % maximum motor input power = inverter output power

Pinv_max=Pmot_max/Inv_eff ;     % max inverter input power

Pbat_max = Pinv_max/Bat_eff;    % max battery power

I_bat_max=Pbat_max/Bvolt   ;    % max battery current = Pmax/ Vmax

Vinv_min=Pinv_max/I_bat_max ;   % min inverter input voltage

Vphase=1.15*Vinv_min/(2*sqrt(2)); % motor phase voltage using an assumed % derating value of 0.7

Iphase=Pmot_max/(3*Vphase*Mot_ph); % motor phase current with assumed derating

Mot_rs=(Pmot_max-Prmax)*0.75/(3*(Iphase^2));  % Motor stator resistance.

            % Assumes 75% of motor loss is in stator winding resistance

Mot_core=(Pmot_max-Prmax)*0.25;     % assume 25% of motor loss is in core

wbase=Prmax/Trmax ;           % base angular speed of the motor

Tnl=Mot_core/wbase;           % no load motor torque

k=(Trmax+Tnl)/(3*Iphase);   % machine constant k   (T =I*k)

% FASTSim Motor\Controller Polynomial Coefficient determination-----------------------------------------

%Motor plus controller loss for FASTSim using polynomial dervived in this % script file

small_adj=-0.06*log(Prmax/1000)+0.24;

poly_pa=[0 9 65 100]; % specified motor outputs given as % e.g 65% of Prated

poly_pa(2)=9+(small_adj*10)*(small_adj>0); % this is an adjustment in FASTSim where

% the 9% point is adjusted upwards when the motor rating is below 54kW

poly_pb=[0.3 0.86 0.88 0.86]; % motor efficiency at specified outputs given above

x1=0:0.1:0.8;  % high detail required between 0% to 0.8% power out, 0.1% steps

x2=1:1:5;   % slightly less detail between 1% to 5% power out, 1% steps

x3=5:5:100; % less detail between 5% to 100% power out, 5% steps

xi=[x1 x2 x3]; % combine the various step sizes into one interpolation range

yi=interp1(poly_pa,poly_pb,xi); % yi contains the interpolated efficiency

        %between 0% output  to 100% power output

Pout_poly= xi*Prmax/1000*0.01;    % range of power outputs from 0 to Prated.

        %Multiplier 0.01 used as variable "a" should be percentages

Pin_interp=Pout_poly./yi;    % interpolated power input values based on     %interpolated efficiency
values We now have a range of data points where     %x,y is either Pin,Pout (when motoring) or
Pout,Pin (when braking). Now need    % to develop two polynomials for these situations
```

```
%Poly_m=polyfit(Pout_poly,Pin_interp,4); % a 4th order polynomial for motoring

% In the datapoints (Pin_interp,Pout), we know Pin_interp is the larger% value. So in motoring mode we will calculate the Pout required and then% use the polynomials to calculate the larger input power value.

%Poly_b=polyfit(Pin_interp,Pout_poly,4); % a 4th order polynomial for braking% during braking the rotor power is higher than the input power so we have% to reverse our data points by thinking of Pin_interp as the rotor power% and Pout as the power coming out of the inverter to the battery.

% ALTERNATIVE POLYNOMIALS----------------------------------------------------------------------------

Poly_m=[x1m x2m x3m x4m x5m];

Poly_b=[x1b x2b x3b x4b x5b];

%  ******           end of polynomial determination       *******

%Drive cycle for this test was loaded above. Here the max time for the cycle % is calculated

tmax=length(u); % last time step in drive cycle. Uses 600 (US06), 765 (HWY)    % 1369 (UDDS) 1200 (NEDC) or a custom value for special       % drive cycle tests

%Initilisation of parameter vectors-----------------------------------------------------------------

a=zeros(1,tmax);       % acceleration of vehicle

u_ave=zeros(1,tmax);    % average time step speed in ADVISOR [m/s]

Frd=zeros(1,tmax);     % road force at constant speed

F_veh=zeros(1,tmax);    % Advisor vehicle force = Frr+Faero+Faccel

Paero=zeros(1,tmax);    % aerodynamic power required (std equations)

Paccel=zeros(1,tmax);   % acceleration power required (std equations)

Proad=zeros(1,tmax);    % Paero + Paccel (add Pgrade here also)

Regen_frac=zeros(1,tmax);% fraction of brake torque available for regen(advisor)

Taxle1=zeros(1,tmax);   % axle torque (coastdown coefficients)

Taxle2=zeros(1,tmax);   % axle torque (std equations)

Taxle3=zeros(1,tmax);   % axle torque (as calculated in ADVISOR)

Taxle3_brake=zeros(1,tmax);   % axle torque available for regen (ADVISOR)

w_axle1=zeros(1,tmax);   % axle speed in [rad/s] using u(n)/Whrad

w_axle2=zeros(1,tmax);  % axle speed in [rad/s]

w_axle3=zeros(1,tmax);  % axle speed in [rad/s] used in ADVISOR with slip

w_axle_ave=zeros(1,tmax); % axle speed in [rad/s] using average speed U_ave(n)

Paxle1=zeros(1,tmax);   % axle power required (coastdown calculation)

Paxle2=zeros(1,tmax);   % Proad+Prolling+Pinertia (std equations)

Paxle3=zeros(1,tmax);   % Proad+Prolling+Pinertia (ADVISOR std equations)

Tr1=zeros(1,tmax);     % torque at motor rotor (coastdown calculation)
```

```
Tr2=zeros(1,tmax);     % torque at motor rotor (std equations)
Tr3=zeros(1,tmax);     % torque at motor rotor (ADVISOR std equations)
w_rot=zeros(1,tmax);   % Rotor speed in [rad/s]
Speed=zeros(1,tmax);   % Rotor speed in [rpm]
Speed3=zeros(1,tmax);  % Rotor speed in [mph] for ADVISOR regen
Pr1=zeros(1,tmax);     % Rotor power required (coastdown calculation)
Pr2=zeros(1,tmax);     % Power at motor rotor (std equations)
Pr3=zeros(1,tmax);     % Power at motor rotor (ADVISOR std equations)
Pin_mot=zeros(1,tmax); % power at the input to the motor
Pinv_loss=zeros(1,tmax);% power loss in the inverter
Pinv1=zeros(1,tmax);   % power at the input to the inverter (SEPV model)
Pinv2=zeros(1,tmax);   % power at the input to the inverter (FASTSim)
Pinv3=zeros(1,tmax);   % power at the input to the inverter (ADVISOR)
Pgross1=zeros(1,tmax); % Power while motoring periods only (SEVP)
Pgross2=zeros(1,tmax); % Power while motoring only (FASTSim)
Pgross3=zeros(1,tmax); % alternative mc calculation motoring only (ADVISOR)
Pregen1=zeros(1,tmax); % Power during regeneration (SEVP)
Pregen2=zeros(1,tmax); % Power during regeneration (FASTSim poly calculated)
Pregen3=zeros(1,tmax); % Power during regeneration (ADVISOR)
Pbat1=zeros(1,tmax);   % power at battery output (SEVP)
Pbat2=zeros(1,tmax);   % power at battery output (FASTSim)
Pbat3=zeros(1,tmax);   % power at battery output (ADVISOR)
Pnet1=zeros(1,tmax);   % Npower at battery output (SEVP)
Pnet2=zeros(1,tmax);   % Net power at battery output (FASTSim)
Pnet3=zeros(1,tmax);   % alternative mc calculation in ADVISOR
Results=zeros(tmax,8); % setting a results space with 8 columns for values
%Calculation of parameters for each timestep up to end of drive cycle,tmax---------------------------------
Pgross1(1)=Paux; % all the drive cycles start at zero speed but aux load is on
Pgross2(1)=Paux;
Pgross3(1)=Paux;
Frr=M*g*Crr;
for n=2:tmax
    % Torque Loss  due to Bearing friction and Brake drag-----------------------------------------------------
```

```
    % loss is a straight line relationship with vehicle mass, so it can    % be determined by a 1D line interpolation using the vehicle mass
    wh_axle_loss_mass=[0 2000];   % (kg)
    wh_axle_loss_trq=[4 24]*.4;   % (Nm)
    if u(n)==0
      T_loss=0;   % no loss bearings\brakes if vehicle stopped
    else
      T_loss=interp1(wh_axle_loss_mass,wh_axle_loss_trq,M);
    end
  a(n)=u(n)-u(n-1);   % acceleration calculated using retrospective method
  u_ave(n)=(u(n)+u(n-1))/2; % average time step speed if stated speed is  % at end of timestep
  w_axle_ave(n)=u_ave(n)/Whrad; % axle rotating speed in advisor [rad/s]
  w_axle1(n)=w_axle_ave(n); % axle rotating speed [rad/s]if stated speed is % ave time step speed
  w_axle2(n)=w_axle1(n); %  default assigned value. Can redefine later in code.
% Wheel Slip Calculation----------------------------------------------------------------------------------------------
 F_veh(n)=(0.5*rho*Cd*Af*u_ave(n)^2)+(M*a(n))+Frr; % vehicle force
 veh_front_wt_frac=0.59;  % estimated.  Not based on data for this
    % specific vehicle.  Fraction of vehicle weight on front axle when     % standing still.
    veh_front_wt=M*g*veh_front_wt_frac; % the weight [N] of the vehicle  % on the front axle
    abs_F_veh(n)=abs(F_veh(n)); % absolute value of vehicle force
    sgn_F_veh(n)=sign(F_veh(n));% sign of vehicle force
    slip_force_coeff(n)= abs_F_veh(n)/veh_front_wt; % Needs max and min   % limits for this derived slip force coeff before using it to find    % the related wheel slip value using 1D interpolation.
    wh_slip_force_coeff=[0 0.3913 0.6715 0.8540 0.9616 1.0212];  % range
    if slip_force_coeff(n)>max(wh_slip_force_coeff)
      slip_force_coeff(n)=max(wh_slip_force_coeff);
    elseif slip_force_coeff(n)<min(wh_slip_force_coeff)
      slip_force_coeff(n)=min(wh_slip_force_coeff);
    end
    % now use linear interpolation to determine the slip value with x - % axis (wh_slip_force_coeff) and y axis (wh_slip)
    wh_slip=[0.0 0.025 0.050 0.075 0.10 0.125];  % range of slip values
    slip(n)=interp1(wh_slip_force_coeff,wh_slip,slip_force_coeff(n));
```

```
    % need to modify the axle speed using the following equation if you    % want to include impact
of slip
    % w_axle3(n)=(1+(slip(n)*sgn_F_veh(n)))*w_axle_ave(n);% the sign of the
    % vehicle force has been added in here again.
  % Calculation method 1  Coastdown using stated mid or average time step speed---------
  if u_ave(n)~=0
    Frd(n)=Acd+Bcd*u_ave(n)+Ccd*u_ave(n)^2; % road force using coastdown parameters
  end
  Taxle1(n)=Frd(n)*Whrad+M*a(n)*Whrad+J*a(n)/Whrad; % total axle torque =
  %sum of road force torque plus acceleration torque plus inertial torque
  % Calculation method 2  Std Equations with averaged time step speed------------------------------
  Paero(n)=0.5*rho*Cd*Af*(u_ave(n))^3; % power loss using speeds values
  Paccel(n)=0.5*M*((u(n)^2)-(u(n-1)^2));%
  Paxle2(n)=Paero(n)+ Paccel(n)+(Frr*u_ave(n)+(0.5*J*(((u(n)/Whrad)^2)-((u(n-1)/Whrad)^2))));
  % Paero+Paccel + Prolling + Pinertia. Pinertia is     % change in rotational kinetic energy
  % Calculation method 3 Std Equations with slip and averaged speeds---------------------------------
  w_axle3(n)=(1+(slip(n)*sgn_F_veh(n)))*w_axle_ave(n);% the sign of the % vehicle force has been
added in here again.
  Taxle3(n)=(F_veh(n)*Whrad)+T_loss+(J*(w_axle3(n)-w_axle3(n-1)));%advisor wheel torque
   % Calculation method 4 Std Equation using stated mid time step speed---------------------------
    Taxle2(n)=(F_veh(n)*Whrad)+(J*a(n)/Whrad);
 % ADVISOR-----------------------------------------------------------------------------------------------
 % using the motor\controller efficiency maps to determine power at input   % of the controller in
either a motoring or regen braking condition.  % This loop is used for ADVISOR calculations
  Paxle3(n)=Taxle3(n)*w_axle3(n);
  w_rot(n)=w_axle3(n)*Gr;     %  Motor rotation speed, advisor [rad/s]
  Speed(n)=w_rot(n)*60/(2*pi); % converting rad/s to rpm
  if Taxle3(n)>=0   % motoring operation
    Tr3(n)=(Taxle3(n)/Gr/Gr_eff)+(Jmot*(w_rot(n)-w_rot(n-1)));    % rotor motoring torque required
    if Tr3(n)>Trmax
      Tr3(n)=Trmax;
    end
  else          % braking operation
```

```
    % ADVISOR assumes some friction braking depending on speed [mph]    % fraction of braking done by driveline, indexed by wh_fa_dl_brake_mph
      wh_fa_dl_brake_frac=[0 0 0.1 0.95 1 1];  %fraction of braking done by
      % front friction brakes,indexed by wh_fa_fric_brake_mph
      %wh_fa_fric_brake_frac=[0.8 0.8 0.4 0.1 0.1];    % (--)
      wh_fa_dl_brake_mph=[-1 0 5 10 15 1000];          % (mph)
      %wh_fa_fric_brake_mph=wh_fa_dl_brake_mph;       % (mph)
      speed3(n)=u_ave(n)/0.447; %*2.23694;   % convert m/s to mph for regen fraction
      Regen_frac(n)=interp1(wh_fa_dl_brake_mph,wh_fa_dl_brake_frac,speed3(n));
      Taxle3(n)=Taxle3(n)*Regen_frac(n);
      Tr3(n)=(Taxle3(n)/Gr*Gr_eff)+(Jmot*(w_rot(n)-w_rot(n-1)));
                % rotor motoring torque available for regen
      if Tr3(n)<-Trmax  % Had to impose a torque limit due to efficiency map
       Tr3(n)=-Trmax;   % range....need to fix in future versions
      end
    end
    Pr3(n)=Tr3(n)*w_rot(n); % calculated rotor power required
    % Alternative Calculation of Motor\Controller loss for advisor----------------------------------------
    % this is based on what is done in ADVISOR script.Commands taken    % directly from ADVISOR file unless comments added
    mc_map_trq=mc_map_trq3;     % converting to same variable as ADVISOR
    mc_map_spd=mc_map_spd3*2*pi/60; % converting to ADVISOR values for speed range
    mc_eff_map=map_eff3;       % converting to same variable as ADVISOR
    [temp_T,temp_w]=meshgrid(mc_map_trq,mc_map_spd);
    temp_mc_outpwr_map=temp_T.*temp_w;
    temp_mc_losspwr_map=(1./mc_eff_map-1).*temp_mc_outpwr_map.*(temp_T>0)+...
    (mc_eff_map-1).*temp_mc_outpwr_map.*(temp_T<0);
    temp_zti=find(mc_map_trq==0);
    temp_zsi=find(mc_map_spd==0);
    if ~isempty(temp_zti)
       temp_mc_losspwr_map(:,temp_zti)=temp_mc_losspwr_map(:,temp_zti+1);
    end
    if ~isempty(temp_zsi)
       temp_mc_losspwr_map(temp_zsi,:)=temp_mc_losspwr_map(temp_zsi+1,:);
```

```
  end
  % compute input power (power req'd at electrical side of motor/inverter set)
  mc_inpwr_map=temp_mc_outpwr_map+temp_mc_losspwr_map;
  Pinv3(n)=interp2(mc_map_trq,mc_map_spd,mc_inpwr_map,Tr3(n),w_rot(n));
  if abs(w_rot(n))<0.001
    Pinv3(n)=0;
  end
  Pbat3(n)=Pinv3(n)+Paux;
 % FASTSim----------
 % Next loop only used for FASTSim calculations where both polynomial  % coefficients that are copied from the FASTSim model using xlsread and  % polynomial coefficients calculated in this script
 if Paxle2(n)==0
    Pinv2(n)=0; % this loop copies what is done in FASTSim.Otherwise there is  % large error in the UDDS energy calculation
 end
 if Paxle2(n)>0
    Pr2(n)=Paxle2(n)/Gr_eff; % motoring condition. Motor rotor power     % the combined motor\inverter polynomial calculates the Power at the inverter input
    if Pr2(n)>Prmax
      Pr2(n)=Prmax;
    end
    Pr2_kw(n)=Pr2(n)/1000;
   Pinv2_kw(n)=polyval(Poly_m,Pr2_kw(n)); % value using derived polys
   Pinv2(n)=Pinv2_kw(n)*1000;
 else
    % negative Paxle implies braking. FASTSim adds a friction braking model     % in here that determines the percentage of axle power available based     % on the vehicle speed
    fregen = 1/(1+(1000*exp(-0.9*((u_ave(n)/0.447)+1)))); % see my notes on FASTSim     % friction braking model. Above values assume max regen =100% and   constant A=2800, B=1.98 for speed in m/s
   Pr2(n)=Paxle2(n)*fregen*Gr_eff; % regeneration condition. Motor rotor power using the combined motor\inverter polynomial to calculate the power at inverter input
   if Pr2(n)<-Prmax
     Pr2(n)=-Prmax;
    end
   Pr2_kw(n)=Pr2(n)/1000;
```

```
  Pinv2_abs_kw(n)=polyval(Poly_b,-Pr2_kw(n)); % using derived poly values
  Pinv2(n)=-Pinv2_abs_kw(n)*1000;
  if Pinv2_abs_kw(n)<(-Pr2(n)/1000*0.3) % to eliminate getting a power in
    % for zero rotor power due to the constant term in the polynomial
    Pinv2(n)=Pr2(n)*0.3;
  end
  % regeneration power only to battery
 end
  Pbat2(n)=Pinv2(n)+Paux;% using derived poly values
% SEVP   % This loop is used for SEVP calculations----------------------------------------------------------------------
 Paxle1(n)=Taxle1(n)*w_axle1(n); % axle power = axle torque * angular speed
  if Taxle1(n)>=0   % motoring operation
    Tr1(n)=Taxle1(n)/(Gr*Gr_eff);   % rotor motoring torque required
    Pr1(n)=Paxle1(n)/Gr_eff;  % rotor power = axle power/gearbox efficiency
  else          % braking operation
    Tr1(n)=Taxle1(n)*Gr_eff/Gr;      % rotor motoring torque available for regen
    Pr1(n)=Paxle1(n)*Gr_eff;  % rotor power = axle power*gearbox efficiency
  end
  Pin_mot(n)=Pr1(n)+(3*((Tr1(n)/(3*k))^2)*Mot_rs)+(w_axle1(n)*Gr*Tnl);% adding the motor
  % loss to the rotor power determines the power at the input to the   % motor. During motoring
rotor power is positive so loss causes input   % power to be larger. During braking, rotor power is
negative so input   % power is lower when losses are added   %
  % calculate inverter losses; This is done by taking the maximum   % inverter loss (based on
assumed efficiency) and multiplying this by   % the ratio of actual torque to the max torque. This is
the same as the   % ratio of actual current to maximum current.
  Pinv_loss(n)=(Pinv_max-Pmot_max)*Tr1(n)/Trmax;
  % need to determine if the motor input power is positive (motoring) or   % negative (braking) and
then use another IF-ELSE_END loop to calculate   % the power input to the inverter
  if Taxle1(n)>=0   % motoring operation or very low regen power (<motor loss)
  Pinv1(n)=Pin_mot(n)+Pinv_loss(n);   % add the inverter loss to the motor input power
  else
  Pinv1(n)=Pin_mot(n)-Pinv_loss(n);   % subtract the inverter loss from the regen   % motor input
power to calculate regen power available at battery input   % Negative sign used here as inverter
loss will be calculated as a   % negative value if Tr is negative, so neg sign converts this loss to a   %
positive value that reduces the regen power available   % Paux always positive which when added to
the regen   % power (negative power value) effectively lowers this regen power to   % the battery
```

```
    end
    Pbat1(n)=Pinv1(n)+Paux;
    % sorting battery power out into motoring and regen power for all simulators used
    %SEVP
    if Pbat1(n)>=0
       Pgross1(n)=Pbat1(n);
    else
       Pregen1(n)=Pbat1(n);
    end
    %FASTSim
     if Pbat2(n)>=0
       Pgross2(n)=Pbat2(n);
    else
       Pregen2(n)=Pbat2(n);
     end
     %ADVISOR
     if Pbat3(n)>=0
       Pgross3(n)=Pbat3(n);
    else
       Pregen3(n)=Pbat3(n);
     end
    % Net power values----------------------------------------------------------------------------
    Pnet1(n)=Pgross1(n)+Pregen1(n); % net power out of battery
    Pnet2(n)=Pgross2(n)+Pregen2(n);
    Pnet3(n)=Pgross3(n)+Pregen3(n);
end
%Printout Section; Start by doing an excel printout-------------------------------------------------
%combine all vector variables of interest into one array called Results
Results(:,1)=Pregen1;
Results(:,2)=Pgross1;
Results(:,3)=Pregen2;
Results(:,4)=Pgross2;
Results(:,5)=Pregen3;
```

```
Results(:,6)=Pgross3;
%Results(:,7)=Pr3;
%Results(:,8)=Pbat3;
xlswrite('test_result',Results);
%xlswrite('test_result',mc_inpwr_map,'mc_map','B3:U22');
% Summarise the drive cycle results
distance=sum(u);
gross_wh1=sum(Pgross1)/3600 % SEVP net energy results summary
regen_wh1=sum(Pregen1)/3600   % SEVP gross energy results summary
%net_wh2=sum(Pbat2)/3600 % FASTSim net energy results summary
gross_wh2=sum(Pgross2)/3600 % FASTSim gross energy results summary
regen_wh2=sum(Pregen2)/3600 % FASTSim gross energy results summary
%net_wh3=sum(Pbat3)/3600 % FASTSim net energy results summary
gross_wh3=sum(Pgross3)/3600 % FASTSim gross energy results summary
regen_wh3=sum(Pregen3)/3600 % FASTSim gross energy results summary
%aux_wh=Paux*tmax/3600;
%end of model
% Revision History
% Version 0  This was just a combination of SEVP, FASTSim models using both % imported
polynomial values (copied from FASTsim model) and calculated % polynomial values.
% Version 1 ADVISOR efficiency maps added to vehicle excel files and are % used to calculate the
cycle energy for each vehicle.
```

APPENDIX C

This appendix contains supplementary material for chapter 5. This appendix mainly contains data for the three Toyota/Lexus HEV IPM motors including: **C.1** FEMM model images for the 2010 Prius, 2007 Camry and 2008 LS600h ; **C.2** the back-emf waveforms, **C.3** the L_q and L_d inductances; **C.4** the locked-rotor torques; **C.5**, **C.6**, **C.7** ORNL efficiency maps; and **C.8** the cogging torques. Sample Matlab scripts developed for FEMM model testing are also provided for: **C.9** back-emf testing; **C.10** determining the L_q and L_d inductances; **C.11** locked-rotor torque testing; and **C.12** iron loss testing.

C.1 FEMM Models for Three HEV Motors

These are the FEMM models for the three IPM motors for HEVs.

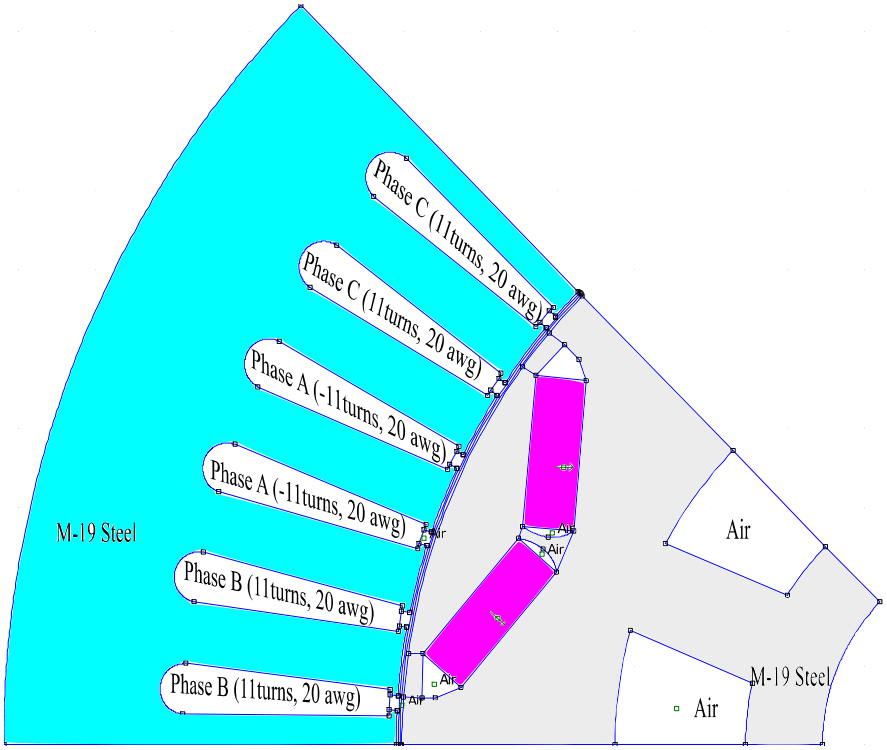

Figure C-1(a). FEMM model of one pole for 2010 Prius motor.

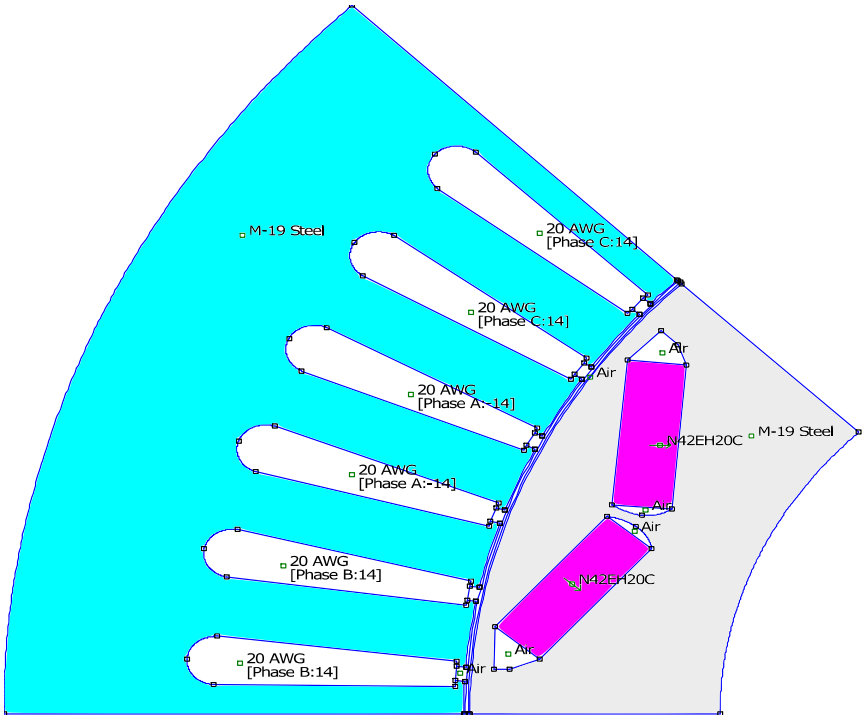

Figure C-1(b). FEMM model of one pole for 2007 Camry motor.

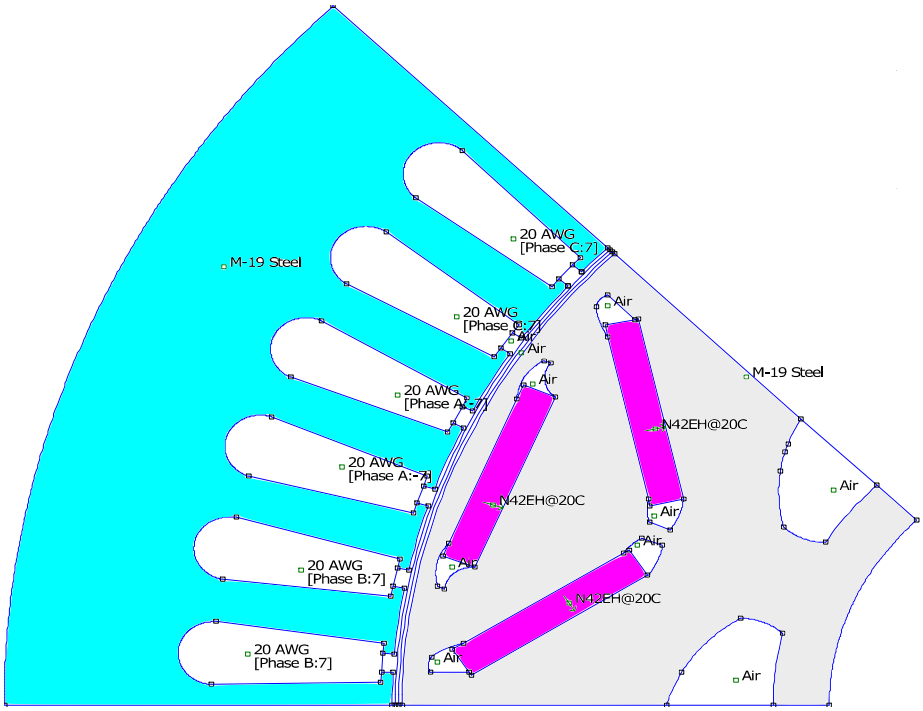

Figure C-1(c). FEMM model of one pole for 2008 LS600h motor.

C.2 Back-emf Test Waveforms

These are the back-emf waveform produced from the FEMM models.

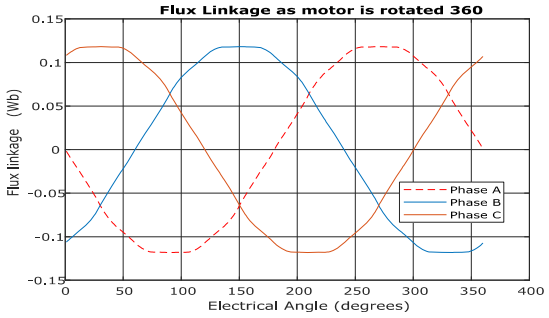

Figure C-2(a). 2010 Prius back-emf waveforms.

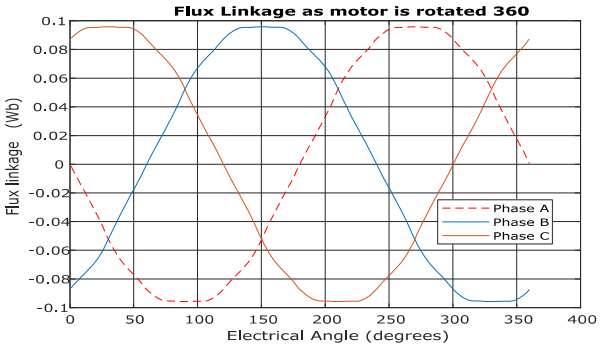

Figure C-2(b). 2007 Camry back-emf waveforms.

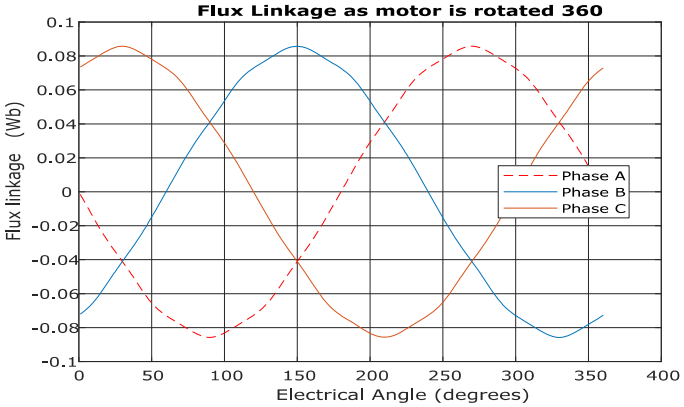

Figure C-2(c). 2008 Lexus LS600h back-emf waveforms.

C.3 Inductance Estimates

These are the dq axis inductance estimates from the FEMM models.

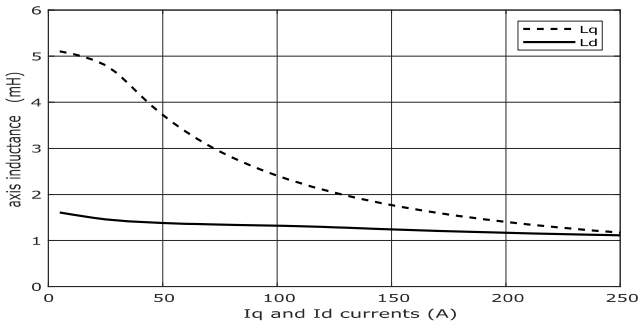

Figure C-3(a). Inductances L_q and L_d for 2004 Prius.

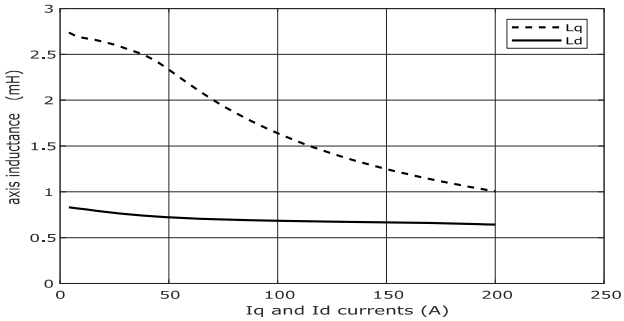

Figure C-3(b). Inductances L_q and L_d for Camry.

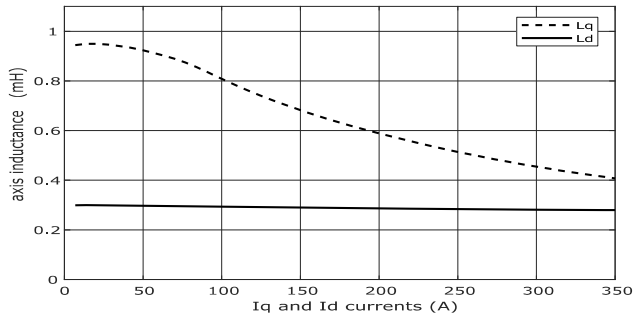

Figure C-3(c). Inductances L_q and L_d for Lexus LS600h.

C.4 Locked Rotor Torque Results

Comparison of FEMM model torques to ORNL locked rotor measurements.

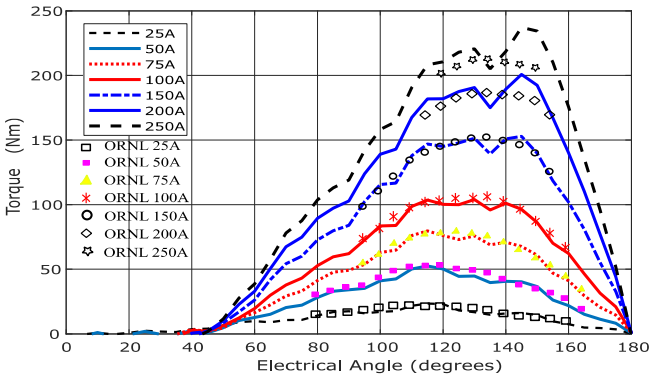

Figure C-4(a). 2010 Prius locked rotor torques.

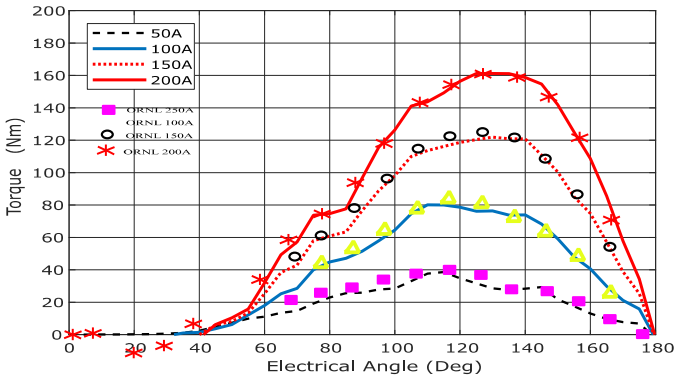

Figure C-4(b). 2007 Camry locked rotor torques.

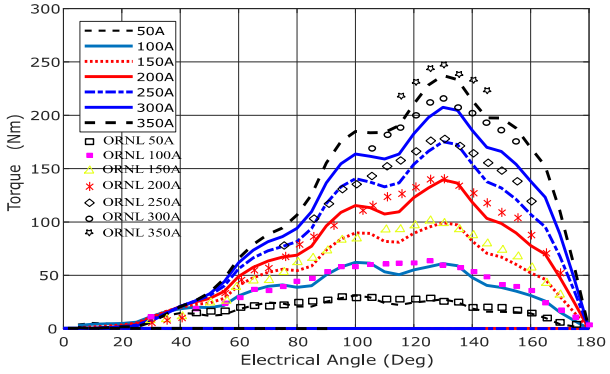

Figure C-4(c). 2008 Lexus LS600h locked rotor torques.

C.5 ORNL Efficiency Maps for 2010 Prius

2010 Prius motor, inverter and combined efficiency maps taken from ORNL.

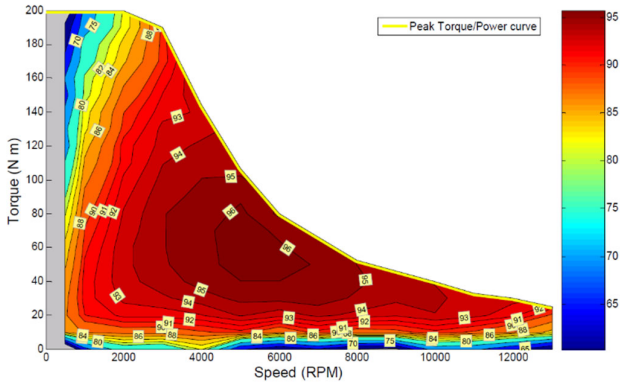

Figure C-5(a). 2010 Prius motor efficiency at 650Vdc.

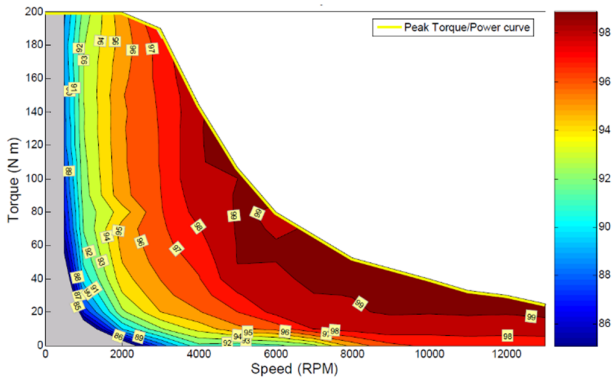

Figure C-5(b). 2010 Prius inverter efficiency at 650Vdc.

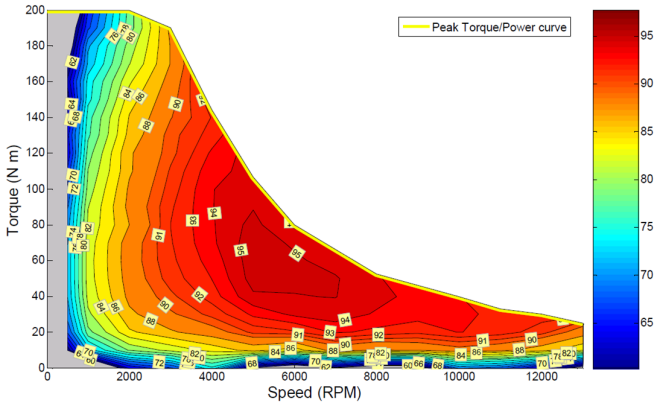

Figure C-5(c). 2010 Prius combined motor and inverter efficiency.

C.6 ORNL Efficiency Maps for 2007 Camry

2007 Camry motor, inverter and combined efficiency maps taken from ORNL.

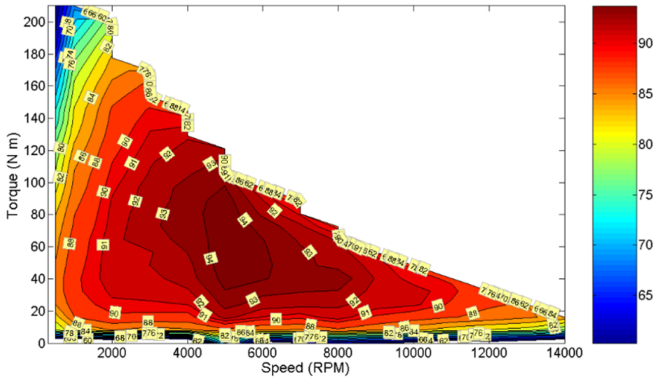

Figure C-2 Camry motor efficiency.

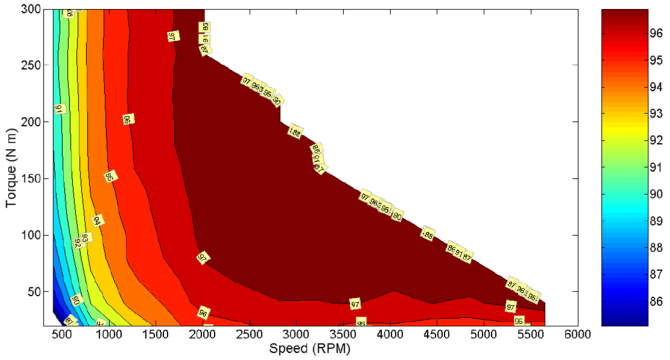

Fig. 3.20. 2007 Camry inverter efficiency contours scaled by 2.47.

Figure C-6(b). Camry inverter efficiency.

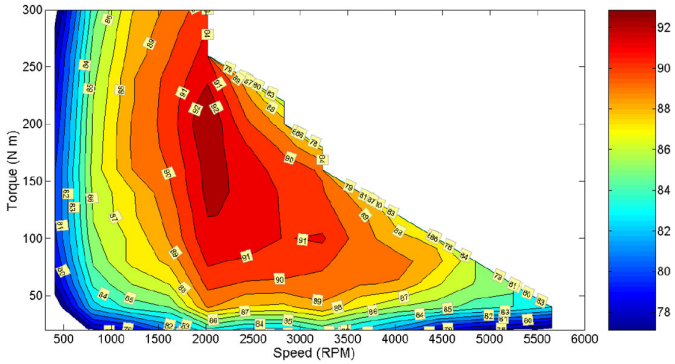

Figure C-6(7). Camry combined motor and inverter efficiency.

C.7 ORNL Efficiency Maps for 2008 Lexus LS600h

2008 Lexus LS600h motor, inverter and combined efficiency maps from ORNL.

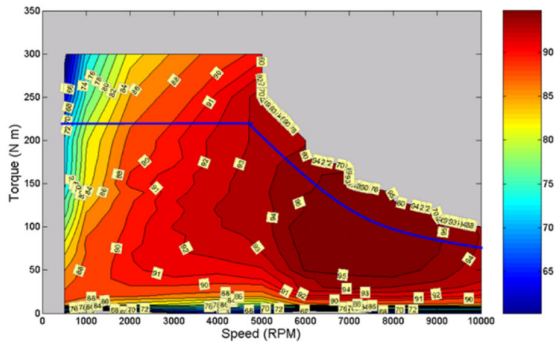

Figure C-7(a). Lexus LS600h motor efficiency

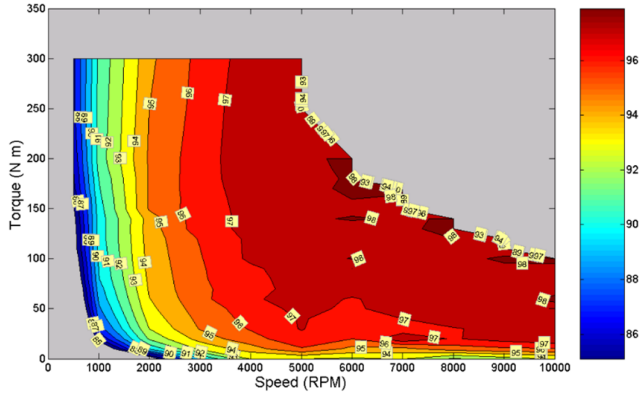

Figure C-7(b). Lexus LS600h inverter efficiency map.

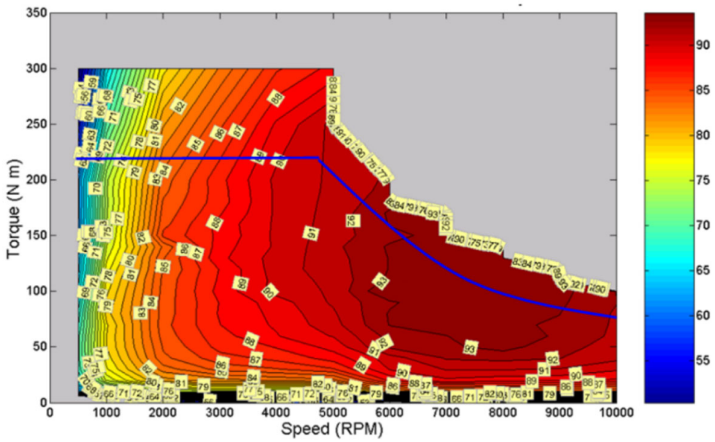

Figure C-7(c). Lexus combined motor and efficiency map.

C.8 Cogging Torques Measured

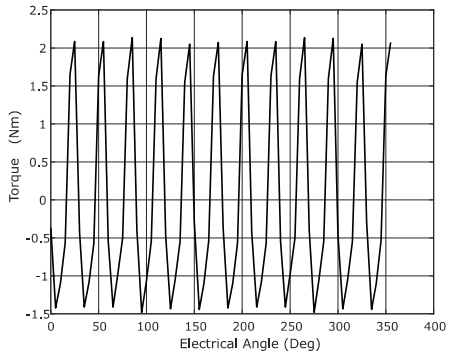

Figure C-8(a). Prius IPM motor cogging torque.

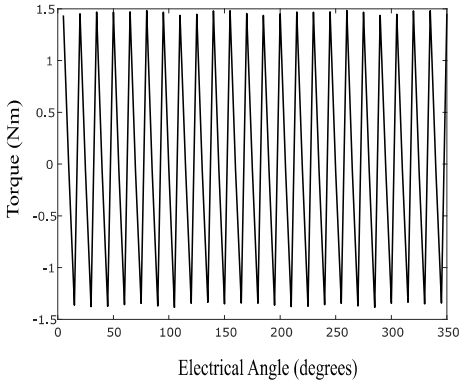

Figure C-8(b). Leaf IPM motor cogging torque.

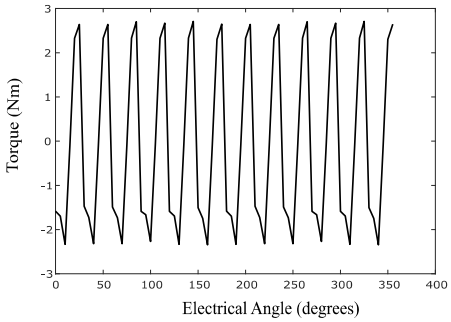

Figure C-8(c). Camry IPM motor cogging torque.

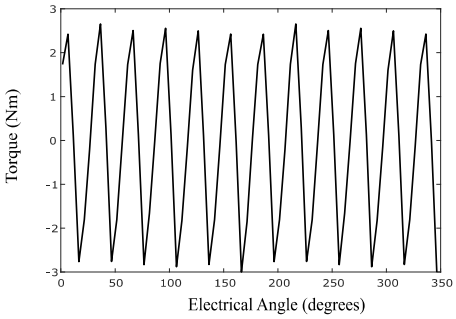

Figure C-8(d). LS600h IPM motor cogging torque.

C.9 MATLAB Code for Back-emf Measurement

```
% Measuring the back emf of the 2012 LEAF. Measure the flux in each
phase % coil as the motor is turned 360 degrees. Total flux depends
on the number % of coils in series. Use these flux measurements to
develop a back-emf % matrix where each row is a speed value and each
column is one deg of % rotation. Finally convert the back-emf values
in each row into one RMS % value for plotting. Plot both LL and LN
Back-emf values. %Only the FEMM file name, max speed and the number
of legs in parallel must % be changed for each motor. % The FEMM
model for the leaf motor is modelled using only half the rotor % so
the final inductance values must be multplied by two in the code. %
this is done by applying a parameter Full_length to the flux values
% written by Kevin Davis August 2019

femmModel='2012_LEAF_sliding.fem';

openfemm(1);

opendocument(femmModel);
```

```
mi_smartmesh(0);
mi_saveas('temp.fem');
Full_length=2; %multiplier to convert results for full rotor length
degToRad=pi/180.;
Rotor_pos=90;%rotor initially at 90 elec deg to phase A
offset=Rotor_pos; %convert to mech radians
Poles=8;
Parallel=4;
Series=Poles/Parallel;
Speedmax=10390;      %rpm maximum speed
Idc=0;         % we want to rotate motor by 360 electrical deg
cols=360;  % setting number of matrix cols to one per rotation deg
Elec_deg=zeros(1,cols);
We_max=Speedmax*(pi/30)*(Poles/2); % speed converted to [rad/s]
Steps=50;            %50 speed testpoints
rows=Steps;         % matrix rows depend on number of speed steps
Bemf=zeros(rows,cols);
Speed=zeros(rows,1);
%Initialise the vector arrays and matrix to zero
Flux_A=zeros(1,cols); Flux_B=zeros(1,cols); Flux_C=zeros(1,cols);
Delta_FluxA=zeros(1,cols);   Delta_FluxB=zeros(1,cols);
Delta_FluxC=zeros(1,cols);   LL_fluxA_B=zeros(1,cols);
LL_emfA_B=zeros(rows,cols);  LN_emfA=zeros(rows,cols);
for n=1:cols %measure flux in 3 phases for each deg of 360 rotation
    starttime=clock;
    mi_modifyboundprop('AGE',10,(n/4));%/ 4 for mech deg rotation
    mi_setcurrent('Phase A', Idc);
    mi_setcurrent('Phase B', -Idc/2);
    mi_setcurrent('Phase C', -Idc/2);
    mi_analyze(1);
    mi_loadsolution;

    cct_a=mo_getcircuitproperties('Phase A');
    cct_b=mo_getcircuitproperties('Phase B');
```

```
    cct_c=mo_getcircuitproperties('Phase C');
    Flux_A(n)=cct_a(3)*Series*Full_length;   %
    Flux_B(n)=cct_b(3)*Series*Full_length;
    Flux_C(n)=cct_c(3)*Series*Full_length;
    Elec_deg(n)=n;
    mo_close;
    fprintf('%i of %i : %f seconds
\n',n,cols,etime(clock,starttime));
end
closefemm;
delete('temp.fem');
delete('temp.ans');
%% Post processing measured data (FEMM not reqd, only saved flux
values)
for m=1:rows
for n=1:cols
      if n>(cols-1)% used in final column to allow script to run
    Delta_FluxA(n)=Delta_FluxA(n-1);
    Delta_FluxB(n)=Delta_FluxB(n-1);
    Delta_FluxC(n)=Delta_FluxC(n-1);
    else   % calculating change in flux for each 1 deg (rads)
    Delta_FluxA(n)=(Flux_A(n+1)-Flux_A(n))/(degToRad); %phase A
d_flux/d_theta
    Delta_FluxB(n)=(Flux_B(n+1)-Flux_B(n))/(degToRad);
    Delta_FluxC(n)=(Flux_C(n+1)-Flux_C(n))/(degToRad);
    end
    LL_fluxA_B(n)=Delta_FluxA(n)-Delta_FluxB(n);% line flux
    LL_emfA_B(m,n)=LL_fluxA_B(n)*We_max/Steps*m;% LL back-emf
    LN_emfA(m,n)=Delta_FluxA(n)*We_max/Steps*m;%  LN back-emf
end    %end of back-emf calculations for this speed
    Speed(m)=Speedmax/Steps*m; %used only plots
 end   %end of back-emf calculations for all speed  % calculate the
values in each row into an RMS value (used for plots)
    LL_RMS=rms(LL_emfA_B,2);%convert back-emf waveform into RMSvalue
    LN_RMS=rms(LN_emfA,2);% RMS LN value here and RMS LL value above
%% Plot flux in Phases A,B and C and then plot the LL\LN back-emfs
```

```
figure(1);
plot(Elec_deg,Flux_A,'--r'); grid on hold on;
plot(Elec_deg,Flux_B); hold on;
plot(Elec_deg,Flux_C);
xlabel('Electrical Angle [Deg]');
ylabel('Flux linkage   []');
title('Flux Linkage as motor is rotated 360 ');
legend('Phase A','Phase B','Phase C','Location','best');
figure(2);
plot(Speed,LL_RMS,'--r') grid on hold on
plot(Speed,LN_RMS,'b')
xlabel('Speed [rpm]');
ylabel('Voltage rms   [V]');
title('Line to Line and Line to Neutral Back EMFs ');
```

C.10 MATLAB Code for Inductance Measurement

```
%Measuring the Lq and Ld inductances at various currents for 2012
LEAF % Measure Lq inductance first as fem first has the rotor in the
90 elec deg % position for this measurement. Then move rotor by 90
elec deg (90/4=22.5 % mech deg)to measure the Ld value. Before
applying current to the windings % for the Ld measurement, the PM
flux must be measured with zero phase % currents. % Four parallel
paths so current divided, two coils in series % The FEMM model for
the leaf motor is modelled using only half the rotor % so the final
inductance values must be multplied by two in the code..% this is
done using parameter Full_length, % written by Kevin Davis August
2019
clear;
femmModel='2012_LEAF_sliding.fem'; % FEMM file
openfemm(1);
opendocument(femmModel);
mi_smartmesh(0);
mi_saveas('temp.fem');
Full_length=2; % multiplier to get full rotor length without a skew
degToRad=pi/180.;
Rotor_pos=90;%rotor initially at 90 elec deg to phase A
Poles=8;
```

```
Flux_multiplier=2/2; % number of coils in series per parallel path
Idcmax=625; % total dc current applied to either axis (q or d)
steps=50; % number of current samples for induct test in each axis
Ipaths=4;          % parallel paths in stator for dc current
%%Set up the program parameters ----------------------------------
%Elec_rotation=360/5;   % full 360 deg rotation
%Elec_deg=zeros(Elec_rotation,1); %trq1=zeros(Elec_rotation,1);
%Id=zeros(Elec_rotation,1); %Iq=zeros(Elec_rotation,1);
%Flux_d=zeros(Elec_rotation,1); %Flux_q=zeros(Elec_rotation,1);
%% measure q-axis inductance at various currents -------------------
offset=0; % rotor not rotated for Lq measurement (0 elec deg)
tta1 = ((Rotor_pos+offset)*degToRad); % specify rotor position angle
in rads (90 deg rotor opposite stator
   for n=1:steps      %testing multiple I for q axis inductance
       Iphase1=(Idcmax/steps)*n/Ipaths;% set  Idc current for step n
    %starttime=clock;
   %tta = ((offset)*degToRad); % elec radians of position
   % mi_modifyboundprop('AGE',10,((n*5)/4));% starting 91 deg to 180
    mi_setcurrent('Phase A', Iphase1);
    mi_setcurrent('Phase B', -Iphase1/2);
    mi_setcurrent('Phase C', -Iphase1/2);
    mi_analyze(1);
    mi_loadsolution;
    cct_a=mo_getcircuitproperties('Phase A');
    cct_b=mo_getcircuitproperties('Phase B');
    cct_c=mo_getcircuitproperties('Phase C');
    Flux_a1(n)=cct_a(3)*Flux_multiplier;
    Flux_b1(n)=cct_b(3)*Flux_multiplier;
    Flux_c1(n)=cct_c(3)*Flux_multiplier;
    Flux_d1(n)=(2/3)*(Flux_a1(n)*cos(tta1)+Flux_b1(n)*cos(tta1-
2*pi/3)+Flux_c1(n)*cos(tta1+2*pi/3));
    Flux_q1(n)=-(2/3)*(Flux_a1(n)*sin(tta1)+Flux_b1(n)*sin(tta1-
2*pi/3)+Flux_c1(n)*sin(tta1+2*pi/3));
    Id1(n)=(2/3)*(Iphase1*cos(tta1)+(-Iphase1/2)*cos(tta1-2*pi/3)+(-
Iphase1/2)*cos(tta1+2*pi/3));
```

```
    Iq1(n)=-(2/3)*(Iphase1*sin(tta1)+(-Iphase1/2)*sin(tta1-
2*pi/3)+(-Iphase1/2)*sin(tta1+2*pi/3));

    Is1(n)=sqrt(Id1(n).^2+Iq1(n).^2)*Ipaths;% Iphase in this test

    Lq1(n)=(Flux_q1(n)./Iq1(n))*1000*Full_length; % 1000 to convert
value to mH

    mo_close;

    fprintf('%i of %i: Lq %f mH  \n',n,steps,Lq1(n));

   end

%% Rotate the rotor by 90 elec deg for Ld inductance measurements

    offset=90; %90 elec deg rotation required

    mi_modifyboundprop('AGE',10,(offset/4));% /4 is elec to mech deg

    tta2 = ((Rotor_pos+offset)*degToRad); % specify rotor position
in rads (90 deg rotor opposite stator

%% Measure the PM in the d-axis

    mi_setcurrent('Phase A', 0);%set all winding currents to zero

    mi_setcurrent('Phase B', 0);

    mi_setcurrent('Phase C', 0);

    mi_analyze(1);

    mi_loadsolution;

    cct_a=mo_getcircuitproperties('Phase A');

    cct_b=mo_getcircuitproperties('Phase B');

    cct_c=mo_getcircuitproperties('Phase C');

    Flux_a0=cct_a(3)*Flux_multiplier;

    Flux_b0=cct_b(3)*Flux_multiplier;

    Flux_c0=cct_c(3)*Flux_multiplier;

    Flux_d0=(2/3)*(Flux_a0*cos(tta2)+Flux_b0*cos(tta2-
2*pi/3)+Flux_c0*cos(tta2+2*pi/3));

    Flux_q0=-(2/3)*(Flux_a0*sin(tta2)+Flux_b0*sin(tta2-
2*pi/3)+Flux_c0*sin(tta2+2*pi/3));

    Flux_PM=Flux_d0;

     mo_close;

   %% measure d-axis inductance at various currents

   for n=1:steps %testing multiple currents for q axis inductance

       Iphase2=(Idcmax/steps)*n/Ipaths;% set the Idc  for step n

        mi_setcurrent('Phase A', Iphase2);

        mi_setcurrent('Phase B', -Iphase2/2);
```

```
        mi_setcurrent('Phase C', -Iphase2/2);
        mi_analyze(1);
        mi_loadsolution;
        cct_a=mo_getcircuitproperties('Phase A');
        cct_b=mo_getcircuitproperties('Phase B');
        cct_c=mo_getcircuitproperties('Phase C');
        Flux_a2(n)=cct_a(3)*Flux_multiplier;
        Flux_b2(n)=cct_b(3)*Flux_multiplier;
        Flux_c2(n)=cct_c(3)*Flux_multiplier;
    Flux_d2(n)=(2/3)*(Flux_a2(n)*cos(tta2)+Flux_b2(n)*cos(tta2-
2*pi/3)+Flux_c2(n)*cos(tta2+2*pi/3));
    Flux_q2(n)=-(2/3)*(Flux_a2(n)*sin(tta2)+Flux_b2(n)*sin(tta2-
2*pi/3)+Flux_c2(n)*sin(tta2+2*pi/3));
    Id2(n)=(2/3)*(Iphase2*cos(tta2)+(-Iphase2/2)*cos(tta2-2*pi/3)+(-
Iphase2/2)*cos(tta2+2*pi/3));
    Iq2(n)=-(2/3)*(Iphase2*sin(tta2)+(-Iphase2/2)*sin(tta2-
2*pi/3)+(-Iphase2/2)*sin(tta2+2*pi/3));
    Is2(n)=sqrt(Id2(n).^2+Iq2(n).^2)*Ipaths;% phase current in test
    Ld2(n)=((Flux_d2(n)-Flux_PM)./Id2(n))*1000*Full_length; % 1000
to convert value to mH
    mo_close;
    fprintf('%i of %i: Ld %f mH  \n',n,steps,Ld2(n));
   end
closefemm;
delete('temp.fem');
delete('temp.ans');
%% Inductance plot
figure(1);
plot(Is1,Lq1,'--r','Linewidth',1.5)
grid on
hold on;
plot(Is2,Ld2,'-k','Linewidth',1.5)
%hold on;
%plot(Elec_deg,-trq_skew1,'k','Linewidth',1.5)
axis([0 625 0 0.6])
xlabel('Iq and Id currents (A)');
```

```
ylabel('axis inductance   (mH)');

%title('LEAF Torque with and without a skew');

legend('Lq','Ld','Location','NorthEast');
```

C.11 MATLAB Code for Locked-Rotor Torque

```
%Measuring the torque at various current advance angles (5 deg
intervals), % This LEAF motor is modelled at half rotor length and
the torque results, % for the other half are skew by 15 deg (elec)
before being added to the, % first torque measurements. To save
time, several currents are tested by, % storing the results in
different columns. Number of columns= number of, % current tested, %
written by Kevin Davis August 2019

clear;

femmModel='2012_LEAF_sliding.fem';

openfemm(1);

opendocument(femmModel);

mi_smartmesh(0);

mi_saveas('temp.fem');

Inum=13;         % number of current values for tests

Idc=[50 100 150 200 250 300 350 400 450 500 550 600 650]; % total
locked torque dc current values from ORNL

Iphase=Idc/4;   % dc current splits into four phases

Elec_rotation=360/5;   % full 360 deg rotation in 5 deg intervals

Elec_deg=zeros(Elec_rotation,Inum);

trq1=zeros(Elec_rotation,Inum);

trq_shift=zeros(Elec_rotation,Inum);

trq_skew0=zeros(Elec_rotation,Inum);

trq_skew1=zeros(Elec_rotation,Inum);

for m=1:Inum

    x=m;

for n=1:Elec_rotation      %only interested in 90deg to 180deg

    %starttime=clock;

    %tta = ((n+offset)*degToRad); % elec radians of position

    mi_modifyboundprop('AGE',10,((n*5)/4));% elec deg to mech deg,
divide by 4

    mi_setcurrent('Phase A', Iphase(x));

    mi_setcurrent('Phase B', -Iphase(x)/2);
```

```
    mi_setcurrent('Phase C', -Iphase(x)/2);
    mi_analyze(1);
    mi_loadsolution;
 trq1(n,x)=mo_gapintegral('AGE',0);
    Elec_deg(n,x)=(n*5)+90; % want to keep values from 0 to 359 deg
so
    if Elec_deg(n,x)>359 % at 360 and above,  we sub 360 to give
      Elec_deg(n,x)=Elec_deg(n,x)-360;% angle of 0,5, 10, 15 deg etc
    end
    mo_close;
    fprintf('%i of %i :  %i \n',n,Elec_rotation,m);
end
end
trq_shift=circshift(trq1,(15/5),1);% 1 indicates a row shift, 2 for
column shift
trq_skew0=trq1+trq_shift;
trq_skew1=circshift(trq_skew0,(-5/5),1);
% for printing of plots need to shift all matrices by 90 deg or 90/5
=18
% intervals to keep results 0 to 180 deg results in consecutive
rows. This
% avoids a gap in the plotted lines
Elec_deg=circshift(Elec_deg,(90/5)); %Moving to fix Plot issue only
trq_skew1=circshift(trq_skew1,(90/5));%Moving to fix Plot issue only
closefemm;
delete('temp.fem');
delete('temp.ans');
%% Torque plot
figure(1);
plot(Elec_deg(:,1),-trq_skew1(:,1),'k','Linewidth',1.5)hold on;
plot(Elec_deg(:,2),-trq_skew1(:,2),'--r','Linewidth',1.5)hold on;
plot(Elec_deg(:,3),-trq_skew1(:,3),'g','Linewidth',1.5)hold on;
plot(Elec_deg(:,4),-trq_skew1(:,4),'--b','Linewidth',1.5)hold on;
plot(Elec_deg(:,5),-trq_skew1(:,5),'c','Linewidth',1.5)hold on;
plot(Elec_deg(:,6),-trq_skew1(:,6),'--m','Linewidth',1.5)hold on;
plot(Elec_deg(:,7),-trq_skew1(:,7),'y','Linewidth',1.5)grid on
```

```
plot(Elec_deg(:,1),-trq_skew1(:,8),'--k','Linewidth',1.5)hold on;

plot(Elec_deg(:,2),-trq_skew1(:,9),'r','Linewidth',1.5)hold on;

plot(Elec_deg(:,3),-trq_skew1(:,10),'--g','Linewidth',1.5)hold on;

plot(Elec_deg(:,4),-trq_skew1(:,11),'b','Linewidth',1.5)hold on;

plot(Elec_deg(:,5),-trq_skew1(:,12),'--c','Linewidth',1.5)hold on;

plot(Elec_deg(:,6),-trq_skew1(:,13),'r','Linewidth',1.5)hold on;

axis([0 180 0 300])

%xlabel('Electrical Angle (Deg)');

%ylabel('Torque   (Nm)');

%title('LEAF Torque with at 1deg and 5deg');

%legend('50A','100A','200A','300A','400A','500A','625A','Location','
NorthWest');
```

C.12 MATLAB Code for Iron Loss Measurement.

```
% Core loss only file, written in Sept 2019 to try to understand
coreloss, % models in IPM motors for EV, % Kevin Davis

clear

MyModel = '2012_LEAF_sliding.fem';

%Block numbers used in model Air=0 Stator Core=1,winding =2, Rotor
core=10,

%Magnets group numbers start at 11 up to 26

%% Motor details

fraction=1/8;% fraction of motor modelled in Femm

Poles = 8;          % Poles in this motor

Full_length=2; %%LEAF only multiplier as FEMM is a half model to
allow for skew

degToRad=pi/180.; %convert degrees to radians

%% Test conditions

nc=1;       % number of current values to test

Idc= [620]; % four test currents to characterise loss

Isplit=4;% two parallel legs in this motor%%not in Prius motors

angle=130;

Initialdqangle=90;  %model drawn at this dq angle

n = 90;   % mechanical rotation required in degrees

dk = 1;                     % step size in mechanical degrees

wbase=1200/60;              % base speed of Prius 2004

SpeedMin = 100;
```

```
SpeedMax = 10000;

SpeedStep = 100;

%% Winding Losses

PhaseResistance = 0.00567; % from ORNL summary table

TemperatureRise = 100;

PhaseOhmic =
3*(PhaseResistance*(1+TemperatureRise*0.004))*(Idc.^2)/2;

%% conversions and material properties

Ke = 0.530; %M19 Eddy current loss coefficient with units
W/(m^3*Tesla*Hz)

Kh = 143.; % M19 hysteresis loss coefficient with units
W/(m^3*Tesla*Hz)

stack = 0.95; %standard stack lamination factor

%% Starting the FEMM model

openfemm(1);  % 1 in brackets hides the FEMM display

opendocument(MyModel); % Opens the required motor file

mi_smartmesh(0);       % turn off smartmesh to use a coarse mesh
solver

mi_saveas('temp.fem'); % temporary copy of FEMM model

%% Ohmic Losses calculation

for xx=1:nc

Id(xx) = Idc(xx).*cos(angle*degToRad)/Isplit;     % IdcCos(angle)

Iq(xx) = Idc(xx).*sin(angle*degToRad)/Isplit;       % IdcSin(angle)

for kk = 1:round(n/dk)  %Number of steps in rotation

 k=(kk-1)*dk;        % rotor angle in mechanical degree

 mi_modifyboundprop('AGE',10,k);% move rotor k mech deg (anti-clock)

 tta = (((Poles/2)*k)+Initialdqangle)*degToRad; % convert mech deg
to elec radians

 Park_d = [cos(tta), cos(tta-2*pi/3), cos(tta+2*pi/3)];%dq to abc

 Park_q =-[sin(tta), sin(tta-2*pi/3), sin(tta+2*pi/3)];%dq to abc

 Iabc =  Id(xx)*Park_d + Iq(xx)*Park_q; % Park conversion dq to abc

 mi_setcurrent('Phase A', Iabc(1)); % setting new phase currents to

 mi_setcurrent('Phase B', Iabc(2)); % keep space vector constant

 mi_setcurrent('Phase C', Iabc(3));

 mi_analyze(1);

 mi_loadsolution;

 mo_smooth('off');  % turns flux smoothing off

       if (k == 0)% loop only runs at starting rotation position
```

```
            nn = mo_numelements; % number of mesh elements calculated
            b = zeros(floor(n/dk),nn); %Flux Density of each element
            z = zeros(nn,1); %Centroid location of each element
            a = zeros(nn,1); % Area of each element
            g = zeros(nn,1); % Block number of each element
                    for m = 1:nn % fill in vectors z, a and g
                    elm = mo_getelement(m);
                    z(m) = elm(4) + 1j*elm(5);
                    a(m) = elm(6);
                    g(m) = elm(7);
                    end
    probinfo=mo_getprobleminfo; %model length, units etc in variable
    end
        u=exp(1j*k*degToRad); % exponent of mech angle in radians
   for m = 1:nn % storing element data
        if(g(m)<11) %store flux density in all other elements
            b(kk,m) = (mo_getb(real(z(m)),imag(z(m)))*[1;1j]);
        end
    end
   fprintf('%i of %i Current %iA  \n',k,n,Idc(xx));
   % prints to Matlab command window the step number of total steps,
   % the time it took to do this step and the torque value
end % repeat loop until all rotation steps completed
%% Add Up Core Losses
ns=n/dk; %n is total mech degrees rotated, dk is angle of each step
bxfft=abs(fft(real(b)))*(2/ns); %FFT of Flux density (real part)
byfft=abs(fft(imag(b)))*(2/ns); %FFT of Flux density(imaginary part)
bsq=(bxfft.*bxfft) + (byfft.*byfft);% Flux density squared
h = probinfo(3);   % length of FEMM model converted
lengthunits = probinfo(4); % Conversion for model units to meters
v = a*h*(lengthunits^2)/fraction; % calculate volume of each element
     g1=(g==10);
    rotor_flux (:,xx)= bsq*(v.*g1)/stack;
    g2=(g==1);
stator_flux(:,xx) = bsq*(v.*g2)/stack;
mo_close; % close the FEMM  post-processor for this mechanical angle
```

```
end
closefemm;      % all rotations completed, close FEMM software
delete('temp.fem');
delete('temp.ans');
results=[];
for thisSpeed=SpeedMin:SpeedStep:SpeedMax
    thisFrequency = thisSpeed/60; % mechanical speed in Hz
    w=0:(ns-1);
    w=2*thisFrequency*w.*(w<(ns/2));
 rotor_loss = (Kh*w+Ke*w.*w)*rotor_flux*Full_length;%Leafmultiplier
stator_loss = (Kh*w+Ke*w.*w)*stator_flux*Full_length;%Leafmultiplier
total_loss = rotor_loss + stator_loss;
results=[results;thisSpeed,rotor_loss,stator_loss,total_loss];
end
    %filename='TestingSept2019';
    %xlswrite(filename,results,'Sheet1','A1')
%% Loss plot
plot(results(:,1),results(:,14),'-k','Linewidth',1.5);hold on
plot(results(:,1),results(:,15),'b','Linewidth',1.5);hold on
plot(results(:,1),results(:,16),'r','Linewidth',1.5); hold on
plot(results(:,1),results(:,17),'g','Linewidth',1.5);hold on
plot(results(:,1),results(:,18),'c','Linewidth',1.5);hold on
plot(results(:,1),results(:,19),'m','Linewidth',1.5);
%xlabel('Speed, RPM');  %ylabel('Core Losses, Watts');
grid on
%axis([0 6000 0 300]); %title('Loss versus Speed');
%legend('Idc=25A','Idc=50A','Idc=75A','Idc=100A','Idc=150A','Locatio
n','northwest');
```

APPENDIX D

The following is an alphabetical list of the symbols and acronyms used throughout this thesis.

Symbols

Symbol	Description	Units
a	vehicle's linear acceleration	m/s^2
A_{brk}	FASTSim brake profile shape coefficient	
A_{cd}	coast-down test coefficient	
A_{CAL}	a curve-fitting pre-exponential coefficient for calendar ageing	
a_0, a_1, a_2, a_x	coefficients fitted to the test data	
A_f	frontal area	m^2
A_{gm}	Lithium-ion cell generic model coefficient	
$Ah_1, Ah_2, Ah_3, Ah_4, Ah_5$	various ampere-hour discharged capacities	Ah
$Ah_{100\%\mathrm{DoD}}$	ampere-hour throughput value over a test period	Ah
Ah_{FC}	battery fully discharge capacity in ampere-hours	Ah
Ah_{LIFE}	ampere-hour throughput value over battery lifetime	Ah
Ah_{RATED}	rated ampere-hour battery capacity	Ah
Ah_x	battery discharge-capacity at time x	Ah
A_R	battery resistance depth of discharge coefficient	
A_{tre}	Tremblay battery model constant	
B_{brk}	FASTSim brake profile shape coefficient	
B_{cd}	coast-down test coefficient	
B_{gm}	Lithium-ion cell generic model coefficient	
b_0, b_1, b_2, b_x	coefficients fitted to the test data	
BAT_{cost}	battery pack replacement cost	$
B_R	battery resistance depth of discharge coefficient	
B_{tre}	Tremblay battery model constant	

Symbol	Description	Units
C_{cd}	coast-down test coefficient	
C_{gm}	Lithium-ion cell generic model coefficient	
C_{rate}	cycle ageing factor due to *C* rate when cycling	
C_d	drag coefficient	
C_{LLE}	Log Linear Exponential battery model coefficient	
C_0	starting coefficient for C_{rr}	
C_P	polarization capacitance of a battery cell	F
C_{P_BP}	polarization capacitance of a battery pack	F
C_{rr}	tyre rolling resistance coefficient	
C_{spd}	speed and tyre pressure related coefficient for C_{rr}	
dk	max reduction in machine constant during saturation	%
D_{LLE}	Log Linear Exponential battery model coefficient	
e	instantaneous phase to neutral back-emf	V
E_A	battery cell activation energy	J/mol
E_O	Tremblay battery model voltage constant	V
E_{on+off}	Combined turn-on and turn-off energies of the IGBT	J
E_{ph}	per phase back emf (rms value)	V
$E_{ph(rated)}$	per phase back emf at rated speed (rms value)	V
E_{rr}	turn-off energy of the diode	J
E_{VEH}	average vehicle consumption	Wh/km
F_a	vehicle's linear acceleration force	m/s^2
f_{axle_f}	fraction of the tractive force applied to the driven axle	
f_{axle_mg}	fraction of the vehicle's mass on the driven axle	
F_c	road grade or climbing force	N
FC_{cost}	fuel cell replacement cost	$
F_D	aerodynamic drag force	N
F_{inert}	rotational acceleration force	N
F_{LLE}	Log Linear Exponential battery model coefficient	

Symbol	Description	Units
F_R	tyre rolling resistance force	N
$F(SOC)$	battery degradation based on state of charge	
f_{sw}	switching frequency of traction inverter devices	Hz
F_{te}	the tractive force at the wheels	N
F_v	vehicle road-load force using coast-down coefficients	
g	acceleration due to gravity (9.81 m/s^2)	m/s^2
$G(I_{bat})$	battery degradation based on current amplitude	
G_{LLE}	Log Linear Exponential battery model coefficient	
$H2_{cost}$	hydrogen fuel cost	$/g
H_{cB}	operating coercivity of PM	A/m
H_{cJ}	intrinsic coercivity of PM	A/m
i	instantaneous battery cell current	A
i_k	instantaneous battery cell current in kth period	A
I_{bat}	magnitude of the battery current	A
$I_{bat(n)}$	magnitude of the battery current at nth time period	A
$I_{bat(max)}$	maximum battery current	A
i_d	peak phase current in *d*-axis	A
I_d	rms phase current in *d*-axis	A
I_{D_ave}	average diode current	A
I_{dc}	current at input to inverter	A
$I_{dc(n)}$	current at input to inverter at nth time period	A
$I_{dc(max)}$	maximum current at input to inverter	A
I_{D_rms}	rms diode current	A
I_{FC}	fuel cell output current	A
$I_{FC(ref)}$	input current demand to fuel cell controller	A
$I_{FC(MAX)}$	maximum output current of the fuel cell	A
$I_{FC-OPT3}$	optimum output current level of the fuel cell (costs)	A
I_{IGBT_ave}	average IGBT current	A
I_{IGBT_rms}	rms IGBT current	A

Symbol	Description	Units
i_T	test current during battery discharge test	A
$\hat{I}_{ph}$	amplitude of the output phase current	A
I_{ph}	rms output phase current of inverter	A
$I_{ph(n)}$	rms output phase current of inverter at nth time period	A
$I_{ph(max)}$	maximum rms output phase current of inverter	A
i_q	peak phase current in q-axis	A
I_q	rms phase current in q-axis	A
I_{RATED}	rated current of the battery pack	A
I_{ref}	test dc current for device rating	A
I_{test_dc}	locked rotor test dc current value	A
J_{axle}	combined inertia of all the rotating components referenced to the drive axle	kg m^2
k	machine constant	Nm/A
k_α	motor core proximity loss coefficient	
$K_{cathode}$	cell generic model cathode empirical factor	ΩAh
k_e	motor core eddy current loss coefficient	
k_h	motor core iron hysteresis loss coefficient	
K_i	Current dependency exponent for diode, ~0.6	
k_p	linearly decreasing proportional control circuit gains	
k_R	linearly decreasing proportional control circuit gains	
k_{sat}	machine constant in saturation region	Nm/A
k_{sus}	linearly decreasing proportional control circuit gains	
K_{tre}	Tremblay battery model constant	
K_{v_diode}	Voltage dependency exponent for diode, ~0.6	
K_{v_IGBT}	Voltage dependency exponent for IGBT, ~1.3…1.4	
L_d	inductance in d-axis	H
L_{dq}	inductance in d-axis due to change in I_q	H
l_{gap}	length of airgap in motor (rotor to stator)	m
l_{mot}	active magnetic length of the motor.	m

Symbol	Description	Units
$L_{pole-pair}$	inductance of a pole-pair of a motor	H
L_q	inductance in q-axis	H
L_{qd}	inductance in q-axis due to change in I_d	H
L_S	per phase synchronous inductance	H
M	vehicle mass	kg
m	modulation index	
$\dot{m}_{H2}$	H_2 mass flow rate	g/s
N_{coil}	number of turns in stator phase winding	
N_g	gear ratio	
N_{series}	number of cell in series in battery pack	
N_{SWITCH}	number of fuel cell switch-on events	
p	poles of the traction motor	
P_{acc}	low-power accessory loads	W
P_{aux}	auxiliary load power = P_{acc} + P_{HVAC}	W
P_{bat}	power of battery pack at output terminals	W
$P_{bat(n)}$	power of battery pack at terminals in n^{th} time period	W
P_{BP}	internal power of battery pack	W
$P_{BP(rated)}$	internal power of battery pack at rated condition	W
P_{cfw}	core, friction, windage power of motor	W
$P_{cfw(rated)}$	core, friction, windage power at rated condition	W
$P_{D(cond)}$	on-state conduction losses in each inverter diode	W
$P_{D(sw)}$	switching losses in each inverter diode	W
P_{dc}	power at traction inverter input	W
$P_{dc(n)}$	power at traction inverter input at n^{th} time period	W
$P_{dc(rated)}$	power at traction inverter input at rated condition	W
$P_{FC(MAX)}$	maximum output power of the fuel cell	W
P_{FC-NOM}	nominal output power of the fuel cell	W
$P_{FC-OPT3}$	optimum output power level of the fuel cell (costs)	W
$P_{gear(loss)}$	power loss across the gearbox	W

Symbol	Description	Units
P_{HVAC}	Heating ventilation air conditioning power	W
$P_{IGBT(cond)}$	conduction losses in each inverter IGBT	W
$P_{IGBT(sw)}$	switching losses in each inverter IGBT	W
P_{inv}	output inverter power	W
$P_{inv(rated)}$	output inverter power at the rated condition	W
$P_{inv(loss)}$	inverter power loss at any torque output	W
$P_{inv(rated\_loss)}$	inverter power loss at rated torque and power output	W
P_{LINK}	output power from boost converter in FCEV	W
$P_{m(loss)}$	motor power loss	W
$P_{m(rated\_loss)}$	motor power loss at rated condition	W
P_r	motor output power at any operating point	W
$P_{r(n)}$	motor output power at n^{th} time period	W
$P_{r(rated)}$	rated motor output power	W
P_{Rs}	total power loss in series resistance of motor	W
P_{te}	tractive effort power at the wheels	W
Q_{bat}	nominal battery capacity	Ah
$Q_{LIFETIME}$	effective battery throughput	As
Q_{loss}	combined battery capacity loss due to ageing	%
Q_{loss_cal}	battery capacity loss due to calendar ageing	%
Q_{loss_cyc}	battery capacity loss due to cycle ageing	%
r	radius of rotor in motor	m
R	universal gas constant	J/mol K
R_{AVE}	battery cell average internal resistance during a discharge	Ω
R_{BP}	battery pack internal resistance	Ω
R_{BP0}	initial battery pack internal resistance	Ω
r_{CE}	Bulk on-state resistance for IGBT	Ω
Reg_{ach}	fraction achieved with the regenerative braking	
Reg_{ach}	maximum regenerative braking fraction	
r_F	Bulk on-state resistance for diode	Ω
R_{INT}	battery cell internal resistance	Ω

Symbol	Description	Units
R_O	battery cell internal ohmic resistance	Ω
R_{O_BP}	battery pack internal ohmic resistance	Ω
R_P	battery cell internal polarization resistance	Ω
R_{P_BP}	battery pack internal polarization resistance	Ω
R_S	per phase stator series resistance	Ω
r_{wh}	radius of the vehicle's wheels	m
s	wheel slip	
s_f,	wheel slip coefficient	
S_{mot}	input apparent power to the motor	VA
$S_{mot(n)}$	input apparent power to the motor at nth time period	VA
SoC	SOC of the battery at any instant	%
SoC_F	SOC of the battery at the end of the drive cycle.	%
T	ambient temperature in Kelvin	K
t	test time-period	s or days
T_{amb}	ambient temperature in degrees C	°C
T_{axle}	wheel axle torque	Nm
T_{check}	calculated motor torque in IPM model	Nm
TC_{Err}	Diode switching-loss temperature coefficient, ~ .006	(1/°C)
TC_{Esw}	IGBT switching-loss temperature coefficient, ~ .003	(1/°C)
T_j	actual component junction temperature.	°C
T_{nl}	No-load torque of the motor	Nm
T_{pm}	torque output due to permanent magnets	Nm
T_r	output torque of the traction motor	Nm
$T_{r(n)}$	output torque of the traction motor at nth time period	Nm
$T_{r(rated)}$	Rated torque of the motor	Nm
T_{ref}	test junction temperature for device rating	°C
T_S	calculation sample period time	s
T_{sat}	torque value where saturation starts	Nm
T_{sr}	torque output due to synchronous reluctance	Nm
v_{air}	headwind speed	m/s

Symbol	Description	Units
v	vehicle linear speed	m/s
$v_{(n)}$	vehicle linear speed at nth time period	m/s
V_b	voltage at the output of the battery cell	V
$V_{b(OC)}$	open-circuit voltage of the battery cell	V
V_{bat}	voltage at the output of the battery	V
$V_{bat(min)}$	minimum voltage at the output of the battery	V
V_{BP}	battery pack open circuit voltage	V
$V_{BP(min)}$	minimum battery pack open circuit voltage	V
V_{CE0}	threshold on-state voltage for IGBT	V
$V_{cell-max}$	maximum fully-charged cell voltage	V
$V_{cell-min}$	minimum fully-discharged cell voltage	V
v_d	peak phase voltage in *d*-axis	A
V_d	rms phase voltage in *d*-axis	A
V_{dc}	dc voltage at the input to the inverter	V
$V_{dc(min)}$	minimum dc voltage at the input to the inverter	V
V_{F0}	threshold on-state voltage for diode	V
V_{FC}	fuel cell output voltage	V
V_{Ls}	per phase voltage drop across synchronous inductance	V
v_{mph}	vehicle linear speed in miles per hour	miles/h
V_{nom}	nominal cell voltage of a battery	V
V_{ph}	inverter rms output phase voltage	V
$V_{ph(n)}$	inverter rms output phase voltage at nth time period	V
$V_{ph(rated\_min)}$	inverter rms output phase voltage at rated condition	V
$\hat{V}_{ph}$	amplitude of the output phase voltage	V
v_q	peak phase voltage in *q*-axis	V
V_q	rms phase voltage in *q*-axis	V
V_r^O	open circuit reversible battery voltage	V
V_{RC}	voltage drop across cell polarization resistance	V
$V_{RC,k}$	voltage drop across cell polarization resistance in time period *k*	V

Symbol	Description	Units
$V_{RC,k-1}$	voltage drop across cell polarization resistance in time period prior to period k	V
V_{ref}	test dc voltage for device rating	V
$V_{sys-nom}$	nominal voltage of battery pack	V
Z_{leg}	number of parallel paths per phase in motor	
Z_{ser}	number of coils in series per phase in motor	

Symbol	Description	Units
$\$_{CHG}$	cost to fully recharge the battery pack at end of drive	$
$\$_{TOT}$	total costs to complete a drive cycle	$

Symbol	Description	Units
α	fuel cell operating-power degradation coefficient	
α_{axle}	angular acceleration of the drive axle	radians/s^2
α_{mat}	MATLAB battery model curve-fit coefficient	
β_{mat}	MATLAB battery model curve-fit coefficient	
$\delta(t)$	operating function degradation of fuel cell (power)	
δ_0	fuel cell operating-power degradation coefficients	
$\Delta_{BAT}(t)$	degradation of the battery pack	%
$\Delta_{FC}(t)$	degradation of the fuel cell	%
ΔI_d	change in *d*-axis current	A
ΔI_q	change in *q*-axis current	A
Δ_{SWITCH}	degradation rate of the fuel cell for each switch-on	
$\Delta\psi_d$	change in *d*-axis flux linkage	Wb
$\Delta\psi_q$	change in *q*-axis flux linkage	Wb
η_{bat}	efficiency of battery	%
η_{BOOST}	efficiency of dc-dc boost converter at fuel cell output	%
η_{chg}	efficiency of on-board charger	%
η_{gear}	transmission efficiency	%
η_{inv}	inverter efficiency	%
$\eta_{inv(rated)}$	inverter efficiency at the rated condition	%
η_{mot}	motor efficiency	%
$\eta_{mot(rated)}$	motor efficiency at the rated condition	%
η_{peak}	peak motor efficiency in FASTSim	%
η_{ptrain}	overall powertrain efficiency	%
θ	electrical angle of the rotor position	degrees
θ_r	road inclination angle	degrees
μ_0	permeability of free space	H/m
μ_r	relative permeability of material	H/m
ρ	Air density (1.225 kg/m^3)	kg/m^3
τ	RC circuit time constant	s
$cos\ \phi$	assumed power factor of motor	
ψ	flux linkage in one phase winding pole	Wb
ψ_a	flux linkage in phase *a* winding	Wb
ψ_b	flux linkage in phase *b* winding	Wb
ψ_c	flux linkage in phase *c* winding	Wb
ψ_d	flux linkage in *d*-axis	Wb
ψ_f	flux linkage	Wb
ψ_{pm}	flux linkage due to permanent magnets	Wb
$\psi_{pm,d}$	permanent magnet flux linkage in *d*-axis	Wb
$\psi_{pm,q}$	permanent magnet flux linkage in *q*-axis	Wb
ψ_{pole_pair}	flux linkage for each pole-pair in motor	Wb
ψ_q	flux linkage in *q*-axis	Wb
ω_e	electrical angular frequency of motor	radians/s
$\omega_{e(rated)}$	electrical angular frequency of motor at rated condition	radians/s
ω_r	motor speed	radians/s
$\omega_{r(n)}$	motor speed at nth time period	radians/s

Acronyms

ANL	Argonne National Laboratories
ADVISOR	ADvanced Vehicle Simulator
Ah	Ampere-hours
As	Ampere-seconds
BEV	Battery Electric Vehicle
BMS	Battery Management System
BOL	Beginning Of Life
BOP	Balance Of Plant
CdSt	Cold Start test
COO	Cost Of Ownership
CPSR	Constant Power Speed Range
CS	Charge Sustaining
DOD (ΔDOD)	Depth Of Discharge (Change of Depth Of Discharge)
DOE	USA Department Of Energy
DP	Dynamic Programming
ECCE	Energy Conversion Congress and Expo
ECMS	Equivalent Consumption Minimisation Strategies
EEC	Equivalent Electrical Circuit
EMF	Electro Motive Force
EMS	Energy Management Strategy
EPA	Environmental Protection Agency
ESARS	Electrical Systems for Aircraft Railways and Ships
EV	Battery Electric Vehicle
FASTSim	Future Automotive Systems Technology Simulator
FC	Fuel Cell
FCEV	Fuel Cell Electric Vehicle
FCVT	Freedom Car Vehicle Technologies
FEA	Finite Element Analysis
FEMM	Finite Element Method Magnetics
FLC	Fuzzy Logic Controller
FWD	Free Wheeling Diode

HEV	Hybrid Electric Vehicle
HPPC	High Power Pulse Characterisation
HWFET	Highway Fuel Economy Test
ICE	Internal Combustion Engine
IEEE	Institute of Electrical and Electronic Engineers
IET	Institution of Engineering and Technology
IGBT	Insulated Gate Bipolar Transistor
INL	Idaho National Laboratories
IPM	Interior Permanent Magnet
ITEC	International Transportation Electrification Conference
Li-ion	Lithium ion
LLE	Log Linear Exponential
LMO	Lithium ion Manganese Oxide
LUT	Look Up Table
M-Sim	Multi Simulator
MTPA	Maximum Torque Per Amp
MTPV	Maximum Torque Per Volt
NCA	Nickel Cobalt Aluminum oxide
NdFeB	Neodymium Iron Boron
NEDC	New European Drive Cycle
NiMH	Nickel Metal Hydride
NMC	Nickel Manganese Cobalt
OCV	Open Circuit Voltage
ORNL	Oak Ridge National Laboratories
PFCV	Plug-in Fuel Cell Vehicle
PHEV	Plug-in Hybrid Electric Vehicle
PI	Proportional Integral
PM	Permanent Magnet
PMP	Pontryagins Minimum Principle
PMSM	Permanent Magnet Synchronous Motor
PNGV	Partnership for a New Generation of Vehicles
PWr	Power to Weight ratio
RC	Resistor Capacitor

SAE	Society of Automotive Engineers
SCAP	SuperCAPacitors
SEVP	Simplified Electric Vehicle Powertrain
SOC	State Of Charge
SPM	Surface Permanent Magnet
SPWM	Sinusoidal Pulse Width Modulation
SVM	Space Vector Modulation
UDDS	Urban Dynamometer Drive Schedule
US06	US06 Supplemental Federal Procedure
V2G	Vehicle 2 Grid
VTS	Vehicular Technology Society
*VTS*TC	VTS Test Cycle
WLTP	Worldwide harmonised Light Vehicle Test Procedure